université
PARIS-SACLAY

HABILITATION À DIRIGER DES RECHERCHES

The hidden forces of Dark Matter

Habilitation à diriger des recherches de l'Université Paris-Saclay

Habilitation présentée et soutenue à Gif-sur-Yvette, le mercredi 26 juin 2024, par

Camila Anahi CORREA
Département d'Astrophysique, CEA Paris-Saclay

Composition du jury

Membres du jury avec voix délibérative

Hai-Bo YU Professeur, University of California, US	Président/Rapporteur
Paola DI MATTEO HDR, Observatoire de Paris-Meudon, France	Examinatrice
Justin READ Professeur, University of Surrey, UK	Rapporteur
Arianna DI CINTIO Professeure, University de La Laguna, Spain	Examinatrice
Claudio DALLA-VECCHIA Professeur, Instituto de Astrofísica de Canarias, Spain	Rapporteur
Frédéric BOURNAUD HDR, Université Paris-Saclay, France	Examinateur

université PARIS-SACLAY

ÉCOLE DOCTORALE
Astronomie
et Astrophysique
d'Île-de-France (AAIF)

Title: The hidden forces of Dark Matter

Abstract: The nature of dark matter is one of the biggest unsolved mysteries of our time. As the search for the enigmatic particle progresses, in recent years several discrepancies between astronomical observations and theoretical predictions have emerged. One of the most puzzling discrepancies is the diversity in the dark matter distribution within dwarf galaxies, ranging from galaxies having excessively low dark matter to being highly dark matter dominated. From the analyses of the evolution of the dwarf satellites galaxies of the Milky Way, I show in this thesis that the diverse dark matter content in these dwarfs can be driven by non-gravitational interactions between the dark matter particles. These interactions can expand or contract the central dark matter core, which results in an increase (or decrease) of the dark matter content in the galaxies' centre. This scenario called self-interacting dark matter (SIDM) has been motivated by observations of the smallest galaxies, but it lacks a solid observational analysis that demonstrates it or rejects it.

With the support of the TangoSIDM team, I develop a novel implementation of dark matter self-interactions in cosmological simulations, and show that the diverse dark matter content observed in the classical dwarfs satellites galaxies of the Milky Way can be explained with the inclusion of dark matter particles interactions. Additionally, the research conducted by the student Noemi Anau Montel shows that satellites galaxies in the TangoSIDM simulations can reproduce the observed distribution of the classical dwarfs in the density, pericenter and halo mass plane, both under SIDM and CDM. However, observations tend to lean toward supporting the CDM model. These findings highlight the need for additional observational probes to constrain SIDM on the small-scales.

In a subsequent analysis that includes the impact of baryonic physics, I demonstrate that the Tully-Fisher plane, which encompasses galaxy sizes, stellar masses, and circular velocities, can serve as a powerful observable for ruling out velocity-dependent SIDM models. While this finding imposes strong constraints on velocity-dependent models, it does not entirely rule them out. The research comprised in this thesis presents a significant advancement in the exploration of the SIDM parameter space. In light of forthcoming more precise cosmological probes and dark matter detection experiments, the concluding chapter of this thesis proposes new strategies and ideas with the goal of gaining insights into the hidden forces of dark matter, impacting models of early universe cosmology, galaxy formation, and physics beyond the Standard Model.

université PARIS-SACLAY

ÉCOLE DOCTORALE
Astronomie
et Astrophysique
d'Île-de-France (AAIF)

Titre: Les forces cachées de la matière noire

Résumé: La nature de la matière noire est l'un des plus grands mystères non résolus de notre époque. Alors que la recherche de cette particule énigmatique progresse, ces dernières années, plusieurs divergences entre les observations astronomiques et les prédictions théoriques sont apparues. L'une des divergences les plus troublantes concerne la diversité dans la distribution de la matière noire au sein des galaxies naines, allant de galaxies ayant une matière noire excessivement faible à celles étant fortement dominées par la matière noire. À partir des analyses de l'évolution des galaxies satellites naines de la Voie lactée, je montre dans cette thèse que la diversité de la matière noire dans ces naines peut être due à des interactions non gravitationnelles entre les particules de matière noire. Ces interactions peuvent étendre ou contracter le noyau central de matière noire, ce qui entraîne une augmentation (ou une diminution) du contenu de matière noire au centre des galaxies. Ce scénario appelé matière noire auto-interagissante (SIDM) a été motivé par des observations des plus petites galaxies, mais il manque une analyse observationnelle solide qui le démontre ou le rejette.

Avec le soutien de l'équipe TangoSIDM, je développe une nouvelle implémentation des auto-interactions de la matière noire dans des simulations cosmologiques, et montre que la diversité du contenu de matière noire observée dans les galaxies satellites naines classiques de la Voie lactée peut être expliquée par l'inclusion des interactions entre les particules de matière noire. De plus, la recherche menée par l'étudiante Noemi Anau Montel montre que les galaxies satellites dans les simulations TangoSIDM peuvent reproduire la distribution observée des galaxies naines classiques dans le plan de densité, de péricentre et de masse halo, tant sous SIDM que sous CDM. Cependant, les observations ont tendance à favoriser le modèle CDM. Ces découvertes soulignent la nécessité de sondes observationnelles supplémentaires pour contraindre le SIDM aux petites échelles.

Dans une analyse ultérieure qui inclut l'impact de la physique baryonique, je démontre que le plan Tully-Fisher, qui englobe les tailles des galaxies, les masses stellaires et les vitesses circulaires, peut servir d'observable puissant pour écarter les modèles SIDM dépendants de la vitesse. Bien que cette découverte impose de fortes contraintes aux modèles dépendants de la vitesse, elle ne les élimine pas entièrement. La recherche comprise dans cette thèse représente une avancée significative dans l'exploration de l'espace des paramètres SIDM. À la lumière des futures sondes cosmologiques plus précises et des expériences de détection de la matière noire, le dernier chapitre de cette thèse propose de nouvelles stratégies et idées dans le but de mieux comprendre les forces cachées de la matière noire, impactant les modèles de cosmologie de l'univers primitif, de formation des galaxies, et de physique au-delà du Modèle Standard.

université PARIS-SACLAY

ÉCOLE DOCTORALE
Astronomie
et Astrophysique
d'Île-de-France (AAIF)

Preface

The content within this thesis is the sole work of the author; however, certain portions were undertaken collaboratively. All utilized data has been appropriately cited within the text. Specific details are outlined as follows:

- Chapter 1, presenting an overview of the current state of research on Dark Matter and the standard cosmological framework, is entirely the work of the author. All referenced works are duly cited in the text. Figures 1 and 2, adopted from other works, are acknowledged accordingly.
- Chapter 2, which formulates an analytic model for the evolution of satellites galaxies of the Milky Way under Self-Interacting Dark Matter, is built upon the study presented in Correa (2021). This study was published in Monthly Notices of the Royal Astronomical Society (MNRAS): *Constraining velocity-dependent self-interacting dark matter with the Milky Way's dwarf spheroidal galaxies*, Correa Camila. A., 2021, *MNRAS*, Volume 503, Issue 1, pp. 920-937 [arXiv: 2007.02958].
- Chapter 3 encompasses an analysis conducted by Noemi Anau Montel, a current PhD student from the University of Amsterdam, who the author has supervised during the project and who has granted permission for the inclusion of her study in this thesis. Noemi Anau Montel's work is currently in preparation and it will be submitted to MNRAS. Furthermore, this chapter contains notes and comments on the authors' philosophy and approach to PhD supervision. Correa et al. (2022) was published in MNRAS: *TangoSIDM: tantalizing models of self-interacting dark matter*. Correa, Camila A.; Schaller, Matthieu; Ploeckinger, Sylvia; Anau Montel, Noemi; Weniger, Christoph; Ando, Shin'ichiro, 2022, *MNRAS*, Volume 517, Issue 2, pp. 3045-3063 [arXiv: 2206.11298].
- Chapter 4, which constrains models of Self-Interacting Dark Matter using the stelllar mass Tully-Fisher relation, was done in collaboration with members (both current and former) from Leiden Observatory, Leiden University. This study has been submitted to MNRAS.
- Chapter 5, which summarizes the author's scientific career is entirely the product of the author's work.
- Chapter 6, which summarizes the content presented in this thesis and discusses ideas for future projects, is also exclusively authored by the present writer.

Dedicated to my husband, Aquiles Carattino,
for always being there at the end of every race

Contents

List of Tables

List of Figures

1 - Introduction

This first chapter introduces the basics of cosmology and dark matter, and highlights the motivation of the research conducted in the thesis.

As we delve deeper into our comprehension of the Universe, it becomes imperative to balance our confidence in established knowledge with our awareness in the speculative nature of our most successful hypotheses. Presently, one of our most successful hypotheses pertains to Dark Matter. Evidence from various cosmological probes (e.g. Planck Collaboration et al. 2020) suggests that approximately one-third of our Universe is comprised of matter ($\Omega_{\rm m} = 0.315 \pm 0.007$). A significant portion of this matter is dark, meaning it does not interact electromagnetically, and cold, implying negligible primordial velocity dispersion. Atoms (baryons) contribute less than 5%. The remaining ∼70% ($\Omega_\Lambda = 0.684 \pm 0.007$) of total energy density arises from a uniformly distributed vacuum energy density or dark energy.

Despite the precision achieved in determining the density of matter in the Universe, a significant challenge looms over our knowledge—the unknown nature of its primary component: cold dark matter. Deciphering the nature of dark matter stands as one of the most urgent pursuits of our era. For decades, substantial efforts involving deep underground experiments and particle colliders have searched for the dark matter particle, unfortunately without much success (e.g. Boveia & Doglioni 2018; Schumann 2019; Aprile et al. 2023). Nevertheless, a global consensus on the existence of dark matter still persists.

In this introductory chapter, I delve into this challenge, reviewing the major evidence supporting the existence of dark matter. Subsequently, I provide a brief overview of the latest endeavors in indirect and direct detection searches. Following this, I question the predominant hypothesis that dark matter is a weakly interacting massive particle, introducing an alternative perspective known as self-interacting dark matter—that explores new physics from the dark sector, to which I have

contributed in recent years. To conclude, I highlight the motivation of the research conducted in the thesis and present a brief outline of its contents.

1.1 . Evidence for Dark Matter

A question that I usually ask myself is what is the nature of dark matter? Yet, before delving into that question, it is imperative to ask: *How do we know that dark matter actually exists? What evidence supports its presence?* In this section, I review the pivotal evidence pointing to the existence of non-baryonic matter in the Universe, which remains undetected through electromagnetic emission or absorption and is therefore dark.

1.1.1 . Cosmic Microwave Background

The anisotropies from the Cosmic Microwave Background (CMB) pose compelling evidence for the existence of non-baryonic matter in the Universe. After the Big Bang, the universe was filled with a dense, hot plasma of matter and radiation. As the universe expanded, this plasma cooled, leading to the formation of neutral atoms as protons and electrons combined. The universe became transparent, allowing photons to freely stream and reach us, forming the CMB, which exhibits a black body spectrum with present-day temperature of $T_0 = 2.725$ K (Dhal et al. 2023). CMB anisotropies, as observed by the Planck satellite, are shown in the top panel of Fig. 1.1.

According to the prevailing paradigm, shortly after the Big Bang (around 10^{-35} seconds), the Universe experienced cosmic inflation—a period of rapid, exponential expansion driven by the vacuum energy of a quantum field. Quantum fluctuations in the vacuum field during inflation generated density perturbations in the hot, dense plasma of matter and radiation. These perturbations were amplified during cosmic inflation and left their imprint on the CMB in the form of anisotropies.

The detailed scale dependence of the temperature anisotropies in the CMB allows for precise measurements of the total, matter, and baryon density parameters. However, the typical amplitude of the fluctuations, measured to be $\Delta T/T \approx 10^{-5}$, already provides robust evidence for the presence of non-baryonic matter.

By assuming that initial density perturbations ($\delta\rho = (\rho - \bar{\rho})/\bar{\rho}$) lead to fluctuations in the gravitational potential ($\nabla^2(\delta\Phi) = 4\pi G\delta\rho$), which in turn generate redshifted and blueshifted photons ($\delta T/T = \delta\Phi/3$), we can obtain the evolution of these density perturbations on sub-horizon scales in an expanding universe as

$$\delta\ddot{\rho} + 2H\delta\dot{\rho} - \frac{3}{2}\Omega_{\rm m}H^2\delta\rho = 0, \tag{1.1}$$

where $H = \dot{a}/a(t)$ corresponds to the Universe rate of expansion, with $a(t)$ is the

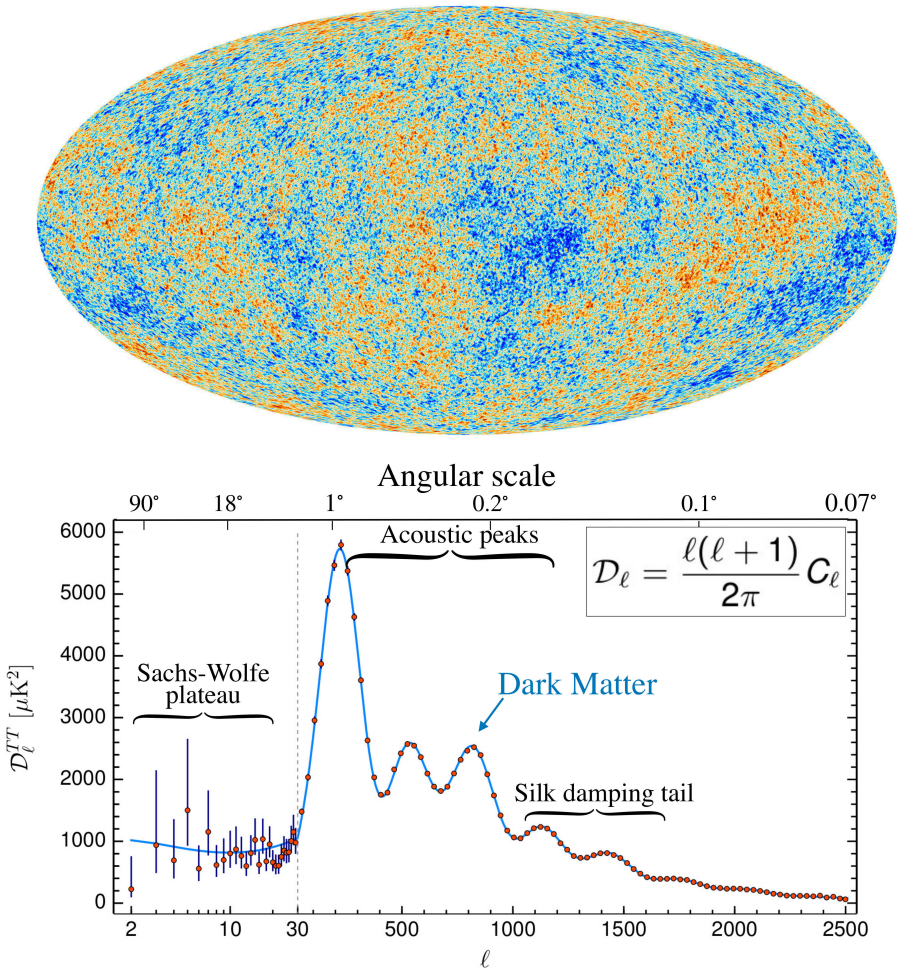

Figure 1.1: *Top*: CMB, as seen by Planck, reveals subtle temperature fluctuations that correspond to regions of slightly different densities. The expansion of the Universe has stretched the CMB radiation approximately 1000 times. So instead of observing the afterglow at 3000 degrees, we observe it at 2.725 K. Copyright: ESA, Planck Collaboration. *Bottom*: Angular power spectrum of the CMB temperature anisotropies, $l(l+1)C_l/2\pi$, as a function of multipole moment l (bottom x-axis) and angular sky (top x-axis). Red dots correspond to the observed data with the error bars showing $\pm 1\sigma$ uncertainties, whereas the blue solid line is the best fit assuming the base-ΛCDM cosmology to the Planck TT (temperature power spectra), TE (correlation between temperature and E-mode polarization), EE+lowE (E-mode polarization patterns specially at low multipoles), and lensing (gravitational lensing effects on the CMB) likelihoods. Copyright: Planck Collaboration et al. (2020).

time-dependent scale factor of the Universe, and $\Omega_{\rm m}$ is the present-day density of matter.

Eq. (1.1) shows that during the radiation domination era ($\Omega_{\rm m} \ll 1$ and $a \propto t^{1/2}$), $\delta\rho(t) \propto \ln t$, while during matter domination ($\Omega_{\rm m} \approx 1$ and $a \propto t^{2/3}$), $\delta\rho(t) \propto C_1 t^{2/3} + C_2 t^{-1}$ (with C_1 and C_2 constants). Hence, density perturbations grow as power-law from radiation-matter equality. However, before decoupling, baryons are tightly coupled to photons, hindering the growth of baryonic perturbations. In a Universe without non-baryonic matter, the initial density perturbations, that are needed for the observed structures to form, account for temperature fluctuations in the CMB of the order of $\Delta T/T \approx 10^{-4}$. Consequently, CMB anisotropies establish a $> 40\sigma$ detection limit for non-baryonic matter.

The positions of the acoustic peaks in the CMB angular power spectrum are largely sensitive to the geometry of the Universe, and hence they have been used to constraint the Universe total matter and energy. Temperature fluctuations can be analysed by expanding them into spherical harmonics, $Y_l^m(\theta, \phi)$,

$$\frac{\Delta T(\theta,\phi)}{\bar{T}} \equiv \frac{T(\theta,\phi) - \bar{T}}{\bar{T}} = \sum_{l=1}^{\infty} \sum_{m=-l}^{l} a_{lm} Y_l^m(\theta,\phi), \tag{1.2}$$

where $\bar{T}$ is the average temperature, $T(\theta, \phi)$ is the temperature in a particular direction, and a_{lm} are the coefficients of the expansion. The angular power spectrum, C_l, calculated by taking the statistical average $C_l = \langle |a_{lm}^2| \rangle$, is shown in the bottom panel of Fig. 1.1. Small values of the multipole moment, l, correspond to large angular separations, and vice versa. Key regions in C_l, that are highlighted in Fig. 1.1, include:

- The 'Sachs-Wolfe' plateau at low l, where temperature variations result from the energy loss of photons leaving gravitational potential wells from large scale structures, superimposed on intrinsic temperature fluctuations.

- The first peak, at an angle $\theta \sim 1^\circ$ on the sky, represents the fundamental mode of sound waves that oscillated once between entering the sound horizon and the time of recombination. Precise measurements of this peak confirm the spatial flatness of the Universe on large scales (e.g. Komatsu et al. 2011; Planck Collaboration et al. 2014a, 2020).

- Acoustic or Doppler peaks at intermediate l, arise from oscillations in the photon-baryon fluid due to the competition between gravity and pressure at recombination. The amplitude of odd peaks increases with higher baryon density, and the height of the 3rd peak is sensitive to cold dark matter density.

- The Silk damping tail at high l is produced by the diffusion of photons during recombination, that leads to damping of temperature fluctuations on small scales.

Additional information can be obtained from the polarization and lensing of the CMB photons. E mode polarization is due to Thomson scattering of the CMB photons off free electrons, while B mode polarization can arise from lensing of E modes, dust, or primordial tensor perturbations. Photons are deflected by gravitational potentials, and this smooths out the acoustic peaks.

Since the discovery of the CMB (Smoot et al. 1992), a number of experiments have measured the CMB anisotropies, notably Boomerang (de Bernardis et al. 2000), MAXIMA (Hanany et al. 2000), VSA (Dickinson et al. 2004), Acbar (Reichardt et al. 2009), WMAP (Bennett et al. 2011) and Planck (Planck Collaboration et al. 2014a).

1.1.2 . Large Scale Structure

From the CMB anisotropies we can also determine that the initial density fluctuations statistics do not significantly deviate from a Gaussian distribution, and that they were predominately adiabatic, meaning that all components (dark matter, baryons, photons) had the same spatial distribution. The power spectrum of these 'initial conditions' seems to be well approximated by a power law $P(k) = \langle|\delta k|^2\rangle = A_{\rm S}k^{n_{\rm S}}$, where δk is the Fourier transform of the density contrast ($P(k)$ is therefore the Fourier transform of the two-point spatial correlation function). The logarithmic slope, $n_{\rm S}$, is close to unity ($n_{\rm S} = 0.965 \pm 0.004$, Planck Collaboration et al. 2020). This shape implies that small scales collapsed first, and afterwards merged to form larger structures. The formation of structures thus appear to proceed hierarchically within a 'cosmic web' of larger structures.

The evolution of cosmic structures, along with the Universe's space-time geometry, its matter, and dynamical evolution, can be described by ΛCDM, the standard model of cosmology. Developed around the Friedman-Lemaître-Robertson-Walker metric, ΛCDM assumes the Cosmological Principle, which states that the Universe is statistically homogeneous and isotropic in space and matter at sufficiently large scales (> 100 Mpc). ΛCDM, as its name suggests, posits that approximately 85% of the matter in the Universe is composed of cold dark matter, with dark energy, or Λ, causing the accelerated expansion of the Universe at late times, which in turn affects the growth of density perturbations and hence the formation of structures of dark matter, commonly refereed to as dark matter haloes (Correa et al. 2015a).

Numerical simulations that assume ΛCDM have successfully reproduced observations of the large scale structure and galaxy clustering (Springel et al. 2006),

and a recent model accurately reproduced the galaxy population of the local group (McAlpine et al. 2022).

Further supporting the ΛCDM paradigm, and by extension, the existence of cold dark matter, is the evolution of acoustic oscillations between the redshift of recombination and the present time. Known as Baryon Acoustic Oscillations (BAO), these oscillations have been predicted to leave an imprint on the matter distribution at low redshift, on scales of approximately 150 Mpc. Measurements using the 2dF (Cole et al. 2005) and SDSS (Eisenstein et al. 2005) galaxy surveys have confirmed the presence of these oscillations, validating the model of a matter-photon plasma filling the Universe before recombination. Additionally, these observations corroborate the late-time acceleration inferred from Type Ia Supernovae (Riess et al. 1998; Perlmutter et al. 1999) and CMB data.

While observations of large-scale structures may not possess the same constraining capabilities for cosmological parameters as CMB anisotropies, they can enhance the precision of constraints. For example, the Dark Energy Survey collaboration (DES, Abbott et al. 2022) conducted an analysis that combined cosmic shear from 100 million source galaxies, galaxy clustering, cross-correlation of source galaxy shear with lens galaxy positions, and galaxy-galaxy lensing. This approach yielded a determination of $\Omega_{\rm m} = 0.339^{+0.032}_{-0.031}$.

Another study by Amon et al. (2023) integrated measurements from the Baryon Oscillation Spectroscopic Survey (Alam et al. 2021), galaxy-galaxy lensing from DES, Hyper Suprime-Cam Subaru Strategic Program (Aihara et al. 2018), and Kilo-Degree Survey-1000 (Kuijken et al. 2019). Employing an emulator-based approach for dark matter halo modeling, they fitted the data under the Planck Cosmology (Planck Collaboration et al. 2020). Their analysis, focused on large scales, showed that the Planck Cosmology provides a satisfactory fit to the data, despite the preference of data from the large-scale structure surveys for a lower amplitude of the power spectrum.

1.1.3 . Galaxy Clusters

Historically, the earliest indication that the Universe might contain non-baryonic matter dates back to 1933. When Fritz Zwicky conducted a study on the velocities of galaxies within the Coma Cluster, and inferred that the total mass needed to keep the cluster together is approximately 400 times greater than the mass in stars. If we consider a self-gravitating system with kinetic energy (T) and potential energy (U), the virial theorem, $2T + U = 0$, indicates that the mean square velocity can be written as

$$\langle v^2 \rangle = \frac{\sum_i m_i v_i^2}{\sum_i mi} = \frac{2T}{M}, \tag{1.3}$$

where $M = \sum_i m_i$ is the total mass of the system. By defining a gravitational radius, R_G, $U = -GM^2/R_G$, the total mass can be written in terms of the mean square velocity and the gravitational radius as $M = R_{\rm G}\langle v^2\rangle/G$. The mean square velocity can be measured from the galaxies speed using the Doppler effect, while the gravitational radius can be estimated from their projected positions (surface distribution of galaxies or stars). This allows us to estimate the total mass, which typically results in a mass-to-luminosity ratio of

$$\frac{M}{L} \sim 400 \frac{\mathrm{M}_\odot}{\mathrm{L}_\odot}. \tag{1.4}$$

Zwicky measured a velocity dispersion of $\langle v^2\rangle \sim 10^8$ cm s^{-1} and obtained $R_{\rm Coma} \approx 10^{24}$ cm from the observed angular diameter of the cluster. He assumed that the Coma Cluster enclosed 800 galaxies with a mass about 10^9 M$_\odot$, which implies $M_{\rm Coma} \sim 8 \times 10^{11}$ M$_\odot$. By applying the virial theorem, he anticipated a velocity dispersion of around 10^6 cm s^{-1}. To reconcile measurements and predictions, the Coma Cluster should have a mass about two orders of magnitude larger compared to the typical luminous mass expected in a cluster at that time. In essence, Zwicky proposed that the Coma Cluster should be predominantly composed of an invisible form of matter, which he termed 'dunkle materie,' the German expression for dark matter.

X-ray emissions in galaxy clusters also provide evidence for the presence of non-baryonic matter. Clusters emit X-rays because of thermal bremsstrahlung generated in the highly ionized gas confined by the gravitational pull of the cluster's potential well. Assuming the gas is spherically symmetrical and in hydrostatic equilibrium, the hydrostatic equation can be expressed as

$$\frac{1}{\rho}\frac{\mathrm{d}P}{\mathrm{d}r} = -\frac{GM(<r)}{r^2}. \tag{1.5}$$

Using the ideal gas law, $P = k_{\rm B}\rho T/\mu m_{\rm p}$, equation (1.5) can be reformulated as

$$\frac{k_{\rm B}T}{\mu m_{\rm p}}\left(\frac{\mathrm{d}\ln T}{\mathrm{d}\ln r} + \frac{\mathrm{d}\ln \rho}{\mathrm{d}\ln r}\right) = -\frac{GM(<r)}{r}. \tag{1.6}$$

The first term on the left side of the equation can be determined from X-ray spectra, while the second term can be measured from X-ray surface brightness data. After the determination of the cluster mass that is needed for gravity to counterbalance the gas pressure, it becomes evident that this mass exceeds the total baryonic mass of the hot gas and stars combined. This leads to an estimation of the baryon fraction, the fraction of the total mass of a galaxy cluster in the form of baryons $f_{\rm b} = M_{\rm b}/M_{\rm tot}$, of $f_{\rm b} \sim 0.144 \pm 0.005$ (e.g. Gonzalez et al. 2013).

Recent numerical simulations indicate that the contribution of non-thermal pressure due to bulk motions and turbulence can lead to significant biases on

the cluster masses measured with the hydrodynamic equilibrium hypothesis (e.g. Scheck et al. 2023). To improve upon this approach, it has been imperative to introduce the gravitational lensing signal in the cluster mass calibration process. Gravitational lensing reefers to the deflection of light caused by the gravitational bending of space-time in the presence of massive objects (the lens). Depending on the distortion effects produced on the background images, gravitational lensing is commonly separated into two categories: strong and weak.

In cases of strong lensing, such as the galaxy cluster RXJ2129[1], the gravitational pull of the cluster creates multiple images of background galaxies. Analyzing the positions and intensities of these images enables the deduction of the mass distribution within the galaxy cluster.

Merging clusters, like the well-known Bullet cluster (Clowe et al. 2006), are a particularly interesting case. In the Bullet cluster, a smaller subcluster of galaxies has passed through the main cluster. However, the hot X-ray emitting gas, which constitutes the predominant baryonic component, interacts and lags behind, forming a bullet-like shock front in the gas of the smaller subcluster. Weak lensing, in this case, allows for the reconstruction of the gravitational potential, revealing that the total mass is concentrated around the galaxies in both the main cluster and the subcluster. This observation implies that the clusters must contain a substantial amount of non-baryonic matter.

1.1.4 . Galaxy Rotation Curves

After Fritz Zwicky's additional analysis in 1937, which highlighted that galaxies associated with such substantial amounts of mass should be detectable as gravitational lenses producing multiple images of background galaxies, it took over 40 years for the existence of dark matter to be generally accepted. The turning point occurred in the mid-1970s with the analysis of rotational curves of spiral galaxies, led by Vera Rubin (Rubin et al. 1978, 1979), alongside studies by Ostriker et al. (1974) and Einasto et al. (1974). These works extended Zwicky's analysis, and concluded that massive halos are necessary around our Milky Way and other nearby galaxies to account for the motions of their satellites.

In a spiral galaxy, stars and gas clouds move in circular orbits due gravity, and their speeds can be measured using the Doppler shift of the Hydrogen 21cm line. Thus, based on Newton's law of gravity, the rotation (or circular) velocity is expressed as $v_{\rm c} = \sqrt{GM(<r)/r}$, providing a means to constrain the total mass enclosed within a radius, r, denoted as $M(<r)$. Additional evidence supporting the existence of dark matter arises from the stability of disk galaxies (Ostriker et al. 1974). Self-gravitating disks tend to form bars unless they possess a large velocity

[1]See for example one of my favorite images from JWST:link

dispersion. Embedding disks in a massive, extended, and roughly spherical halo presents a solution to this issue.

1.2 . Alternatives to Dark Matter?

Over the years, the ΛCDM model has firmly established itself as the standard paradigm for structure formation due to its numerous successes. These include: the observed baryon density aligning with estimates derived from cosmic nucleosynthesis, the Hubble constant corresponding to direct measurements, the dark energy density matching inferences from Type Ia supernovae, and the large-scale clustering in today's Universe coinciding with measurements from extensive galaxy surveys and weak gravitational lensing.

Despite its achievements, the ΛCDM model confronts various challenges, which will be further discussed in Section 1.4. However, a central predicament of ΛCDM, that pertains this thesis and is the focus of the following sections, is the lack of the detection of the dark matter particle.

The overwhelming observational evidence for dark matter presented in the previous sections relies solely on its gravitational effects. Consequently, it's reasonable to question whether these observations could be explained by modifying the laws of gravity. While Newton's laws have been tested with high accuracy on terrestrial scales, the possibility remains that the laws of gravity could differ on cosmological scales.

One leading theory attempting to explain observations by modifying gravity's laws is the Modified Newtonian Dynamics (MOND) theory (Milgrom 1983). Milgrom suggests that the mass discrepancy within galaxies and galaxy clusters arises because we are trying to apply a gravitational theory well beyond its proven domain of applicability, i.e. the solar system. One version of MOND involves a modification of Newton's inverse square law of gravity, replacing it with

$$F_{\rm G} = G\frac{Mm}{\mu(a/a_0)r^2}\begin{cases}\mu \approx 1, & \text{if } a \gg 1\\ \mu \approx a/a_0, & \text{if } a \ll 1\end{cases} \tag{1.7}$$

where a_0 is a new constant of nature with the dimensions of acceleration, which has been empirically determined to be 1.2×10^{-10} m s^{-2} (Li et al. 2018; McGaugh et al. 2018).

MOND has successfully explained various observations on the scale of galaxies, such as the rotation curves of galaxies, (e.g. Li et al. 2018), the baryonic Tully-Fisher relation (e.g. McGaugh 2012), and the radial acceleration relation (e.g. Brouwer et al. 2021). However, when it comes to larger scales, MOND encounters challenges, especially in explaining observations of merging clusters without invoking dark matter. In low acceleration conditions, MOND creates a 'phantom' field

that behaves similarly to the presence of non-baryonic dark matter in Newtonian gravity. For example, in the case of the Bullet cluster, the phantom field of MOND would be distributed around the baryonic matter traced by X-ray emission, rather than holding the galaxies together, as dark matter does. Some proposals aim to address this by introducing sterile neutrinos (e.g. Banik & Zhao 2022), although this somewhat contradicts MOND's original concept of explaining dynamics without dark matter. The offset of neutrinos with the baryonic mass is explained by an internal collision of two components of the cluster.

Another interesting case is the galaxy cluster 'El Gordo', which has been considered as a test supporting MOND + light sterile neutrinos. El Gordo is an extremely massive galaxy cluster ($M_{200} \approx 3 \times 10^{15}$ $\mathrm{M}_{\odot}$) at redshift $z = 0.87$, composed of two subclusters with a mass ratio of 3.6 merging at a speed of $V_{\mathrm{infall}} \approx 2500$ km s^{-1}. Such a fast collision between rare massive clusters is too unexpected in ΛCDM cosmology at such high z (Asencio et al. 2021).

In the scale of galaxy clusters, a long-standing problem for MOND has been the mass determination from the virial theorem (discussed in Section 1.1.3). In MOND, there was a deficit (by around a factor of two) of predicted dynamical mass derived from the virial theorem with respect to observations. The explanation behind this is that galaxy clusters are so massive that they capture sterile neutrinos. These sterile neutrinos add the factor of two in missing mass. In MOND, a sterile neutrino needs to have a rest mass of about 11 eV c^{-2}, while in ΛCDM sterile neutrinos can be much lighter. The currently favoured MOND-cosmological model assumes that there is about 5 times as much mass in sterile neutrinos than in ordinary matter and thus the 'νHDM cosmological model' has the same expansion history as the standard ΛCDM model. The first hydrodynamical cosmological simulations in the νHDM framework has recently been published (Wittenburg et al. 2023), but further research is needed to determine whether MOND with νHDM can explain observations that span from the CMB to galaxy clustering.

1.3 . Dark Matter detection searches

If we assume that dark matter exists, the question that naturally arises after examining the observational evidence outlined in Section 1.1 is: *What constitutes dark matter?*

The current concept of dark matter was initially influenced by the work of Peebles (1982), who proposed that dark matter consists of fundamental weakly interacting massive particles (WIMPs). These subatomic particles would exhibit extremely weak interactions with their environment, posing significant challenges for their experimental detection. Since the 1980s, parallel to the efforts of the astrophysics community, particle physicists embarked on their quest to unveil the

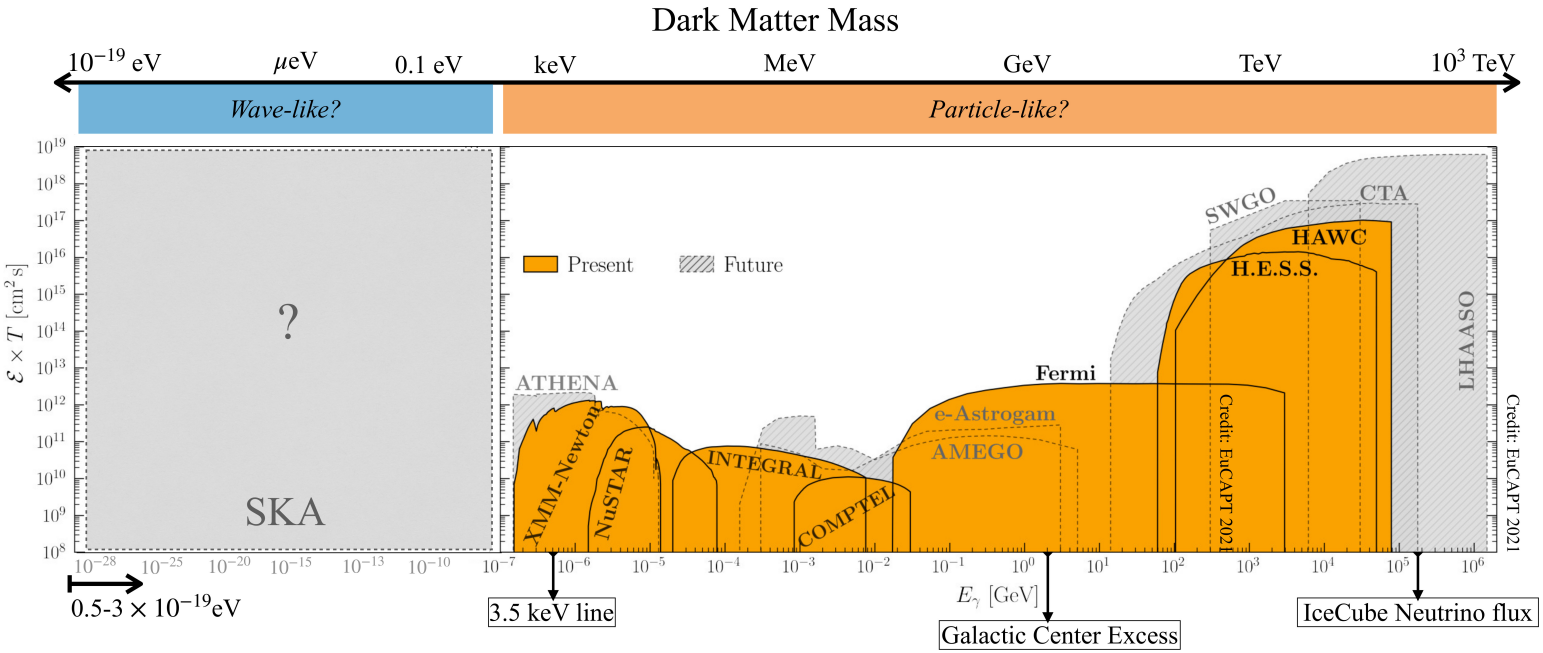

Figure 1.2: Adapted from Boddy et al. (2022), the figure shows the exposure of existing and upcoming X-ray and γ-ray instruments which can search for the decay or annihilation of dark matter, as a function of the recoil energy (bottom x-axis) and dark matter mass (top x-axis). Orange regions in the figure indicate the region in the parameter space currently covered by ongoing probes, whereas grey regions mark the expected future observational detection of upcoming instruments. The three interesting signals at different energies, 3.5 keV line, Galactic Center excess, and neutrino flux, have been attributed to dark matter. In the low mass regime (dark matter mass $<$ eV), dark matter can effectively be treated as a classical field. Studies of ultra-faint dwarf galaxies, Lyman-alpha forest, Milky Way satellites and stellar streams have set robust constrains on a lower mass of $(0.5 - 3) \times 10^{-19}$ eV (see text for details). For the rest of the parameter space, radio interferometers such as SKA may be capable of placing further constrains.

nature of dark matter. Over the years, various theoretical candidates, such as neutralinos, photinos, and gravitinos, have been proposed as potential WIMPs. While the neutralino predicted by supersymmetry models (Gelmini & Gondolo 2006) was favored for an extended period, recent results from the LHC are imposing stringent constraints on the model's parameter space (e.g., Barman et al. 2021).

Another popular candidate for dark matter proposed in the literature are sterile neutrinos. These particles are Standard Model singlet fermions that interact with ordinary matter only through mixing with the neutrinos. The denomination 'neutrino' refers to their fermionic nature and their electric charge neutrality, the adjective 'sterile' indicates their neutrality under weak interactions. The Standard Model predicts the existence of three generations of left-handed massless neutrinos. However, neutrino oscillation data observed in experiments involving atmospheric and solar neutrinos, as well as accelerator and reactor neutrinos, suggest that these particles are massive. The value of the sum of their active masses eigenstate has currently an upper bound of $\sum m_\nu < 0.12$ eV (Planck Collaboration et al. 2020). If sterile neutrinos exist, they can give mass to the active neutrinos, explain the neutrino oscillation data (Boyarsky et al. 2019), and represent a suitable candidate for dark matter.

To detect dark matter, including sterile neutrinos, there are currently three primary types of experiments underway: experiments utilizing particle colliders, direct detection experiments, and indirect detection experiments.

In collider experiments, the expected signature of a dark matter particle involves missing energy, particularly in the case of WIMPs due to their neutral and weakly interacting nature. However, to date, there is no indication of any signature from any particle accelerator (Boveia & Doglioni 2018).

Direct detection searches focus on measuring the nuclear recoil energy resulting from the scattering of dark matter particles off target nuclei. The actual collision between a dark matter particle and a standard model particle in a detector is negligible due to the anticipated low interaction rate between the two. However, these detectors can detect signals predicted from dark matter particles, such as an annual modulation of the recoil rate linked to the Earth's varying speed along its orbit around the Sun, and/or a daily modulation associated with the planet's rotation. Typically, these detectors probe masses between GeV and TeV scales. Examples include XENON, LUX, DAMA, CRESST, CDMS.

For over two decades, the DAMA/LIBRA experiment has claimed to observe seasonal variations in the measured event rate, consistent with a signal from WIMP particles (Bernabei et al. 2021). They report yearly fluctuations in flashes recorded by the sodium iodide crystals of their detector, with the number of events peaking in June and declining in December. This aligns with expectations of dark matter particles coming from the Milky Way. The caveat, however, is that none of the

numerous other dark matter experiments, based on various technologies, have observed signals compatible with DAMA/LIBRA's findings. To rigorously test this claim, physicists began building detectors with the same sodium iodide crystal in the mid-2010s. Preliminary results from two of these experiments, COSINE-100 in the Yangyang underground laboratory in South Korea and ANAIS-112 at the Canfranc Underground Laboratory in the Spanish Pyrenees, failed to reproduce the anticipated modulation. The Korean team did reproduce the modulation but attributed it to background composition, which exhibits time-dependent decay (Adhikari et al. 2023).

In contrast to direct detection experiments, indirect detection experiments operate on the premise that dark matter particles may undergo annihilation or decay, giving rise to a diverse range of standard model particles. Should dark matter undergo annihilation or decay, the anticipated outcome includes an elevated production of photons, neutrinos, or even cosmic rays, which would serve as signals of dark matter. Fig. 1.2, adapted from Boddy et al. (2022), illustrates the exposure of current and upcoming X-ray and γ-ray instruments designed to explore the decay or annihilation of dark matter, as a function of the recoil energy (bottom x-axis) and dark matter mass (top x-axis). The exposure, a product of effective area ($\mathcal{E}$) and observation time (T), plays a role in determining how many photons an instrument is likely to detect on average for a given dark matter flux. The orange regions in the figure signify the parameter space currently probed by ongoing experiments, while the grey regions indicate the anticipated future observational reach of upcoming instruments. At the time of writing, there are three noteworthy signals attributed to dark matter at different energy levels that have been highlighted in Fig. 1.2.

- An unidentified 3.5 keV line detected by XMM-NEWTON (and other telescopes like Suzaku) in the spectra of galaxy clusters, the Milky Way and Andromeda. One plausible interpretation suggests that this line results from the decay of dark matter particles, specifically sterile neutrinos with a mass of 7 keV. However, this hypothesis has faced recent challenges. A study utilizing over 30 megaseconds of XMM-Newton blank-sky observations, equivalent to roughly twenty years of X-ray images, found no evidence of the 3.5 keV line emission from the Milky Way halo (Dessert et al. 2020).

- In the the Galactic Centre, the Femi-LAT telescope observed bump-like features peaking at energies around 2-4 GeV, which have been interpreted as a diffuse gamma-ray excess emitted by dark matter particles. The interpretation of this gamma-ray excess is currently a subject of debate. The leading interpretation suggests the presence of an unresolved population of millisecond pulsars in the galactic bulge (Macias et al. 2021). However, a recent study (Miller & Zhao 2023) utilizing results from LIGO/Virgo's all-

sky search for quasi-monochromatic gravitational-wave signals from isolated neutron stars, which is estimated to cover about 20-50% of the population, found null results, excluding a substantial portion of the parameter space in the pulsar luminosity function. Another claim by the Fermi-LAT team (Hooper 2022) suggests that the observed gamma-ray excess exhibits approximate spherical symmetry, not tracing any known stellar populations, favoring the hypothesis that the Galactic Center Gamma-Ray Excess results from annihilating dark matter.

- The IceCube collaboration has measured a TeV-PeV diffuse flux of neutrinos, the origin of which remains puzzling. Various astrophysical sources, such as blazars, supernovae, galaxies, pulsar wind nebulae, γ-ray bursts, and radio-bright active galactic nuclei, have been proposed, but none can adequately explain this observation. An intriguing alternative explanation posits that the IceCube diffuse flux originates from long-lived heavy dark matter particles (e.g., Bhattacharya et al. 2019).

If the previously detected signals do not correspond to the dark matter particle, it raises the possibility that the dark matter particle might not be massive. Alternatively, it could be light, with a mass much less than approximately an electronvolt ($\sim$eV). In such a scenario, the dark matter number density within a galaxy would be sufficiently high for dark matter to be effectively treated as a classical field, prompting the question of whether $dark\ matter\ is\ fundamentally\ wave\text{-}like\ or\ particle\text{-}like?$

If we assume that dark matter consists of ultra-light bosons, with a mass of $\sim 10^{-22}$ eV, we enter the realm of Fuzzy Dark Matter (FDM). Numerical simulations demonstrate that the wave-like behavior, including interference effects, of FDM leads to the formation of a soliton core at the center of haloes and density granules on scales smaller than a kiloparsec (e.g., Sipp et al. 2023). In this context, a recent study by Powell et al. (2023) utilized a gravitational lens system observed at a resolution of ≤ 5 milli-arcseconds with very long baseline interferometry. The study placed a lower bound on the mass of the FDM particle, m_χ, ruling out $m_\chi \leq 4.4 \times 10^{-21}$ eV. Additional constraints on FDM have been derived from the stellar velocity dispersion in ultra-faint dwarf galaxies (Dalal & Kravtsov 2022), Lyman-alpha forest (Iršič et al. 2017; Rogers & Peiris 2021), Milky Way satellites (Nadler et al. 2021), and stellar streams (Banik et al. 2021), resulting in a lower limit of $m_\chi \geq (0.5 - 3) \times 10^{-19}$ eV, as illustrated in Fig. 1.2.

Another relevant dark matter candidate in the very low mass regime is the axion, a hypothetical elementary particle proposed by the Peccei-Quinn theory in 1977 to address the strong charge-parity (CP) problem in quantum chromodynamics (QCD). The axion field undergoes oscillations about the minimum of the

effective potential due to QCD effects, known as the misalignment mechanism. This generates a cosmological population of cold axions, and with a mass above 5 μeV/c^2 (10-11 times the electron mass), axions could potentially account for dark matter while also resolving the strong CP problem.

Recent years have seen significant development in indirect probes of axion dark matter (see e.g. Boddy et al. 2022, and reference therein). A common approach involves leveraging the axion-photon coupling, which can be detected through the decay of axions into photons (stimulated or resonantly enhanced) or axion-photon mixing in an external magnetic field. Axion dark matter may resonantly convert to photons in the magnetosphere of neutron stars, possibly producing observable radio signals on Earth. The radio signal is anticipated to manifest as a forest of spectral lines centered around the axion mass, with each line originating from a single neutron star in the Galactic population. If dark matter is predominantly in miniclusters rather than smoothly distributed, these events may appear as transient signals spanning hours to weeks. Preliminary estimates suggest that upcoming radio interferometers like the Square Kilometer Array (SKA) could potentially detect the QCD axion.

1.4 . Challenges for ΛCDM

The lack of detection of the dark matter particle presents a significant obstacle to the ΛCDM model, yet it is not the only challenge. This section examines the principal challenges the ΛCDM model is currently facing, which further hinder our comprehension of dark matter and the physics driving the late-time accelerated expansion of the Universe.

The Hubble H_0 tension currently stands as a 5σ challenge to ΛCDM. This tension arises from differences between low redshift measurements of the Hubble constant, H_0, and those inferred from the angular scale of fluctuations in the CMB. While Planck/ΛCDM best fit value is $H_0 = 67.4 \pm 0.5$ km s^{-1}Mpc^{-1} (Planck Collaboration et al. 2020), local measurements using Cepheid calibrators by the SH0ES team indicate $H_0 = 73.04 \pm 1.04$ km s^{-1}Mpc^{-1} (Riess et al. 2022). In a parallel analysis, the SH0ES team (Riess et al. 2021), using the Gaia Early Data Release 3 parallaxes (Gaia Collaboration et al. 2021), reported a value of $H_0 = 73.2 \pm 1.3$ km s^{-1}Mpc^{-1}, which results in a 4.2σ tension with the prediction from Planck18 CMB observations (Planck Collaboration et al. 2020). Proposed explanations to the Hubble tension include new physics before the time of recombination (e.g. Poulin et al. 2019; Agrawal et al. 2023), a modification of the Hubble expansion rate at late times (e.g. Alestas et al. 2020), or a recalibration of the Type Ia supernovae absolute luminosity due to late time new physics (e.g. Marra & Perivolaropoulos 2021).

Another important challenge is the growth tension, which highlights discrepancies in the growth rate of cosmological perturbations as indicated by direct measurements, e.g., weak lensing, redshift space distortions, cluster counts, compared to values derived from the Planck/ΛCDM parameters. The present value of the mass variance at $8h^{-1}$ Mpc, namely σ_8, by Planck is $\sigma_8 = 0.811 \pm 0.006$ (Planck Collaboration et al. 2020), while local measurements yield smaller values, such as 0.75 ± 0.03 from Sunyaev-Zeldovich cluster counts (Planck Collaboration et al. 2014b), $0.808^{0.009}_{-0.027}$ from DES (Abbott et al. 2022), and 0.772 ± 0.029 from KiDS-450 weak-lensing surveys (Hildebrandt et al. 2017). Various proposed solutions include dynamical dark energy models (e.g. Beltrán Jiménez et al. 2021), interacting dark energy models, which modify the evolution of linear matter fluctuations as well as the $H(z)$ (e.g. An et al. 2018), the effect of massive neutrinos, where neutrinos become non-relativistic but with significant velocities at late times to slow down the growth of structure (e.g. Diaz Rivero et al. 2019), and non-thermal dark radiation (e.g. Das et al. 2022).

These tensions, along with others (see e.g. Perivolaropoulos & Skara (2022) for a recent review), may hint towards new physics. Therefore, an important strategy to distinguish between potential new physical models is to study the distribution of matter not only at large scales but also at small scales. In the realm of small scales, the ΛCDM paradigm has faced a 'small-scale crisis' around famous tensions, namely the missing satellites problem, the too-big-to-fail problem, the core-cusp problem, also refereed to as the diversity problem, and the plane of satellites (see e.g. Sales et al. 2022 for a recent review).

The missing satellites problem refers to an initial mismatch between the number of Milky Way subhaloes capable of hosting observable satellite galaxies, and those predicted by N-body simulations, with the latter being originally estimated to be 5-10 times higher than the observed number (Klypin et al. 1999). However, advancements in observations over the past two decades have led to the discovery of dozens of faint satellite galaxies (e.g. Simon 2019). Furthermore, improvements in numerical simulations, incorporating baryonic physics and increasing numerical resolution, have shown consistent predictions (within reasonable uncertainties) with the observed numbers of satellites around the Milky Way and M31 (e.g. Font et al. 2021; Engler et al. 2021).

Nonetheless, the investigation into satellite number counts and faint galaxies remains crucial. On one had, it serves as a test for galaxy formation, since it allows to determine the leading mechanisms that can suppress the formation of low-mass galaxies. Namely the photoionisation background, which can be large enough to suppress the cooling of primordial gas, or reionization, and/or supernova feedback. On the other hand, it can serve as a test for CDM. The discovery of extremely low-mass galaxies in the coming years would imply that dark matter is cold, it had

negligible velocity dispersion at the moment of decoupling from equilibrium with primordial plasma, and therefore dark matter subhaloes can efficiently form down to a mass of 10^{-6} $M_{\odot}$ (e.g. for a 100 GeV WIMP, Wang et al. 2020). Conversely, the absence of low-mass and faint galaxies would indicate that either they have not formed due to baryonic physics, or that dark matter is warm. Warm dark matter indicates that in the early universe, dark matter particles decoupled while being relativistic, which prevented their clustering and allowed them to stream freely. This erases primordial density perturbations at scales below their free streaming scale, suppressing the formation dark matter subhaloes. Presently, there are indications of a degeneracy between baryonic physics and warm dark matter when predicting the number of faint satellite galaxies (Nadler et al. 2024), which presents the need for additional scaling relations or observables. This will be further discussed in Chapter 6.

Another small-scale tension is the too-big-to-fail problem, which indicates that the most massive dark matter substructures around simulated Milky Way-like haloes are significantly more massive than the estimated dwarf galaxy masses derived from line-of-sight velocity measurements (Boylan-Kolchin et al. 2011, 2012). This problem can be alleviated by lowering the mass assumed for the Milky Way-mass host halo (e.g. Wang et al. 2012), or by incorporating baryonic physics in the simulations, that reduces the predicted amount of dark matter in the inner regions (e.g. Brooks & Zolotov 2014; Garrison-Kimmel et al. 2014; Wetzel et al. 2016) and increases the tidal stripping of the Milky Way in satellites (due to effect of the Milky Way disc), making subhaloes more prone to mass loss (e.g. D'Onghia et al. 2010; Kelley et al. 2019). However, it has been argued that the too-big-to-fail problem is present in other galaxies besides the Milky Way, such as in central galaxies within the Local Group (Papastergis et al. 2015) and M31 (Tollerud et al. 2014). Therefore it is still argued that the solution of the too-big-to-fail problem is less clear for galaxies in the field.

In recent years, the too-big-to-fail has taken a turn in its formulation. Kaplinghat et al. 2019 revisited the too-big-to-fail problem of Milky Way dwarf spheroidal (dSphs) galaxies, and identified an anti-correlation between the central dark matter densities of the bright dSphs and their orbital pericenter distances, so that the dSphs that have come closer to the Milky Way centre are more dense in dark matter than those that have not. While this result has been confirmed by subsequent studies (e.g. Hayashi et al. 2020; Andrade et al. 2023), the existence of the anti-correlation is still debatable. Recently, Cardona-Barrero et al. (2023) analized the correlation between various datasets for the inner density of the dSphs and their orbital pericenter distances, and concluded that the anti-correlation is statistically significant at the 3σ level only in a minority of the dataset combinations. In Chapters 2 and 3, we explore the implications of this anti-correlation for the nature

of dark matter.

Another longstanding small-scale problem is the cusp-core problem. Simulations of structure formation in a CDM universe predict a universal density profile, with $\rho \propto 1/r$ in the central regions, irrespective of halo mass or cosmology (Navarro et al. 1997). This increasing central density towards the centre of a dark matter halo is known as a cusp. On the other hand, observations of dwarf galaxies (e.g. de Blok et al. 2008; Oh et al. 2011) typically favour the presence of a shallower central density slope, or even constant density dark matter core.

Solutions to this apparent discrepancy within a CDM framework typically invoke baryonic feedback processes. These processes generate low dark matter central densities due to the fluctuations in the gravitational potential induced by the gas inflow/outflow from cooling, stellar winds, and supernovae (e.g. Governato et al. 2010, 2012; Pontzen & Governato 2012; Teyssier et al. 2013; Oñorbe et al. 2015; Dutton et al. 2016). Another proposed solution points to potential observational biases that might lead to inferring a core when a cuspy halo is actually present (e.g. Macciò et al. 2016; Brooks et al. 2017). Nevertheless, not all observed galaxies appear to have cores (Oman et al. 2015), and this issue is now more accurately described as a discrepancy in the rotation curves, where observed galaxies appear to have more $diverse$ rotation curves than simulated ones, with some observed galaxies having large deficits in the inferred amount of mass in their inner regions.

Recent findings indicate that the extended range of dark matter diversity observed in gas-rich dwarf galaxies cannot be reproduced in cosmological simulations (e.g. Oman et al. 2015; Santos-Santos et al. 2020), that have been constrained by independent observations (such as the stellar-halo mass relation, cosmic star formation rate and galaxy mass function). Consequently, it has been argued that the observed diversity may stem from incorrectly determined distances and inclinations of these dwarf galaxies (e.g. Oman et al. 2015; Read et al. 2016), or other observational systematic in the observed kinematic data (Roper et al. 2023).

Explaining the diversity in the dark matter central density of gas-poor dwarf galaxies also proves challenging with baryonic physics, given the absence of gas inflow/outflow in these galaxies. Examples of gas-poor galaxies include the dwarf spheroidal and ultra-faint satellites of the Milky Way (e.g. Charles et al. 2022; Borukhovetskaya et al. 2022; Hayashi et al. 2022, 2021; Read et al. 2019), and ultra-diffuse dwarf galaxies (e.g. Mancera Piña et al. 2022; Kong et al. 2022). Currently, the work of Read et al. (2019) provides the most comprehensive explanation of the observed dark matter diversity in these systems. Read et al. (2019) argue that those dwarf galaxies with high central densities (consistent with cold dark matter cusps) stopped forming stars over 6 Gyrs ago, whereas dwarfs with more extended star formation favor shallow dark matter cores. However, the recent study of Charles et al. (2022) is showing that the dwarfs Andromeda XXV,

Andromeda XXI and Fornax challenge this theory.

Other proposals to the origin of the diversity are based on tidal interactions, that remove dark matter from the central regions (e.g. Genina et al. 2022), leading to low central dark matter densities. However, this idea only applies to satellite galaxies, not to dwarfs in the field, and it lacks consensus since it requires fine-tuning of the galaxies orbits.

1.5 . Self-Interacting Dark Matter

The small-scale crisis discussed in the previous section has not only motivated a deep exploration of the impact of baryonic physics on the inference of the underlying dark matter distribution within low-mass galaxies, but it has also prompted the consideration of alternative models to cold dark matter (Spergel & Steinhardt 2000; Yoshida et al. 2000). In recent years, there has been a major effort dedicated to investigating the possibility that dark matter is composed of particle species (e.g. Kaplan et al. 2010; Boddy et al. 2014a, 2016; Essig et al. 2019; Tsai et al. 2020; Alvarez & Yu 2020; Cline 2021). Just as baryonic matter is made of different fundamental particles, so too could dark matter. Under this scenario, the various dark matter particle species would undergo non-gravitational interactions, whose potential effect at the level of structure formation could be detected. This scenario is called the self-interacting dark matter paradigm (hereafter SIDM), which postulates that dark matter particles communicate with ordinary particles through gravitational interactions while they have non-gravitational interactions among themselves. Under this paradigm, forces between dark matter particles are mediated by analogues to electroweak or strong forces (e.g. Arkani-Hamed et al. 2009; Buckley & Fox 2010; Boddy et al. 2014b; Tulin & Yu 2018).

What makes the SIDM paradigm intriguing is its potential to produce detectable astrophysical signatures. Tentative self-interactions of dark matter have been measured in the shape and collisions of nearby galaxy clusters. When galaxy clusters collide, the resulting dark matter interactions induce a drag-like force, causing dark matter to temporarily lag behind stars (Randall et al. 2008; Dawson et al. 2013; Massey et al. 2015; Harvey et al. 2015). This lag results in an offset between the inferred position of the dark matter structure and the center of galaxies, with offsets ranging between 4 and 151 kpc (see Wittman et al. 2018, for a recent compilation). These offsets provide a means to measure the dark matter self-interaction cross-section per unit of dark matter mass, denoted as σ/m_χ, with the tightest constraints to date being $\sigma/m_\chi < 1.25$ cm^{2}g^{-1} (e.g. Harvey et al. 2019; Sagunski et al. 2021; Andrade et al. 2022).

For Milky Way-mass haloes, robust constraints on the dark matter self-interaction cross-section are lacking. It has been suggested that at this mass-scale, the cross

section should be bounded by an upper limit of 10 cm^2g^{-1} (Correa 2023). Beyond this upper limit, excessive satellite destruction could occur due to enhanced interactions between dark matter particles from satellites and those from the host, leading to an unrealistic Milky Way satellite system (Vogelsberger et al. 2016; Nadler et al. 2020).

In the regime of low mass galaxies such as dwarf galaxies, the rate and cross section of dark matter interactions also remain uncertain, due to the diverse dark matter content in dwarf galaxies that complicates the analysis. Studies suggest that if $\sigma/m_\chi > 1$ cm^2g^{-1}, dwarf galaxies should have little central dark matter due to the frequent interactions among dark matter particles that expel particles in further out orbits (e.g. Rocha et al. 2013; Zavala et al. 2013). Conversely, if $\sigma/m_\chi < 1$ cm^2g^{-1}, weak self-interactions result in no changes to the central dark matter density over time, leading to dwarf galaxies containing large amounts of dark matter in their centres (Read et al. 2018; Hayashi et al. 2021). The fact that there are observations showing both cases—dwarf galaxies with low central dark matter densities (e.g., Fornax, Andromeda XXV, Eridanus II, Crater II, Antlia II) and those with high central dark matter densities (e.g., Draco, Wilman I, among other ultra-faint and classical spheroidal galaxies)—have made it particularly challenging to derive robust constraints in the realm of low-mass galaxies.

1.6 . Thesis Outline and Motivation

This introductory chapter summarizes compelling astronomical measurements that, reveal the existence of dark matter and demonstrate its pivotal role in the evolution of structure in the universe. While the confirmation of dark matter would signify a significant triumph for ΛCDM, it would simultaneously reveal the incompleteness of the otherwise successful Standard Model of particle physics, which describes the fundamental particles and forces, since none of the known elementary particles can serve as dark matter. The enigma of dark matter points towards a new piece of fundamental law of nature, and its lack of detection demands that we move beyond the WIMP paradigm, and explore new physics from the dark sector.

The self-interacting dark matter paradigm emerges as a compelling scenario, motivated by both particle physics studies and the observations of dwarf galaxies. Until recently, however, SIDM was not considered as a favourable model that could explain the diversity in the rotational curves of dwarf galaxies. This is because there were no astrophysical indications that would motivate very frequent dark matter interactions with $\sigma/m_\chi > 10$ cm^2g^{-1} on dwarf galaxy scales. From the high dark matter densities in some dwarfs, various studies have concluded that dark matter is only weakly self-interacting with $\sigma/m_\chi < 0.57$ cm^2g^{-1} (Read et al. 2018; Valli

& Yu 2018; Hayashi et al. 2021; Ebisu et al. 2022). However, the caveat with these studies is that they could not offer an explanation as to why there are gas-poor dwarf galaxies with low dark matter densities (e.g. Borukhovetskaya et al. 2022; Charles et al. 2022) without invoking the impact of baryons and/or tidal interactions.

Can SIDM offer a plausible explanation for the diverse dark matter content in dwarf galaxies? What cross section is required for the dark matter interactions to account for this diversity? Does dark matter truly exhibit self-interactions? This thesis delves into the SIDM framework, examining its potential to shed light on these questions. It introduces a novel parameter space and investigates its implications, revising the observational connections that support SIDM and offering fresh constraints on its parameter range. The structure of this thesis is outlined as follows.

Chapter 2 investigates the anti-correlation between the central dark matter densities of the bright dSphs of the Milky Way and their orbital pericenter distances. It prompts the question: if this correlation were attributed to SIDM, what cross sections would be needed to produce it? The analysis concludes that, to establish the observed anti-correlation, the cross section on dwarf galaxy scales would need to be as large as 100 $\mathrm{cm}^2\mathrm{g}^{-1}$.

In Chapter 3, the TangoSIDM cosmological simulation set is introduced. This work, led by Noemi Anau Montel, a PhD student at the University of Amsterdam, challenges the findings of Chapter 2. The TangoSIDM simulations indicate that large cross sections on dwarf galaxy scales lead to a more diverse dark matter distribution within dwarfs compared to CDM (Correa et al. 2022), so that some SIDM models can produce a correlation between the central dark matter densities and pericenter distances of dwarf satellites. However, doubts arise regarding the existence of the anti-correlation that originally motivated the consideration of such large cross sections, primarily due to potential inaccuracies in the determining satellite pericenter distances (Cardona-Barrero et al. 2023). The chapter shows that both CDM and SIDM can account for the observed central density-pericenter distance correlation, contingent upon the specific observational dataset used for comparison. To resolve this ambiguity, we propose utilizing data on central dark matter densities, pericenter distances, and total halo mass from classical spheroidal dwarf galaxies.

Chapter 3 deviates slightly in style from the rest of the thesis. While it highlights the scientific contributions made by Noemi Anau Montel throughout the project, it also includes clarifications regarding my own involvement, feedback, contributions, and supervisory approach.

Chapter 4 further scrutinizes the SIDM paradigm. This chapter analyses the predictions derived from the TangoSIDM cosmological simulations, that incorpor-

ate baryonic physics. By analyzing the SIDM parameter space for Milky Way-mass galaxies, it shows that significant deviations from the observed stellar mass Tully-Fisher relation place robust constraints on the rate of dark matter interactions. Consequently, this chapter establishes that, within the range of Milky Way-mass galaxies, velocity-dependent SIDM suggests that cross sections surpassing 10 cm^2g^{-1} are unlikely.

Chapter 5 offers insight into my scientific background and details my contributions to student supervision. Finally, Chapter 6 summarizes the key findings presented in this thesis, provides a retrospective analysis on SIDM, and proposes potential avenues for future projects.

2 - Constraining Velocity-dependent SIDM with the Milky Way's dwarf spheroidal galaxies

This chapter investigates whether the observed anti-correlation between the central dark matter densities of the bright Milky Way dwarf spheroidal galaxies and their orbital pericenter distances poses a potential signature of self-interacting dark matter (Correa, 2021).

2.1 . Introduction

The standard cosmological paradigm of Λ collisionless cold dark matter (ΛCDM) accurately predicts the large-scale structure of the Universe (Springel et al. 2006), however its success is less certain over the small scales, the regime relevant to the substructure within galactic haloes. The deficit of observed low-mass satellite galaxies within the Local Group relative to predictions from analytical theory (Press & Schechter 1974) and CDM N-body simulations (Klypin et al. 1999), along with the discrepancy between the low dark matter densities of some galaxies and the cuspy and dense subhaloes predicted by simulations (e.g. Flores & Primack 1994; Moore 1994; Moore et al. 1999), motivated to question the cold and collisionless nature of dark matter (DM). The alternative was that DM might have non-negligible self-interactions (Spergel & Steinhardt 2000).

Self-interacting dark matter (hereafter SIDM) assumes that DM particles experience collisions with each other, these collisions transfer heat towards the colder central regions of DM haloes, lowering central densities and creating constant density cores (e.g. Davé et al. 2001; Colín et al. 2002; Vogelsberger et al. 2012; Rocha et al. 2013; Dooley et al. 2016; Vogelsberger et al. 2019; Robles et al. 2019). DM particle collisions also lead to less concentrated subhaloes that are more prone to tidal disruption, as well as to the evaporation of subhaloes via ram pressure strip-

ping exerted by the larger host (e.g. Buckley et al. 2014; Cyr-Racine et al. 2016; Vogelsberger et al. 2016; Nadler et al. 2020).

An important disagreement between the prediction of pure CDM simulations and observations is the so-called too-big-to-fail problem (hereafter TBTF), which states that the most massive subhaloes in CDM simulations are too dense in the centre to host the observed satellites of the Milky Way (Boylan-Kolchin et al. 2011, 2012). The TBTF problem, although solved by invoking baryonic physics and environmental effects (e.g. Sawala et al. 2016; Dutton et al. 2016; Wetzel et al. 2016; Fattahi et al. 2016), has been revisited in the SIDM paradigm due to its prevalence in other galaxies besides the Milky Way (e.g. Garrison-Kimmel et al. 2014; Papastergis et al. 2015).

The SIDM models that alleviate the TBTF problem require a velocity-independent DM interaction cross section per unit mass, σ/m_χ, to be larger than $\sigma/m_\chi{>}1$ cm^{2}g^{-1} (Zavala et al. 2013). Despite its success in solving the TBTF problem and other small-scales discrepancies (e.g. Rocha et al. 2013; Kamada et al. 2017; Ren et al. 2019), the excitement caused by SIDM diminished due to the strong constraints set by X-ray and lensing observations of galaxy clusters, that set an upper-limit on the velocity-independent scattering cross section of the order of 1 cm^{2}g^{-1} (Miralda-Escudé 2002; Peter et al. 2013). This upper-limit was later supported by observations of bounds from major mergers (Randall et al. 2008; Harvey et al. 2015; Wittman et al. 2018) and bright central galaxy wobbles (Kim et al. 2017; Harvey et al. 2019).

However, as early as Yoshida et al. (2000), it has been suggested that the cross section must depend on the relative velocity of DM particles, in such a way that DM behaves as a collisional fluid on small scales while it is essentially collisionless over large scales, for SIDM models to reproduce the cores of dwarf galaxies as well as the galaxy clusters' apparent shapes. Such velocity-dependence is supported by many theoretical models that argue that DM exists in a 'hidden sector', where forces between DM particles are mediated by analogues to electroweak or strong forces (e.g. Pospelov et al. 2008; Arkani-Hamed et al. 2009; Buckley & Fox 2010; Feng et al. 2010; Boddy et al. 2014b; Tulin & Yu 2018). Velocity-dependent SIDM models have been explored on galaxy cluster scales (e.g., Robertson et al. 2017, 2019; Banerjee et al. 2020) and Milky Way (MW)-mass systems (e.g. Vogelsberger et al. 2012; Zavala et al. 2013; Nadler et al. 2020).

The works of Read et al. (2018) and Valli & Yu (2018) analysed the density profiles of the MW dwarf spheroidal galaxies (dSphs), aiming to place constraints on σ/m_χ on dwarf galaxy scales. Read et al. (2018) focused on Draco and claimed that its high central density gives an upper bound on the SIDM cross section of $\sigma/m_\chi{<}0.57$ cm^{2}g^{-1}. Valli & Yu (2018) used a similar methodology as Read et al. (2018), although they also found that Draco's high central density could

be described by a $\sigma/m_\chi \sim 0.4$ cm^{2}g^{-1}, they concluded that the remaining dSphs probed different cross sections, ranging between 0.1 and 40 cm^{2}g^{-1}.

Recently, Kaplinghat et al. (2019) have revisited the TBTF problem of MW dSphs. They have reported an interesting anti-correlation between the central DM densities of the bright dSphs and their orbital pericenter distances, so that the dSphs that have come closer to the MW centre are more dense in DM than those that have not come so close. Read et al. (2019) proposes that the anti-correlation is the result of baryonic effects. The gas expelled by stellar feedback 'heats' the surrounding DM, lowering the haloes' central density (Navarro et al. 1996). If the effect repeats over several cycles of star formation, it accumulates, leading eventually to transform the DM cusp into a core (e.g. Read & Gilmore 2005; Pontzen & Governato 2012). However, for dwarf galaxies, such as Draco and Ursa Minor, that are DM-dominated and stopped forming stars long ago (~ 10 Gyr), the DM cusp is formed again, thus explaining the high DM central densities. Read et al. (2019) modelled the stellar kinematics to infer the DM distribution of the MW dSphs, and showed that all dwarfs except for Fornax, are well fitted by a cuspy profile. Even if the 'lack' of baryonic effects is responsible for the high DM densities in the dSphs, it does not explain the origin of the anti-correlation with pericenter distance.

SIDM, on the contrary, can potentially explain the observed anti-correlation. DM collisions lead to an outward heat transfer that induces gravothermal core collapse, i.e. the central density increases with time (Balberg et al. 2002; Elbert et al. 2015). This gravothermal collapse would be accelerated by mass loss via tidal stripping (Nishikawa et al. 2020) and correlate with how close the satellite galaxies come to the centre of the MW. According to this scenario, the anti-correlation could not only be a potential signature of SIDM (Kaplinghat et al. 2019; Nishikawa et al. 2020; Sameie et al. 2020), but it would also invalidate the upper limits on σ/m_χ from Read et al. (2018) and Valli & Yu (2018), since their analysis does not include the effects of gravothermal collapse.

The goals of this study are to investigate the possibility that the anti-correlation is a signature of SIDM, map out the velocity-dependence of the SIDM cross section with MW satellites, and analyse how the uncertainties in the MW halo mass and orbital parameters, as well as initial conditions, affect the constraint of the velocity-dependent σ/m_χ. To do so, we simulate the orbital evolution of dSphs subhaloes around the MW by adopting the proper motions from the Gaia mission (Helmi et al. 2018; Fritz et al. 2018), assuming an analytical form for the MW gravitational potential and including a consistent characterization of gravitational tidal stripping. The evolution of the density profile of SIDM subhaloes is simulated using the gravothermal fluid formalism, which was originally developed to study the evolution of globular clusters (Lynden-Bell & Eggleton 1980), but it has also been applied to

isolated SIDM haloes (Balberg et al. 2002; Koda & Shapiro 2011; Shapiro 2018). This method allows us to track the DM halo evolution within scales smaller than 100 pc, which are largely expensive to resolve with N-body simulations, as well as to easily cover a wide range of parameter space.

This work is organised as follows. Section 2.2 outlines our model setup. We present our results in Section 2.3 and compare to observational data. We discuss constraints on the cross section-velocity relation in Section 2.3.3. Comparison with previous works, as well as the challenges of the model and impact of initial conditions are discussed in Section 2.4. Finally, Section 2.5 summarises our key results.

2.2 . SIDM halo model

The SIDM halo model derived in this work connects the gravothermal fluid approximation, with orbit integration and tidal stripping modelling. The model considers a spherical halo with a density profile $\rho(r,t)$, in isolation and quasi-static virial equilibrium. It evolves the halo in time following the gravothermal fluid formalism described in Subsection 2.2.1. The evolution begins when the Universe is 3.5 Gyrs old (redshift $z = 1.87$), and continues for 10 Gyrs, until present time (redshift $z = 0$). The halo is initialized with a given initial density profile, $\rho_{\rm init}$, and a SIDM scattering cross section per unit mass, σ/m_χ.

The SIDM halo model also includes orbital evolution, it calculates the haloes orbits during the 10 Gyr period, so that at each time step it knows the distance between the halo and MW center, d_{GC}. Since a given halo hosts a MW dwarf spheroidal galaxy, the orbit integration model uses the orbital parameters from the Gaia mission corresponding to the dwarfs. The orbital evolution is introduced in Subsection 2.2.2.

The haloes' density profile, $\rho(r,t)$, is modified every few time steps as it allows for mass loss from gravitational tidal interactions. The SIDM model uses d_{GC} to calculate the tidal radius and rate of mass loss at each time step. Subsection 2.2.3 describes the gravitational tidal stripping modelling. Finally, Subsection 2.2.4 summarises the complete model and describes the initial conditions.

2.2.1 . Gravothermal collapse

We consider a spherical halo in isolation and in quasi-static virial equilibrium, with a density profile $\rho(r,t)$ and an enclosed mass of $m(<r,t)$ at radius r and time t. We assume that the ensemble of gravitating particles is well approximated by a fluid-like description, where the effective temperature is identified with the square of the one-dimensional velocity dispersion, $v(r,t)$, and thermal heat conduction is employed to reflect the manner in which the close-encounter large-angle (hard-sphere) scatterings combine to transfer energy in the system. The quasi-static approximation means that, while the fluid evolves thermally, it always satisfies hydrostatic equilibrium at each moment.

The fundamental equations of the model are mass conservation, hydrostatic equilibrium, energy flux equation, and the first law of thermodynamics,

$$\frac{\partial m}{\partial r} = 4\pi r^2 \rho, \tag{2.1}$$

$$\frac{\partial(\rho v^2)}{\partial r} = -\frac{Gm\rho}{r^2}, \tag{2.2}$$

$$\frac{L}{4\pi r^2} = -\kappa \frac{\partial T}{\partial r}, \tag{2.3}$$

$$\frac{\partial L}{\partial r} = -4\pi r^2 \rho v^2 \left(\frac{\partial}{\partial t}\right)_m \log\left(\frac{v^3}{\rho}\right), \tag{2.4}$$

where $L(r)$ the luminosity through a sphere at r.

The flux equation (eq. 2.3) can be written into a single expression that considers both the cases where the the mean free path between collisions is significantly shorter (known as SMFP regime) or larger (LMFP regime) than the system size (Balberg et al. 2002), as follows

$$\frac{L}{4\pi r^2} = -\frac{3}{2} b\rho v \left[\left(\frac{1}{\lambda}\right) + \left(\frac{v t_r}{CH^2}\right)\right]^{-1} \frac{\partial v^2}{\partial r}, \tag{2.5}$$

where $H \equiv \sqrt{v^2/(4\pi G\rho)}$ is the gravitational scale height of the system, λ is the collisional scale for the mean free path given by $\lambda = 1/(\rho\sigma_m)$, with $\sigma_m = \sigma/m_\chi$ the cross section per unit mass, and $t_r \equiv \lambda/(av)$ is the relaxation time, with $a = \sqrt{16/\pi}$ for hard-sphere scattering of particles with a Maxwell-Boltzmann velocity distribution (Balberg et al. 2002).

In the SMFP regime the continuum assumption applies and the collection of particles can accurately be treated as a continuous fluid. From this regime, the effective impact parameter $b = 25\sqrt{\pi}/32 \approx 1.38$ in eq. (2.5) can be derived from first principles (e.g. Chapman et al. 1990). In the LMFP regime the model needs to be calibrated using N-body simulations. Previous studies have tested

the parameter C that determines the radial heat conduction for isolated (Balberg et al. 2002; Koda & Shapiro 2011; Essig et al. 2019) and cosmological N-body simulations (Elbert et al. 2015; Nishikawa et al. 2020; Essig et al. 2019) with purely elastic DM self-interactions.

Essig et al. (2019) and Nishikawa et al. (2020) assumed spherical symmetry but not isolation. Essig et al. (2019) used the cosmological simulation from Elbert et al. (2015) and showed that $C = 0.45 - 0.6$ closely reproduces the density and velocity dispersion from the simulation. Nishikawa et al. (2020) also used Elbert et al. (2015) simulation and concluded that for $\sigma/m_\chi > 10$ cm^{2}g^{-1}, $C = 0.75$ and $b = 0.003$ is needed to reproduce the subhalo's DM density. Both studies also reported differences with respect to the simulation in the subhalo density of up to a factor of 2 for $\sigma/m_\chi = 50$ cm^{2}g^{-1}. We take this discrepancy into account when we constrain the cross section in Section 2.3.3, and adopt $C = 0.75$ as reported by Balberg et al. (2002), who assumed spherical symmetry and isolation for the modelling of SIDM haloes. However, we also discuss how the different values of $C = 0.45 - 0.6$ and $b = 0.003 - 1.38$ impact on our key results in Subsection 2.4.2.

Haloes with gravitating particles that undergo hard-sphere scatterings can experience gravothermal core-collapse, a process that changes the pressure of the system, taking it out of hydrostatic equilibrium and making therefore such assumption invalid. The dynamical time-scale of dwarf galaxies is $t_d \approx 0.1$ Gyr for typical densities of 10^7 M$_\odot$kpc^{-3}. The gravothermal core collapse time-scale, usually defined as $t_c \approx (150/C)(r_s \rho_s \sigma/m)^{-1}(4\pi G \rho_s)^{-1/2}$ (Essig et al. 2019), is $t_c \approx 200$ Gyr for $\rho_s = 10^7$ M$_\odot$/kpc^3, $r_s = 2$ kpc and $\sigma/m = 10$ cm^{2}g^{-1} and $t_c \approx 20$ Gyr when increasing σ/m to 100 cm^{2}g^{-1}. Since $t_d \ll t_c$, hydrostatic equilibrium is a valid assumption.

2.2.2 . Orbital evolution of MW spheroidal galaxies

Throughout this work we model the internal dynamics and orbital evolution of the nine most luminous MW dSph galaxies. These include Ursa Minor (hereafter UM), Draco, Sculptor, Sextans, Fornax, Carina, LeoII and LeoI, and Canes Venatici I (hereafter CVnI). We focus on these systems because they have the highest quality kinematic data and the largest samples of spectroscopically confirmed member stars to resolve the dynamics at small radii.

The second data released by the Gaia mission (Brown et al. 2018; Helmi et al. 2018) has largely increased the precision and amount of astrometric data of Galactic stars, making possible the determination of spatial motions of many dSphs orbiting the MW halo (Helmi et al. 2018; Fritz et al. 2018). Using the proper motions determined by Fritz et al. (2018), and the publicly available code galpy[1] (Bovy

[1] http://github.com/jobovy/galpy

2015), we integrate the orbits of the dSphs adopting the static MWPotential14 model (without dynamical friction), which has been shown to be consistent with various observations (see Bovy 2015 for details). For the MW dark matter halo mass we assume a virial mass of $M_{200} = 10^{12}\,\mathrm{M}_{\odot}$, defined as the total within R_{200}, radius within which the mean density is equal to 200 times the critical density of the Universe, ρ_{crit}. In Appendix A.5 we show that assuming a lighter MW halo mass of $0.8 \times 10^{12}\,\mathrm{M}_{\odot}$ or a heavier model of $1.6 \times 10^{12}\,\mathrm{M}_{\odot}$ does not largely affect our key results.

Fig. 2.1 shows the time evolution of the galactocentric distance of the MW dSph galaxies. The black dashed line indicates the time evolution of the MW's virial radius, R_{200}, calculated using the halo accretion history model

$$M(z) = M(z=0)(1+z)^{\alpha} e^{\beta z}, \tag{2.6}$$

from Correa et al. (2015a,c)[2]. It can be seen from Fig. 2.1 that the dSphs of UM, Draco, Sculptor and Carina became satellites of the MW nearly 8-9 Gyrs ago and since then they have completed many orbits, whereas LeoII, Sextans, CVnI and Fornax have completed two orbits around the MW. LeoI crossed the MW's virial radius for the first time roughly 2 Gyrs ago.

Note that the starting point of the model is when the Universe is 3.5 Gyrs old (redshift $z = 1.87$), therefore it first calculates the orbits using present-day Gaia data but it initializes the halo evolution using the galactocentric distance of haloes 10 Gyrs ago.

2.2.3 . Gravitational tidal stripping

An important aspect in the evolution of small subhaloes relative to haloes in the field, is that when subhaloes are accreted by a larger halo, they begin to lose mass due to the strong gravitational tidal interactions exerted by the larger host. Studies using numerical simulations have shown that gravitational tidal stripping can even lead to the complete disruption of a large fraction of subhaloes (Han et al. 2016; Jiang & van den Bosch 2017; van den Bosch 2017; van den Bosch et al. 2018), likely enhanced in the presence of SIDM (Dooley et al. 2016; Nadler et al. 2020).

We calculate the rate of mass loss, dm/dt, of the subhaloes hosting the dSphs as they orbit around the MW by adopting the following tidal stripping rate

$$\frac{dm}{dt} = \frac{m(>r_t)}{\tau_{\mathrm{orb}}/\alpha}, \tag{2.7}$$

[2]https://camilacorrea.com/code/commah/

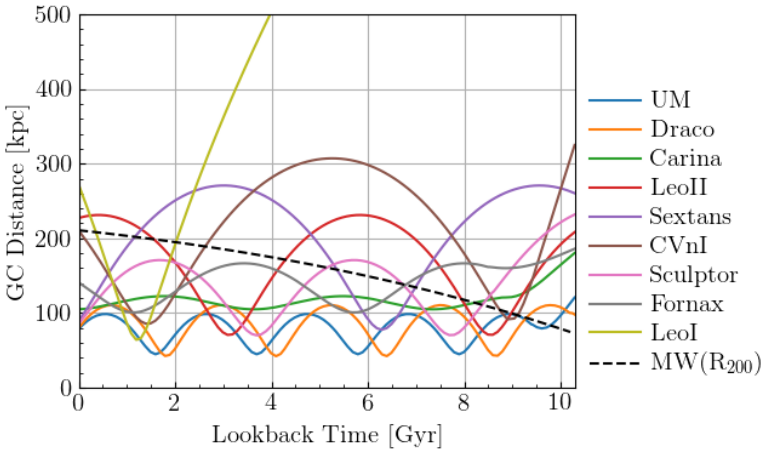

Figure 2.1: Time evolution of the galactocentric distance of the MW dSphs over the past 10 Gyrs. The black dashed line indicates the time evolution of the virial radius of the MW's dark matter halo, R_{200}, which increases with time under the growing mass of the dark halo. Note, however, that the integration of the dSphs orbit was done assuming the MWPotential14 static model from Bovy (2015).

where $m(>r_t)$ is the subhalo mass outside the instantaneous tidal radius r_t, $\tau_{\rm orb} = 2\pi/\omega$ with ω the instantaneous angular velocity of the subhalo, and $\alpha = 1$ (see van den Bosch et al. 2018). The tidal radius is calculated as

$$\left(\frac{r_t}{R}\right)^3 = \frac{m(<r_t)/M(<R)}{2 + \frac{\Omega^2 R^3}{GM(R)} - \frac{d\ln M}{d\ln R}|_R}, \tag{2.8}$$

which corresponds to the scenario where a subhalo of mass m is on a circular orbit of radius R, with angular speed $\Omega(= V_{\rm circ}(R)/R)$, around a halo of mass M (e.g., King 1962; Tollet et al. 2017).

Eq. (2.7) gives the approximate amount of mass stripped from the subhalo over a short time-step, but it does not indicate how the density profile is modified by it. To model the truncation in the density profile, we employ the fitting functions of Green & van den Bosch (2019), that follow the structural evolution of a tidally truncated subhalo and solely depend on the fraction of mass stripped.

Green & van den Bosch (2019) used the DASH library (Ogiya et al. 2019) of high-resolution, idealized dark matter only collisionless N-body simulations that follow the evolution of an individual subhalo as it orbits within the fixed, analytical potential of its host halo. Both the fixed host halo and the initial subhalo are spherically symmetric, each with a Navarro-Frenk-White (hereafter NFW, Navarro et al. 1997) density profile,

$$\rho(r) = \frac{\rho_s}{r/r_s(1+r/r_s)^2}, \tag{2.9}$$

where ρ_s and r_s are the scale density and radius where the logarithmic density slope is equal to -2. The ratio between the halo's virial radius R_{200} and the scale radius, r_s, defines the concentration parameter $c_{200} = R_{200}/r_s$ of the profile.

Green & van den Bosch (2019) provide the best-fit parameters for the transfer function, $H(r, t, f_b, c_{200})$, defined as the ratio of the evolved subhalo density profile relative to the initial profile, $H(r, t, f_b, c_{200}) = \rho(r, t)/\rho(r, t = 0)$, with f_b the bound fraction (mass that remains bound to the subhalo while it is tidally stripped) and c_{200} subhalo concentration parameter at $t = 0$ (see Green & van den Bosch 2019 for more details).

In our model, however, the subhalo DM density profile depends exclusively on the density profile at the previous time-step, not on the initial profile. We therefore assume that the density profile at time-step t_n, $\rho(r, t_n)$, is calculated from the density profile at a previous time-step t_{n-1}, $\rho(r, t_{n-1})$, via the transfer function as

$$\rho(r, t_n) = \rho(r, t_{n-1}) \times H(r, t_n, f_b, c_{200}(t_{n-1})), \tag{2.10}$$

where H depends on the bound fraction, $f_b = (1 - dM)/M(t_n)$ defined as the fraction of mass that remains bound after it lost dM mass between t_n and t_{n-1}, and $c_{200}(t_{n-1})$ the concentration parameter of the density profile at t_{n-1}. Although we calculate the amount of mass loss during each t_n, we do not apply eq. (2.10) at the end of every time step. This is because the time-step size can become very small, making dM a negligible quantity. Instead, we apply eq. (2.10) and truncate the density profile every 250 Myr. We have found that during this period of time, the cumulative mass loss of subhaloes reaches on average $1 - 2\%$ of their total mass. In Appendix A.6 we show that truncating the density profile every 350 Myr, instead of 250 Myr, slightly decelerates gravothermal collapse, conversely a more frequent truncation of the density accelerates gravothermal collapse. Section 2.5 discusses the impact of the truncation time parameter on our key results.

Note that eq. (2.10) is a strong variation of the Green & van den Bosch (2019) model. We compare the outcome by evolving a $10^{8.84}\,\mathrm{M}_\odot$ subhalo that has an initial NFW profile with concentration 15.7, it follows the orbit of UM and loses roughly 40% of its initial mass. We evolve the subhalo using the Green & van den Bosch (2019) model, as well as the modified model shown in eq. (2.10).

The top panels of Fig. 2.2 show the density (top-left) and enclosed mass (top-right) as a function of radius of a NFW subhalo. The dashed lines in the panels correspond to the initial density and mass profile, whereas the solid lines correspond to the final profiles after 10 Gyr of evolution. From the top-left panel it can

be seen that the density profile is largely truncated when we apply eq. (2.10) in comparison to the Green & van den Bosch (2019) model, however the large difference only occurs in the outskirts of the halo, beyond the virial radius. The top-right panel shows that the final masses agree, indicating that the truncation imposed by eq. (2.10) closely follows the rate of mass loss of the Green & van den Bosch (2019) model.

An important caveat to consider when we apply eq. (2.10) is that the transfer function H was fitted according to the structural evolution of an NFW CDM subhalo. However, throughout this work we are applying the transfer function to SIDM subhaloes, whose density profile largely derviates from the NFW shape in the inner regions. We test the transfer function to non-NFW profiles by comparing it to the tidal heating model (Gnedin et al. 1999; Pullen et al. 2014). We find very good agreement in the evolution of the density profiles (shown in Appendix A.2) concluding that applying the transfer function to SIDM haloes is a good approximation.

The bottom panels of Fig. 2.2 show the evolution of a SIDM subhalo with an initial cored-shape density profile. After 10 Gyrs of evolution, the subhalo loses roughly 43% of its initial mass, in close agreement with the evolution of the CDM subhalo. Like in the top panels, the density profile is largely truncated when we apply eq. (2.10) in comparison to the Green & van den Bosch (2019) model, but mostly beyond the virial radius.

Given the good agreement between the rate of mass loss and truncated profiles of SIDM and CDM subhaloes in the outer regions, we assume that applying eq. (2.10) to the truncation of SIDM subhaloes is a good approximation. Note, however, that the rate of mass loss given by eq. (2.7) should be taken as a lower limit. SIDM subhaloes lose more mass due to ram-pressure stripping and the presence of baryons, effects that we do not model in this work. Ram-pressure stripping is caused by DM self-interactions with the host halo particles, that drive material out of subhaloes, to the extend of being able to completely evaporate subhaloes (e.g. see Vogelsberger et al. 2019). Baryons will not affect the gravothermal SIDM modelling presented in Subsection 2.2.1, but will enhance the effect of tidal stripping due to the presence of a Galactic disk.

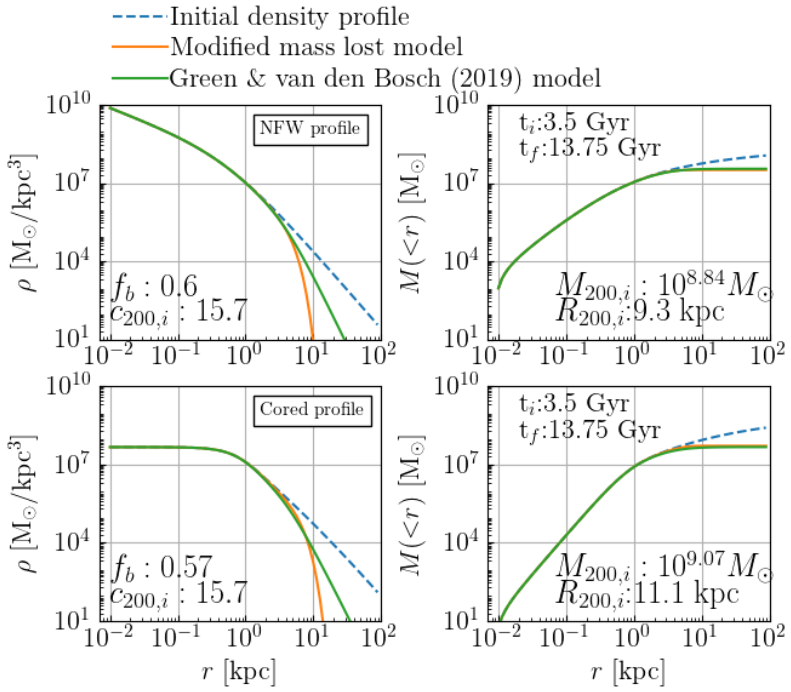

Figure 2.2: Top panels: Density (left) and enclosed mass (right) as a function of radius for a subhalo that has an initial virial mass of $10^{8.84}\,\mathrm{M}_\odot$, an initial NFW profile with concentration 15.7, it follows the orbit of UM over 10 Gyr as it loses 40% of its initial mass ($f_b = 0.6$). The dashed line corresponds to the initial density and mass profile, whereas the solid lines correspond to the final profiles after 10 Gyr. Bottom panels: same as top panels but for a subhalo with an initial virial mass of $10^{9.07}\,\mathrm{M}_\odot$ and an initial cored profile. From the left panels it can be seen that the density profiles are largely truncated when we apply eq. (2.10) in comparison to the Green & van den Bosch (2019) model, however the large difference only occurs in the outskirts of the halo, beyond the virial radius. The right panels show that the enclosed mass of the two models agree when initializing with NFW-shape or cored-shape profile.

2.2.4 . Integration of the equations & initial conditions

The gravothermal model comprises eqs. (2.1-2.5) that govern the evolution of the subhalo's density profile given the cross section per unit mass, σ/m_χ, and the initial subhalo density profile, $\rho_{\rm init}$. We set $\rho_{\rm init}$ to follow an NFW profile, and divide the spherical subhalo into 150 logarithmically spaced concentric shells, ranging between $r_{\rm min} = 10^{-2}$ kpc and $r_{\rm min} = 10^{2}$ kpc.

We solve the gravothermal model by re-writing the equations into non-dimensional form, to do so we introduce a characteristic mass, density and radius, and numerically integrate the equations over a time-step Δt. For each iteration, Δt is restricted to be

$$\Delta\tilde{t} = \min\left[\frac{2}{3}\frac{\tilde{\rho}}{\tilde{v}}(\Delta\tilde{r})^2(ab^{-1}\tilde{\sigma_m}^2 + (C\tilde{\rho}\tilde{v}^2)^{-1})\right], \tag{2.11}$$

where "$\sim$" denotes the variables non-dimensional form, and Δr the radial spacing of the density profile. We further describe the non-dimensional terms and solution of the gravothermal equations in Appendix A.

We combine the gravothermal model with the orbit integration model, so that at each time-step we calculate the subhalo's distance to the galaxy centre, d_{GC}, as well as the instantaneous angular velocity, ω. We use these quantities to determine the amount of mass lost between two consecutive time-steps using eqs. (2.7) and (2.8). At each time step we also evolve the MW's virial mass following eq. (2.6), as well as the MW's halo density profile, which we assume to be an NFW profile that follows the concentration-mass relation of the form

$$\begin{aligned}\log_{10} c_{200}(M_{200}, z) &= \alpha(z) + \beta(z)\log_{10}(M_{200}/\,{\rm M}_\odot) \times \\ &\quad [1 + \gamma(z)(\log_{10} M_{200}/\,{\rm M}_\odot)^2],\end{aligned} \tag{2.12}$$

from Correa et al. (2015c). Every 250 Myrs, we apply eq. (2.10) in order to truncate the density profile according to the amount of mass lost during that period.

Subhaloes hosting the MW dSphs are initialised with the orbital parameters taken from Fritz et al. (2018), namely the distance to the MW centre, d_{GC}, radial velocities, v_R and tangential velocities, v_T, which are used to calculate the orbital evolution of each subhalo. Fritz et al. (2018), as well as Helmi et al. (2018), reported uncertainties in the dwarf distances and radial velocities of the order of $7-8\%$. We have found that such errors do not change the results presented in the following section. The errors of the tangential velocities, however, are larger, of the order of 20% for all dwarfs except CVnI, LeoI and LeoII, which range between 60 and 110%. These errors can change the orbits of the dwarfs to a great extent, thus altering the rate of mass loss and affecting the period of gravothermal collapse. In Section 2.4.5 we discuss how the errors in v_T impact on our results.

Besides the orbital parameters, each subhalo is initialised with two free parameters: the cross section per unit mass, σ/m_χ, and the initial subhalo virial mass, $M_{200,\mathrm{init}}$. The latter is used to estimate the DM halo concentration parameter at the initial cosmic time $t = 3.5$ Gyr (redshift $z = 1.87$), using the concentration-mass relation of Correa et al. (2015c), which in turn is used to initialise ρ_{init}.

Table 2.1 lists the orbital parameters taken from Fritz et al. (2018), the initial virial mass and set of parameters that describe the initial NFW profile for each subhalo. Note that the initial concentrations for the dSphs are quite low ($c_{200} \sim 6-7$), in opposite to typical $z = 0$ values for $10^9\,\mathrm{M}_\odot$ systems of $c_{200} \sim 15-20$. This is because of two reasons. First $c_{200,\mathrm{init}}$ is set by assuming that 10 Gyrs ago, before the dSph galaxies became MW's satellites, those galaxies were hosted by field haloes that followed the median concentration-mass relation for $z = 1.87$. Secondly, the concentration-mass relation from Correa et al. (2015c) is not a best-fit extrapolation from cosmological simulations, it is a semi-analytic model that combines an analytic model for the halo mass accretion history, based on extended Press Schechter (EPS) theory (Press & Schechter 1974), with an empirical relation between concentration and formation time (Correa et al. 2015c). Because the semi-analytic model is based on EPS theory, it can be applied to wide ranges in mass, redshift and cosmology. Throughout this work we assume Planck13 cosmology (Planck Collaboration et al. 2014a) with Ω_{m}, Ω_Λ, h, σ_8, n_s equal to 0.307, 0.693, 0.6777, 0.8288, 0.9611, respectively. In Section 2.4.4 we discussed how changing the initial values of the concentration parameter impacts on our results.

We run the SIDM halo model for the nine systems hosting the most massive MW dSphs. The evolution begins when the Universe is 3.5 Gyr old, at a point when none of the systems have yet crossed the MW's virial radius, and it finishes at present time, covering 10.2 Gyrs of evolution. In Section 2.4.3 we show that using an NFW profile for the initial density profile of subhaloes and MW, rather than a cored profile, does not modify our results.

2.3 . Results

In this Section we present the results obtained with the SIDM halo analytic model. We begin by illustrating how the joint framework of gravothermal evolution and gravitational tidal stripping shapes the evolution of the density profile of each system. We next describe the range of values of the free parameters, σ/m_χ and $M_{200,\mathrm{init}}$, that reproduce the central DM densities reported in Kaplinghat et al. (2019). Finally we show that there is a promising range of velocity-dependent cross section models that explain the anti-correlation of central density and pericenter distance for the nine most massive MW dSphs.

Name	Orbital parameters			Initial Conditions			
	$d_{\rm GC}$ [kpc]	$v_{\rm R}$ [km/s]	$v_{\rm T}$ [km/s]	$M_{200,\rm init}$ [$10^9\,{\rm M}_\odot$]	$c_{200,\rm init}$	$\rho_{\rm s,init}$ [$10^7\,{\rm M}_\odot/{\rm kpc}^3$]	$r_{\rm s,init}$ [kpc]
UM	78	−71	136	0.60	6.87	1.84	1.30
Draco	79	−89	134	3.46	6.36	1.54	2.52
Carina	105	2	163	2.13	6.53	1.62	2.09
Sextans	89	79	229	0.67	6.99	1.83	1.34
CvnI	211	82	94	1.09	6.68	1.73	1.63s
Sculptor	85	75	184	4.74	6.28	1.49	2.82
Fornax	141	−41	132	3.54	6.38	1.53	2.54
LeoII	227	20	74	0.14	7.30	2.13	0.76
LeoI	273	167	72	3.23	6.40	1.55	2.44

Table 2.1: Form left to right: list of orbital parameters and initial conditions. The first column indicates the name of the dSph galaxy that corresponds to the observational estimates for the galactocentric distance, $d_{\rm GC}$, radial and tangential velocities, $v_{\rm R}$ and $v_{\rm T}$, taken from Fritz et al. (2018). The fifth and sixth columns from the left correspond to the initial virial mass and concentration, $M_{200,\rm init}$ and $c_{200,\rm init}$, each subhalo is initialised at cosmic time 3.5 Gyr ($z = 1.87$) before infalling onto the MW system. The seventh and eighth columns indicate the respective scale density and radius, $\rho_{\rm s}$ and $r_{\rm s}$, of the initial NFW density profile, $\rho_{\rm init}$.

2.3.1 . SIDM halo evolution

In this Section we show the evolution of the subhalo that hosts the galaxy Carina. For this system the model was initialised with a cross section of $\sigma/m_\chi = 40$ cm^{2}g^{-1}. We assume that 10.2 Gyrs ago (redshift $z = 1.87$), Carina had a virial mass of $M_{200} = 2 \times 10^9\,{\rm M}_\odot$, and its density followed the NFW profile with a scale density and radius of $4.2 \times 10^6\,{\rm M}_\odot{\rm kpc}^{-3}$ and 2.09 kpc, respectively.

Fig. 2.3 shows the density (left panels) and velocity (right panels) profiles at different times. The velocity corresponds to the particles' average collision velocity, $\langle v \rangle = (4/\sqrt{\pi})v$ (for a Maxwellian distribution), with v the 1-D velocity dispersion. Each line in the figure is coloured according to the lookback time as shown by the colour bars on the right. In the top panels, the dark blue lines correspond to the density and velocity of the system when it begins to evolve, 10.2 Gyrs ago, whereas the orange lines correspond to the evolution of the system between 7.4 and 8.8 Gyrs ago. It can be seen that after a few time-steps the cusp in the central region disappears, the central density decreases and a core of roughly constant density begins to form.

The top right panel shows that while the density profile rapidly forms a central core, the particles' velocity increases. The density in the inner regions decreases due to DM-DM collisions, that expel some DM particles from the central regions into further out orbits, at the same time the velocity increases because collisions increase the mean velocity of particles.

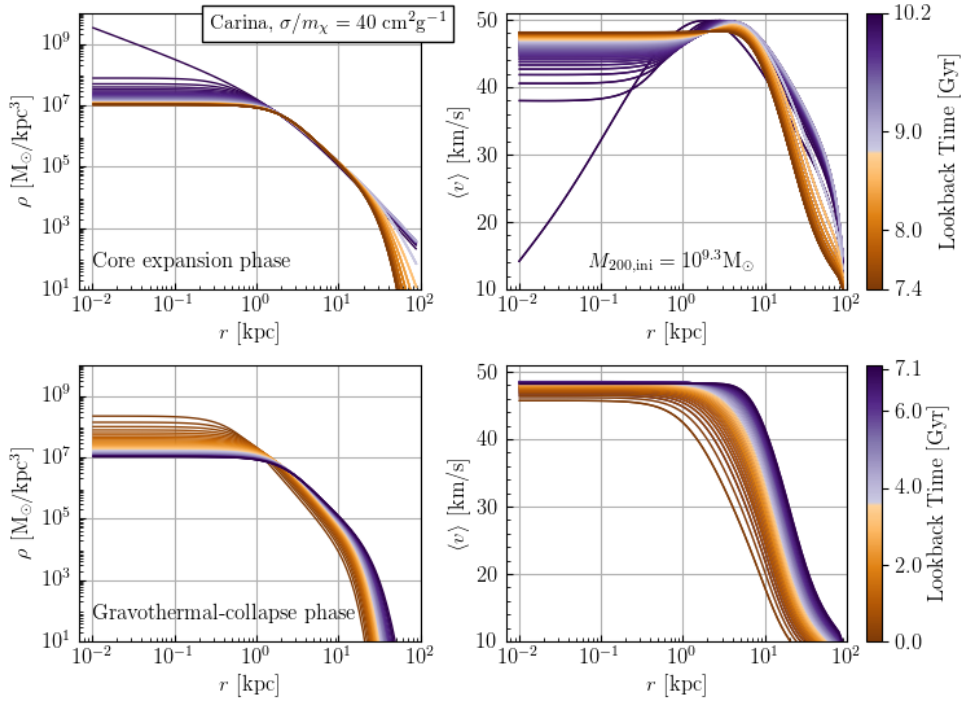

Figure 2.3: Top panels: Density (left) and velocity profile (right) as a function of radius for the subhalo hosting the galaxy Carina. In this example the model was initialised with a cross section of $\sigma/m_\chi = 40$ cm^{2}g^{-1} and a virial mass of $M_{200} = 10^{9.3}\,\mathrm{M}_\odot$. The subhalo was evolved for 10.2 Gyrs from an initial NFW profile with scale density and radius of $4.2 \times 10^6\,\mathrm{M}_\odot\mathrm{kpc}^{-3}$ and 2.09 kpc, respectively. Each line in the panels is coloured according to the lookback time, as shown in the colour bar at the top. Bottom panels: same as top panels but for the last 7 Gyrs of evolution, when the system undergoes the gravothermal collapse phase.

DM-DM particle collisions add energy to the core, causing particles to move into larger orbits at lower velocities. Through collisions the subhalo's core becomes a system with negative heat capacity, where adding energy cools down the system, while the extended subhalo becomes a large thermal reservoir that absorbs the core's energy. The subhalo stabilises as it forms a high temperature core with negative heat capacity. This is the period between the end of the core expansion phase and the beginning of the gravothermal collapse-phase, that began roughly 9 Gyrs ago for this system and lasts for roughly 3 Gyrs. The bottom panels of Fig. 2.3 show the evolution of the subhalo in the gravothermal-collapse phase. During this phase, the high temperature, negative-heat capacity core in contact with the cold extended halo gives up heat, getting hotter rather than colder. The hot core then contracts, the central density increases, leading to the gravothermal collapse phase. In the case of Carina, the subhalo reaches a stable central density of $10^7\,\mathrm{M}_\odot\mathrm{kpc}^{-3}$. During the last 7 Gyrs, as it goes into the gravothermal collapse phase, its density increases an order of magnitude, reaching a value of $2\times10^8\,\mathrm{M}_\odot\mathrm{kpc}^{-3}$.

An important aspect in the evolution of Carina is the result of the joint gravothermal evolution and gravitational tidal stripping modelling. Differently from previous studies, the contraction phase of the core is not followed by an increase in the particle's velocity as it would be expected. Instead the particles' velocity decreases during the last 4 Gyr of evolution, this is because during this period hydrostatic equilibrium significantly lowers the pressure of the subhalo when it loses mass, causing the velocity to decrease. Since heat flows towards the colder extended halo, heat is diffused at a faster rate when mass is tidally stripped, leading to a faster formation of the isothermal core and thus an accelerated evolution for core collapse.

All systems undergo a similar evolution to the one described in this section, with the only difference that a few systems reach a higher or lower central density during the gravothermal collapse phase, and others lose more or less mass as they orbit around the MW. The following section describes the dependence of central density evolution on the scattering cross section.

2.3.2 . Central density evolution

The evolution of the central DM density of the subhalo, along with its mass loss rate, largely depends on the scattering cross section. At fixed initial mass, a large cross section leads to a larger rate of DM-DM collisions that produce a shallower and lower density core. Similarly, the larger rate of DM-DM collisions leads to less concentrated subhaloes, making them more prone to tidal disruption and mass loss.

This dependency on the cross section can be seen in Fig. 2.4, that shows the

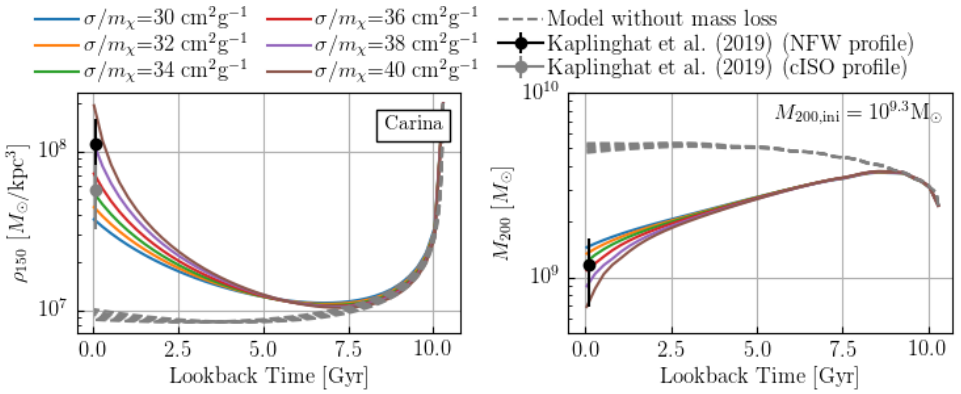

Figure 2.4: Left panel: Carina's DM density at 150 pc, ρ_{150}, as a function of lookback time. The coloured lines correspond to the subhalo model initialised with a different cross section value, ranging from $\sigma/m_\chi = 32$ cm^{2}g^{-1} to $\sigma/m_\chi = 40$ cm^{2}g^{-1}, but the same initial virial mass, $M_{200,\mathrm{init}} = 2 \times 10^9\,\mathrm{M}_\odot$. The dashed lines show the evolution of ρ_{150} (and M_{200}) in the scenario that the subhalo does not lose mass from tidal interactions. The black symbols show the values of ρ_{150} (and M_{200}) taken from Kaplinghat et al. (2019), who assumed an isothermal cored profile as well as NFW. Right panel: same as left panel, but showing the evolution of Carina's virial mass, M_{200}, as a function of lookback time.

evolution of Carina's DM density at 150 pc, ρ_{150} (left panel), and virial mass, M_{200} (right panel). The coloured lines in the figure correspond to the subhalo model initialised with different values for the cross section, ranging from $\sigma/m_\chi = 32$ cm^{2}g^{-1} to $\sigma/m_\chi = 40$ cm^{2}g^{-1}, but the same initial virial mass, $M_{200,\mathrm{init}} = 2 \times 10^9\,\mathrm{M}_\odot$. The dashed lines show the evolution of ρ_{150} and M_{200} without imposing loss of mass from tidal interactions. The black symbols show the values of ρ_{150} and M_{200} reported by Kaplinghat et al. (2019), who assumed both an isothermal cored (grey symbol), as well as NFW (black symbol), profile. We derive M_{200} from the V_{max} and R_{max} estimations of Kaplinghat et al. (2019) assuming an NFW profile for the subhalo density.

The left panel of Fig. 2.4 shows that the central density quickly drops when the core of the subhalo forms, and it rises again as the core begins to collapse. For both cases, with or without tidal stripping, the central density reaches a minimum stable value, roughly independent of the cross section. For the model that includes mass loss from tidal stripping, the collapse time becomes shorter than the age of the Universe (as also shown by e.g. Nishikawa et al. 2020), and the central density reaches higher values for a higher cross section.

The right panel shows that for the case of no tidal stripping, the subhalo's virial mass slightly increases during its evolution, this is because M_{200} is calculated

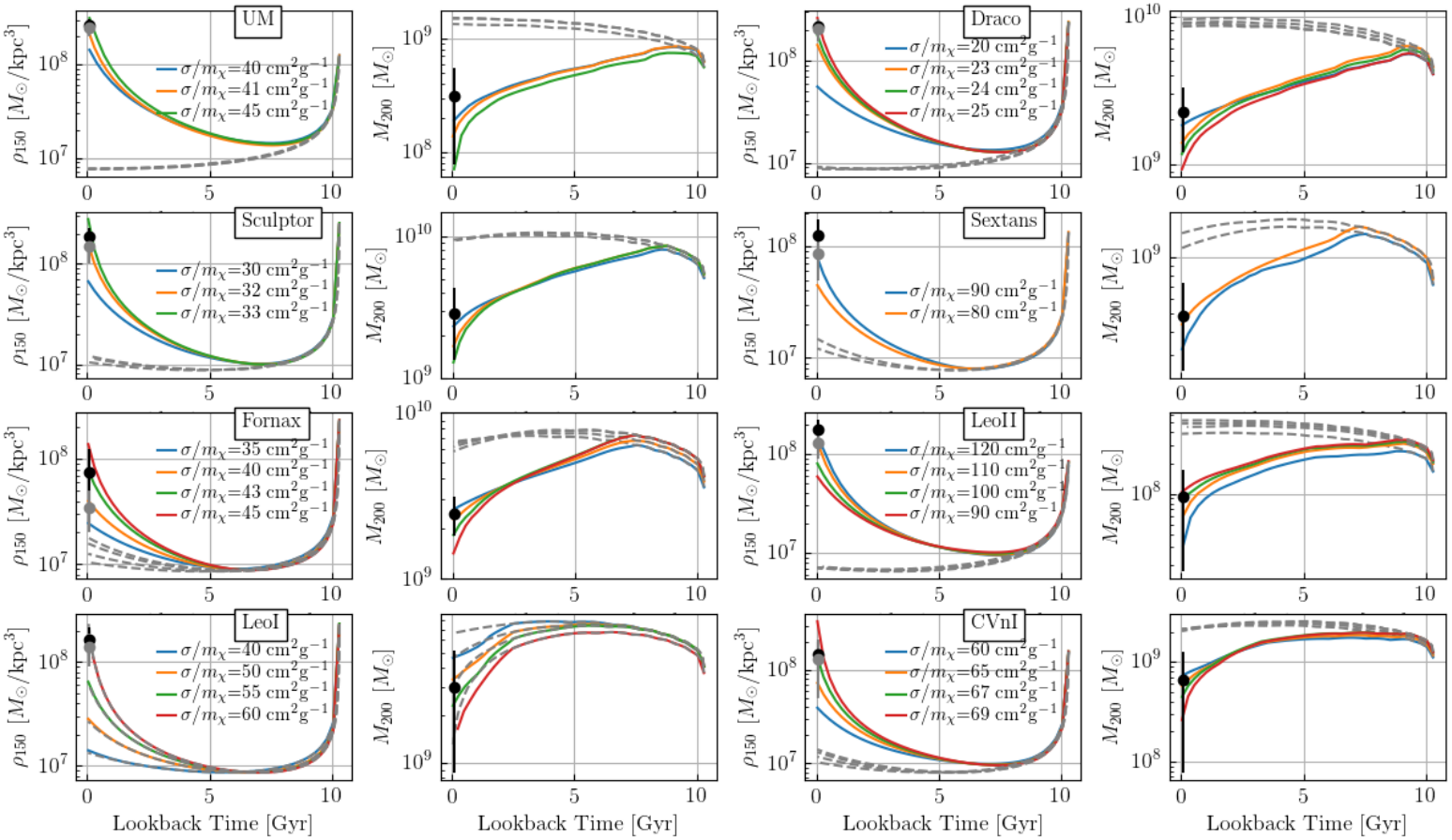

Figure 2.5: Same as Fig. 2.4 for the remaining subhaloes hosting the MW dSphs as indicated in each panel.

by integrating the subhalo's density profile until the mean density is $200 \times \rho_{\rm crit}$, with $\rho_{\rm crit}(z)$ decreasing with decreasing lookback time (decreasing redshift). For the model with tidal stripping, the panel shows that during the last 2.5 Gyr, the rate of mass loss is higher for higher cross sections.

Fig. 2.4 shows that cross sections ranging between $\sigma/m_\chi = 32$ cm^{2}g^{-1} and $\sigma/m_\chi = 40$ cm^{2}g^{-1} are able to explain the observed central DM density of Carina (within the uncertainty), as well as the final virial mass of the system. However, this range of parameters seems to only apply to Carina. Fig. 2.5 shows the evolution of DM density at 150 pc and virial mass for the remaining subhaloes hosting the MW dSphs: UM, Draco, Sculptor, Sextans, Fornax, LeoII, LeoI and CVnI. From the figure it can be seen that there is a large variety of cross sections that reproduce the observed central densities. Draco, for instance, prefers lower values of σ/m_χ, ranging between $\sigma/m_\chi = 23$ cm^{2}g^{-1} and $\sigma/m_\chi = 25$ cm^{2}g^{-1}, whereas LeoII requires σ/m_χ ranging between $\sigma/m_\chi = 120$ cm^{2}g^{-1} and $\sigma/m_\chi = 90$ cm^{2}g^{-1}.

An interesting case shown in Fig. 2.5 is that of LeoI, since this subhalo crossed the MW's virial radius roughly 2 Gyrs ago, it has not lost a large amount of mass from tidal interactions with the MW. Therefore the models with and without mass loss agree.

Fig. 2.5 shows that large cross sections are needed in order to reproduce the observed central DM densities of the local dSphs. Interestingly, such large cross sections are not ruled out by observational constraints related to the TBTF. Vogelsberger et al. (2012) produced zoom simulations of MW-size hosts using SIDM with velocity-dependent σ/m_χ values tuned to have small values (~ 0.1 cm^{2}g^{-1}) on cluster scales and large values (~ 10 cm^{2}g^{-1}) on the scale of dwarf galaxies. They showed that the velocity-dependent SIDM model resolved the TBTF problem, and it provided a particular good match to the spread in dwarf satellite central densities seen around the MW. Elbert et al. (2015) showed that even larger cross sections, e.g. $\sigma/m_\chi = 50$ cm^{2}g^{-1}, also alleviate the TBTF problem and produce constant density cores of size 300-1000 pc, comparable to the half-light radii of $\sim 10^{5-7}\,{\rm M}_\odot$ stellar mass dwarfs.

Table 2.2 summarises the final density profiles for the SIDM subhaloes presented in this section. From left to right, it shows the hosted dSph galaxy name, virial mass, concentration parameter, core size and the preferred range of cross section values. Note that the virial mass is calculated by integrating the density profile up to the virial radius, which in turn is estimated as the radius within which the mean density is 200 times $\rho_{\rm crit}(z=0)$. The core radius, $r_{\rm c}$, is calculated by fitting an isothermal profile ($\rho(r) = \rho_0/(r_{\rm c}^2 + r^2)$).

Figs. 2.4 and 2.5 show that all MW dSphs need to be in gravothermal core collapse in order to explain the observational data. This result, however, strongly depends on the initial virial mass of the systems, $M_{200,{\rm init}}$, which is not chosen

Name	Final profile			Preferred cross section
	M_{200} $[10^9\,\mathrm{M}_\odot]$	c_{200}	$r_{\rm core}$ [pc]	σ/m_χ $[\mathrm{cm}^2\mathrm{g}^{-1}]$
UM	0.13	34.2	180.8	$40-50$
Draco	1.17	26.8	472.9	$20-30$
Carina	1.09	19.1	648.4	$40-50$
Sextans	0.32	20.8	395.5	$70-120$
CVnI	0.46	25.7	356.8	$50-80$
Sculptor	1.65	25.8	553.2	$30-40$
Fornax	2.29	15.3	1036.7	$30-50$
LeoII	0.05	30.6	148.8	$90-150$
LeoI	1.17	31.1	410.8	$50-70$

Table 2.2: Form left to right: name of the dSph galaxy, present-time virial mass, concentration parameter and core size of the subhalo hosting the dSph and range of preferred cross section values that reproduce the observed DM central densities.

at random, it is tuned so that the systems, in their final state, have a virial mass that reproduces the observational estimations. If we disregard this and increase the initial mass of the systems, lower values of σ/m_χ will be needed to reproduce the observed central DM densities. But again, they would not be a good theoretical representation of the dSphs because, even considering that the model's rate of mass loss is a lower limit, the systems would too massive.

In Appendix A.4 we show that changing $M_{200,\rm init}$ in 20% can change the final central DM densities of subhaloes in up to 50%. Although the final DM central density is quite sensitive to the choice of initial mass, it also largely depends on σ/m_χ. Fig. 2.4 shows that for a constant $M_{200,\rm init}$, changes in σ/m_χ of up to 25% lead to changes of 80% in the final central DM densities.

2.3.3 . Velocity-dependent cross section

In this section we analyse the range of cross sections that match the observed central DM densities shown in Figs. 2.4 and 2.5. To understand its dependence with the particles velocity we calculate the average collision velocities, $\langle v\rangle$, of DM particles within each system's core. We define $\langle v\rangle = (4/\sqrt{\pi})v$ (for a Maxwellian distribution), with v the average 1-D velocity dispersion of each system's core. We find that for the case of Carina for example (Figs. 2.3 and 2.4), observations favour a cross section range between 32 and 40 $\mathrm{cm}^2\mathrm{g}^{-1}$, as its core reaches a stable collision velocity of ≈ 48 km/s.

We find that there is a strong correlation between σ/m_χ and $\langle v\rangle$. This is shown in Fig. 2.6, that highlights the range of values for each dSph. From the figure it can be seen that for systems such as LeoII, characterised by $\langle v\rangle \approx 21$ km/s, observations favour a large cross section, whereas for Draco, which has a $\langle v\rangle \approx$58 km/s, observations favour lower cross sections. We determine the range

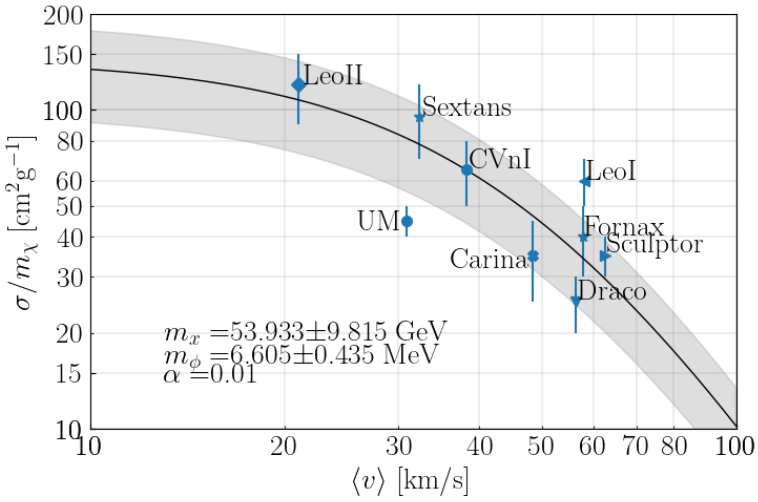

Figure 2.6: Cross section per unit mass, σ/m_χ, as a function of the average collision velocity, $\langle v \rangle$, of DM particles within each subhalo's core. Symbols show the range of σ/m_χ needed for the SIDM model to reproduce the central DM densities reported by Kaplinghat et al. (2019). The solid line corresponds to the best-fit relation given by eq. (2.15) to the MW dSph data.

of cross sections for each dSph by analysing the models with fixed σ/m_χ that are able to reproduce the DM central densities (Fig. 2.5), and also by considering that DM densities from the gravothermal model may differ from N-body simulations by up to a factor of 2 (Essig et al. 2019). We used this uncertainty to further extend the range of σ/m_χ.

Fig. 2.6 indicates that the range of cross sections needed to reproduce the observed DM densities are not random, instead they point towards an intrinsic velocity-dependent relation. We investigate this relation in the context of particle physics models for SIDM, where a DM particle χ of mass m_χ interacts under the exchange of a light mediator ϕ, with the self-interactions being described by a Yukawa potential

$$V(r) = \pm \frac{\alpha_\chi}{r} e^{-m_\phi / r}, \tag{2.13}$$

with r the separation between DM particles, α_χ the analog of the fine-structure constant in the dark sector, and m_ϕ the mediator mass.

There is no analytical form for the differential scattering cross section due to a Yukawa potential, but by using the Born-approximation (valid when the scattering potential can be treated as a small perturbation), the analytical form that approximates the true differential cross section results (see e.g. Ibe & Yu 2010; Tulin

et al. 2013; Tulin & Yu 2018)

$$\frac{\mathrm{d}\sigma}{\mathrm{d}\Omega} = \frac{\sigma_0}{4\pi}\left[1 + \frac{v^2}{w^2}\sin^2\left(\frac{\theta}{2}\right)\right]^{-2}, \tag{2.14}$$

where v is the relative velocity between interacting DM particles, $w \equiv m_\phi/m_\chi$ is a characteristic velocity, $\sigma_0 = 4\pi\alpha_\chi^2 m_\chi^2/m_\phi^4$ is the amplitude of the cross section, and θ is the scattering angle in the frame of the centre of mass. Given that the Yukawa-scattering model (eq. 2.14) is anisotropic, we calculate the momentum transfer cross-section, $\sigma_T/m_\chi \equiv 2\int(1-|\cos\theta|)\frac{\mathrm{d}\sigma}{\mathrm{d}\Omega}\mathrm{d}\Omega$, which has been shown to be a more relevant quantity than the total cross-section for determining the rate at which cores form in isolated DM haloes (Robertson et al. 2017). After integrating over the solid angle σ_T/m_χ results

$$\begin{aligned}
\sigma_T/m_\chi &= \sigma_{0T}\frac{4w^4}{v^4}\left[2\ln\left(1+\frac{v^2}{2w^2}\right) - \ln\left(1+\frac{v^2}{w^2}\right)\right], \qquad (2.15)\\
&\text{with}\\
\sigma_{0T} &= 274.4\left(\frac{\alpha_\chi}{0.01}\right)^2\left(\frac{m_\chi}{10\,\mathrm{GeV}}\right)\left(\frac{10\,\mathrm{MeV}}{m_\phi}\right)^4,\\
w &= 300\left(\frac{m_\phi}{10\,\mathrm{MeV}}\right)\left(\frac{10\,\mathrm{GeV}}{m_\chi}\right)\,\mathrm{km\,s^{-1}}.
\end{aligned}$$

We fit eq. (2.15) to the dSphs values in order to determine the values of DM mass and mediator mass that reproduce the relation. We assume $\alpha_\chi = 0.01$ and find that the relation is best fitted by a DM particle mass of $m_\chi = 53.933 \pm 9.815$ GeV and a mediator mass of $m_\phi = 6.605 \pm 0.435$ MeV. This best-fit relation is shown in Fig. 2.6 in solid line, the grey region highlights the uncertainty by propagating the errors of m_χ and m_ϕ.

Fig. 2.7 extends the cross section-velocity plane to include MW- ($v \sim 150-300$ km/s) and cluster-size ($v \sim 1000-5000$ km/s) haloes, and it shows the velocity-dependence of self-interactions in terms of the mean velocity-weighted cross section per unit mass $\langle\sigma v\rangle/m_\chi$. In the figure the values for the MW dSph galaxies are shown in blue symbols, whereas the red symbols correspond to the latests constraints from Sagunski et al. (2021), who applied the SIDM Jeans modelling to a sample of galaxy groups and clusters from Newman et al. (2015). The black dashed line highlights the best-fit relation to both the MW dSph data points from this work and the groups/clusters data from Sagunski et al. (2021). We find that eq. (2.15) is best fitted by a DM particle mass of $m_\chi = 10.86 \pm 1.9$ GeV and a mediator mass of $m_\phi = 9.05 \pm 0.27$ MeV. The blue solid line shows the best-fit relation to the MW dSph data (Fig. 2.6) extrapolated to large scales.

Fig. 2.7 also includes additional observational constraints. For characteristic DM velocities of MW-size haloes, the upper limit of $\sigma/m_\chi < 10$ cm^{2}g^{-1} is set by

subhalo evaporation, where collisions between DM particles within subhaloes and in the host are frequent enough to unbind material from the halo. In this case, energy transfer is determined by the relative velocity of the colliding particles, which is of the order of the orbital velocity, therefore the mass loss in subhaloes is enhanced and the subhalo abundance is depleted relative to the CDM case, particularly in the central regions (e.g. Vogelsberger et al. 2012; Rocha et al. 2013; Zavala et al. 2013). Note that the large values of σ/m_χ on dwarf-scales does not translate into evaporation of substructure, this is because the relative velocity between the subhalo and its host halo is set by the velocity dispersion of the latter, for which the cross section is suppressed.

The lower limit of $\sigma/m_\chi > 1$ cm^{2}g^{-1} has been imposed to solve the cusp-core and TBTF problem, otherwise dwarfs and low surface brightness galaxies in SIDM models end up too dense and do not produce large enough core radii (e.g. Davé et al. 2001; Kaplinghat et al. 2016). For $\sigma/m_\chi = 1$ cm^{2}g^{-1}, Robles et al. (2019) find very similar substructure abundance around the MW between the SIDM model and CDM. Differently, Nadler et al. (2020) performed high-resolution zoom-in simulations of a MW-mass halo and reported that 56% was disrupted and erased due to subhalo-host halo interactions for a $\sigma/m_\chi = 2$ cm^{2}g^{-1}. Neither of these works included baryons in their simulations, but Robles et al. (2019) embedded subhaloes in a baryonic potential to capture effects of the disk and bulge contributions.

For characteristic DM velocities of cluster-size haloes, the upper limits in the figure correspond to strong lensing measurements of the ellipticity and central density of clusters (Peter et al. 2013), measurements of the offset between the DM and galaxy centre (e.g. Kahlhoefer et al. 2015; Harvey et al. 2015; Wittman et al. 2018; Harvey et al. 2019) and measurements of the mass-to-light ratio of the Bullet Cluster (Randall et al. 2008). Fig. 2.7 shows that the best-fit relation to the MW dSph galaxies data points (blue solid line) lies in good agreement with the observational constraints shown in orange. The best-fit relation to the MW dSph data and the groups/clusters data from Sagunski et al. (2021) (black dashed line), is in good agreement with the upper limits for cluster-size haloes, but overshoots the upper limit for MW-size haloes.

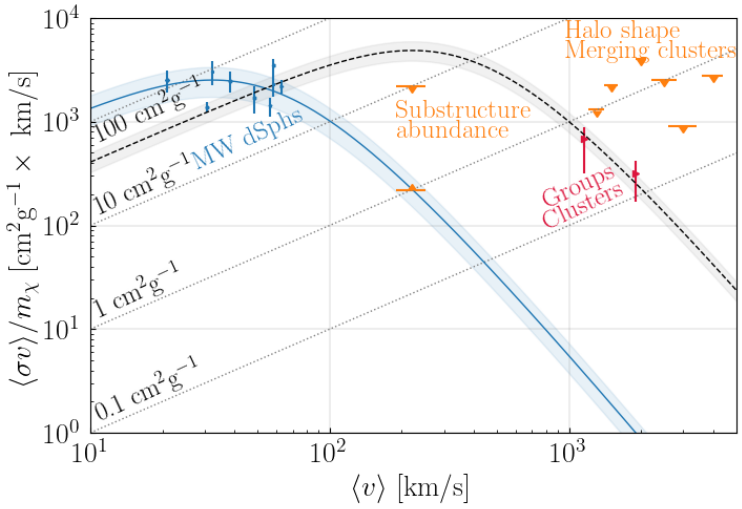

Figure 2.7: Velocity-dependence of self-interactions in terms of the mean velocity-weighted cross section per unit mass $\langle\sigma v\rangle/m_\chi$, extended to cover the range of MW- ($\sim$200 km/s) and cluster-size ($\sim 1000 - 5000$ km/s) haloes' velocities. The figure shows in orange symbols upper and lower limits for σ/m_χ taken for substructure abundance studies (e.g. Volgelsberger et al. 2012 and Zavala et al. 2013), as well as based on halo shape/ellipticity studies and cluster lensing surveys (see text). It also includes the MW dSphs data from this work (blue symbols) and the latests constraints of groups and clusters from Sagunski et al. (2021) (red symbols). The black dashed line highlights the best-fit relation to both the MW dSph data points from this work and the groups/clusters data. The blue solid line shows the best-fit relation to the MW dSph data (Fig. 2.6) extrapolated to large scales.

2.4 . Discussion

2.4.1 . Comparison with previous works

Recent works have also investigated the evolution of MW dSph galaxies aiming to constrain the SIDM cross section. Read et al. (2018) and Valli & Yu (2018) considered a subhalo's inner region (limited by a radius r_χ), within which the average scattering rate per particle times the halo age ($t_{\rm age}$) is equal to unity. At $r = r_\chi$, therefore, the cross section can be constrained from the relation

$$\sigma/m_\chi \simeq (\sqrt{\pi}/4)\rho(r_\chi)^{-1}v(r_\chi)^{-1}t_{\rm age}^{-1}, \tag{2.16}$$

where $\rho(r)$ is the density profile and $v(r)$ the velocity dispersion.

Valli & Yu (2018) analysed the stellar kinematic dataset for the MW dSphs, applying the standard Jeans analysis, to infer the stellar and DM density and velocity dispersion. They assumed $t_{\rm age}$ to be flatly distributed in the range 8-12 Gyr and found that UM, Draco, LeoI and LeoII probed cross sections $\sim 0.1 - 1$ cm^{2}g^{-1}, whereas Sextans and Fornax had cross section values that peaked around $\sim 20 - 40$ cm^{2}g^{-1}. Sculptor and Carina probed intermediate cross section values of $\sim 2 - 7$ cm^{2}g^{-1}.

Read et al. (2018) focused on Draco and first calibrated the parameters r_χ and $t_{\rm age}$ using Vogelsberger et al. (2012) SIDM cosmological zoom simulations of MW-mass haloes. They found that Draco's high central density gives an upper bound on the SIDM cross section of $\sigma/m_\chi < 0.57$ cm^{2}g^{-1}.

The model given by eq. (2.16) does not include the effects of core collapse, we test it by applying eq. (2.16) to our simulated subhaloes assuming $t_{\rm age}$ in the range 8-12 Gyr, and never recover a σ/m_χ larger than 1 cm^{2}g^{-1}. In addition, the model is only valid if the SIDM subhalo density profile follows a cored profile. Observational studies, however, have reported that only Fornax exhibits a prominent core (e.g. Jardel & Gebhardt 2012; Pascale et al. 2018), Draco (e.g. Read et al. 2018) and the remaining MW dSphs are better described by a cuspy profile (e.g. Read et al. 2019 and references therein). Interestingly, for Fornax, Valli & Yu (2018) reported a $\sigma/m_\chi \approx 40$ cm^{2}g^{-1}, in agreement with our results

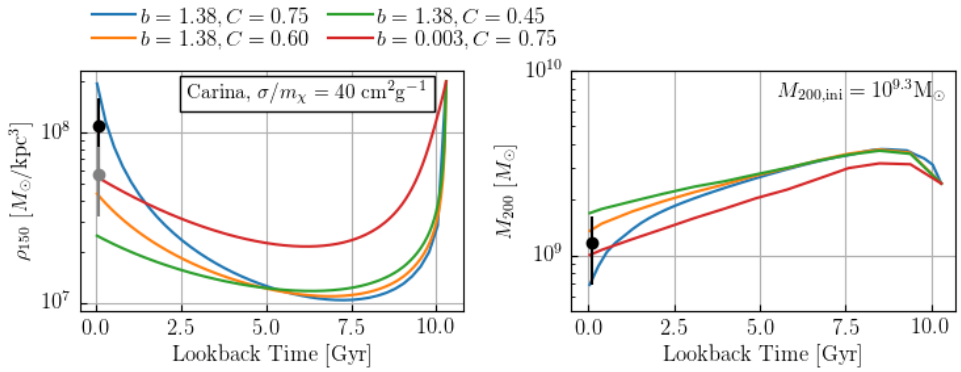

Figure 2.8: Left panel: Carina's DM density at 150 pc, ρ_{150}, as a function of lookback time. The coloured lines correspond to the subhalo model initialised with a cross section of $\sigma/m_\chi = 40$ cm^{2}g^{-1}, but different values for the parameters C and b that govern the gravothermal collapse model (see Section 2.2.1 for further details). The symbols show the values of ρ_{150} (and M_{200}) taken from Kaplinghat et al. (2019), who assumed an isothermal cored profile (grey symbol) as well as NFW (black symbol). Right panel: same as left panel, but showing the evolution of Carina's virial mass, M_{200}, as a function of lookback time. The figure shows that the parameters C and b impact on our results but not by a large factor.

2.4.2 . Challenges

An important caveat of the gravothermal collapse model is that the parameter C cannot be derived from first principles, instead it needs to be calibrated using N-body simulations. Previous works have done it (Balberg et al. 2002; Koda & Shapiro 2011; Essig et al. 2019; Nishikawa et al. 2020), but have not reach to a consensus of its value, other than it ranges between 0.45 and 0.75. In this section we investigate how changing C from 0.75 (assumed so far) to 0.45 or 0.6 (and $b = 0.003$ as suggested by Nishikawa et al. 2020) impact on our results.

Fig. 2.8 shows the DM density at 150 pc, ρ_{150} (left panel), and virial mass, M_{200} (right panel), of a subhalo hosting a Carina-like dSph galaxy. The coloured lines correspond to the subhalo model initialised with a cross section of $\sigma/m_\chi = 40$ cm^{2}g^{-1} and same initial profile, but different values for the parameters C and b.

For all models, a cross section of $\sigma/m_\chi = 40$ cm^{2}g^{-1} yields close agreement with the estimations from Kaplinghat et al. (2019) (shown as grey and black symbols). For a fixed cross section and $b = 1.38$, a larger C accelerates core collapse. In this manner the figure indicates that the range of cross sections (presented in Section 2.3), derived with a model that assumes $C = 0.75$, should be taken as a lower limit. A model with $b = 1.38$ and $C = 0.45$ requires a factor of $\approx$1.5 larger cross sections to reproduce the observed central DM densities and

virial masses.

The model with $C = 0.75$ and $b = 0.003$ largely differs from the rest. It does not lower the central DM density as much during the core expansion phase, and the rate at which the central DM density increases during the core collapse phase seems to agree with the model with $b = 1.38$ and $C = 0.45$. For a fixed cross section and $C = 0.75$, a lower b yields lower central DM densities and a 'slower' core collapse in comparison to the $C = 0.75$ and $b = 1.38$ model. Therefore, according to this model, the range of cross sections presented in Section 2.3 should also be taken as lower limits, since assuming $b = 0.003$ would result in larger values of σ/m_χ being able to reproduce the observations.

Another important caveat to consider is the assumption of mass conservation in the gravothermal collapse model (eq. 2.1), that is inconsistent with the fact that the subhalo loses mass every 250 Myrs. To solve this we impose that after the subhalo loses mass, it returns to hydrostatic equilibrium, readjusting its density and pressure within each shell. After that the gravothermal model is called back, and the new evolution of the truncated density profile begins. Further details of the numerical implementation of the gravothermal model are presented in Appendix A.1.

2.4.3 . Impact of initial conditions: NFW profile

The SIDM halo model presented in this work evolves the subhaloes hosting the most massive MW dSphs for 10.2 Gyrs, starting when the Universe is 3.5 Gyr old (redshift 1.87) at a point when the subhaloes' initial density ($\rho_{\rm init}$) is assumed to follow the NFW profile. This, however, may not be a good assumption. Harvey et al. (2018) analysed the evolution of 19 low-mass dwarf spheroidal galaxies using a SIDM numerical simulation with $\sigma/m_\chi = 10$ cm^{2}g^{-1}, finding that the dwarf galaxies were already forming a core within the first 2 Gyrs of cosmic time.

It is possible that initializing subhaloes with a cored profile will induce an earlier gravothermal collapse, that will yield lower estimates for the cross sections with respect to the ones reported in Section 2.3.3. In this section we investigate if this occurs by analysing the evolution of Carina and Leo II, that were modelled with $\sigma/m_\chi = 40$ cm^{2}g^{-1} and $\sigma/m_\chi = 120$ cm^{2}g^{-1}, respectively, and initialized with three different density profiles.

The middle panels of Fig. 2.9 show the initial density profile for the models of Carina (top) and Leo II (bottom). In the panels the red dashed lines correspond to the NFW density profile, characterized by a cuspy and cold inner region surrounded by a hot extended halo. Note that we are refering to the inner region as cold because the velocity dispersion (proxy for temperature) is low in the central regions.The regions beyond 1 kpc have a larger velocity dispersion and for that reason they are referred as hot. In the panels the solid lines correspond to two different core

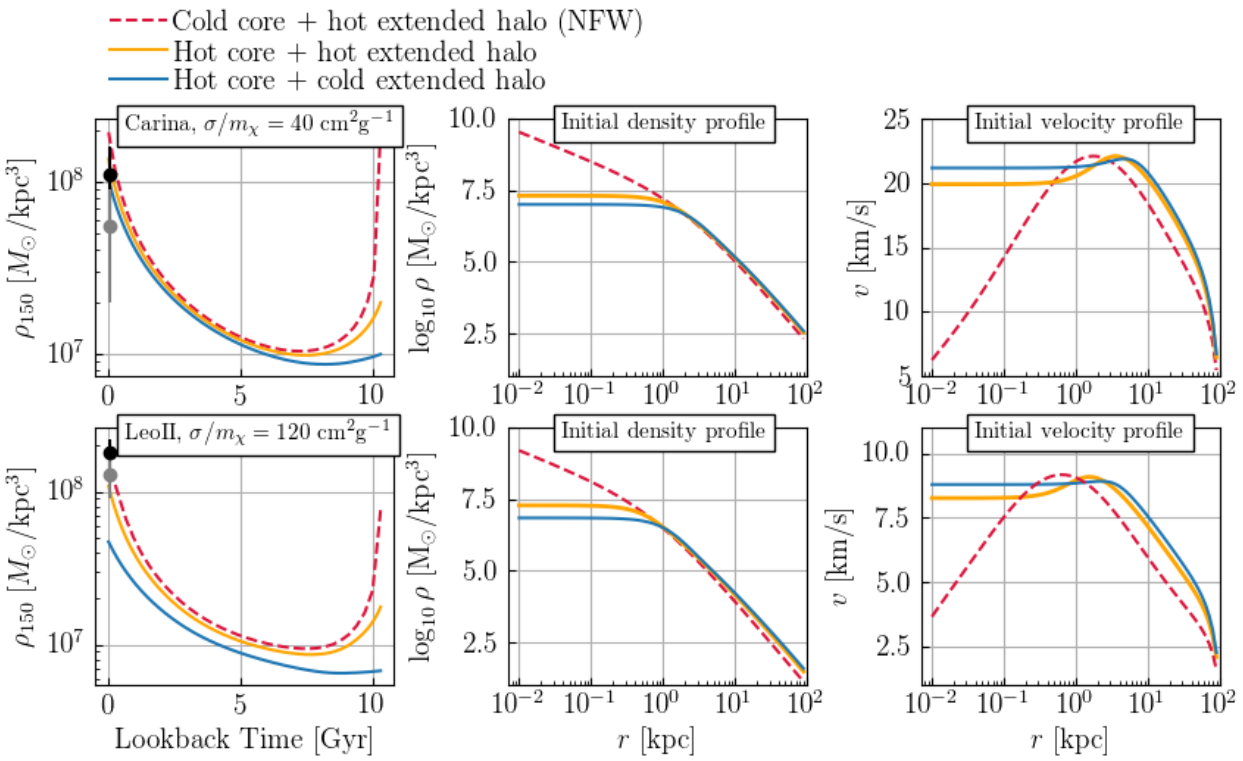

Figure 2.9: DM density at 150 pc, ρ_{150}, as a function of lookback time (left), initial density profile (middle) and initial 1-D velocity dispersion profile (right) for Carina (top panels) and Leo II (bottom panels). Carina was initialized with a cross section of $\sigma/m_\chi = 40$ cm^{2}g^{-1}, whereas Leo II has a cross section of $\sigma/m_\chi = 120$ cm^{2}g^{-1}. The coloured lines correspond to the subhalo model initialised with a NFW density profile (red dashed lines), cored profile with a hot extended halo (yellow solid lines) and cored profile with a cold extended halo (blue solid lines). The symbols show the values of ρ_{150} taken from Kaplinghat et al. (2019), who assumed an isothermal cored profile (grey symbol) as well as NFW (black symbol). The figure shows that initializing the subhaloes' density profile with either an NFW profile or cored profile (with hot extended halo) does not impact the results presented in Section 2.3, however initializing the subhaloes' density with a cored profile surrounded by a hot extended halo slightly alters the evolution of subhaloes.

profiles, one where the inner region is hot and it is surrounded by a hot extended halo (yellow solid lines), and the other where the extended halo is cold (blue solid lines). This can be seen in the right panels that show the 1-D velocity dispersion as a function of radius. The difference between these profiles is that they correspond to different evolutionary stages of SIDM haloes. The hot core + hot extended halo corresponds to a SIDM halo that has a hot inner region due to DM-DM particle interactions (that heat the inner core increasing the central velocity dispersion), but has a hotter periphery due to dynamical heating, induced by mergers and large DM accretion (Colín et al. 2002). On the contrary, the hot core + cold extended halo corresponds to a SIDM halo that has been in isolation.

The left panels of Fig. 2.9 show the evolution of the DM density at 150 pc, ρ_{150}, for Carina (top) and Leo II (bottom). It can be seen from the top-left panel that initializing Carina with either an NFW profile or cored profile does not impact the results presented in Section 2.3. Differently, the bottom-right panel shows that initializing Leo II with a core profile of hot inner region and cold extended halo, changes the evolution ρ_{150}, reaching lower values at present time. We find, however, that the 'hot core + hot extended halo' profile better represents the initial stages of subhaloes hosting the MW dSphs. When the Universe is 3.5 Gyr old, is very likely that the dSph subhaloes have undergone recent mergers or had large rates of mass accretion, since at that point none of them have yet crossed the MW's virial radius.

Another important assumption of the SIDM halo model is the NFW profile for the MW halo. We find, however, that this is a good approximation for our models. At MW halo scale, $\sigma/m_\chi \sim 1-5$ cm^{2}g^{-1}, according to the σ/m_χ-velocity relation shown in Fig. 2.7. For these cross sections, Robles et al. (2019) has shown that the SIDM MW halo embedded in a baryonic potential not only exhibits a remarkably similar density profile to that of a CDM MW-like halo, but it also has no discernible core.

2.4.4 . Impact of initial conditions: halo concentration

It has previously been shown that the core collapse time-scale, $t_{\rm c}$, is (Kaplinghat et al. 2019; Essig et al. 2019; Nishikawa et al. 2020)

$$t_{\rm c} \propto C^{-1}(\sigma/m_\chi)^{-1} M_{200}^{-1/3} c_{200}^{-7/2}, \tag{2.17}$$

where C is the free parameter described in Subsection 2.4.2. Eq. (2.17) indicates that for fixed σ/m_χ, $c_{200,\rm init}$ and $M_{200,\rm init}$, the larger parameter C accelerates core collapse as shown in Fig. 2.8. It also indicates that a larger cross section and/or virial mass accelerates core collapse. Section 2.3.2 comments that in our model, the initial virial mass of the systems is constrained by the tidal evolution model

and observations. This leaves us wondering about the impact of the concentration parameter, $c_{200,\mathrm{init}}$, on the SIDM subhalo evolution.

Sameie et al. (2020) explored the tidal evolution of SIDM subhaloes in the MW's tides. They produced N-body simulations of dwarf spheroidal galaxies orbiting around the MW, modelled with a static potential that included both the disk and bulge components. They found that a constant cross section of $\sigma/m_\chi = 3$ cm^{2}g^{-1} can reproduce the observed DM density profiles of the MW dSphs Draco and Fornax. However, this was only possible if subhaloes were initialised with a large concentration parameter, such as 29.5 for Draco. They showed that if the concentration parameter was lowered to 22.9, not even the model of $\sigma/m_\chi = 10$ cm^{2}g^{-1} was able to reproduce the large DM densities of Draco, and a model with higher cross section was needed (see also Kahlhoefer et al. 2019).

We test the impact of $c_{200,\mathrm{init}}$ by running the models of Draco and Fornax initialized with a concentration of $c_{200,\mathrm{init}} = 15$ and $\sigma/m_\chi = 3$ cm^{2}g^{-1}. We find that both models reproduce the observed central DM densities, in agreement with Sameie et al. (2020). This result is presented in Appendix A.3.

We believe, however, that setting such large initial concentrations is not well justified. In the starting point of our model, subhaloes represent typical $z = 1.87$ low-mass subhaloes in the field, whose density profiles follow the median $z = 1.87$ concentration-mass relation. Correa et al. (2015c) showed that at high redshift ($z > 1$), the halo has large rates of accretion, with its mass history mainly characterized by an exponential growth. During this time, the scale radius increases simultaneously with the virial radius, hence the concentration hardly grows. At low redshift ($z < 1$), there is a drop in the accretion and merger rates of small haloes, and the halo mass increases due to the evolution of the reference density used in the spherical overdensity definition of the halo (ρ_{crit} in this case, also referred as pseudo-evolution phase). This leads subhaloes to have roughly constant scale radius but growing virial radius, which produces the rapid growth of concentrations. In our initial conditions, subhaloes have not reached the pseudo-evolution phase, therefore their concentrations should be set to low values. We conclude that due to the strong prior on the concentration parameter, we are unable to fit the models with low cross sections that do not lead to the core-collapsing regime.

2.4.5 . Uncertainty in orbital parameters

This work analyses whether the anti-correlation between the central DM density of MW dSphs, ρ_{150pc}, and their pericenter passages, r_P (Kaplinghat et al. 2019), is the result of SIDM effects. The errors in the orbital parameters reported by the Gaia collaboration (Fritz et al. 2018; Helmi et al. 2018; Brown et al. 2018), however, can weaken the anti-correlation. The parameter that produces the largest uncertainties in the pericenter distances is the tangential velocity, v_T, whose errors are around 20% for Carina, UM, Draco, Fornax, Sculptor and Sextans, but increase to $60 - 100\%$ for CVnI, LeoI and LeoII.

Like the $\rho_{150pc}-r_P$ anti-correlation, the cross section-velocity relation obtained in Section 2.3.3 can be affected by the uncertainties of v_T. In this section we investigate this further by analysing how the central DM densities of the dSphs Carina, Fornax and LeoII depend on 20% (50% for LeoII) changes in the tangential velocity.

Fig. 2.10 shows ρ_{150} (left panels), virial mass, M_{200} (middle panels) and galactocentric distance (right panels) as a function of lookback time, for Carina (top panels), Fornax (middle panels) and LeoII (bottom panels). The coloured lines correspond to the subhalo models initialised with the same cross section, initial mass, galactocentric distance and radial velocity, but different tangential velocities. The default values of v_T for Carina, Fornax and LeoII are 163, 132 and 74 km s^{-1}, respectively, these are shown in orange solid lines. Blue solid lines indicate the evolution of the models with 20% (50%) larger v_T than the default models, whereas green solid lines show the evolution of the models with 20% (50%) lower v_T than the default models.

The top panel shows that lowering v_T in 20%, decreases the galactocentric distance, increasing the rate of mass loss and accelerating the gravothermal collapse. As a result, Carina reaches a $\sim 50\%$ higher ρ_{150} at present time with respect to the default model. Similarly, increasing v_T in 20%, increases the galactocentric distance, decreases the rate of mass loss, and Carina reaches a $\sim 60\%$ lower ρ_{150}.

For the evolution of Fornax, lowering v_T in 20% yields an earlier infall onto the MW gravitational potential, further increasing the rate of mass loss and accelerating the gravothermal collapse. For this case Fornax reaches over an order of magnitude higher ρ_{150} at present time with respect to the default model. Increasing v_T, on the other hand, results in a final central DM density in close agreement with the default model.

The changes in v_T for LeoII are of the order of 50%. The bottom panels of the figure show that decreasing v_T does not yield a large disagreement between the final DM central densities. This is because both models experience similar rates of mass loss, despite the difference in their orbits. Differently, the model with 50%

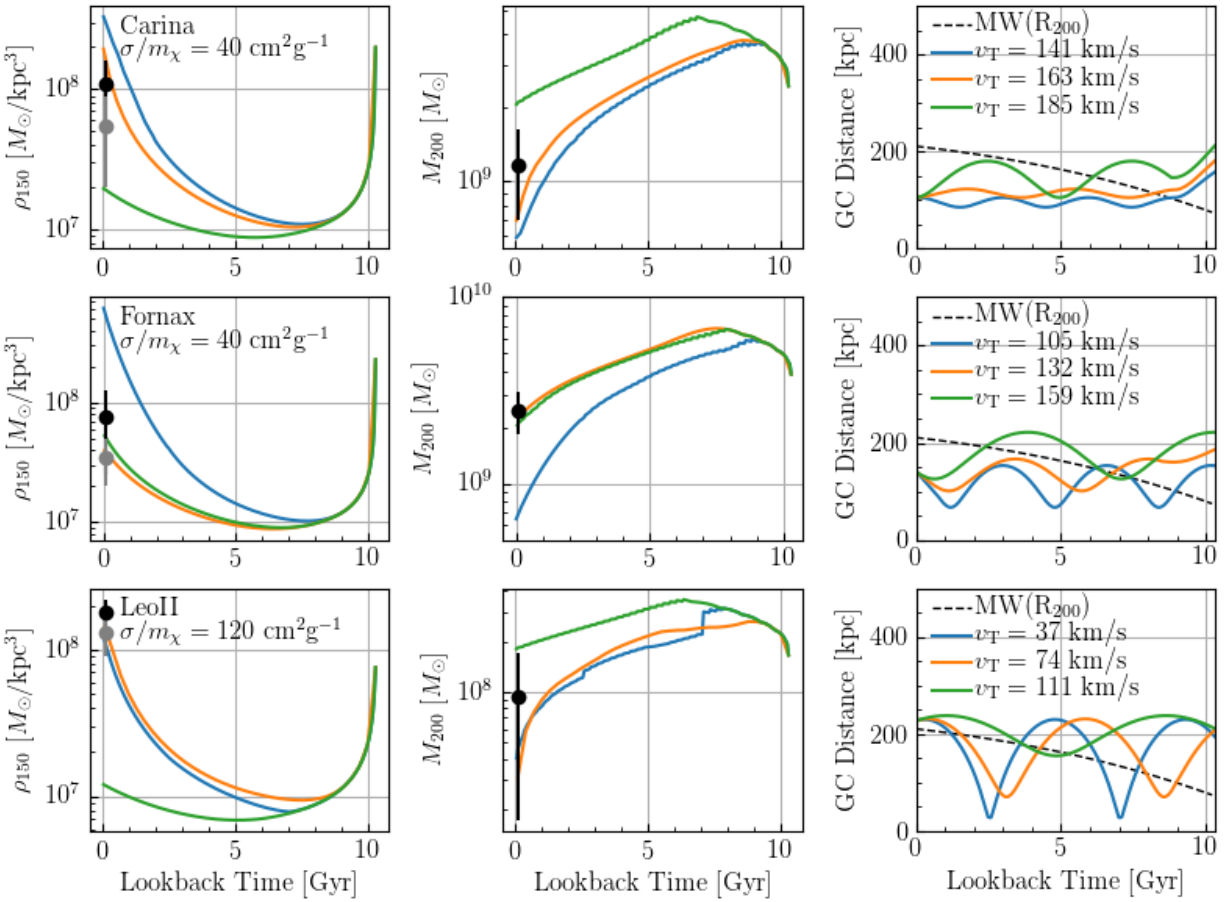

Figure 2.10: DM density at 150 pc, ρ_{150} (left panels), virial mass, M_{200} (middle panels), and galactocentric distance (right panels) as a function of lookback time for Carina (top panels), Fornax (middle panels) and LeoII (bottom panels). The coloured lines correspond to the subhalo models initialised with the same cross section (of $\sigma/m_\chi = 40$ cm^{2}g^{-1} for Carina and Fornax, and $\sigma/m_\chi = 120$ cm^{2}g^{-1} for LeoII), initial mass, galactocentric distance and radial velocity, but different tangential velocities, v_T. The symbols show the values of ρ_{150} (and M_{200}) taken from Kaplinghat et al. (2019), who assumed an isothermal cored profile (grey symbol) as well as NFW (black symbol). The dashed lines in the right panels indicate the MW virial radius. The figure shows that changes in the tangential velocity of 20% and 50% can largely impact on the final subhaloes DM density at 150 pc.

larger v_T, orbits around the MW only once and it does not lose as much mass from tidal interactions, therefore the gravothermal collapse is delayed, reaching an order of magnitude lower ρ_{150} at present time, with respect to the default model.

We conclude that the uncertainties in the galaxies tangential velocities can change the range of cross sections that reproduce the central DM densities, altering the cross section-velocity dependence. In a coming study we will analyse the evolution of truncated SIDM density profiles from gravitational tidal stripping and ram pressure, to further improve the modelling of subhaloes hosting the local dwarf galaxies and provide robust constraints of σ/m_χ on dwarf galaxy scales. Such constraints will be adjusted by the uncertainties of the orbital parameters.

2.5 . Conclusions

Self-Interacting Dark Matter (SIDM) offers a promising solution to the small-scale challenges faced by the otherwise-remarkably successful Cold Dark Matter (CDM) model. However, robust constraints of the SIDM scattering cross section per unit mass, σ/m_χ, on dwarf galaxy scales seem to be missing. The anti-correlation between the central DM densities of the bright Milky Way (MW) dwarf spheroidal galaxies (dSph) and their orbital pericenter distances (Kaplinghat et al. 2019), poses a potential signature of SIDM. In this work, we have investigated such possibility and found that there is a cross section-velocity relation that is able to explain the diverse DM profiles of MW dSph satellites, and is consistent with observational constraints on larger scales.

To model the evolution of SIDM subhaloes hosting the MW dSphs, we have applied the gravothermal fluid formalism for isolated, spherically symmetric self-gravitating SIDM haloes, and extended it to include the orbital evolution around the MW gravitational potential, along with a consistent characterization of gravitational tidal stripping. We have adopted the proper motions from the Gaia mission (Fritz et al. 2018) and used the code galpy (Bovy 2015) to integrate the orbits of the dSphs. We have also used the fitting functions from Green & van den Bosch (2019) to model the truncation of subhaloes' density from tidal mass loss. Our model has the advantage of tracking the subhalo evolution within scales smaller than 100 pc, largely expensive to resolve with N-body simulations, while easily covering a wide range of parameter space for the SIDM scattering cross section per unit mass, σ/m_χ.

We have applied the model to the classical dSph galaxies, namely, Ursa Minor, Draco, Sculptor, Sextans. Fornax, Carina, LeoII, LeoI and Canes Venatici I, and investigated the range of σ/m_χ that produces subhaloes with central DM densities that match those of the classical dwarfs. There is not single range of σ/m_χ able to reproduce the observed data, instead each subhalo is characterized by

a specific range (Fig. 2.5). Draco, for instance, prefers lower values of σ/m_χ, ranging between σ/m_χ = 23 cm^{2}g^{-1} and σ/m_χ = 25 cm^{2}g^{-1}, whereas LeoII requires σ/m_χ ranging between σ/m_χ = 120 cm^{2}g^{-1} and σ/m_χ= 90 cm^{2}g^{-1}.

Such large cross sections naturally predict that the classical dwarfs are in gravothermal core-collapse. Lower cross sections are not fitted by the model due to the strong priors in the concentration parameter. We are setting the initial subhaloes concentration based on the $z = 1.87$ concentration-mass relation of haloes in the field, differently if we initialize the models with higher concentrations, cross sections as low as 3 cm^{2}g^{-1} can reproduce the observed central DM densities (Fig. A.2). We argue however that large initial concentrations are not well justified. At high redshift ($z > 1$), the halo has large rates of accretion, with its mass history mainly characterized by an exponential growth. During this time, the scale radius increases simultaneously with the virial radius, hence the concentration hardly grows (Correa et al. 2015c). In a coming study we will be analysing the evolution of subhaloes concentration from cosmological hydrodynamical simulations with SIDM, to further assess if the priors in the concentration parameter can be relaxed. The preferred ranged of cross sections, along with the parameters describing the final profiles of the subhaloes hosting the dSphs (final mass, concentration and core size), are summarized in Table 2.2.

We have addressed the impact of the large uncertainties in the galaxies orbital parameters. While our results are robust to the uncertainties in the galactocentric distances and radial velocities, they are not to the large uncertainties of the galaxies tangential velocities (Fig. 2.10), that can potentially weaken the anti-correlation of central DM densities with pericenter passage reported by Kaplinghat et al. (2019). Changes in the galactic orbits affect the rate of mass loss, thus altering the evolution in the subhaloes density profile and the timescale of core-collapse, this in turn can increase/decrease the predicted ranges of σ/m_χ.

An interesting finding of this work is that the cross sections that reproduce the classical dwarfs densities correlate with the average collision velocity of DM particles within each subhalo's core. This result points towards an intrinsic velocity-dependent relation (Fig. 2.6), that can be fitted by a particle physics model for SIDM, where DM particles interact under the exchange of a light mediator with the self-interactions being described by a Yukawa potential. We have shown that the σ/m_χ-velocity relation is a feasible velocity-dependent model for SIDM that lies in agreement with current observational constraints on larger scales (Fig. 2.7).

In this paper we have made a first assessment of the viability of a velocity-dependent SIDM model able to explain a specific observable, the anti-correlation between the central DM densities of the bright MW dSph and their orbital pericenter distances. We have found that there is such model, that explains the diverse DM profiles of MW dSph satellites, it is consistent with observational constraints

on larger scales and predicts that the dSphs are undergoing gravothermal collapse. However more evidence will be gathered in a coming study, to further support or exclude such scenario. We will also assess the impact of baryons, as well as the evolution of truncated SIDM density profiles from gravitational tidal stripping and ram pressure, to further improve the modelling of subhaloes hosting the local dwarf galaxies and provide robust constraints of σ/m_χ on dwarf galaxy scales. Such constraints will be adjusted by the uncertainties in the orbital parameters.

3 - TangoSIDM: internal and orbital properties of satellite galaxies of Milky Way-mass halos

This chapter is a work in preparation. It discusses the internal and orbital properties of satellite galaxies of Milky Way-mass halos under Self-Interacting Dark Matter (Anau Montel & Correa, in. prep.). It also includes comments on my supervision approach and supervision philosophy.

3.1 . Introduction

Supervision approach: The first step I follow when commencing a new project with a student involves requesting a literature review on the subject matter. The goal of this is to promote critical thinking, initiate a clear communication around the project, and to teach the student on how to become a subject specialist. It is also a great opportunity for the student to delve into good research questions, and seek out advanced knowledge. My wish is always for the students to deepen the literature review on their own initiative.

In this case, the initial project was motivated by the studies of Kaplinghat et al. (2019) and Hayashi et al. (2020). However, Noemi Anau Montel demonstrated diligence in staying up-to-date with the latest developments in the relevant literature. Our discussions on the recent studies of Cardona-Barrero et al. (2023) and Andrade et al. (2023) prompted a shift in the directions of this project from its original formulation. The question we both want to answer is: how likely is that the observed anti-correlation between central dark matter density and pericenter can be drawn from simulations that assume CDM vs SIDM?

Self-Interacting Dark Matter (hereafter SIDM) is a theoretical framework wherein dark matter particles can exchange energy and momentum (Spergel & Steinhardt, 2000). These interactions, while infrequent enough to preserve the large-scale structure of the Universe in comparison to the Cold and Collisionless Dark Matter (CDM) paradigm (Springel et al., 2006; Kaplinghat et al., 2016; Tulin & Yu,

2018), possess sufficient strength to alter the internal structure of dark matter haloes (Vogelsberger et al., 2012; Robles et al., 2017; Zavala et al., 2013).

The study of SIDM on sub-galactic scales is well motivated by the possibility that it might alleviate the small-scale discrepancies of the CDM paradigm with observations. Notably, the diversity in dark matter profiles observed in Milky Way dwarf spheroidal galaxies (dSphs) and ultra-faint dwarf spheroidal galaxies (UFDs) (Oman et al., 2015; Santos-Santos et al., 2020; Sales et al., 2022; Nadler et al., 2023). Additionally, self-interactions are also motivated by quintessence-based models of dark energy, which could introduce novel long-range interactions among dark matter particles (Farrar & Peebles, 2004; Amendola & Tocchini-Valentini, 2002).

SIDM predicts that dark matter haloes undergo two evolutionary phases: core-formation and core-collapse in dark haloes. In the former phase, the formation of constant-density cores results from heat transfer between dark matter particles from the outer layers to the inner regions of haloes (Vogelsberger et al., 2012; Elbert et al., 2015; Kummer et al., 2019). The extend of this thermalization process depends on the self-interaction cross-section that characterises a specific SIDM model (Rocha et al., 2013; Nishikawa et al., 2020; Nadler et al., 2020). As dark matter particles in the core become hotter, infalling into more bound orbits, a denser and more cuspy central density forms, leading to the gravothermal core-collapse phase (Lynden-Bell & Wood, 1968). The time scales for SIDM halo core-collapse depend on the self-interaction cross-section, with higher cross-sections accelerating the process (Balberg et al., 2002; Elbert et al., 2015; Turner et al., 2021). Additionally, subhaloes' core-collapse can be accelerated by tidal forces, as the stripping process pulls out dark matter particles from the subhaloes' exterior layers, facilitating heat outflow (Nishikawa et al., 2020; Zeng et al., 2022). A rich heterogeneity of structure formation outcomes emerges from the core formation and collapse processes (Robles et al., 2017; Tulin & Yu, 2018; Nishikawa et al., 2020; Yang et al., 2023; Nadler et al., 2023). Therefore, density measurements over a large range of halo mass scales can constrain the interaction cross-section of the dark matter particles in a SIDM Universe.

Originally, SIDM models assumed velocity-independent and isotropic scattering cross-section per unit mass, σ/m_χ, (*e.g.* Vogelsberger et al. 2012; Rocha et al. 2013; Zavala et al. 2013). However, SIDM models with velocity-dependent cross-sections (Loeb & Weiner, 2011) and anisotropic scattering (*e.g.* Robertson et al. 2017) were proposed since preferred cross-sections are different depending on the scales (Kahlhoefer et al., 2013).

In recent years, Gaia measurements of the Milky Way satellites' proper motion (Brown et al., 2018) have revealed an anti-correlation between the inferred inner dark matter densities of the dSphs and their orbital pericenters (Kaplinghat et al.,

2019). While this result has been confirmed by subsequent studies (*e.g.* Hayashi et al., 2020; Andrade et al., 2023), the existence of the anti-correlation is still debatable. Recently, Cardona-Barrero et al. (2023) analized the correlation between various datasets for the inner density of the dSphs and their orbital pericenter distances, and concluded that the anti-correlation is statistically significant at the 3σ level only in a minority of the dataset combinations.

If the anti-correlation exists, it requires a mechanism that explains why surviving subhaloes in the inner regions of the Milky Way become the densest. This mechanism can be attributed to baryonic effects (*e.g.* Robles et al., 2019), or to dark matter microphysics (*e.g.* Yang et al., 2023). Correa (2021) proposed that the anti-correlation is a potential signature of velocity-dependent SIDM scenarios, wherein low-mass subhaloes efficiently core-collapse, surviving the tidal effects of the Milky Way galaxy, and raising in central density.

The hypothesis for dark matter microphysics, along with the debatable existence of the dark matter densities and pericenters anti-correlation, motivates a thorough study of how velocity-dependent self-interactions affect subhaloes' inner densities as a function of the orbital pericenter radius. Various SIDM simulations have predicted the impact of self-interactions on small-scale structures and the anti-correlation (*e.g.* Hayashi et al., 2020; Robles & Bullock, 2021; Ebisu et al., 2022; Yang et al., 2023; Andrade et al., 2023). In this work, we improve upon previous efforts by investigating the impact of a velocity-dependent cross-section on satellites of Milky Way size haloes using cosmological simulations from the TangoSIDM suite (Correa et al., 2022). We benefit from the statistical sample of Milky Way haloes in the cosmological boxes, we track the satellite orbits, reconstruct their orbital pericenters, and estimate central densities. We explore correlations between pericenter and estimated inner density of the satellites, and contrast our results with observed Gaia data, within the context of different dark matter models.

This paper is organized as follows. In Section 3.2, we provide details on our cosmological N-body simulations, a part of the TangoSIDM project, and describe our satellite sample. Section 3.3 presents our results on how the internal properties of dark matter satellites correlate with their orbits. In Section 3.4, we discuss future analysis improvements and compare our findings with previous works. Finally, we present the conclusions in Section 3.5.

3.2 . Simulations

Contributions and comments: Noemi has been involved in the TangoSIDM project since the beginning. Although she didn't directly modify the SWIFT code to integrate dark matter particle interactions, she contributed to analysing early simulation results. These included examining small cosmological boxes of 6 Mpc and 12 Mpc on a side. She tested various aspects, such as the core/cusp formation and the total number of interactions over cosmic time. Her analyses were instrumental in assisting me with debugging and refining the design process of the simulations.

The simulations analysed in this paper are part of the TangoSIDM ('TANtalasinG mOdels of Self-Interacting Dark Matter') project, a suite of cosmological simulations of structure formation in a Λ self-interacting dark matter (ΛSIDM) universe presented in Correa et al. (2022). In this section we briefly summarise the key elements of the SIDM model, with further details available in the aforementioned reference.

The main parameter that controls the rate of dark matter particles interactions in the numerical simulations is the scattering cross-section per unit mass, σ/m_χ. For anisotropic scattering, it is useful to introduce the momentum transfer cross-section,

$$\sigma_T/m_\chi \equiv 2\int(1-|\cos\theta|)\frac{\mathrm{d}\sigma}{\mathrm{d}\Omega}\mathrm{d}\Omega \tag{3.1}$$

for which interactions that lead to a small amount of momentum transfer are down-weighted, while those that transfer a larger momentum contribute more.

In this work we focus on six simulations, each employing a different dark matter model. One of these simulations assumes CDM, and therefore it does not contains dark matter particles interactions. Two assume elastic and isotropic interactions, featuring a constant scattering cross section of $1\ \mathrm{cm}^2/\mathrm{g}$ (`SigmaConstant01`), and $10\ \mathrm{cm}^2/\mathrm{g}$ (`SigmaConstant10`). The remaining three cosmological boxes model interactions as elastic and anisotropic collisions, incorporating a σ/m_χ that depends on the particles velocity. Specifically, the model reaching $\sigma_T/m_\chi = 20\ \mathrm{cm}^2/\mathrm{g}$ at $10\ \mathrm{km\,s}^{-1}$ is referred as `SigmaVel20`, while the models reaching 60 and $100\ \mathrm{cm}^2/\mathrm{g}$ at $10\ \mathrm{km\,s}^{-1}$ are referred to as `SigmaVel60`, and `SigmaVel100`, respectively.

All simulations analysed are dark matter-only simulations encompassing a volume of $25\ \mathrm{Mpc}^3$ and tracking the evolution of 752^3 dark matter particles. These simulations achieve a spatial resolution of $650\ \mathrm{pc}$ and a mass resolution of $1.44\times10^6\ \mathrm{M}_\odot$. The comoving softening length is $1.66\ \mathrm{kpc}$ at early times, and freezes at a maximum physical value of $650\ \mathrm{pc}$ at $z = 2.8$.

Halo catalogues are generated using the `VELOCIraptor` halo finder (Elahi et al., 2011, 2019a; Cañas et al., 2019), which identifies field haloes using a 3D-friends of

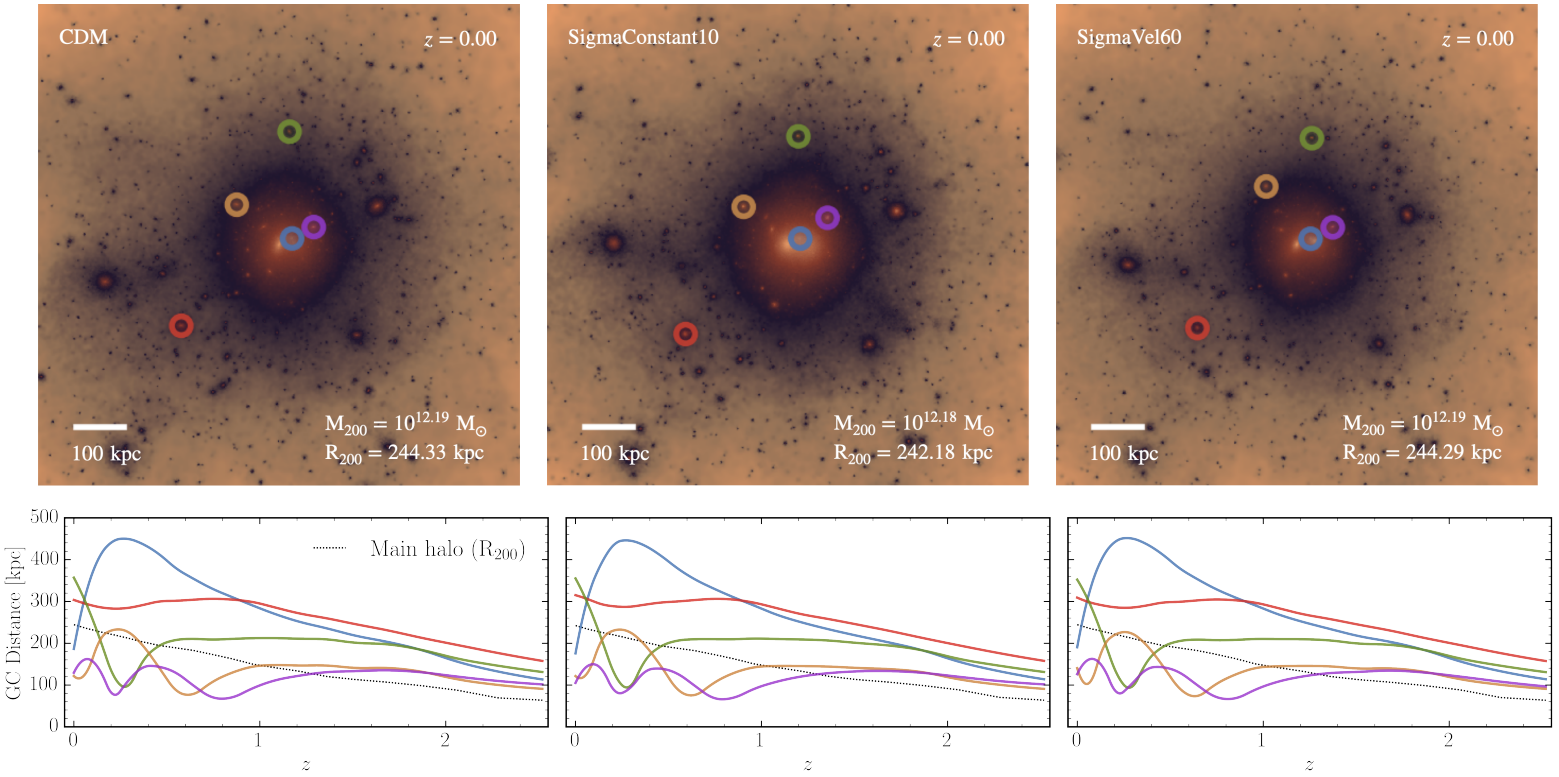

Figure 3.1: *Top panels:* Density projections at redshift $z = 0$ of the same central halo for three different dark matter models (white upper left labels) described in Section 3.2. The central halo has a mass of $10^{12.19}\ \mathrm{M}_\odot$ in the CDM case, (top-left panel). Note that this can slightly vary depending on the SIDM model (top-center and top-right panels). We circle and color code five random satellites, whose orbital evolution we show in the lower panels. *Bottom panels:* Time evolution up to redshift $z = 2.5$ of the galacto-centric (GC) distance of the five randomly selected satellites. We indicate with a black dashed line the time evolution of the virial radius R_{200} of the host dark matter halo.

friends (FOF) algorithm, and subsequently applies a 6D-FOF algorithm to separate virialised structures and identify subhaloes. The FOF algorithm associates the central halo with the one nearest to the minimum of the potential, typically the most massive one. The remaining haloes within the FOF halo are its satellites, its subhaloes.

Halo merger trees are generated using `TreeFrog` (Elahi et al., 2019b), specifically designed to work on the outputs of `VELOCIraptor`. From these merger trees, we track the evolution of satellites across simulations snapshots, saving the satellites' mass and distance between each satellite and its parent halo. This is then used to map the satellites' orbits, which are completed by applying an interpolation method. For each satellite, we calculate its pericenter, defined as the minimum distance reached from their host halo between redshifts 2 and 0.

`VELOCIraptor` provides virial masses, M_{200}, virial radii R_{200}, concentration parameters c_{200} for main haloes and subhaloes, and maximum circular velocity $\mathrm{V}_{\mathrm{max}}$. Throughout this work, parent haloes are assigned M_{200} defined as all matter within R_{200}, for which the mean internal density is 200 times the critical density, $\rho_{\mathrm{crit}}(z = 0) = 127.5\ \mathrm{M}_{\odot}\mathrm{kpc}^{-3}$. For subhaloes we adopt two distinct mass definitions. Firstly, $\mathrm{M}_{\mathrm{bound}}$, defined as the total dark matter mass that is gravitationally bound to the subhalo. Secondly, peak mass, $\mathrm{M}_{\mathrm{peak}}$, defined as the $\mathrm{M}_{\mathrm{bound}}$ mass that the satellite had before being accreated by a central more massive halo, and becoming a satellite. For each satellite, the redshift of infall, z_{infall}, is identified as the redshift at which `VELOCIraptor` halo finder flags the halo as a subhalo and not a field halo during its evolution.

3.2.1 . Sample selection

Supervision approach: When it comes to analyzing cosmological simulation datasets, I typically ask the students to set up a Git repository linked to our research project (e.g. github.com). This serves a dual purpose: it tests their proficiency in git version control and programming, usually in Python, while also providing me with a tool to monitor their progress, offer contributions, comments, and feedback. I often use methods like pull requests or opening issues for this purpose.

For instance, Noemi has a GitHub repository for our current project at github.com/NoemiAM/TangoSIDMsatellites. Likewise, Leon Kamermans, a master student from the University of Amsterdam (see further details in Chapter 5), utilized a repository (github.com/JLKamermans/SWIFTsim) to modify the SWIFT code and document his changes and contributions. Another example is Fabian Zimmer, a PhD student from the University of Amsterdam, who recently published his work on relic neutrino clustering along with

his github repository (github.com/FabianZimmer/neutrinoclustering). Currently, I'm supervising Anna Preto, an intern from Paris Observatory, who is learning git and Python (see e.g. github.com/Annapreto/TangoSIDM).

This aspect of my supervision focuses heavily on training programming skills. I believe that enabling students to create and analyze datasets cultivates analytical thinking, while tracking progress (e.g. via version control) imparts confidence and fosters independence in their research methodology. Transparency in methods and calculations, as well as the emphasis on reliability and reproducibility in research, are also key principles I strive to impart to my students.

Throughout this study, we focus on analyzing the most massive satellites orbiting parent haloes with virial masses ranging between 6×10^{11} $\mathrm{M}_\odot$ and 2×10^{12} $\mathrm{M}_\odot$ at $z=0$. Within each cosmological box, an average of 33 Milky Way's mass haloes is identified. For every host halo, we select a maximum of twenty most massive satellites, each with bound masses above 10^9 $\mathrm{M}_\odot$ to ensure they surpass the resolution floor. Our analysis achieves statistical robustness with approximately 400 satellite haloes in each box, with a minimum of 329 satellite haloes for the `SigmaConstant10` model. Additional details regarding data selection and mass distribution of the sample can be found in Appendix B.1.

3.2.2 . Satellites inner densities

Analyses of dark matter densities in dwarf galaxies (dSphs) often use the satellites' densities at the radius of 150 pc, denoted as $\rho(150\ \mathrm{pc})$ (see *e.g.* Kaplinghat et al. 2019; Hayashi et al. 2020; Ebisu et al. 2022; Yang et al. 2023). Read et al. (2019) first proposed this common radius of 150 pc after showing it is a good tracer of the central density of dwarf galaxies, since it is able to distinguish between cored and cusped density profiles (Read et al., 2019, Figure 1).

In our simulations, we can not directly measure $\rho(150\ \mathrm{pc})$ because it falls below the resolution floor, set by the softening length of 650 pc. To overcome this limitation, we estimate $\rho(150\ \mathrm{pc})$ by fitting the subhalo density profiles, and extrapolating the fit to the inner regions. We fit the data following three different profiles: the Navarro-Frenk-White (NFW) profile (Navarro et al., 1997), a dynamic core-NFW profile (Read et al., 2019), and a cored-isothermal profile (Kaplinghat et al., 2016; Robertson et al., 2021).

To estimate the central density of each system, we perform a Markov chain Monte Carlo (MCMC) scan over the scale radius and density parameters (ρ_s, r_s) for the NFW profile, (r_s, r_c, n) for core-NFW, and (ρ_0, r_0) for the isothermal profile. Further details regarding the fitting procedure are provided in Appendix B.2.

3.3 . Results

Supervision approach: In my view, compiling scientific results stands out as the most crucial aspect of a PhD student's journey. While I do expect students to present their weekly results to me in the form of plots, what I really emphasize is:

(i) Thinking and reflecting: Are the results as anticipated? Have they been adequately tested? Do they agree with previous studies?

(ii) Asking questions: Does the student grasp the significance of the results? Can they interpret them effectively?

(iii) Engaging in discussions: Whether it's during our one-on-one meetings, interactions with fellow students, or group sessions with colleagues, I encourage open debate and dialogue.

These steps are instrumental for me to evaluate a student's capacity to articulate thoughts, formulate arguments, and address unexpected questions posed by others.

A general study of the subhalo population in the TangoSIDM simulations was done in Correa et al. (2022). In this work, we present a complementary study on the satellites of Milky Way-size haloes. This section presents our findings regarding the interactions among dark matter particles on the evolution and on the internal structure of satellites of Milky Way-size haloes in TangoSIDM simulations.

3.3.1 . Satellites orbital evolution

We begin by examining the distribution of satellites around haloes and their corresponding orbital trajectories. Fig. 3.1 shows the density projections of the same central halo at $z = 0$ under `CDM`, and SIDM models, `SigmaConstant10` and `SigmaVel60` (top panels). Matching haloes between simulations is possible since the TangoSIDM simulations were all run from the same initial conditions. In the figure, the central halo has a virial mass of $10^{12.19}\ \mathrm{M}_\odot$ and a virial radius of $244.33\ \mathrm{kpc}$ in the `CDM` simulation. The top panels reveal that in `SigmaConstant10`, which is the model with more frequent dark matter particle collisions, the central halo appears slightly more spherical. The bottom panel of Fig. 3.1 shows the evolution of the galactocentric distance of five randomly selected satellite haloes (highlighted in the top panels with circles of matching color) around the selected host halo. Each panel shows the orbits under each dark matter model: `CDM` (bottom-left), `SigmaConstant10` (bottom-middle), `SigmaVel60` (bottom-right). When comparing the satellites' orbits across the simulations, we find no significant difference between them. We extend this analysis to our satellite sample and find no significant differences in the distribution of pericenter distances across different

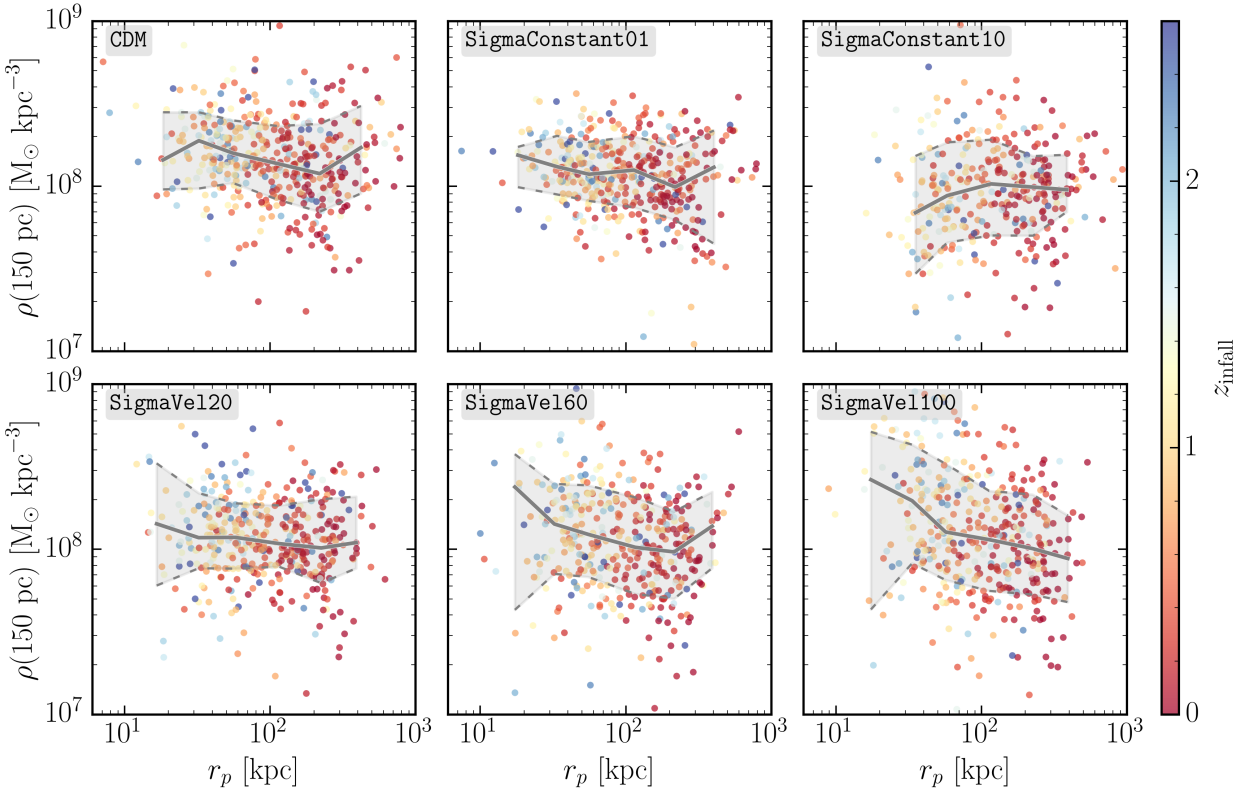

Figure 3.2: Satellites density at 150 kpc, $\rho(150\ \mathrm{kpc})$, versus their pericenter radius, r_p. Each point corresponds to a satellite halo, with an infall redshift z_{infall} highlighted by the colour bar. We obtain the value of $\rho(150\ \mathrm{kpc})$ by fitting the density profiles of the satellites and extrapolating to 150 pc, as described in Appendix B.2. The solid lines represent the median trends, whereas the shaded regions represent the 16-84th percentiles for the `CDM` (top-left), `SigmaConstant1` (top-middle), `SigmaConstant10` (top-right), `SigmaVel20` (bottom-left), `SigmaVel60` (bottom-middle) and `SigmaVel100` (bottom-right) models.

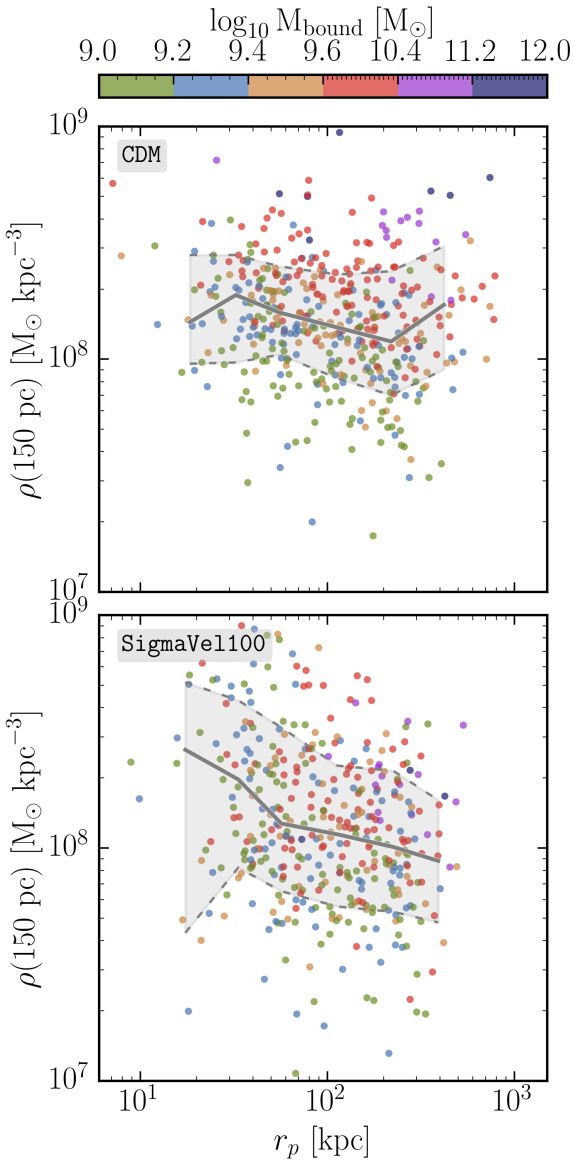

Figure 3.3: Same as Figure 3.2, but with the bounded mass M_{bound} of the satellite haloes highlighted by the colour bar for `CDM` (top panel) and `SigmaVel100` (bottom panel) models.

dark matter models (see details in Appendix B.3). There is only a slightly larger scatter in the satellites orbits from the SigmaConstant10 model, along with a larger pericenter distance median, expected due to the larger interactions between dark matter particles from the satellites and their host in this model. However, our analysis indicates that dark matter particle interactions do not substantially alter the orbital dynamics of satellites within their host haloes.

3.3.2 . Impact of self-interactions on satellite structural and orbital properties

We investigate how strongly velocity-dependent self-interactions affect the subhaloes' inner densities as a function of the orbital pericenter distance.

Figure 3.2 shows the satellites' inner densities at 150 kpc, $\rho(150\ \mathrm{kpc})$, as a function of their pericenter radius, r_p, coloured by the redshift at their time of infall, z_{infall}. Since a direct measurement of $\rho(150\ \mathrm{kpc})$ from our simulations is precluded by the resolution floor, we estimate this quantity by assuming an NFW profile and following the fitting procedure outlined in Appendix B.2. Median trends (grey solid lines) and the 16-84th percentiles (shaded regions) are shown for CDM (top-left), SigmaConstant1 (top-middle), SigmaConstant10 (top-right), SigmaVel20 (bottom-left), SigmaVel60 (bottom-middle) and SigmaVel100 (bottom-right). It can be seen from the different panels of Fig. 3.2 that satellites with larger pericenter distances were accreted more recently, so that satellites with pericenters lower than 100 kpc were mostly accreted by their host at $z_{\mathrm{infall}} > 1$. This is consistent in all models, CDM and SIDM. It can also be seen that there is no correlation between central density and pericenter in the CDM model. This lack of correlation persists even when considering a subset of the ten most massive satellites per Milky Way-mass host halo. Similarly, we do not find a correlation in the simulated data from the models: SigmaConstant01, SigmaConstant10, or SigmaVel20. The SigmaVel60 and SigmaVel100 models, on the other hand, exhibit a weak anti-correlation, with SigmaVel100 producing the largest Spearman correlation coefficient of -0.26. This is in agreement with the work of Yang et al. (2023), who performed a high-resolution cosmological zoom-in simulation of a Milky Way-like system, and reported that only self-interactions (with a cross section-dependence similar to our SigmaVel100 model) sufficiently diversify the satellites central densities in order to explain the observed $\rho(150\ \mathrm{kpc}) - r_p$ anti-correlation from the classical satellites. While we cannot explicitly determine the satellites' central density due to the limiting resolution of the simulations, our results indicate that the anti-correlation can arise in the SigmaVel100 model, when also considering a cosmological sample of Milky Way-size haloes, as was proposed in Correa (2021).

Figure 3.3 directly compares CDM and SigmaVel100 models. In this case, satellites are color-coded based on their bounded mass at redshift $z = 0$, denoted as $\mathrm{M_{bound}}$. It can be seen from the top panel that, in the CDM model, there is a correlation between $\mathrm{M_{bound}}$ and both, the pericenter distance and the inner density. Satellites with larger pericenters and higher inner densities tend to exhibit larger bounded masses. This highlights the survivor bias effect in the relation, meaning that low-mass satellites with low r_p do not survive due to tidal stripping, and are therefore missing in the $\rho(150\ \mathrm{kpc}) - r_p$ plane.

In the bottom panel of Figure 3.3, which corresponds to the SigmaVel100 model, the correlation between $\mathrm{M_{bound}}$, the pericenter distance and the inner density is less evident. While, in the CDM model, at fixed r_p, satellites with higher $\rho(150\ \mathrm{kpc})$ have higher $\mathrm{M_{bound}}$, this is not found in the SIDM model. At fixed r_p, satellites with large inner densities in the SigmaVel100 model can also have lower $\mathrm{M_{bound}}$ values. This suggests that the relationship between $\mathrm{M_{bound}}$, pericenter distance, and inner density could serve as an additional probe for imposing observational constraints on both CDM and SIDM models.

3.3.3 . Central density - pericenter distance

The previous section indicates that while satellites from the CDM simulation typically don't exhibit a correlation in the central density-pericenter plane, this isn't the case for satellites from the SigmaVel100 simulation. There appears to be a weak correlation under SIDM. This can be explained by the gravothermal core collapse of satellites, which was extensively discussed in Chapter 2. In the SigmaVel100 model, the self-interaction cross section reaches 100 $\mathrm{cm}^2\ \mathrm{g}^{-1}$ on the scale of dwarf-size galaxies. With such a large cross section, dark matter particle interactions heat the central core of dark matter, causing it to contract and increase in density, leading to core collapse. Interestingly, core collapse accelerates when dark matter haloes lose mass (Nishikawa et al., 2020). This means that as satellites have lower pericenter distances, they tend to lose more mass than their counterparts with larger pericenters. Consequently, their central densities tend to increase due to accelerated core collapse. However, a question raises: Do observations actually indicate the existence of a central density-pericenter plane for classical dwarf spheroidal galaxies?

The study by Cardona-Barrero et al. (2023) examined how different assumptions affect the density-pericenter relation of the classical dwarfs. They found that using density measurements from Kaplinghat et al. (2019), who employed the NFW profile to solve the spherical Jeans equation for classical dwarfs' line-of-sight velocity dispersion, along with pericenter distances from Battaglia et al. (2022) based on Gaia 3DR3 data, it resulted in a clear correlation in the density-pericenter plane.

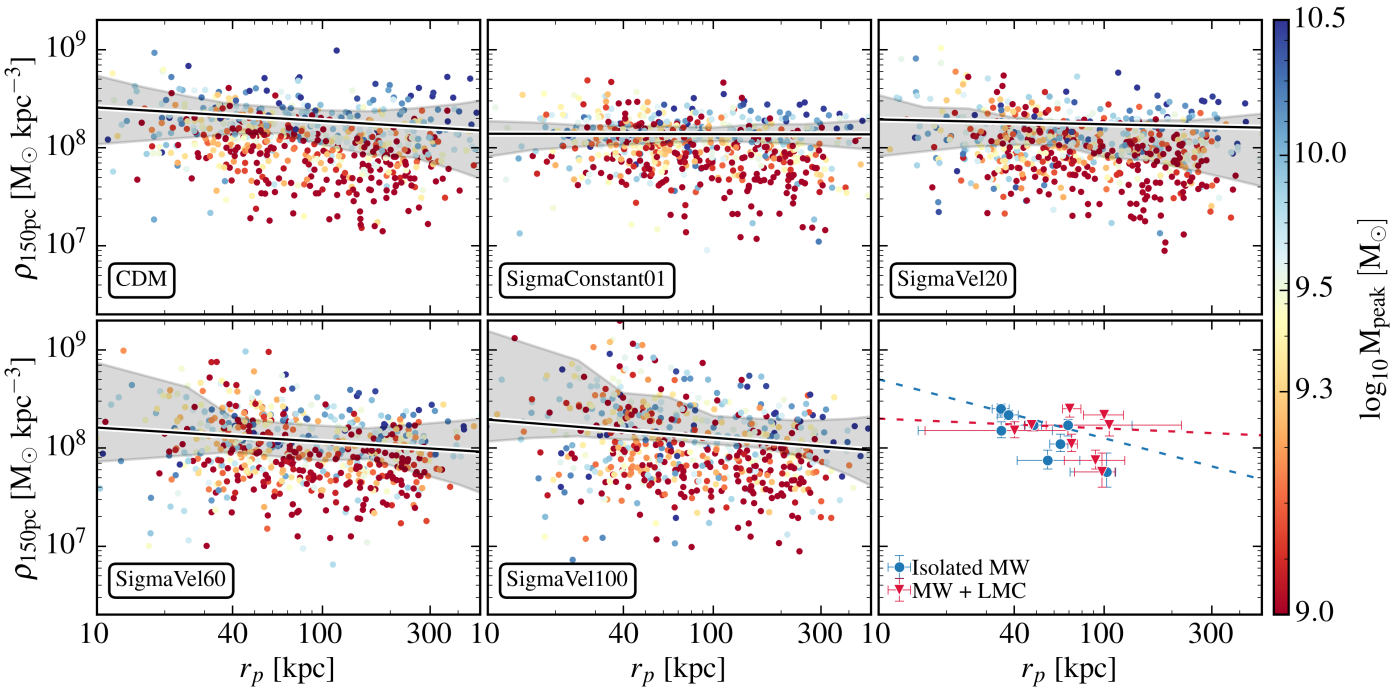

Figure 3.4: Similar to Fig. 3.2, but in this case satellites are colored by their peak halo mass, $M_{\rm peak}$. Each panel shows the best-fit relation with shaded regions highlighting the 16th-84th percentiles. The panels show the data from `CDM` (top-left), `SigmaConstant1` (top-middle), `SigmaVel20` (top-right), `SigmaVel60` (bottom-left), `SigmaVel1000` (bottom-middle) and the observational data set (bottom-right). In this last panel central densities ($\rho(150$ kpc$)$) correspond to the determination from Kaplinghat et al. (2019) (under a NFW profile), whereas pericenters were taken from Battaglia et al. (2022) under an isolated MW potential (blue circular symbols) and a MW + LMC potential (red symbols). The blue and red dashed lines correspond to the best-fit relation calculated by Cardona-Barrero et al. (2023).

Specifically, they obtained a logarithmic slope of -0.6 ± 0.4. However, when they used the pericenter distances from Battaglia et al. (2022), calculated assuming a Milky Way potential perturbed by the Large Magellanic Cloud (LMC), the correlation vanished. In this case, the logarithmic slope was -0.1 ± 0.5.

The findings of Cardona-Barrero et al. (2023) raise doubts about the existence of the density-pericenter correlation, and therefore, we cannot conclusively state that the data compilation from classical dwarfs favors SIDM. To further investigate this, we iterate around MW-like systems for each simulation, select the 8th most massive satellites from each system and fit their density-pericenter relation assuming a power-law form

$$\log_{10}\left(\frac{\rho_{150\mathrm{pc}}}{10^7\ \mathrm{M}_\odot\ \mathrm{kpc}^{-3}}\right) = q + m\log_{10}\left(\frac{r_p}{\mathrm{kpc}}\right), \tag{3.2}$$

where q and m are the logarithmic zero-point and slope. For each MW-like sytem, we store the q and m parameters, and determine the median and uncertainties of the relation (see Fig. 3.4) by propagating the q and m distributions.

Fig. 3.4 illustrates the central density ($\rho(150\ \mathrm{kpc})$)-pericenter relation from the simulations (`CDM`, `SigmaConstant1`, `SigmaVel20`, `SigmaVel60`, `SigmaVel1000`) as well as the observational data (bottom-right panel). In the panels showing the simulated data, the solid black line marks the best-fit relation, with shaded regions indicating the 16th-84th percentiles. The panel showing the observational data set presents central densities ($\rho(150\ \mathrm{kpc})$) determined by Kaplinghat et al. (2019) under a NFW profile, along with pericenters distances from Battaglia et al. (2022) under an isolated MW potential (blue circular symbols), and a MW + LMC potential (red symbols). The blue and red dashed lines depict the best-fit relations calculated by Cardona-Barrero et al. (2023).

An analysis of Fig. 3.4 reveals that by integrating the density-pericenter relation from each MW-like satellite system in the simulations, we obtain a weak anti-correlation under CDM (with a slope of $m = -0.13$), and a slightly stronger anti-correlation under the SigmaVel100 ($m = -0.18$), albeit with greater scatter. Fig. 3.5 shows the distribution of the logarithmic slope of the relation, $m = \frac{\mathrm{d}\log_{10}\rho_{150\mathrm{pc}}}{\mathrm{d}\log_{10} r_\mathrm{p}}$, represented by different colours from each simulation, along with data from observations (taken from Cardona-Barrero et al. 2023). The figure suggests that both the CDM and SigmaVel100 models tend to produce no correlations, which match the observations when considering the MW + LMC potential. However, SigmaVel100 also matches observations when the potential includes just the MW potential.

To quantitatively compare the slopes of the density-pericenter relations from simulations with observations, we calculate the probability that a given slope from the simulations is drawn from the observed slope distributions. To this end we

resort to the Bootstrap method. This helps us estimate the probability (p-value) of getting slopes as extreme as the observed ones. For each simulation, we calculate the distribution of density-pericenter slope from its MW-type systems, and we randomly sample (with replacement) 1000 times. We do the same for the observed slopes, assuming they follow a Gaussian distribution. Then, we calculate the p-value as the frequency of bootstrap samples from simulations being equal to or greater than the observed sample.

In the CDM simulation, we obtain a p-value of 0.21 when comparing with observations with pericenters calculated based only on the MW potential, and 0.48 when including the MW + LMC potentials. This suggests that the CDM simulations lean towards the dataset including both potentials. Also, we could consider rejecting the assumption that the CDM simulation and observations with just the MW potential come from the same distribution, with $\sim$80% confidence.

For the SigmaVel100 model, the p-values are 0.66 and 0.38, respectively. These high values mean we cannot reject the null hypothesis. So, with the SigmaVel100 model, both observed and simulated data aren't significantly different and could come from the same distribution. The other models (SigmaConstant1, SigmaVel20, and SigmaVel60) have p-values around 0.07, 0.21, and 0.27, respectively, when compared with MW-derived pericenter data. This suggests we can reject the null hypothesis with confidence levels of about 93% and $\sim$80%, for the SigmaConstant1 and SigmaVel20 models, respectively.

Based on this comparison, we can't determine which model (or set of models) better reproduces the observations. The CDM model suggests no correlation in the central density-pericenter relation for the largest satellites in MW-type systems. However, SigmaVel100 doesn't align with this, as it includes MW-type systems that agrees with both correlated and uncorrelated observations. We find that 30% of the MW-type systems in the SigmaVel100 yield and strong density-pericenter correlation with a slope $m < -0.5$. In CDM, this occurs in less than 10% of the systems.

3.3.4 . Central density - halo mass relation

There is an interesting aspect of the density-pericenter relation that was discussed in Section 3.3.2 and that it can also be seen in Fig. 3.4. It is the correlation between the satellites central density at $150\ \mathrm{kpc}$, $\rho(150\ \mathrm{kpc})$, and their total dark matter mass. While CDM clearly shows that at fixed pericenter, higher density satellites have larger M_{peak}, this is not the case under SIDM. Fig. 3.6 further illustrates this. It shows the satellites' central density as a function of M_{peak} for the 8th most massive satellites (from each MW-type system) under CDM (top panel) and SigmaVel100 (bottom panel). In the figure, the grey shaded area marks the

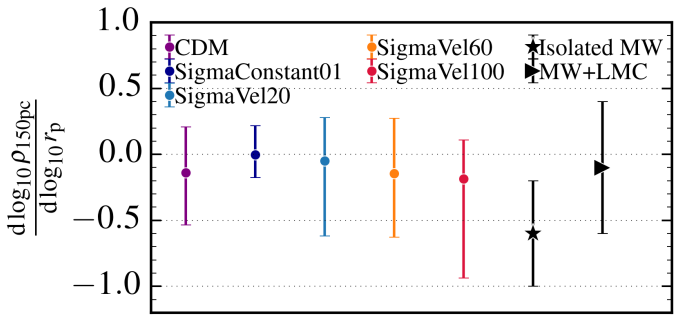

Figure 3.5: Logarithmic slope of the central density-pericenter relation from the simulations (`CDM`, `SigmaConstant1`, `SigmaVel20`, `SigmaVel60`, `SigmaVel1000`) shown in coloured symbols, and the observational data (black symbols). For the observations, the slopes (and their 1σ uncertainties) were taken from Cardona-Barrero et al. (2023), so that in the relation with pericenters taken from Battaglia et al. (2022) under an isolated MW potential are highlighted by a black star symbol, and a MW + LMC potential by a black triangle symbol.

resolution floor of the models, while the green region indicates the halo mass where the cusp-to-core transformation due to baryons becomes efficient (Di Cintio et al., 2014). Fornax, for example, fall within this green region. We also included observational data from from Read et al. (2019) for the classical dwarfs, and Hayashi et al. (2020) for the most massive ultra-faint dwarfs. Both studies used the abundance matching technique to determine the peak dark matter mass of the satellites.

In Fig. 3.6, we can see a notable difference in how density relates to halo mass between CDM and SigmaVel100. With CDM, there's a small scatter and a clear correlation: denser satellites tend to be in more massive haloes. However, with SigmaVel100, this correlation isn't as strong. The scatter in the relationship is about five times larger compared to CDM, and there doesn't seem to be a distinct pattern of correlation.

Given the uncertainty in determining pericenters from the classical dwarfs, we further investigate the relationship between the central density of satellites and their total dark matter, aiming to discriminate between them models and understand which one better reproduces the observations. To quantify whether denser satellites were in larger mass haloes before falling in, we calculate the Spearman correlation coefficient. The observational data yields a correlation coefficient, r_S, of 0.035, suggesting no correlation. By excluding Fornax due to its density possibly being affected by baryonic physics, the coefficient becomes 0.3, indicating a weak correlation. In addition, if we remove Fornax and include the three most massive ultra-faint satellites from Hayashi et al. (2020) data (with $M_{\rm peak} > 10^9$ M$_\odot$), the coefficient r_S is 0.06. This shows how the presence of a correlation heavily depends

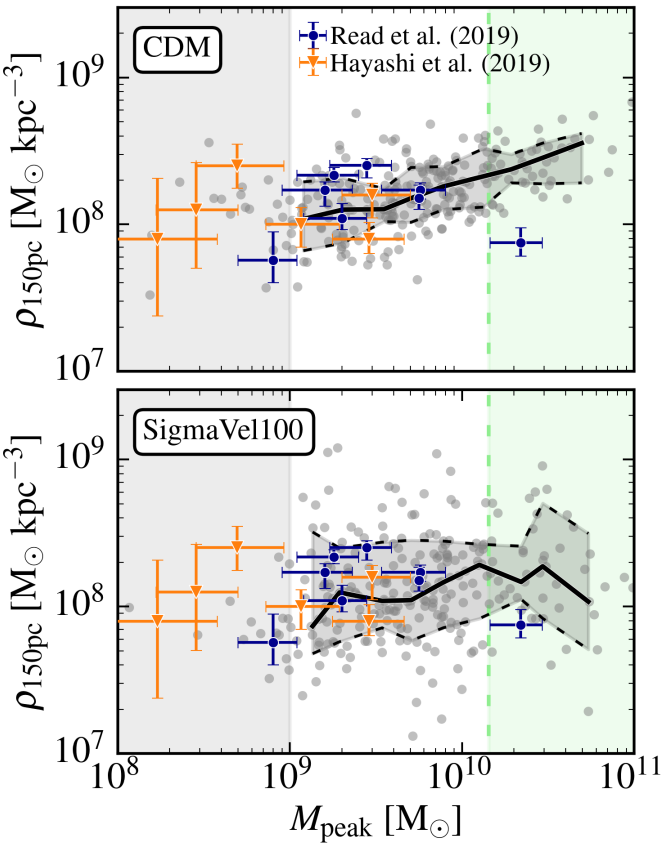

Figure 3.6: Relation between central density at 150 kpc, $\rho(150\ \mathrm{kpc})$ and peak halo mass. The grey dots correspond to the 8th most massive satellites from each MW-type system from the simulations under CDM (top panel) and SigmaVel100 (bottom panel). The grey shaded area indicates the simulations resolution floor, whereas the green region marks the halo mass above which the cusp-core transformation due to baryons becomes efficient. The observational data corresponds to Read et al. (2019) for the classical dwarfs and Hayashi et al. (2020) for the most massive ultra-faint dwarfs.

on the data analyzed. In this analyse we do not consider the p-values from the Spearman test, due to the low number of data points.

In the simulations, under CDM, all MW-systems show a correlation coefficient above 0.5, with a median estimate of r_S=$0.56^{0.03}_{-0.02}$. Under SigmaVel100, r_S=0.22 ± 0.03, with only 3% of the sample having $r_S > 0.3$. As expected, there is a strong correlation in the density-halo mass relation for CDM and not for SIDM. From this we can conclude that the classical dwarfs (without Fornax) better align with the CDM prediction, and therefore favour CDM over SigmaVel100.

However, if we exclude all subhaloes from the MW-systems with $M_{\rm peak} > 10^{10}$ $\rm M_\odot$, reasoning that their central densities might be influenced by baryonic physics, and thus their current $\rho(150\ \rm kpc)$ values from dark matter-only simulations may not be accurate, we obtain that 32% of the MW-sytems from CDM have $r_S > 0.3$ (with a median $r_S = 0.26^{0.10}_{-0.21}$), and 6% from SigmaVel100 have $r_S > 0.3$ (with a median $r_S = 0.18^{0.05}_{-0.04}$). In both models, the correlation is weak, except in 30% of the CDM sample. In this setup, we are again unable to robustly justify the preference of the observational dataset for one model over the other. This motivates us to explore another relation in future research that could more effectively discriminate between the models and help narrow down the parameter space for SIDM in dwarf galaxies. This will be further discussed in Chapter 6 of this thesis.

3.4 . Discussion

In this section we discuss the limitations of our analysis and future improvements. We also compare our findings with previous related works in the literature.

Supervision approach: Throughout the project, I encourage students to keep a log where they can write down notes and comments of papers we discuss during the meetings. This serves multiple purposes: it helps them stay organized as the project progresses, and it encourages reflection on the strengths and limitations of our work. To facilitate this process, I recommend using tools like Obsidian for note-taking, Notion for project management, and Zotero for storing preprints. This section provides an example illustrating how Noemi effectively organized her notes from our discussions and put them in clear writing.

3.4.1 . Model limitations and caveats

In this work we have investigated the impact of constant and velocity-dependent cross-sections on the internal properties of satellites of Milky Way's mass host haloes as a function of the orbital pericenter distance. However, our investigation is limited by the resolution of the cosmological boxes. With a softening length of $650\ \mathrm{pc}$ we can only estimate the inner density $\rho(150\ \mathrm{pc})$ via a MCMC fit. Significantly, the assessment of numerical effects stemming from resolution and gravitational softening on halo substructure has been extensively explored in the realm of CDM N-body simulations, as highlighted by prior research (see, for instance, Ludlow et al. 2019b). However, this remains an active line of research in SIDM N-body simulations. Notably, a recent work by Mace et al. (2024) tested their impact in the context of gravothermal core collapse studies.

Although our analysis focused on dark matter-only boxes, future work will need to delve into the impact of baryons on TangoSIDM cosmological simulations. The non trivial correspondence between SIDM models and structural properties of satellite haloes will be further influenced by the presence of baryons. The inclusion of a Galactic disk potential, for instance, is expected to preferentially reduce the densities of subhaloes with smaller pericenter distances (Kelley et al., 2019; Robles et al., 2019), due to enhanced tidal stripping processes. This could possibly alter the relationship between the inner density and the pericenter radius.

Some of the limitations inherent in this analysis can be addressed by semi-analytical methods, *e.g.* such as the one discussed in Folsom et al. (2023). Unlike numerical simulations, these approaches are not susceptible to numerical artifacts and allow for the tracking of satellites in arbitrary environments without concerns regarding low resolution (particularly in high-density regions such as at their orbital pericenter), or artificial disruption.

3.4.2 . Related works in the literature

This section provides a brief review of previous studies in the literature that explored the correlation between the structural properties of dSphs and their orbital pericenter radius. We highlight their key findings and discuss the differences between their cosmological box implementations and our models.

Using observational data from the Gaia collaboration (Brown et al., 2018), Kaplinghat et al. (2019) first identified a tight anti-correlation between the central dark matter density of the dSphs and the pericenter distance to the Milky Way. This anti-correlation persisted for different Milky Way mass models, and density measurements and models of its dSphs. Suspecting a "survivor" bias to higher densities in subhaloes that come closer to the Milky Way and withstand its tidal effects, they demonstrated this bias to be absent in the analyzed 50 most massive

subhaloes in the high-resolution ELVIS CDM simulation named Kauket (Garrison-Kimmel et al., 2014). However, the same anti-correlation was not observed for the UFDs. Possible reasons include larger scatter due to increased dispersion in the stellar-to-halo mass relation at the ultra-faint end, underestimated errors in the measurements for the UFDs, and potential connections to dark matter physics, in particular to dark matter self-interactions.

Hayashi et al. (2020) also found a similar anti-correlation for the subhaloes in the high resolution dark matter only N-body simulation named Phi-4096 (Ishiyama et al., 2021), that contains 4096^3 dark matter particles in a comoving box with a side length of $16\mathrm{h}^{-1}\mathrm{Mpc}$. They also observed that the maximum circular velocity over the formation history of subhaloes, V_{peak}, depended on their central density and pericenter. Specifically, subhaloes with larger V_{peak} formed at earlier times and with dense central densities, surviving strong tidal effects.

Expanding this work, Ebisu et al. (2022) examined the impact of dark matter self-interaction on this anti-correlation comparing three high-resolution cosmological N-body simulations: one with a CDM model, and two with a SIDM with $\sigma/m_\chi = 1\ \mathrm{cm}^2/\mathrm{g}$ and $\sigma/m_\chi = 3\ \mathrm{cm}^2/\mathrm{g}$ respectively. These simulations comprise of 1024^3 dark matter particles in a comoving cubic box with a side length of $8h^{-1}\mathrm{Mpc}$. By fitting the simulated subhaloes central densities with an NFW profile and a Burkert profile, they showed how the dependence of $\rho(150\ \mathrm{pc})$ on the pericenter disappears in the SIDM simulations. This can be explained by the absence of gravothermal core-collapse events in their SIDM simulations, leading dark matter self-interactions between subhalo's particles, more effective in the central regions, to make the density profile cuspier.

Furthermore, Robles & Bullock (2021) tested the effects of dark matter self-interactions and a baryonic disk on simulated subhaloes density and circular velocity. They performed zoom-in simulations of a Milky Way like galaxy in a CDM model and in a SIDM one with elastic cross section over mass of $1\ \mathrm{cm}^2/\mathrm{g}$. Their simulations were run with and without a time-dependent embedded potential to reproduce the effects of the baryonic disk and bulge. Comparing simulations with and without baryons, they demonstrated the impact of the disk on the central densities of the subhaloes, showing that it can reduce the circular velocities at $300\ \mathrm{pc}$ by $20-30\%$ for most subhaloes. Moreover, they showed how in both dark matter models, at fixed maximum circular velocity, subhaloes with smaller pericenters are denser. Including the embedded potential, the same trend holds, consistently with Gaia data for dSphs.

Yang et al. (2023) performed a zoom-in cosmological simulation of a Milky Way-like system using a CDM model and a SIDM one, similar to our `SigmaVel100` model. Their high-resolution particle mass is $4\times10^4\ h^{-1}\mathrm{M}_\odot$. In both their CDM and SIDM boxes they find the anti-correlation between dark matter density at

150 pc and the pericenter distance. However, the main difference between the CDM and the SIDM boxes is that in the latter subhaloes with lower $V_{\rm peak}$ tend to have higher inner densities due to core collapse, and vice versa for higher-$V_{\rm peak}$ subhaloes due to core formation. Similar results were observed by Hayashi et al. (2020, Fig. 8) and in Ebisu et al. (2022, Fig. 1).

Recently, Andrade et al. (2023) reexamined and confirmed the anti-correlation found by Kaplinghat et al. (2019). They compared the observed Gaia data for the dSphs with simulated data from the Phat ELVIS simulations Kelley et al. (2019), restricting their analysis to the 20 most massive satellites around Milky Way-type host haloes. They found an inconsistency between observed and simulated data, with the latest exhibiting a positive correlation between the density at 150 kpc and the pericenter.

3.5 . Conclusions

In this study, we have examined the influence of velocity-dependent cross-sections on satellites of Milky Way size haloes using a subset of the TangoSIDM cosmological N-body simulations that encompass both CDM and constant/velocity-dependent SIDM models. Our analysis focused on quantifying the pericenter distance, the central density at 150 pc, and the maximum halo mass of each selected satellite before infalling in their Milky Way-sized host haloes. By comparing these structural and orbital properties with observational data from the Gaia collaboration for classical Milky Way dSphs, we aimed to shed light on the impact of dark matter microphysics on galactic-scale dynamics.

Our findings highlight several key insights into the interplay between dark matter properties and satellite galaxy evolution:

- **Orbital dynamics**: In Subsection 3.3.1 and Appendix B.3, we showed that dark matter particle interactions do not significantly alter the orbital trajectories of satellites within their host haloes. While slight deviations were noted in the SIDM models, particularly in the `SigmaConstant10` scenario, the overall orbital behavior remains consistent across different dark matter models.

- **Structural properties**: In Subsections 3.3.2 and 3.3.3, we analysed the impact of self-interactions on satellite structural and orbital properties. Analysis of the satellites' central densities at 150 pc reveals no correlation under CDM and somewhat pronounced anti-correlation in the `SigmaVel100` model (see Figures 3.2 and 3.4). These findings suggest that velocity-dependent self-interactions can influence the density profiles of satellite galaxies, potentially impacting their observable properties.

- **Observational probes**: Among the analysed simulations, the `CDM` and `SigmaVel100` models exhibit trends consistent with observational data for classical Milky Way dSphs. This demonstrates the necessity for new observational probes able to put rigorous constraints and distinguish between CDM and SIDM scenarios. As discussed in Subsection 3.3.3, the fit of inner density and pericenter distance leads to inconclusive results (see Fig. 3.5). The CDM model suggests no correlation in the central density-pericenter relation, and therefore it aligns with the observational dataset where pericenters were estimated assuming the MW-potential perturbed by the LMC. However, SigmaVel100 differs from this. In the model, 30% of the MW-type systems show a strong density-pericenter correlation with a slope $m < -0.5$. SigmaVel100 aligns with both observations, that indicate the presence of a correlation (r_p from MW isolated potential) or no correlation (r_p from MW+LMC potential).

  As an alternative, we examined the inner density-peak halo mass relation as a potential probe for imposing stringent observational constraints on CDM and SIDM (see e.g. Fig. 3.6). However, we also arrived at inconclusive results. While CDM suggests a strong correlation, with denser satellites typically found in more massive haloes, this isn't the case for SIDM. Drawing a robust conclusion from the observations is challenging. The density-mass distribution of classical dwarfs (excluding Fornax) better matches the CDM prediction, favoring CDM over SigmaVel100. However, including Fornax alters this conclusion. Similarly, if we exclude all Fornax-like subhaloes from the simulations, on the basis that their central densities could be affected by baryonic physics, we find very weak correlations in both CDM and SIDM models, except in 30% of the CDM sample.

In conclusion, our study underscores the need for more extensive investigations into the role of dark matter microphysics within dwarf spheroidal galaxies, and its interplay with baryonic environmental effects. Future investigations leveraging larger spectroscopic surveys hold promise for refining and constraining our understanding of these complex systems, which serve as invaluable laboratories for probing dark matter and galaxy formation processes.

Supervision style: My approach to supervision is based upon my accumulated experience as well as examples in the guidance of my mentors. When I start working with a student, I assume a teaching and monitoring role, facilitating the student's integration into the research project. As the student progresses in both, subject matter comprehension and proficiency in numerical methods, I transition towards a consultant and collaborator mode. This phase emphasizes

fostering discussions and cultivating critical thinking.

Each week, I expect students to come with specific questions, interesting findings, or technical challenges. I view supervision sessions as invaluable opportunities for mutual learning and for the student to gain assistance on how to approach scientific problems.

Supervision philosophy: My supervision is multifaceted, I aim to:

(i) Empower students by encouraging a sense of ownership over their work, and foster shared decision-making processes.

(ii) Cultivate open and transparent communication channels, wherein students are encouraged to freely express ideas and concerns. I prioritize active listening and provide timely, constructive feedback.

(iii) Establish high yet achievable standards for performance and research quality. I challenge students to continuously refine their skills and strive for excellence, mirroring the approach that was instrumental in my own development.

(iv) Support the professional growth and advancement of my students by identifying opportunities for skill enhancement and career progression, thereby fostering a culture of lifelong learning..

(v) Address conflicts openly and constructively, with the aim of maintaining a positive and cohesive team dynamic.

(vi) Acknowledge and celebrate the contributions and achievements of my students, nurturing motivation, satisfaction, and confidence in their research endeavors.

(vii) Embrace adaptability in response to evolving circumstances and challenges that may impact my students' research capabilities.

(viii) Foster a collaborative and inclusive research team culture that values diverse perspectives and ensures that all students feel respected and empowered to contribute.

4 - TangoSIDM Project: Is the Stellar Tully-Fisher relation against SIDM?

This chapter shows that the Tully-Fisher plane, which encompasses galaxy sizes, stellar masses, and circular velocities, can serve as a powerful observable for ruling out the velocity-dependent SIDM models studied in this work. (Correa, et al., in. prep.)

4.1 . Introduction

The self-interacting dark matter paradigm (SIDM) postulates that dark matter particles engage in gravitational interactions with ordinary particles while exhibiting non-gravitational interactions among themselves. Arising as a natural prediction of dark sector models beyond the Standard Model (e.g. Spergel & Steinhardt 2000; Tulin & Yu 2018), SIDM is expected to manifest detectable astrophysical signatures (e.g. Adhikari et al. 2022). Moreover, it offers a potential explanation for the most challenging discrepancy between Λ cold dark matter (ΛCDM) numerical simulations and observations: the diverse distribution of dark matter within dwarf galaxies (see e.g. Oman et al. 2015; Santos-Santos et al. 2020; Hayashi et al. 2021; Sales et al. 2022; Borukhovetskaya et al. 2022).

Within the SIDM framework, interactions among dark matter particles dynamically alter the internal structure of dark matter halos. This modification involves the transfer of heat from the outer parts to the inner halo, resulting in an increase in the velocity dispersion, and a reduction of dark matter densities in the central regions (e.g. Davé et al. 2001; Colín et al. 2002; Vogelsberger et al. 2012; Rocha et al. 2013; Dooley et al. 2016; Vogelsberger et al. 2016). The crucial parameter governing the rate of dark matter particle interactions is the cross section per unit mass, denoted as σ/m_χ (e.g. Robertson et al. 2017; Kahlhoefer et al. 2019; Kummer et al. 2019; Vogelsberger et al. 2019; Banerjee et al. 2020; Shen et al. 2021).

Measurements derived from the shape and collision of nearby galaxy clusters constrain this parameter to be $<1\ \mathrm{cm}^2\mathrm{g}^{-1}$ (e.g. Randall et al. 2008; Dawson et al. 2013; Massey et al. 2015; Harvey et al. 2015; Wittman et al. 2018; Harvey et al. 2019; Sagunski et al. 2021; Andrade et al. 2022).

While various studies have explored the impact of SIDM under a small and constant cross section, prevailing particle physics models advocate for a velocity-dependent framework, where σ/m_χ allows dark matter to behave as a collisional fluid on small scales while remaining essentially collisionless over large scales (e.g. Pospelov et al. 2008; Arkani-Hamed et al. 2009; Buckley & Fox 2010; Feng et al. 2010; Boddy et al. 2014b; Tulin & Yu 2018). Under this velocity-dependent scheme, σ/m_χ can be $<1\ \mathrm{cm}^2\mathrm{g}^{-1}$ for high dark matter velocities at large scales, aligning with the constrains of cluster-size haloes, and exceed $>100\ \mathrm{cm}^2\mathrm{g}^{-1}$ for low dark matter velocities in order to explain the diverse dark matter distribution within dwarf galaxies (e.g. Correa 2021; Gilman et al. 2021; Correa et al. 2022; Yang et al. 2023; Silverman et al. 2023; Nadler et al. 2023; Shah & Adhikari 2023; Gilman et al. 2023). Although SIDM has been robustly constrained on galaxy cluster scales, uncertainties persist in the lower-mass galaxy regime due to the difficulty in isolating the impact of baryonic physics from dark matter interactions.

Recent studies exploring the co-evolution of baryons and SIDM in isolated systems indicate that non-bursty stellar feedback may not significantly alter SIDM density profiles in dwarf galaxies (e.g. Vogelsberger et al. 2014; Robles et al. 2017; Sameie et al. 2021). Conversely, hydrodynamical simulations incorporating SIDM and a bursty stellar feedback model reveal distinctions in velocity dispersion profiles between SIDM and CDM haloes (Burger et al. 2022), suggesting the need for more detailed investigations into the interplay between SIDM and various feedback models. In more massive systems, the intricate interplay between SIDM and baryons is even more challenging. Studies that modelled the evolution of Milky Way-like systems and galaxy clusters (e.g. Robertson et al. 2019; Despali et al. 2019; Sameie et al. 2021; Rose et al. 2022) found that baryon contraction results in the formation of denser and cuspier central density profiles under SIDM compared to CDM. Analytical studies focusing on the gravitational contribution of a baryonic disc and bulge reached similar conclusions (Robles et al. 2019; Silverman et al. 2023; Jiang et al. 2023). However, uncertainties persist regarding how the increased cuspiness of SIDM haloes depends on the specific SIDM model parameters or the strength of galaxy feedback models.

This paper seeks to address this knowledge gap by introducing a new set of cosmological hydrodynamical simulations. These simulations integrate the SIDM model derived from the TangoSIDM project, with the baryonic physics from the SWIFT-EAGLE galaxy formation model. The goals of the TangoSIDM project are to derive robust constraints on the dark matter cross section from observations of

dwarf and Milky Way-type galaxies. In this study, we take a pivotal first step by demonstrating how the stellar mass Tully-Fisher relation, a well-established galaxy scaling relation, can be leveraged to derive robust constraints on the parameter space of velocity-dependent SIDM models. The structure of this paper is organized as follows. Section 4.2 describes the SIDM and baryonic subgrid models employed in our simulations. In Section 4.3, we show how SIDM influences key galaxy properties, including stellar masses, sizes, and star formation rates. Section 4.4 compares the dark matter density profiles of haloes between CDM and various SIDM models. Section 4.5 undertakes an in-depth analysis of the stellar mass Tully-Fisher relation, and demonstrates it rules out the velocity-dependent SIDM models studied in this work. Section 4.6 discusses the SIDM parameter space, and Section 4.7 summarizes the paper's findings.

4.2 . Simulation setup

TangoSIDM[1] is a simulation project dedicated to modelling cosmological simulations that capture the intricacies of structure formation within a ΛSIDM universe. This work introduces the first realization of hydrodynamical cosmological volumes, each spanning 25 Mpc on a side, as integral compontents of the TangoSIDM project. To produce these simulations, the SWIFT[2] code (Schaller et al. 2023) was employed. SWIFT includes advanced hydrodynamics and gravity schemes. The gravity solver employs the Fast Multiple Method (Greengard & Rokhlin 1987) with an adaptive opening angle, while for hydrodynamics the SPHENIX SPH scheme (Borrow et al. 2022), specifically designed for galaxy formation sub-grid models, was utilized.

The simulations follow the evolution of 376^3 dark matter particles and 376^3 gas particles to redshift $z = 0$. The softening is set to 2.66 comoving kpc at early times, but is frozen a physical value of 700 pc at $z = 2.8$. The dark matter particle mass is 9.70×10^6 $\mathrm{M}_\odot$ and the gas initial particle mass is 1.81×10^6 $\mathrm{M}_\odot$. The starting redshift of the simulations is $z = 127$. The initial conditions were calculated using second-order Lagrangian perturbation theory with the method of Jenkins (2010, 2013). The adopted cosmological parameters are $\Omega_\mathrm{m} = 0.307$, $\Omega_\Lambda = 0.693$, $h = 0.6777$, $\sigma_8 = 0.8288$ and $n_\mathrm{s} = 0.9611$ (Planck Collaboration et al. 2014a).

[1] www.tangosidm.com
[2] www.swiftsim.com

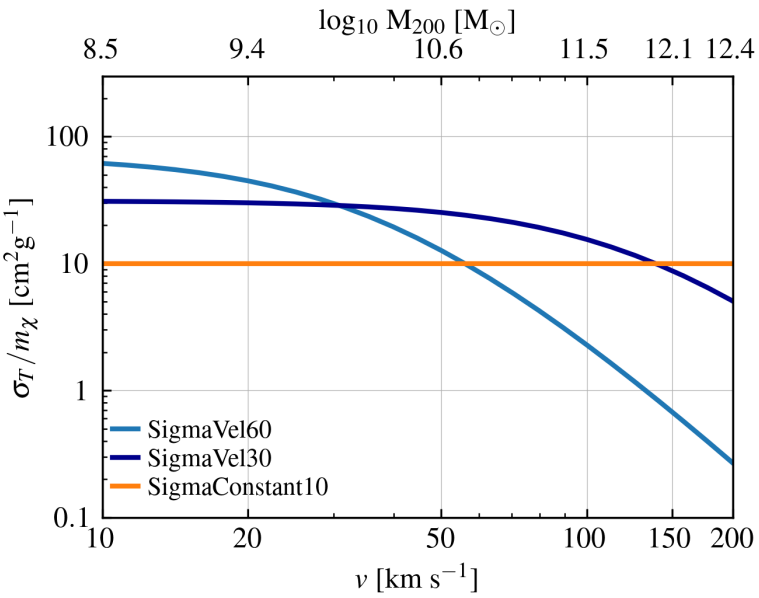

Figure 4.1: Momentum transfer cross section as a function of the relative scattering velocity among dark matter particles for the SIDM models featured in this work (Table 4.1). The figure shows two velocity-dependent models, namely SigmaVel60 (light blue line) and SigmaVel30 (dark blue line), alongside SigmaConstant10 (orange line), which uses a constant cross section, $\sigma_T/m_\chi = 10$ cm^{2}g^{-1}. The top x-axis indicates the typical halo mass that hosts orbits of the velocities indicated on the bottom x-axis.

4.2.1 . TangoSIDM model

The TangoSIDM project, encompassing its models and SIDM implementation, was presented in Correa et al. (2022). In this section we briefly summarise the key elements of the SIDM model, with further details available in the aforementioned reference.

Four dark matter models were generated for this study: the cold collisionless dark matter model (hereafter CDM); a SIDM model with a constant scattering cross section of 10 cm^{2}g^{-1} (hereafter SigmaConstant10); and two SIDM models featuring velocity-dependent cross sections (see Fig. 4.1). Although the SigmaConstant10 model has been ruled out by observations of galaxy clusters (e.g. Harvey et al. 2015, 2019), it serves as a control model for comparative analysis. Among the velocity-dependent models, one has a cross section that is below 1 cm^{2}g^{-1} at high velocities (v>150 km s^{-1}) and increases with decreasing velocity, reaching 60 cm^{2}g^{-1} at 10 km s^{-1} (hereafter SigmaVel60 model). The other velocity-dependent

model has a cross section smaller than 8 $\mathrm{cm}^2\mathrm{g}^{-1}$ at velocities surpassing 200 km s^{-1} (dropping below 1 $\mathrm{cm}^2\mathrm{g}^{-1}$ at ≈ 1000 km s^{-1}) and increases with decreasing velocity, reaching 30 $\mathrm{cm}^2\mathrm{g}^{-1}$ at 10 km s^{-1} (hereafter SigmaVel30 model).

The SigmaVel60 and SigmaVel30 models represent two extreme scenarios for the rate of dark matter interactions in Milky Way-mass systems. Despite both models adhering to the SIDM constraints derived from cluster-size haloes, there are important differences. In SigmaVel60, interactions reach 1-2 $\mathrm{cm}^2\mathrm{g}^{-1}$ around 100 km s^{-1}, therefore this model produces a low rate of interactions in the center of Milky Way-like haloes. In contrast, SigmaVel30 exhibits a cross section of 10-20 $\mathrm{cm}^2\mathrm{g}^{-1}$ at 100 km s^{-1}, imposing a stronger rate of interaction.

The velocity-dependent cross sections are modelled under the assumption that dark matter particle interactions are mediated by a Yukawa potential dependent on three parameters: the dark matter mass m_χ; the mediator mass m_ϕ; and the coupling strength α_χ. While there is no analytical form for the differential scattering cross-section due to a Yukawa potential, the Born-approximation (Ibe & Yu 2010)—applicable when treating the scattering potential as a small perturbation—yields the differential cross-section of the dark matter-dark matter interactions

$$\frac{\mathrm{d}\sigma}{\mathrm{d}\Omega} = \frac{\alpha_\chi^2}{m_\chi^2 (m_\phi^2/m_\chi^2 + v^2 \sin^2(\theta/2))^2}. \tag{4.1}$$

While in the model with a constant cross section the dark matter scattering is isotropic, in the velocity-dependent cross section models the scattering is anisotropic. For anisotropic scattering the momentum transfer cross section, defined as

$$\sigma_T / m_\chi = 2 \int (1 - |\cos\theta|) \frac{\mathrm{d}\sigma}{\mathrm{d}\Omega} \mathrm{d}\Omega, \tag{4.2}$$

is useful to consider, because it is weighted by the scattering angle and therefore it does not overestimate the scattering with $\theta > \pi/2$ (Kahlhoefer et al. 2015). Table 4.1 shows the SIDM model parameters adopted in this work and Fig. 4.1 shows the momentum transfer cross sections. The figure shows the velocity-dependent models (light blue and dark blue lines) and the constant cross section model (orange line). While the bottom x-axis shows the relative velocity between dark matter particles, the top x-axis indicates the typical halo mass that hosts circular orbits of such velocities.

Table 4.1: SIDM models analysed in this work. Form left to right: Model name, SIDM parameters for each model (dark matter mass, m_χ, mediator mass, m_ϕ, and coupling strength, α) and type of dark matter interaction.

	SIDM parameters			DM interaction
Model Name	m_χ [GeV]	m_ϕ [MeV]	α	
CDM	-	-	-	No interaction
SigmaConstant10	-	-	-	Isotropic
SigmaVel30	2.227	0.778	4.317×10^{-5}	Anisotropic
SigmaVel60	3.855	0.356	1.027×10^{-5}	Anisotropic

4.2.2 . SWIFT-EAGLE model

The SWIFT-EAGLE model, an open-source galaxy formation model implemented in SWIFT, is derived from the original EAGLE model (Schaye et al. 2015; Crain et al. 2015). While it has common modules to those of EAGLE, SWIFT-EAGLE includes new developments and improvements. A detailed model description can be found in Bahé et al. (2022) and Borrow et al. (2022, 2023). Below we provide a summary.

SWIFT-EAGLE incorporates the element-by-element sub-grid radiative gas cooling and photoheating prescription from Ploeckinger & Schaye (2020), which accounts for the inter-stellar radiation field and self-shielding of dense gas, as well as the UV/X-ray background from galaxies and quasars according to Faucher-Giguère (2020). Star formation is implemented stochastically, following the Schaye & Dalla Vecchia (2008) pressure law, as in the original EAGLE model. A polytropic equation of state, $P \propto \rho^{4/3}$, sets a minimum limit on the gas pressure. The star formation rate per unit mass is calculated from the gas pressure, employing an analytical formula designed to reproduce the observed Kennicutt–Schmidt law (Kennicutt 1998) in disc galaxies. A gas particle is star-forming if its temperature $T < 1000$ K, or if its density (expressed in units of hydrogen particles per cubic cm, $n_{\rm H}$) is $n_{\rm H} > 10\ {\rm cm}^{-3}$ and temperature $T < 10^{4.5}$ K.

The stellar initial mass function assumes the form of Chabrier (2003) within the range 0.1-100 $M_\odot$, with each particle representing a simple age stellar population. Stellar feedback is implemented stochastically, following the prescription of Dalla Vecchia & Schaye (2012), where stars with masses between 8 $M_\odot$ and 100 $M_\odot$ explode as core-collapse supernovae. The resulting energy is transferred as heat to the surrounding gas, following Chaikin et al. (2022).

The energy injected into the gas corresponds to 10^{51} erg per supernova times a dimensionless coupling efficiency factor, $f_{\rm E}$, that follows the same scaling function as in EAGLE,

$$f_{\rm E} = f_{\rm E,max} - \frac{f_{\rm E,max} - f_{\rm E,min}}{1 + \exp\left(\frac{-\log_{10} {\rm Z}/{\rm Z}_0}{\sigma_{\rm Z}}\right) \exp\left(\frac{\log_{10} {\rm n_H}/{\rm n_{H,0}}}{\sigma_{\rm n}}\right)}. \tag{4.3}$$

As can be seen, $f_{\rm E}$ depends on a number of free parameters: $f_{\rm E,min}$ and $f_{\rm E,max}$, which set the minimal and maximal feedback energies, $n_{\rm H,0}$ and Z_0 defined as the density and metallicity pivot point around which the feedback energy fraction plane rotates, and σ_Z and σ_n, the width of the feedback energy fraction sigmoids in the metallicity and density dimensions.

In addition to the energy released through star formation, star particles also release metals into the inter-stellar medium (ISM) through four evolutionary channels: AGB stars, winds from massive stars, core-collapse supernvae and Type Ia supernovae. This process follows the methodology discussed in Wiersma et al. (2009) and Schaye et al. (2015). The abundances of 9 elements (H, He, C, N, O, Ne, Mg, Si, Fe) are tracked.

The formation and growth of supermassive black holes are modelled following Bahé et al. (2022). Initially seeded within friends-of-friends dark matter groups, black holes accretion rates follow the Eddington-limited Bondi accretion rate. The feedback mechanism from active galactic nucleus (AGN) activity is implemented following Booth & Schaye (2009). The energy depends on the accreted mass, Δm, onto the black hole as, $\Delta E = \epsilon_{\rm r}\epsilon_{\rm f}\Delta m c^2$, where $\epsilon_{\rm r} = 0.1$ is the default value. This energy is stored in a reservoir carried by each black hole particle until it can be utilized to heat the nearest gas particle, inducing a temperature increase of $\Delta T_{\rm AGN}$. The coupling efficiency, $\epsilon_{\rm f}$, and the heating temperature of AGN feedback are free parameters.

4.2.3 . Reference & WeakStellarFB SWIFT-EAGLE models

This work investigates the evolution of galaxies for two distinct SWIFT-EAGLE models. In the first, referred to as the Reference model, the free parameters described in the previous subsection were calibrated in a (25 Mpc)^3 volume to reproduce the galaxy stellar mass function and galaxy mass-size relation. The second, named the WeakStellarFB model, adopts parameters that produce Milky Way-mass galaxies with very weak stellar feedback. Table 4.2 provides a comprehensive listing of the subgrid parameter values for both models.

The parameters for the Reference model were derived within the CDM framework using emulators that employed the Gaussian Process Regression-based python module SWIFTEmulator (Kugel & Borrow 2022). Further details on the calibration and emulation technique can be found in Borrow et al. (2023). Note that the SIDM simulations with the SWIFT-EAGLE Reference model adopt the parameters listed in Table 4.2, no re-calibration was performed to account for the SIDM

Table 4.2: Subgrid parameter values of the SWIFT-EAGLE galaxy formation model that regulate stellar and AGN feedback. The left column identifies each parameter, with detailed descriptions provided in the text. The middle and right columns list the parameter values adopted in the Reference and WeakStellarFB models, respectively.

Parameters	Reference	WeakStellarFB
$f_{\rm E,min}$	0.388	0.5
$f_{\rm E,max}$	7.37	5.0
$n_{\rm H,0}$ [cm^{-3}]	0.412	1.46
$\sigma_{\rm Z}$	0.311	0.275
Z_0	0.00134	0.00134
$\sigma_{\rm n}$	0.428	1.77
$\epsilon_{\rm f}$	0.035	0.1
$\Delta T_{\rm AGN}$ [K]	$10^{8.62}$	$10^{8.5}$

effects.

The original parameters from the EAGLE simulations were calibrated to reproduce the $z = 0.1$ galaxy stellar mass function, the relation between galaxies stellar mass and galaxies' central black hole masses, as well as disc galaxy sizes (Crain et al. 2015). While the SWIFT-EAGLE model was inspired by EAGLE, significant differences exist, such as the gravity and hydrodynamics solver, cooling rates, supernovae and AGN feedback energy deposition into the ISM. Because of these differences, applying the original EAGLE parameter values in the SWIFT-EAGLE model yields different results. Relative to the Reference model, the WeakStellarFB model exhibits a weaker stellar feedback at the specific mass scale of 10^{12} M$_\odot$ haloes, attributed to the lower value of $f_{\rm E,max}$ and higher $n_{\rm H,0}$. This combination results in a lower coupling efficiency factor $f_{\rm E}$ at fixed hydrogen number density, justifying its nomenclature "WeakStellarFB".

In Section 4.3 and Appendix C.1, we show that both the Reference and WeakStellarFB models yield stellar mass functions, specific star formation rates, and stellar-to-halo mass relations that closely align with observational data. However, the stellar feedback in the WeakStellarFB model is less efficient in Milky Way-mass systems, making them more compact by redshift zero. The primary objective of exploring SIDM under these two galaxy models is to understand the impact of dark matter collisions in the central regions of galaxies. We aim to discern how SIDM coevolves with the dynamical heating from supernova explosions and evaluate whether our conclusions regarding the impact of SIDM on galaxies remain robust in the face of variations in feedback models.

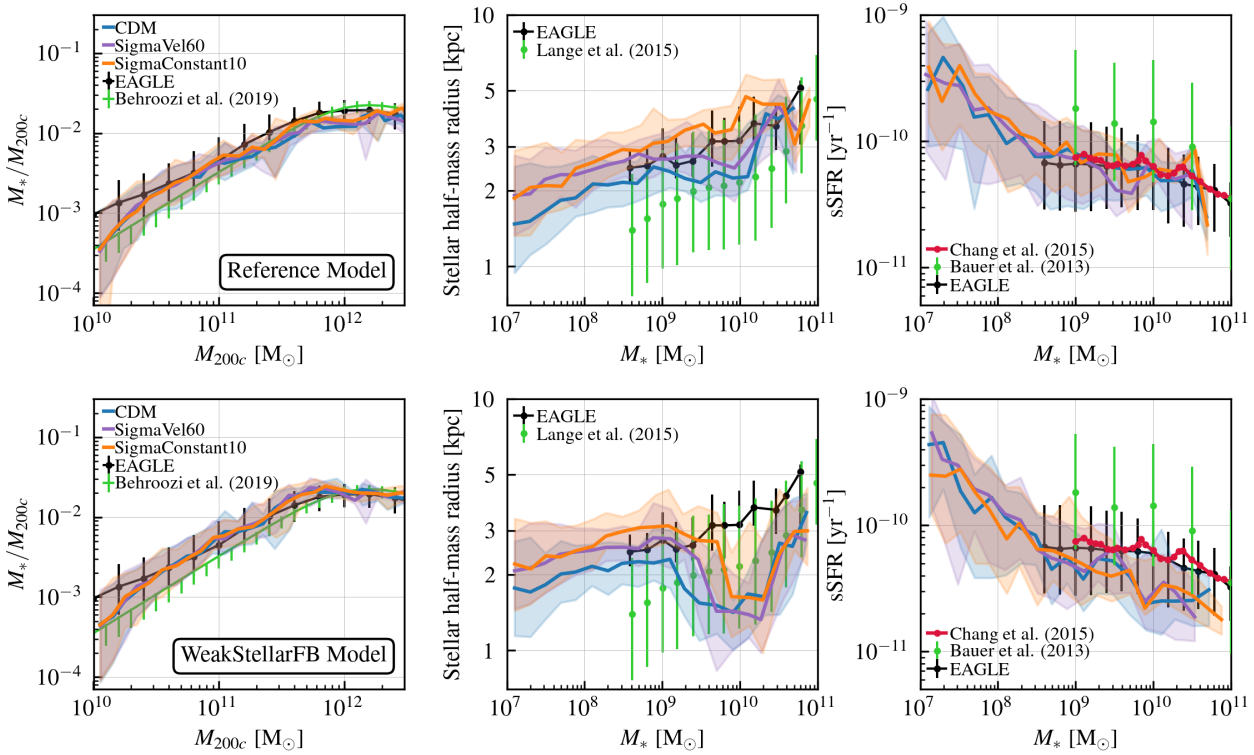

Figure 4.2: Galaxy scaling relations at redshift $z = 0$ for the Reference (top panels) and WeakStellarFB model (bottom panels). The columns show the stellar-to-halo mass ratio (M_*/M_{200c}) as a function of halo mass (left), the projected stellar half-mass radius as a function of stellar mass (middle) for all galaxies, and the specific star formation rate (sSFR, SFR/M_*) as a function of stellar mass for actively star forming-galaxies (right). In all panels the curves correspond to the median for the Reference and WeakStellarFB models produced in CDM (blue lines), SigmaVel60 (purple lines) and SigmaConstant10 (orange lines) frameworks. SigmaVel30, though not shown, follows a similar trend as SigmaVel60. The shaded regions mark the 16th-84th percentiles of the relations. These models are contrasted with various observational datasets and the EAGLE simulations (black lines). The left panels show the stellar-to-halo mass relation from Behroozi et al. (2019). In the middle panels, galaxy sizes are compared with citetLange15 (green circles) dataset. The right panels compare the sSFR with those reported by Bauer et al. (2013) and Chang et al. (2015). SIDM appears to have minimal impact on galaxy masses and star formation rates. However, it significantly alters galaxy sizes, leading to increases by up to a factor of 2 for SigmaConstant10.

4.2.4 . Halo catalogue and definitions

Halo catalogues were generated using the VELOCIraptor halo finder (Elahi et al. 2011, 2019a; Cañas et al. 2019). VELOCIraptor uses a 3D-friends of friends (FOF) algorithm to identify field haloes, and subsequently applies a 6D-FOF algorithm to separate virialised structures and identify sub-haloes of the parent haloes (Elahi et al. 2019a). Throughout this work, virial halo masses ($M_{200\mathrm{c}}$) are defined as all matter within the virial radius $R_{200\mathrm{c}}$, for which the mean internal density is 200 times the critical density, ρ_{crit}, which is $127.5\mathrm{M}_{\odot}\mathrm{kpc}^{-3}$ at $z = 0$. In each FOF halo, the 'central' subhalo is the one with the most gravitationally bound particle, which is nearly always the most massive. The remaining subhaloes within the FOF halo are its satellites. The resolution of the simulations is sufficient to resolve (sub-)haloes down to $\sim 10^{10}$ $\mathrm{M}_{\odot}$ with 10^3 particles within R_{200}. Galaxy stellar masses, sizes and star formation rates are always defined within an aperture of 50 kpc.

4.3 . Galaxy properties

In this section we analyse key galaxy properties from the Reference and WeakStellarFB models: the $z = 0$ stellar-to-halo mass relation, projected galaxy sizes, and star formation rates, and we compare them against observational data. It is important to point out that during the calibration of the subgrid parameters for feedback under CDM, the $z = 0$ galaxy stellar mass function and the stellar mass-size relation were considered, and as a result, the simulations do not provide predictions for these. We remind the reader that the subgrid parameters from the Reference model were only calibrated under the CDM framework and not under SIDM. The SIDM simulations use the same subgrid parameter values as CDM for both the Reference and WeakStellarFB models. The z=0 galaxy stellar mass function is presented in Appendix C.1.

Fig. 4.2 illustrates three galaxy scaling relations from the Reference (the top panels) and WeakStellarFB models (bottom panels). In the left panels, the ratio between the galaxy stellar mass and halo mass ($M_*/M_{200\mathrm{c}}$) is plotted as a function of the host halo mass. Coloured curves represent the median relations for central galaxies, with shaded regions indicating the 16-84th percentiles. A comparison is made with the stellar-to-halo mass relation from the EAGLE simulation and from UNIVERSEMACHINE (Behroozi et al. 2019). Notably, the WeakStellarFB model aligns best with the EAGLE data (McAlpine et al. 2016). At fixed halo mass, galaxies from the WeakStellarFB model are more massive than those from the Reference model (consistent with a comparison of the stellar mass functions). The dark matter framework does not significantly alter the stellar-to-halo mass

relation. For clarity, the SigmaVel30 model is not shown, as it follows a trend similar to SigmaVel60.

Moving to the middle panels of Fig. 4.2, the stellar half-mass radius is shown as a function of stellar mass. The half-mass radius is defined as the radius that encloses 50 per cent of the stellar mass, and is computed from all bound star particles within a projected 2D circular aperture of 50 kpc radius. The simulations are compared against the GAMA survey (Lange et al. 2015), and the EAGLE simulation (McAlpine et al. 2016). An interesting feature emerges in the bottom middle panel, revealing a U-shape trend in the galaxy size-mass relation. Galaxies within the mass range of 10^9 to 10^{11} $\mathrm{M}_\odot$ become too compact due to excessive radiative losses at high gas densities. To counteract this issue, the EAGLE model introduced a dependence of the stellar feedback energy on the gas density (eq. 4.3), so that higher density gas receives a larger amount of energy from stellar explosions (Crain et al. 2015). The WeakStellarFB model incorporates the density-dependent stellar feedback energy, but its parameter values are such that the feedback strength remains inadequate. The coupling efficiency factor applied to the supernova energy that is injected into that gas is smaller than in the Reference model. Therefore, while stellar and AGN feedback in the WeakStellarFB model can prevent the formation of excessively massive galaxies, it does not guarantee the formation of extended galaxies with realistic sizes. A more careful approach, or tuning of the energy parameters, is required for feedback to effectively eject low-angular momentum gas, increase the median angular momentum of the ISM gas that remains to form stars, and form more extended galaxies (e.g. Brook et al. 2012).

For stellar masses $\approx 10^9$ $\mathrm{M}_\odot$ the WeakStellarFB model predicts galaxies with sizes that agree with EAGLE, and do not seem to suffer from overcooling and compactness. However, these sizes appear large when compared to the dataset of Lange et al. (2015). The Reference model, calibrated to match the size-mass relation from Lange et al. (2015), yields galaxies that are still overly extended, partly due to the sampling noise in gravitational interactions between stars and dark matter, that leads to spurious size growth (Ludlow et al. 2019a, 2023).

The middle panels also show the evident impact of SIDM on galaxy sizes. Dark matter particle interactions heat the inner halo, leading to core formation in the central regions and dynamically heating the surrounding gas and stars, promoting the formation of more extended galaxies. However, this is insufficient to counteract the overcooling and compactness observed in the WeakStellarFB model for galaxies more massive than 10^{10} $\mathrm{M}_\odot$. The top middle panel shows that the SigmaVel60 model, characterized by a large cross section for galaxies less massive than $10^9 M_\odot$, produces sizes that are close to those for the SigmaConstant10 model. For these masses, as the cross section decreases, the galaxy sizes from SigmaVel60 decrease

relative to those for SigmaConstant10, and become similar to those of CDM.

Ludlow et al. (2023) found than in CDM hydrodynamical simulations like EAGLE, which share the same numerical resolution as the TangoSIDM simulations, the galaxies' half-mass radius remains robust against spurious collisional heating only for halo masses $M_{200c} \gtrsim 10^{11.7}$ $M_\odot$. This suggests that our galaxies' sizes are free from spurious heating if the galaxies are more massive than $M_* \gtrsim 5 \times 10^{11}$ $M_\odot$. We note, however, that resolution effects may have a stronger impact on CDM simulations than on SIDM simulations, in which case the effect of SIDM on sizes relative to CDM may be underestimated.

The right panels of Fig. 4.2 display the median specific star formation rates (sSFR) for actively star forming-galaxies, with galaxies classified as star-forming if their sSFR $>10^{-11}$ yr^{-1}. The panels reveal that the $z = 0$ sSFR from the Reference model are in agreement with the sSFR from the EAGLE simulations and the dataset from Chang et al. (2015), and are within a factor of 5 from the Bauer et al. (2013) data. The WeakStellarFB model has sSFR lower than Reference. Interestingly, there are no differences in the median sSFR trends between simulations with CDM vs. SIDM.

4.4 . Dark Matter Density profile

Figure 4.3: Figure in page 88. Dark matter density profiles, $\rho_{\rm DM}$, of 10^{11} $M_\odot$, $10^{11.5}$ $M_\odot$ and 10^{12} $M_\odot$ haloes from the Reference (purple solid lines) and WeakStellarFB (blue dot-dashed lines) models under CDM (left panels), SigmaConstant10 (second panels from the left), SigmaVel30 (third panels from the left) and SigmaVel60 (right panels). The panels compare $\rho_{\rm DM}$ between hydrodynamical (CDM and SIDM) simulations and dark matter-only simulations (orange dashed lines). The coloured lines highlight the median values and the shaded regions the 16-84th percentiles. Additionally, the black solid line corresponds to the NFW profile (estimated using the concentration-mass relation from Correa et al. 2015c), and the black dotted and dashed-dotted lines indicate the convergence radii (see text for definition). The differences in the profiles between haloes of the same mass highlights the impact of baryonic effects and dark matter particle interactions on the central haloes densities.

In the following analysis, we compare our findings with prior studies on SIDM. Specifically, we examine the dark matter density profiles of central haloes with masses in the range of $10^{10.9} - 10^{11.1}$ $M_\odot$, $10^{11.4} - 10^{11.6}$ $M_\odot$ and $10^{11.9} - 10^{12.1}$ $M_\odot$ from both the Reference and WeakStellarFB models under CDM, SigmaConstant10, SigmaVel30 and SigmaVel60.

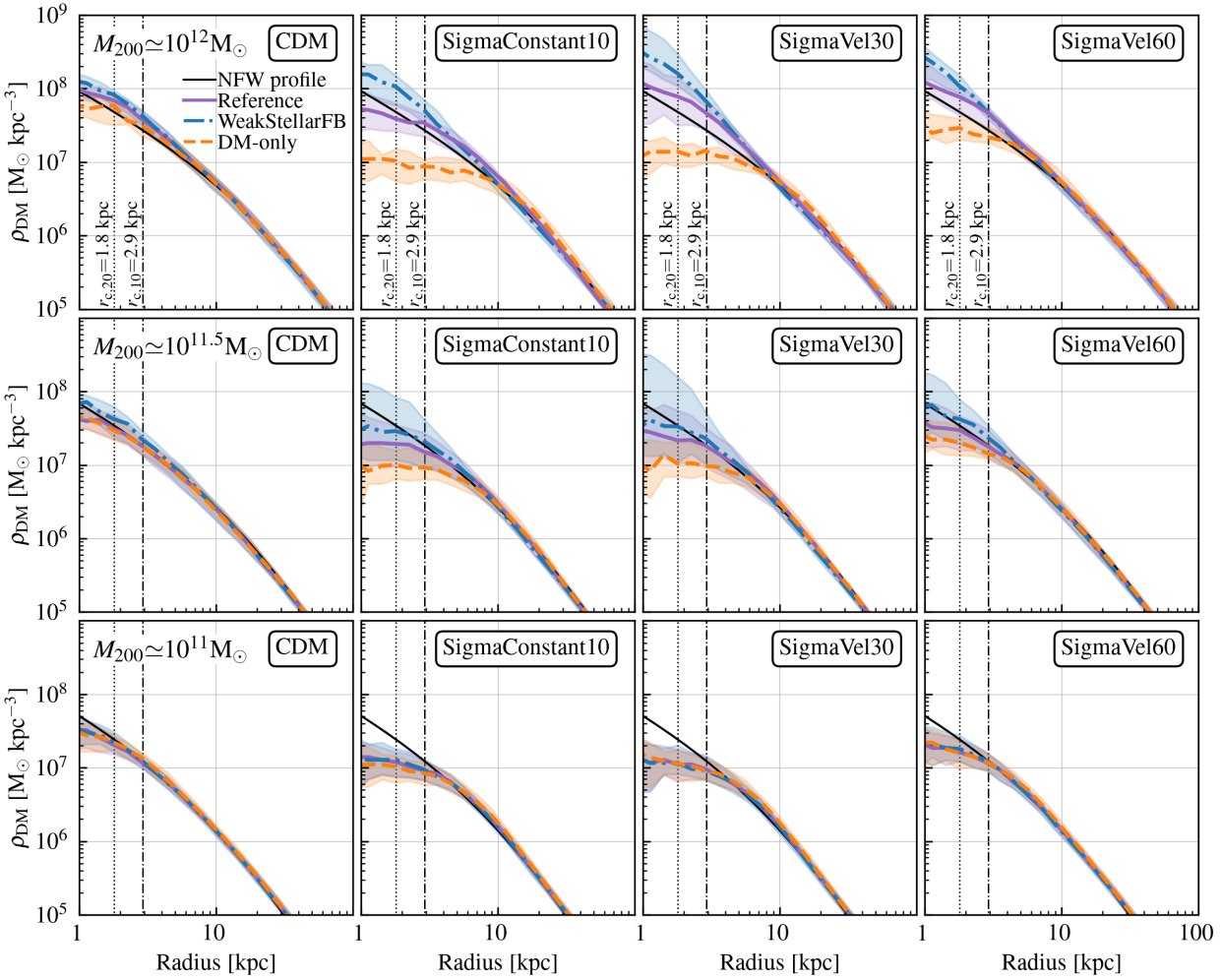

Figure 4.3: See caption at the beginning of Section 4.4.

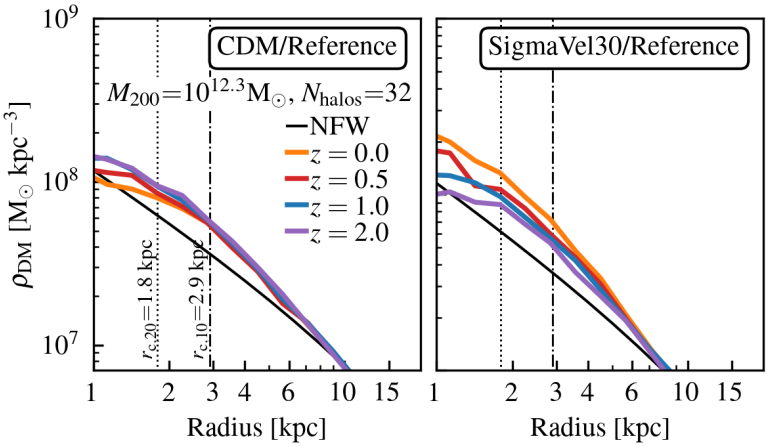

Figure 4.4: Stacked dark matter density profiles, $\rho_{\rm DM}$, of the 32 most massive haloes in the box (with masses larger than 10^{12} M$_\odot$) at $z = 0$ from the Reference model under CDM (left panel) and SigmaVel30 (right panel). The panels show the median density evolution between redshifts 0 and 2. The coloured lines highlight the median values and the black solid line shows the NFW profile of the haloes at redshift zero (estimated using the concentration-mass relation from Correa et al. 2015c). The black dotted and dashed-dotted lines indicate the convergence radii (see text for definition). While there is no large difference in the median density profiles of haloes over time in the CDM, the SigmaVel30 model shows that the central density increases.

The panels in Fig. 4.3 compare the dark matter density profiles, $\rho_{\rm DM}$, between hydrodynamical simulations (CDM and SIDM) of the Reference model (purple solid lines) and the WeakStellarFB model (blue dot-dashed lines). Additionally, dark matter-only simulations are presented as orange dashed lines. To facilitate the comparison, the NFW density profile (black solid lines) is included, estimated using the concentration-mass relation from Correa et al. (2015c). We also include convergence radii defined as the minimum radius where the mean density converges at the 20 and 10 per cent level, $r_{\rm c,20}$ (dash-dotted lines) and $r_{\rm c,10}$ (dotted lines) respectively, relative to a simulation of higher resolution. The convergence criterion $r_{\rm c,10}$, presented by Ludlow et al. (2019b), is defined as $r_{\rm c,10} = 0.055 l(z)$, where $l(z)$ is the (comoving) mean inter-particle separation. At $z = 0$ this separation is $l = L_{\rm b}/N_{\rm p}^{1/3} = 52.7$ kpc, given $L_{\rm b} = 25$ cMpc and $N_{\rm p} = 2 \times 376^3$ particles. In addition to Ludlow et al. (2019b) criterion, we include a relaxed convergence criterion given by $r_{\rm c,20} = 0.034 l(z)$. This is motivated by the findings of Schaller et al. (2015), who showed that the differences in the mean density profiles from the EAGLE hydrodynamical and DM-only simulations are significantly larger than 10%. The value of 0.034 is obtained from eq. (18) of Ludlow et al. (2019b) after decreasing $\kappa_{\rm P03} \equiv \frac{t_{\rm relax}}{t_{200}}$ by a factor of 2.

The bottom panels of Fig. 4.3 show that, in 10^{11} M$_\odot$ haloes, baryons do not affect $\rho_{\rm DM}(r)$ beyond $r_{\rm c,20}$. Under both CDM and SIDM, the hydrodynamical and DM-only simulations yield consistent $\rho_{\rm DM}$. In the CDM models, $\rho_{\rm DM}(r)$ agrees with the NFW prediction for $r > r_{\rm c,20}$, while in SIDM models, dark matter particle interactions create the expected constant-density isothermal cores (see also e.g., Colín et al. 2002; Vogelsberger et al. 2012; Peter et al. 2013; Rocha et al. 2013, and Correa et al. 2022 for DM-only TangoSIDM density profiles). This cored $\rho_{\rm DM}$ corresponds to the median profile of the central 10^{11} M$_\odot$ halo population. However, note that since the velocity-dependent SIDM models under consideration exhibit large cross sections at the 10^{11} M$_\odot$ mass-scale, some SIDM haloes may potentially undergo core-collapse and form a cuspy central density profile.

The bottom panels of Fig. 4.3 reveal that galaxies with stellar masses as high as 10^9 M$_\odot$ do not produce sufficiently strong feedback to affect the underlying dark matter distribution. In agreement with our results, Robles et al. (2017) modelled dwarf galaxies within 10^{10} M$_\odot$ haloes under both CDM and SIDM using the zoom-in FIRE cosmological model. They concluded that, for these low-mass systems, the final density profile of SIDM haloes was not strongly influenced by the stellar mass of the galaxy, exhibiting cored density profiles regardless of hosting galaxies with stellar masses ranging from 10^5 to 10^7 M$_\odot$. Furthermore, Burger et al. (2022) showed that both CDM and SIDM can yield haloes with cored density profiles. The difference lies in the fact that, under SIDM, galaxies can be embedded in haloes with cored central dark matter profiles, irrespective of whether they have

a smooth star formation history and non-bursty supernova feedback. In contrast, under CDM, galaxies would require a bursty star formation rate to generate strong supernova feedback that leads the impulsive cusp-core transformation.

Back to our results, the middle panels of Fig. 4.3 show that, in $10^{11.5}$ $M_\odot$ haloes, baryons impact on the dark matter distribution from the SIDM models. Under CDM, $\rho_{\rm DM}(r)$ from the Reference hydrodynamical and DM-only simulations agree, but under SIDM, they diverge. The SIDM DM-only simulations produce lower-density and larger-core profiles compared to the SIDM hydrodynamical simulations, which more closely follow the NFW prediction. The WeakStellarFB model generates cuspier density profiles than the Reference model, both under CDM and SIDM. This result suggests that the increased baryonic concentration in the WeakStellarFB model, relative to the Reference model, enhances the central concentration of the dark matter distribution.

The influence of baryons becomes more pronounced in 10^{12} $M_\odot$ haloes, as shown in the top panels of Fig. 4.3. In all dark matter models (CDM and SIDM), the density profiles between hydrodynamical and DM-only simulations no longer agree. Hydrodynamical-CDM models produce a cuspier $\rho_{\rm DM}(r)$ than the NFW profile (in line with predictions from adiabatic contraction models (e.g. Gnedin 2006). Similarly, hydrodynamical-SIDM models produce a very cuspy $\rho_{\rm DM}(r)$, in contrast to the cored $\rho_{\rm DM}$ profiles produced in the DM-only SIDM models. Consistent with our results, previous works by Elbert et al. (2018), Sameie et al. (2021) and Rose et al. (2022) showed that, under SIDM, dark matter density profiles can be either cuspy or even cuspier than their CDM counterparts, depending on the baryonic concentration. Sameie et al. (2021) analysed the density profiles of 10^{12} $\rm M_\odot$ haloes, modelled in high-resolution zoom-in simulations of SIDM within the FIRE galaxy formation scheme (Hopkins et al. 2018). Their study showed that SIDM haloes can reach higher and steeper central densities than their CDM counterparts. In a similar approach, Rose et al. (2022) presented zoom-in SIDM simulations of Milky Way-like galaxies with the IllustrisTNG (Pillepich et al. 2018) galaxy formation model. They concluded that baryon contraction begins to have an impact on the density profiles of haloes when their embedded galaxies reach stellar masses of 10^8 $\rm M_\odot$. For higher-mass systems such as groups and clusters, the work of Robertson et al. (2021) concluded that the haloes profile strongly depends on the final baryonic distributions. They showed this from the analysis of dark matter halo densities modelled with SIDM and the baryonic physics model of EAGLE (Schaye et al. 2015) in a zoom-in simulation. Similarly, Despali et al. (2019), employing zoom-in SIDM simulations of galaxies with the IllustrisTNG model, showed that smaller-size galaxies were embedded in cuspy SIDM haloes, while more extended galaxies resided in cored-profile haloes.

The gravitational influence of baryons not only increases central dark matter

densities in SIDM models, but also diversify the haloes' dark matter distribution, which can be seen from the increased scatter around the median density profiles (shaded region in Fig. 4.3). This diversity could be attributed to variations in the assembly history of galaxies, influencing whether baryons dominate the central gravitational potential sooner or later.

In Fig. 4.4, we investigate how the haloes assembly history shapes the evolution of the DM density profile. We select the 32 most massive haloes (with masses larger than 10^{12} $\mathrm{M}_{\odot}$) at $z = 0$ in the cosmological box from the Reference model under CDM (left panel) and SigmaVel30 (right panel). The panels show the evolution of the median ρ_{DM} between redshifts 0 and 2 (coloured lines). The black solid line shows the NFW profile of the haloes at redshift zero (estimated using the concentration-mass relation from Correa et al. 2015c). The left panel shows that except for the inner few kpc, there is minimal evolution of $\rho_{\mathrm{DM}}(r)$ under CDM. In this case, haloes formed a cuspy profile by redshift two, the subsequent impact of the central galaxies, through ejection of energy via supernova- and AGN-driven winds, leads to the formation of small cores in the center.

Under SIDM, the haloes' density evolves. At redshift two, the central dark matter density of SIDM haloes is lower than for their CDM counterparts. However, as galaxies in SIDM haloes grow in mass, baryons start to dominate the central potential. In response dark matter particles thermalise through frequent interactions and accumulate in the center of the baryonic-dominated potential. Over time, this results in an overconcentration of dark matter, manifesting as a highly cuspy density profile. This can be seen in the increasing central density of SIDM haloes in the right panel of Fig. 4.4. In the WeakStellarFB models, however, the situation is slightly different. Due to the early domination of baryons of the central potential, SIDM haloes quickly formed highly cuspy density profiles, with minimal evolution in the redshift range zero to two. Further details are presented in Appendix C.2.

In this section we have shown how baryons impact on the dark matter distribution under SIDM and CDM. While not an entirely novel result, this study presents the first cosmological simulations of a galaxy population under different velocity-dependent SIDM models and baryonic feedback schemes. The resulting features of the galaxy population have important implications for studies aiming to constrain SIDM by directly comparing to observational datasets. This is shown and discussed in the next section.

4.5 . Tully-Fisher Relation

The galaxy sample from the TangoSIDM simulations is characterized by distinct sizes, varying from highly extended to compact, depending on the stellar feedback model (Reference versus WeakStellarFB, as illustrated in Fig. 4.2). Simultaneously, the sample includes haloes with distinct dark matter distributions, with SIDM haloes having densities that deviate significantly from the NFW profile, as shown in Fig. 4.3. The sample's stellar-to-halo mass relation is consistent with observations (as depicted in the left panels of Fig. 4.2), and therefore haloes of a given mass host galaxies of the correct mass range. In this section, we test our galaxy sample with the stellar-mass Tully-Fisher relation, which establishes a correlation between the stellar mass and circular speed at a characteristic radius of spiral galaxies. First investigated by Tully & Fisher (1977), the relation has since become one of the best studied galaxy scaling relations (see e.g. Bell & de Jong 2001; Ziegler et al. 2002; Pizagno et al. 2007; Avila-Reese et al. 2008; Reyes et al. 2011; Catinella et al. 2023; Ristea et al. 2024), so that numerous studies have delved into its cosmological origin using both semi-analytical approaches and simulations (see e.g. Steinmetz & Navarro 1999; Dutton & van den Bosch 2012; Cattaneo et al. 2014; Desmond & Wechsler 2015; Ferrero et al. 2017).

Our analysis in this section demonstrates that when TangoSIDM galaxies are too compact or when dark matter is overly concentrated in the center, their rotation curves peak at much higher velocities than observed. This poses a powerful challenge for the validity of SIDM models. To quantify the significance of this constraint, Section 4.5.3 assesses which simulated galaxy samples, drawn from the Reference versus WeakStellarFB models under the various dark matter scenarios (presented in Section 4.5.1), are consistent with the observational sample (introduced in Section 4.5.2). This consistency test implies assessing the likelihood that the two sets of samples (simulated and observational) were drawn from the same, albeit unknown, probability distribution. Following this, in Section 4.5.4, we analyse the deviation of TangoSIDM galaxies from the observed Tully-Fisher relation. Subsequently, we evaluate the statistical significance of this deviation in Section 4.5.5.

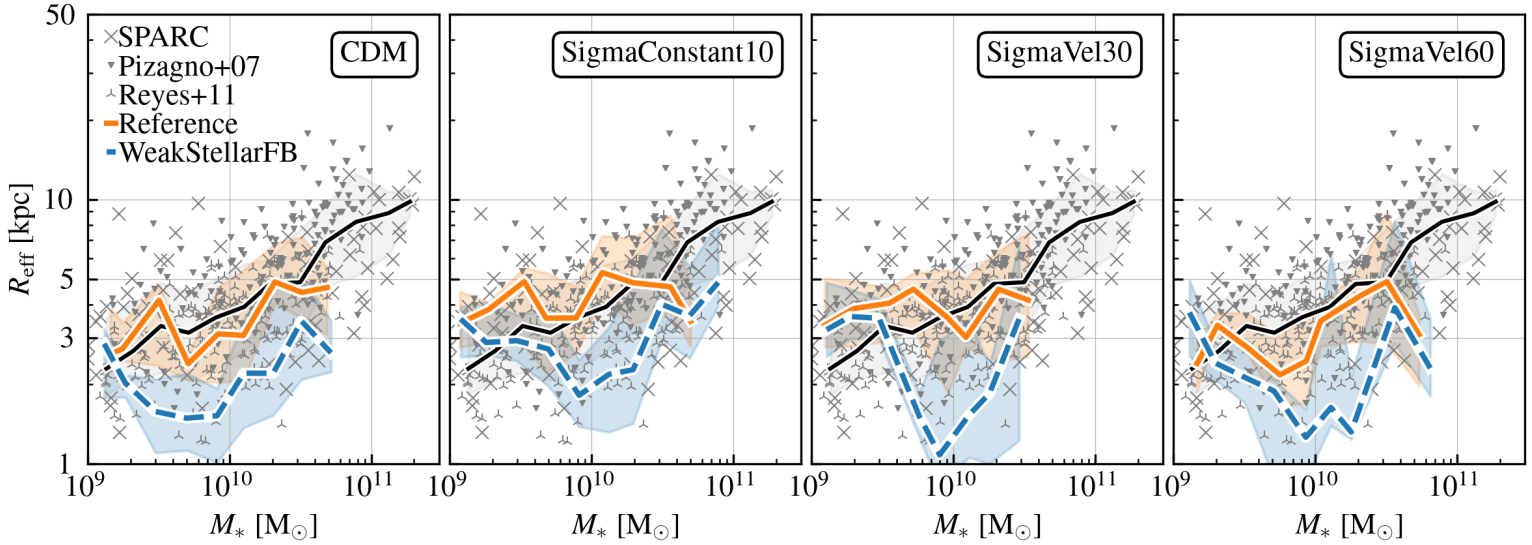

Figure 4.5: Effective radius as a function of stellar mass for $z = 0$ disc-type galaxies from the Reference (orange solid line) and WeakStellarFB (blue dashed line) models under CDM (left panel), SigmaConstant10 (second panel from the left), SigmaVel30 (third panel from the left) and SigmaVel60 (right panel). The observational sample is shown in grey symbols, with crosses corresponding to the SPARC dataset, triangles to the Pizagno et al. (2007) catalog and stars to the Reyes et al. (2011) data. The solid lines indicate the median relations for both the compiled observational sample (black) and the simulated sample (in color), while the shaded regions highlight the 16-84th percentiles. A visual inspection suggests that the simulated samples from the Reference model closely agree with the observational data, whereas the samples from the WeakStellarFB model do not. A statistical analysis using the Kolmogorov-Smirnov test reveals that only the massive ($M_* \geq 10^{10}$ $M_\odot$) simulated galaxies from the Reference model under CDM, SigmaVel30 and SigmaVel60 are not significantly different from the observational sample.

4.5.1 . Simulated sample

We create a subsample of disc-type galaxies using the fraction of stellar kinetic energy invested in ordered co-rotation, $\kappa_{\rm co}$, defined as

$$\kappa_{\rm co} = \frac{K_{\rm co-rot}}{K} = \frac{1}{K} \sum_{i}^{r<50{\rm kpc}} \frac{1}{2} m_i \left[L_{z,i}/(m_i\, R_i)\right]^2 , \tag{4.4}$$

to quantify morphology (see e.g. Correa et al. 2017). In eq. (4.4), the sum is over all stellar particles within a spherical radius of 50 kpc centered on the minimum of the potential, m_i is the mass of each stellar particle, $K(=\sum_i^{r<50{\rm kpc}} \frac{1}{2} m_i v_i^2)$ the total kinetic energy, $L_{z,i}$ the particle angular momentum along the direction of the total angular momentum of the stellar component of the galaxy and R_i is the projected distance to the axis of rotation. See also Sales et al. (2010) and Correa & Schaye (2020) for more details on $\kappa_{\rm co}$.

To create a disc-type galaxy subsample within each simulation, we use the criterion $\kappa_{\rm co}{>}0.3$ following Correa & Schaye (2020), who showed that values in the range $\kappa_{\rm co}{=}0.3-0.35$ select disc-type galaxies from the EAGLE simulations that agree with the distribution of disc galaxies from SDSS in the morphology-stellar mass-halo mass plane. This results in a selection of 61 disc-type galaxies per simulation with stellar masses ranging from 10^9 M$_\odot$ to 1.2×10^{11} M$_\odot$ and effective sizes, denoted as $R_{\rm eff}$, ranging from 1.4 kpc to 17.3 kpc. Note that $R_{\rm eff}$ is defined as the 2D projected size enclosing 50 per cent of the total K-band luminosity. The total luminosity is computed from all bound star particles within a projected 2D circular aperture of 50 kpc radius. The luminosities are intrinsic (i.e. dust-free) and are calculated at each output time and for each star particle, accounting for its age, mass, and metallicity. This calculation is performed by the SWIFT code using the photometric tables from Trayford et al. (2015). Finally, we estimate the circular velocity at the effective radius, $V_{\rm circ}(R_{\rm eff})$, as follows $V_{\rm circ}(R_{\rm eff}) = \sqrt{GM(<R_{\rm eff})/R_{\rm eff}}$, where the sum $M(<R_{\rm eff})$ considers the total mass of baryons (stars and gas) and dark matter enclosed within $R_{\rm eff}$.

4.5.2 . Observational sample

We compile an observational sample by joining the catalogs of disk galaxies from Lelli et al. (2016), Pizagno et al. (2007) and Reyes et al. (2011), resulting in a dataset of 429 disc galaxies with stellar masses within the range of 10^9 M$_\odot$ to 2×10^{11} M$_\odot$, and effective radii, $R_{\rm eff}$, spanning from 1.2 kpc to 18.5 kpc. Note that $R_{\rm eff}$ is defined as the radius encompassing half of the total galaxy luminosity. Rotational curves at $R_{\rm eff}$ were either directly extracted or estimated from each catalog. In the following, we provide a more detailed overview of these datasets.

Lelli et al. (2016) presented the Spitzer Photometry and Accurate Rotation Curves (SPARC) dataset, a galaxy catalog of 175 disc galaxies with near-infrared photometry at 3.6 μm and well-defined, high-quality HI rotation curves. For our analysis, we extracted inclination-corrected circular velocities, total luminosity at 3.6 μm, and effective radii directly from SPARC. We followed Lelli et al. (2017) and determined stellar masses using a constant mass-to-light ratio of $\Gamma = 0.5\ \mathrm{M}_\odot/\mathrm{L}_\odot$, which was motivated by stellar population synthesis models (Schombert & McGaugh 2014) using a Chabrier IMF. The total circular velocity at the effective radius was computed by interpolating the rotational curves.

The catalog derived by Pizagno et al. (2007) consists of 163 spiral galaxies featuring resolved H_α rotation curves. We utilized the effective radius and circular velocity at the effective radius directly from this catalog and estimated stellar masses using the i-band magnitudes, assuming a constant I-band mass-to-light ratio of 1.2, $M_* = 1.2 \times 10^{0.4(i_\odot - i)}\ \mathrm{M}_\odot$ with $i_\odot = 4.11$. The mass-to-light-ratio is adopted for a Chabrier IMF and it assumes the contribution of disc+bulge (Portinari et al. 2004). The effective radius for this sample is defined as the radius at $2.2 \times R_{\mathrm{disk}}$, where R_{disk} is the disc exponential scale length.

Finally, Reyes et al. (2011) provided an improved estimate of disk rotation velocities for a subset of SDSS galaxies. This dataset includes the i-band Petrosian half-light radius, r-band Petrosian absolute magnitude (M_r), and $g - r$ colour, all k-corrected to $z = 0$ and corrected for Galactic and internal extinction. Stellar masses were estimated following Bell et al. (2003),

$$M_* = 10^{[\log_{10}(L_r/L_{r,\odot}) + \log_{10}(M_*/L_r) + \log_{10} h^2]}\ \mathrm{M}_\odot, \tag{4.5}$$

where $\log_{10}(L_r/L_{r,\odot}) = -0.4(M_r - M_{r,\odot} + 1.1z)$ with $M_{r,\odot} = 4.76$, and $\log_{10}(M_*/L_r) = -0.306 + 1.097 \cdot (g - r) - 0.093$, where the last term, -0.093, corresponds to the conversion from a modified Salpeter IMF to a Chabrier IMF (as indicated in Gallazzi et al. 2008).

To estimate the rotation velocity at R_{eff}, we used the arctangent model

$$V_{\mathrm{circ,obs}}(R') = V_0 + \frac{2}{\pi} V_{\mathrm{c,obs}} \arctan\left(\frac{R' - R_0}{R_{\mathrm{TO}}}\right). \tag{4.6}$$

Reyes et al. (2011) fitted this model to each rotational curve from the sample and provided the four free parameters: the systemic velocity V_0, the asymptotic circular velocity $V_{\mathrm{c,obs}}$, the spatial center R_0, and the turn-over radius R_{TO}, at which the rotation curve starts to flatten out. We use the above expression for $V_{\mathrm{circ,obs}}(R')$ and estimate it at R_{eff}, by converting R_{eff} into arcsecond units and correcting for inclination as follows $V_{\mathrm{circ}} = V_{\mathrm{circ,obs}}(R')/\sin(i)$.

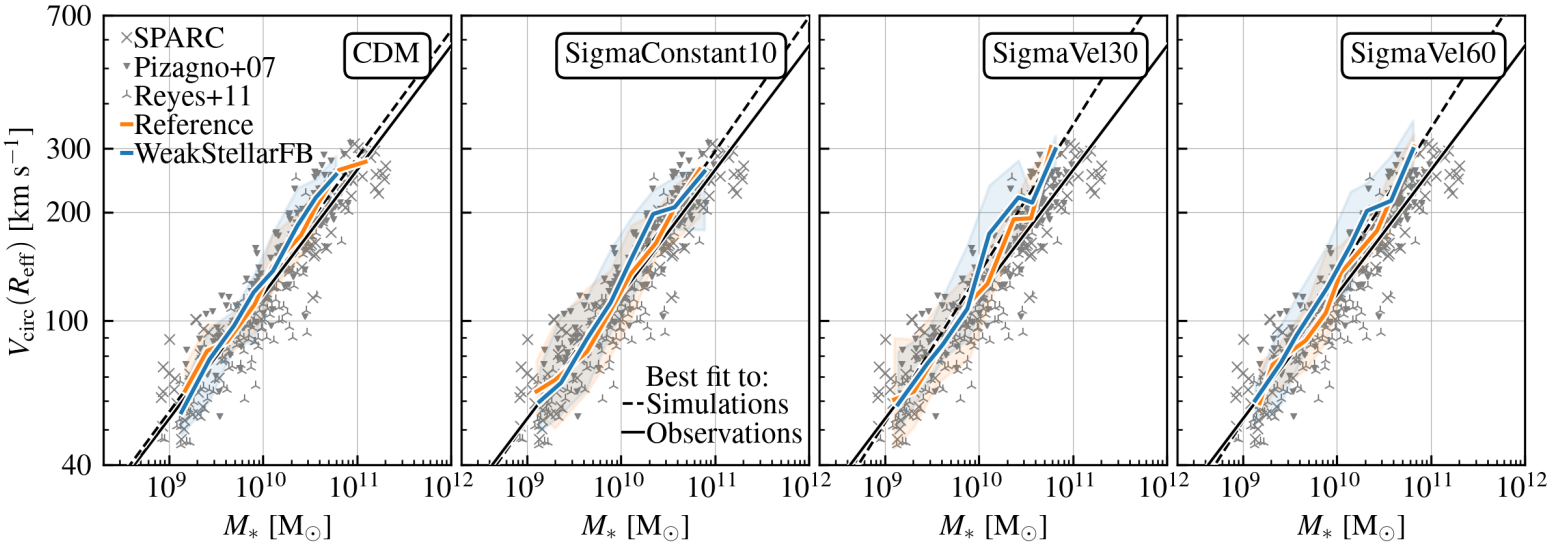

Figure 4.6: The stellar mass Tully-Fisher relation, i.e. total circular velocity at the effective galactic radius as a function of stellar mass for disc-type galaxies. The median relations for disc galaxies in the Reference and WeakStellarFB models are represented by orange and blue lines, respectively, with shaded regions highlighting the $1-99$th percentiles. The panels show the Tully-Fisher relation for simulated galaxies under CDM (left panel), SigmaConstant10 (second panel from the left), SigmaVel30 (second panel from the right) and SigmaVel60 (right panel). Similar to Fig. 4.5, the panels also display the observational sample in grey symbols, with crosses corresponding to the SPARC dataset, triangles to the Pizagno et al. (2007) catalog and stars to the Reyes et al. (2011) data. The solid and dashed lines depict the best-fitting linear relations to the observational sample and simulated samples, respectively. The figure reveals a close agreement between observations and the Reference and WeakStellarFB models under CDM. However, this agreement is not maintained for SIDM. Under SIDM, the slope of the Tully-Fisher relation from the simulated sample deviates from the observed relation, with the most significant deviation occurring in the SigmaVel30 model, followed by SigmaVel60. The deviation between the relations (observational vs. simulated) is statistically significant at the 98% level in the SigmaVel30 model for galaxies with masses $\geq 10^{10}$ M$_\odot$, and at the 95% confidence level in the SigmaVel60 model for galaxies with masses $\geq 1.3\times 10^{10}$ M$_\odot$.

4.5.3 . The mass-size plane

We compare the observational sample in the mass-size plane with a sample of disc-type galaxies taken from the simulations. Fig. 4.5 shows the effective radius as a function of stellar mass for disc-type galaxies from the Reference (orange solid line) and WeakStellarFB (blue dashed line) models under CDM (left panel), SigmaConstant10 (second panel from the left), SigmaVel30 (third panel from the left) and SigmaVel60 (right panel). The coloured lines represent the median relations, and the shaded regions depict the 16-84th percentiles. The observational sample is shown in grey symbols, and its median relation is depicted in solid black line.

The panels in Fig. 4.5 indicate that the median trend of the simulated samples from the Reference model agrees with the observational data, while the simulated galaxies from the WeakStellarFB do not, as they become quite compact around a stellar mass of 10^{10} $\mathrm{M}_{\odot}$. To determine the statistical significance of the differences in the mass-size plane between the simulated and observational samples, we perform a Kolmogorov-Smirnov test (KS) for two samples. Given that the observed sample is not a volume-limited sample, we opt not to account for the mass distribution. Instead, we make a quantitative analysis by dividing the samples into bins of stellar mass and comparing the size distributions. For each stellar mass bin, we test the null hypothesis that the two samples—observational and simulated—were drawn from the same distribution. A confidence level of 95% is chosen, implying that we reject the null hypothesis if the p-value is less than 0.05. The aim of the KS test is to identify the simulated galaxy sample that is most likely drawn from the distribution function of the observational sample, making it statistically equivalent.

We separate the samples into three stellar mass bins ([10^9, $3{\times}10^9$], [$3{\times}10^9$, 10^{10}], and [10^{10}, $3{\times}10^{10}$ $\mathrm{M}_{\odot}$]), and compare the observational sample and simulated galaxies from the Reference model under CDM. The KS statistical analysis returns p-values of 0.36, 0.02 and 0.13, respectively under each mass bin. The low p-value of 0.02 for simulated galaxies with stellar masses between $3{\times}10^9$ and 10^{10} $\mathrm{M}_{\odot}$ indicates that those galaxies do not conform to the observed size distribution, whereas galaxies in the other mass bins do. We further analyse the samples of galaxies from Reference + SigmaConstant10, SigmaVel30 and SigmaVel60, contrasting them with the observational sample. For Reference + SigmaConstant10, the analysis returns the following p-values of $8{\times}10^{-4}$, 0.78 and 0.15. Similarly, Reference + SigmaVel30 returns p-values of $8{\times}10^{-4}$, 0.31 and 0.09, whereas Reference + SigmaVel60 yields p-values of 0.59, $5{\times}10^{-3}$ and 0.06. For all Reference models (CDM + SIDM), the large p-values in the stellar mass bins $10^{10} - 3{\times}10^{10}$ $\mathrm{M}_{\odot}$ indicate that we cannot reject the null hypothesis. Therefore, at the high mass end the samples, both observational and simulated, are not

significantly different at the 95% confidence level and could be drawn from the same size distribution.

Differently, the WeakStellarFB model (under CDM or SIDM) fails to produce galaxies with sizes that agree with the observations. The KS test returns small p-values (<0.01) for galaxies more massive than 3×10^9 $\mathrm{M}_\odot$. For lower mass galaxies, in the regime where the overcooling of the model has a lesser impact (as discussed in Section 4.3), the KS test yields p-values of 0.06, 0.1 and 0.98 for WeakStellarFB + SigmaConstant10, + SigmaVel30, and + SigmaVel60, respectively. From what we conclude that in the low mass end, the WeakStellarFB model under SIDM, produces galaxies whose sizes are not statistically different from the observations.

4.5.4 . Tully-Fisher relation

The Tully-Fisher relation is shown in Fig. 4.6, where the y-axis corresponds to the total circular velocity at the effective galactic radius and the x-axis corresponds to the stellar mass. The left panel displays the Tully-Fisher relation for disc galaxies from the Reference (orange solid line) and WeakStellarFB (blue solid line) models under CDM. Moving from left to right, the subsequent panels show the relation for disc galaxies under the SigmaConstant10 model, SigmaVel60 model, and SigmaVel30 model. Similar to Fig. 4.5, the panels also show the observational sample in grey symbols. Coloured lines highlight the median relations from the simulations, while shaded regions represent the 1-99th percentiles.

The figure shows a tight correlation between circular velocity and stellar mass, as expected. This correlation is further highlighted by the best-fitting linear relation to the observational sample (black solid lines). The best-fitting parameters of the relation, $\log_{10}(V_{\rm circ}/\mathrm{km\ s^{-1}}) = a\log_{10}(M_*/10^{10}\mathrm{M}_\odot)+b$, are $a = 0.34\pm0.01$ and $b = 2.07\pm0.01$. The parameters and $5-95\%$ confidence intervals were estimated by bootstrapping the observational sample.[3] Similarly, we created a joint sample of galaxies from both the Reference and WeakStellarFB models, and via the bootstrap method we estimated the best-fitting linear relations from the simulations, which are depicted by black dashed lines in the panels.

Fig. 4.6 shows the close agreement between the Tully-Fisher relation derived from the observational sample and that of the simulated sample of disc galaxies from both the Reference and WeakStellarFB models under CDM. However, this agreement is not maintained when considering the SIDM models. Under the SIDM framework, the slope of the Tully-Fisher relation from the simulated sample begins to deviate relative to the observed Tully-Fisher relation. The largest deviation

[3]In each bootstrap iteration i, we created a random observational subsample and estimated the best-fitting parameters a_i and b_i of the subsample utilizing the `stats.linregress` function from the `scipy` package.

occurs in the SigmaVel30 model, followed by the SigmaVel60 model. The shift in $V_{\rm circ}(R_{\rm eff})$ found in galaxies within the SIDM models is attributed to the large central dark matter densities that result from the dark matter particle interactions. Consequently, at constant M_*, the increased enclosed dark matter mass drives a higher $V_{\rm circ}(R_{\rm eff})$ compared to CDM, thereby altering the slope of the relation.

Our analysis in the previous subsection established that only the disc galaxies from the Reference model under CDM, SigmaVel30 and SigmaVel60 were statistically comparable to the observational sample. This was not found for galaxies from the WeakStellarFB model under any dark matter model. Nonetheless, in Fig. 4.6, we intentionally include the trend from the WeakStellarFB model to highlight how the deviation from the observed Tully-Fisher relation increases under SIDM, particularly when galaxies become more compact. Notably, under CDM, the Tully-Fisher relations from both the Reference and WeakStellarFB models closely agree. This finding appears to contradict the conclusions drawn by Ferrero et al. (2017), who posited that ΛCDM models should be capable of matching the observed Tully-Fisher relation, provided that galaxy sizes are well reproduced, and that halos respond approximately adiabatically to galaxy assembly. This will be further addressed in future work, with more variations of the stellar feedback model and larger number statistics from the simulated sample.

4.5.5 . Statistical analysis

The panels in Fig. 4.6 reveal a discernible departure of the Tully-Fisher relation from disc galaxies under SIDM relative to the observed Tully-Fisher relation. To quantify the significance of this deviation and to assess the likelihood of a similar deviation in the observational sample, we perform a statistical analysis focusing on the observational sample and the simulated samples from the Reference model under SigmaVel30 and SigmaVel60. Reference+SigmaConstant10 is not considered in the analysis because this particular SIDM model has already been ruled out by observations of galaxy clusters. Additionally, the WeakStellarFB models are excluded from the analysis due to their significant difference from the observations (as established in Section 4.5.3).

Given that the deviation in the SIDM models is prominent in massive galaxies, as demonstrated in Section 4.4 for haloes more massive than 10^{12} $\rm M_\odot$, and considering that these galaxies are statistically equivalent to the observational sample in terms of their size distribution, as demonstrated in Section 4.5.3, we apply a selection cut in stellar mass of 10^{10} $\rm M_\odot$. This allows us to analyse the Tully-Fisher relation for only massive galaxies, while disregarding the influence of low-mass systems that do not present significant changes in their central density profiles relative to CDM. This stellar mass cut results in a subsample of 287 real galaxies and 33

simulated galaxies from each SIDM model.

We perform a bootstrap analysis around these subsamples using 10,000 iterations. In each iteration, we create random samples (with replacement) for both the observational and simulated datasets, and calculate the slopes of their respective Tully-Fisher relations. After all iterations, we calculate the mean value and confidence intervals of the slopes. For the observational sample, a slope of $a = 0.34 \pm 0.02$ is obtained. When comparing this slope with its value for the entire sample (calculated in Section 4.5.4), we find that the observed Tully-Fisher relation does not change when we consider only the subsample of massive galaxies.

For the simulated sample from the SigmaVel30 model, we find a slope of $a = 0.48 \pm 0.08$, and for the SigmaVel60 model, a slope of $a = 0.41 \pm 0.07$. The SigmaVel30 model exhibits a strong deviation from the observed Tully-Fisher relation, as indicated by the different slope. When we assess the differences between these slopes, we obtain a p-value of 0.012, which indicates the frequency that each random bootstrap sample from the simulations had a slope lower than the slope from the observational bootstrap sample. Consequently, we conclude that the Reference+SigmaVel30 model, despite producing galaxies with stellar masses and sizes in good agreement with the observations (Fig. 4.5), it produces a Tully-Fisher relation that deviates from the observed one at the 98% confidence level.

The Tully-Fisher relation from the SigmaVel60 model also deviates from the observed relation, although it is not as pronounced as in the SigmaVel30 case. The difference between these slopes yields a p-value of 0.13, signifying that in $\sim 13\%$ of the bootstrap samples from the SIDM model, a slope equivalent or lower than the one derived from the observations arises. Therefore, we cannot reject the null hypothesis that both Tully-Fisher relations, from the observations and simulations, are drawn from the same distribution.

We further investigate this and calculate the minimum stellar mass above which the simulated galaxy sample from SigmaVel60 produces a Tully-Fisher relation that deviates significantly from the observed one. This cut is identified for galaxies with $M_* \geq 1.3 \times 10^{10}$ $\mathrm{M}_\odot$. For these refined subsamples, the observational sample yields a slope of $a = 0.32 \pm 0.03$, while the SigmaVel60 model produces a slope of $a = 0.45 \pm 0.09$. The bootstrap analysis yields a low p-value of 0.042, indicating that over this mass range, the SigmaVel60 model produces a Tully-Fisher relation that deviates from the observed one at the 95% confidence level. As a control test, we assess the difference in the Tully-Fisher relations from the Reference+CDM model and observations over this mass range of $> 1.3 \times 10^{10}$ $\mathrm{M}_\odot$. We obtain a p-value of 0.26. Thus, we affirm that the Reference+CDM model maintains a good agreement with the observations.

The deviation of the Tully-Fisher relation from disc galaxies (under the Reference+SigmaVel30 models) relative to the observed Tully-Fisher relation is non-

negligible. In this section, we have shown that it is statistically significant, which indicates that we can rule out the SigmaVel30 model over the mass range $\gtrsim 10^{10}\ \mathrm{M}_{\odot}$ with 98% confidence. The rejection of this SIDM model relies on the assumption that the Reference galaxy formation model is valid, as we have demonstrated through the good agreement of the stellar mass-halo mass relation (Fig. 4.2), stellar masses (Fig. C.1) and galaxy sizes (Fig. 4.5, supported by statistical analysis of Section 4.5.3) with observations.

The deviation of the Tully-Fisher relation, relative to observations, is driven by the impact of SIDM, which produces haloes with high central dark matter densities (Fig. 4.3). SIDM therefore raises $V_{\mathrm{circ}}(R_{\mathrm{eff}})$ at fixed stellar mass, and increases the slope of the relation as shown in this section. This physical effect, constrained by the Tully-Fisher relation, is ruled out. Note, however, that the rejection of the SigmaVel30 model is specific to a certain "mass range" (i.e. $\gtrsim 10^{10}\ \mathrm{M}_{\odot}$), because halo density evolution depends on the value of the cross section, which in turn depends on halo mass (Fig. 4.1). Therefore, only cross sections influencing the steepness of the haloes' density throughout their evolution are ruled out. In a similar manner, we argue that the Tully-Fisher relation can be utilized to rule out the SigmaVel60 model over the mass range $\gtrsim 1.3 \times 10^{10}\ \mathrm{M}_{\odot}$ with 95% confidence. These findings have significant implications for the SIDM parameter space, which are discussed in the next section.

4.6 . Discussion

4.6.1 . SIDM parameter space

The SIDM parameter space, characterized by the self-interaction cross section as a function of the relative velocities between dark matter particles, is a topic of extensive debate. Robust constraints on the cross section at large scales (high dark matter particle velocities) have been established by studies of galaxy clusters (e.g. Randall et al. 2008; Dawson et al. 2013; Massey et al. 2015; Harvey et al. 2015; Wittman et al. 2018; Harvey et al. 2019; Sagunski et al. 2021; Andrade et al. 2022). However, the cross section for Milky Way-size galaxies and lower-mass systems remains highly uncertain. Recent proposals suggest that the cross section in dwarf-size galaxies should be as large as $100\ \mathrm{cm}^2\mathrm{g}^{-1}$ (e.g. Correa 2021; Turner et al. 2021; Silverman et al. 2023; Slone et al. 2023; Yang et al. 2023), in order to address the diversity problem through halo core expansion and core collapse. At the scale of Milky Way-mass galaxies, Correa (2023) argues that the cross section should be lower than $10\ \mathrm{cm}^2\mathrm{g}^{-1}$. Otherwise the frequent interactions between the Milky Way-mass systems and their satellites would lead to excessive mass loss and destruction of satellites, giving rise to unrealistic satellite populations.

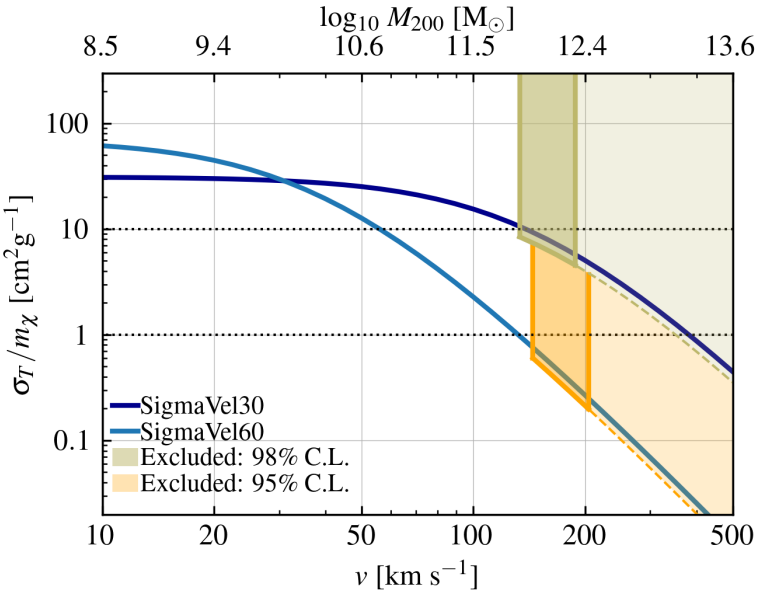

Figure 4.7: Momentum transfer cross section, $\sigma_{\rm T}/m_\chi$, plotted as a function of relative scattering velocity of dark matter particles. The blue solid lines shows the velocity-depenent SIDM models presented in this work, SigmaVel30 and SigmaVel60 (see Table 4.1 for details). The bottom x-axis indicates the relative velocity between dark matter particles, while the top x-axis indicates the typical halo mass that hosts orbits of such velocities. The shaded regions demarcate areas of the SIDM plane excluded by this work. The dark green and orange shaded regions highlight the excluded parameter space that is directly extracted from the simulations. The lighter green and orange shaded regions mark larger regions that are excluded based on the assumption that higher mass haloes under SIDM models with larger cross sections would exhibit a large deviation in the Tully-Fisher plane from the observations.

This section discusses the new constraints on the SIDM parameter space presented in Section 4.5.5. Our work has shown that the co-evolution of baryons and dark matter self-interactions strongly impacts the evolution of galaxies. Compared with CDM, galaxies in SIDM hydrodynamical simulations not only tend to grow more extended (Section 4.3), but also contain enhanced dark matter central densities (Section 4.4). This behavior results in a deviation in the Tully-Fisher relation relative to an observational dataset (Section 4.5.4). In Section 4.5.5, we found that this deviation is statistically significant in the SigmaVel30 model for galaxies more massive than $\gtrsim 10^{10}$ $\mathrm{M}_{\odot}$, and in the SigmaVel60 model for $\gtrsim 1.3 \times 10^{10}$ $\mathrm{M}_{\odot}$. Next, we place these constraints on the velocity-$\sigma_{\mathrm{T}}/m_{\chi}$ plane.

In what follows we argue that we can rule out velocity-cross section pairs that govern the evolution of haloes hosting the massive disc galaxies that significantly deviate from the observations in the Tully-Fisher plane. To identify the velocity-cross section pairs, we therefore select all disc galaxies from the Reference + SigmaVel30 and Reference + SigmaVel60 models with stellar masses larger than 10^{10} $\mathrm{M}_{\odot}$ and $1.3{\times}10^{10}$ $\mathrm{M}_{\odot}$, respectively. We follow the assembly histories of the haloes hosting these galaxies across the simulation snapshots until redshift 2, the redshift below which the haloes' density profiles are well resolved and commence substantial evolution (refer to Fig. 4.4, Section 4.4 and Appendix C.2). We determine the median and 16-84th percentiles of their mass accretion histories, $M_{200}(z)$, and convert these to the circular velocity, $V_{\mathrm{circ}}(z)$. We assume that $V_{\mathrm{circ}}(z)$ is the average velocity of the dark matter particles within these haloes over the redshift range 0-2, and using eqs. (4.1) and (4.2) we estimate the haloes' average dark matter cross section. The individual haloes' $M_{200}(z)$, $V_{\mathrm{circ}}(z)$ and cross sections are shown in Appendix C.3.

The derived velocity-cross section pairs establish the limits above which the SigmaVel30 and SigmaVel60 models produce overly enhanced central dark matter densities in massive disc galaxies. Therefore, we mark these limits as regions where the SigmaVel30 and SigmaVel60 models are ruled out with 98% and 95% confidence, as shown in the green and orange shaded areas in Fig. 4.7. The figure depicts the momentum transfer cross section, $\sigma_{\mathrm{T}}/m_{\chi}$, as a function of relative dark matter particle scattering velocity. The curves show the velocity-dependent SIDM models presented in this work, SigmaVel30 and SigmaVel60 (see Table 4.1). While the bottom x-axis highlights the relative velocity between dark matter particles, the top x-axis indicates the typical halo mass that hosts orbits of such velocities. The dark green and orange shaded regions highlight the newly excluded parameter space that is directly extracted from the simulations. The lighter green and orange shaded regions mark further excluded regions under the assumption that higher mass haloes under SIDM models with higher cross sections would exhibit a large deviation in the Tully-Fisher plane from the observations.

While this finding imposes strong constraints on velocity-dependent models, it does not entirely rule them out. There is still room for models where the cross section reaches $100\ \mathrm{cm^2 g^{-1}}$ at 10 km s^{-1}, provided that it decreases to less than $1\ \mathrm{cm^2 g^{-1}}$ at 150 km s^{-1}. In Fig. 4.7, we refrain from extending the SIDM parameter space to velocities larger than 500 km s^{-1}, since those are not covered by the simulations. Our future plans include expanding this analysis to larger scales, employing larger cosmological boxes and more statistical power through increased numerical resolution to model a more extensive sample with lower mass disc galaxies. Additionally, we aim to explore the circular velocities of dwarf galaxies in more detail. We anticipate that with sufficient resolution and statistics, the modelling of dwarf galaxies, even with the inclusion of baryons as shown in the bottom panels of Fig. 4.3, may yield lower values of $V_{\mathrm{circ}}(R_{\mathrm{eff}})$ relative to an observational sample at fixed stellar mass, consequently resulting in a deviation of the Tully-Fisher relation. This analysis, coupled with methodology improvements such as mock observations of HI discs for extracting rotational curves, will be the focus of future work.

4.7 . Conclusions

The SIDM parameter space, while extensively explored in recent years, remains notably uncertain, particular for Milky Way-size galaxies and smaller systems. This uncertainty arises due to the inherent challenge of isolating the impact of baryonic physics from dark matter interactions. Recent studies (e.g. Robertson et al. 2019; Despali et al. 2019; Sameie et al. 2021; Rose et al. 2022; Burger et al. 2022; Jiang et al. 2023) have reported that the prevalence of baryons in the central gravitational potential leads to the formation of denser and more cusp-like central density profiles under SIDM compared to CDM. Nevertheless, uncertainties persist regarding how the increased cuspiness of SIDM haloes correlates with the specific SIDM model parameters and the strength of galaxy feedback. To address these uncertainties, this study introduces a new set of cosmological hydrodynamical simulations. These simulations include the SIDM model derived from the TangoSIDM project (Correa et al. 2022) and leverage the baryonic physics from the SWIFT-EAGLE galaxy formation model (Borrow et al. 2023; Schaller et al. 2023).

Two cosmological simulation suites were generated: The Reference model, calibrated in a (25 Mpc)^3 volume to reproduce the galaxy stellar mass function and galaxy mass-size relation; and the WeakStellarFB model, featuring less efficient stellar feedback around Milky Way-like systems. Each galaxy formation model (Reference and WeakStellarFB) was simulated under four dark matter cosmologies: CDM, SigmaConstant10 (a SIDM model with a constant cross section of 10 cm^{2}g^{-1}), and SigmaVel30 and SigmaVel60, two SIDM models with velocity-

dependent cross sections (see Fig. 4.1). SigmaVel60 has a cross section smaller than 1 cm^{2}g^{-1} at high velocities (v>150 km s^{-1}) and increases with decreasing velocity, reaching 60 cm^{2}g^{-1} at 10 km s^{-1}. SigmaVel30 has a cross section smaller than 8 cm^{2}g^{-1} at velocities surpassing 200 km s^{-1} (dropping below 1 cm^{2}g^{-1} at $\approx$1000 km s^{-1}) and it also increases with decreasing velocity. These SIDM models we selected to represent two extreme scenarios for the rate of dark matter interactions in Milky Way-mass systems. The SWIFT-EAGLE models were selected to determine whether the impact of SIDM on galaxies remains robust when subjected to variations in feedback models.

Our findings indicate that SIDM does not significantly alter global galaxy properties such as stellar masses and star formation rates, but it does impact galaxy sizes, making galaxies more extended (Fig. 4.2). Dark matter particle interactions heat the inner halo, leading to core formation in the central regions of haloes less massive than 10^{11} M$_\odot$ and dynamically heating the surrounding gas and stars, promoting the formation of more extended galaxies. However, we have found that the impact of SIDM is insufficient to counteract the gas overcooling and size compactness in galaxies from the WeakStellarFB model.

In massive haloes ($\sim 10^{12}$ M$_\odot$), baryonic influence on SIDM distributions result in steeper dark matter density profiles than those produced in CDM from adiabatic contraction (Fig. 4.3). This feature is enhanced in the WeakStellarFB model, suggesting that the increased baryonic concentration in the model, relative to the Reference model, enhances the central concentration of the dark matter distribution. Under SIDM, the haloes density profile evolved differently (Fig. 4.4). As galaxies grow in mass, baryons begin to dominate the central gravitational potential, causing dark matter particles to thermalise through frequent interactions and accumulate in the center, resulting in cuspy dark matter density profiles.

The enhanced dark matter density at the centers of galaxies results in a notable deviation in the slope of the Tully-Fisher relation, significantly diverging from observations. We assembled an observational sample of $z \approx 0$ disc galaxies by combining the catalogs from Pizagno et al. (2007), Reyes et al. (2011) and Lelli et al. (2016). Our analysis reveals that while the simulated massive galaxies from the Reference model under SigmaVel30 and SigmaVel60 are not significantly different from the observational sample in the galaxy mass-size plane (Fig. 4.5), they strongly deviate in the Tully-Fisher plane (Fig. 4.6). This is due to a shift in $V_{\rm circ}(R_{\rm eff})$ found in galaxies within the SIDM models, driven by the large central dark matter densities that result from the dark matter particle interactions. Consequently, at constant M_*, the increased enclosed dark matter mass leads to a higher $V_{\rm circ}(R_{\rm eff})$ compared to CDM, altering the slope of the relation. In contrast, the Tully-Fisher relation derived from CDM models aligns well with observations.

We have conducted a statistical analysis to assess the significance of the dis-

crepancy between the SIDM models and observations in the Tully-Fisher plane. Our findings indicate that galaxies from the Reference+SigmaVel30 model more massive than 10^{10} $\mathrm{M}_{\odot}$ deviate from the observational sample at the 98% confidence level, while galaxies with masses exceeding $1.3{\times}10^{10}$ $\mathrm{M}_{\odot}$ from the Reference+SigmaVel60 model deviate at the 95% confidence level. These constraints, when translated into the velocity-$\sigma_{\mathrm{T}}/m_{\chi}$ plane (Fig. 4.7), reveal that the cross section should be smaller than 0.5 cm^{2}g^{-1} for velocities of $\sim$150-200 km s^{-1} and smaller than 10 cm^{2}g^{-1} for velocities of 110-180 km s^{-1}.

Our study reveals that the Tully-Fisher plane, encompassing galaxy sizes, stellar masses, and circular velocities, serves as a powerful observable for discerning and excluding velocity-dependent SIDM models. In future work we will focus on improving the datasets (higher numerical resolution and larger cosmological box size for the simulations, as well as larger data compilation from observational surveys) and refining the methodology, including the creation of mock HI rotation curves, with the goal of carrying out more accurate and precise comparisons.

5 - Research Career

This chapter summarizes the scientific career of the author.

5.1 . Scientific and technical contributions

My area of research is theoretical astrophysics with a primary focus on investigating the nature of dark matter. In addition, my research encompasses various aspects of galaxy formation physics, ranging from galaxy morphology to the evolution of gas in the circumgalactic medium. Since October 2023, I serve as a researcher at CEA Paris-Saclay, leading multiple research lines.

Prior to my current position, I held a NWO-VENI Fellowship at the University of Amsterdam in the Netherlands from 2019 to 2023. Preceding this, I conducted postdoctoral research at Leiden Observatory (Leiden University), in the Netherlands, from 2016 to 2019. I earned my Ph.D. degree at the University of Melbourne (Australia) in 2016, specializing in Cosmology and Galaxy formation.

At the time of writing I have contributed to the field by co-authoring 23 scientific papers, with 12 as first author. In the following sections, I outline and expand upon my main scientific contributions, categorized by research topics.

5.1.1 . The nature of dark matter

As discussed in the introduction of this thesis, observations of spiral galaxies, gravitational lensing, and the Cosmic Microwave Background strongly support the existence of dark matter. These observations indicate that galaxies are embedded in extensive regions of dark matter called haloes. However, our understanding of the mass assembly of dark matter haloes under an expanding universe was rather incomplete. The first contribution of my scientific career was to show through analytical modelling that the evolution of the halo mass growth over cosmic time can be described by an exponential function of redshift in the high-redshift regime. However, in the low-redshift regime the mass growth slows down due to the accelerated expansion of the Universe. This analytical framework enabled me to explore the relationship between cosmological parameters and the density structure of dark matter haloes, which is characterized by a single parameter known as concentration. I showed that halo concentration depends on halo mass growth and can be predicted based on a given cosmology. This work, presented in three publications (Correa et al. 2015a,b,c), has been widely applied in X-ray and gravitational lensing studies, galaxy formation models, and studies related to indirect dark matter searches.

Uncovering the nature of dark matter is one of the most pressing pursuits of our time. While deep underground experiments and particle colliders have yet to directly detect dark matter, astronomical observations continue to strengthen the evidence for its existence. Observations of colliding galaxies reveal the possibility that dark matter particles may interact non-gravitationally with each other. To date, these tentative interactions have been measured in the collision and shape of galaxy clusters, which have set robust upper limits on the interaction cross section per unit of dark matter mass, σ/m_χ, at $\sigma/m_\chi < 1.25$ cm^{2}g^{-1} (e.g. Wittman et al. 2018). However, in the regime of low-mass dwarf galaxies, the cross section of dark matter interactions remains uncertain. This is because the central dark matter content within dwarf galaxies is extremely diverse. It ranges from galaxies having excessively low dark matter in their centre (e.g. Charles et al. 2022; Borukhovetskaya et al. 2022), to being highly dark matter dominated (e.g. Read et al. 2019; Hayashi et al. 2022). The origin of the diversity in the dark matter distribution within dwarf galaxies is currently unknown. Studies that assume the cold and collisionless dark matter paradigm and include the impact of baryonic physics, have been unable to fully account for the observed diversity (Sales et al. 2022).

The self-interacting dark matter paradigm (hereafter SIDM) emerges as a compelling model to reconcile theoretical predictions with observed discrepancies in galaxy models. It is also predicted by particle physics models due to the inher-

ent interaction between particles in nature (Arkani-Hamed et al. 2009; Buckley & Fox 2010; Boddy et al. 2014b; Tulin & Yu 2018). SIDM introduces a novel scenario where dark matter interacts gravitationally with ordinary particles, while undergoing non-gravitational interactions with itself (self-interactions).

In Correa (2021), expanded in Chapter 2, I illustrated that SIDM can explain the diverse dark matter distribution within dwarf galaxies. Depending on the evolutionary stage of the galaxy, dark matter self-interactions can either expand or contract the central core, resulting in an increase or decrease of the dark matter content at the galaxy's center. For such core evolution to occur, I estimated that σ/m_χ should be larger than $\sigma/m_\chi > 10$ cm^{2}g^{-1} on dwarf galaxy scales but lower than $\sigma/m_\chi < 1$ cm^{2}g^{-1} on galaxy cluster scales, thereby introducing a previously unexplored region of parameter space. The findings of Correa (2021) are supported by Correa et al. (2022), where we developed state-of-the-art cosmological simulations of SIDM with $\sigma/m_\chi > 10$ cm^{2}g^{-1} to demonstrate that the expansion or collapse of dark matter naturally occurs in dwarf galaxies within a cosmological context. My work has stimulated interest in searching for dark matter through core collapse signals in strong lensing (Yang et al. 2023; Gilman et al. 2023), as well as in galaxies in the field (Orkney et al. 2022).

Conferences/Seminars: For this work I have been invited as a review speaker for the "cosmological simulations as a test of the nature of dark matter" session at the TeVPA conference in Chicago (US) in Aug/2024. I have also contributed to the Identification of Dark Matter meeting (Vienna, Austria 2022), and to symposiums during the European Astronomical Society (EAS) annual meeting (Valencia, Spain 2022; Leiden, The Netherlands 2021). I have been invited to give colloquiums and discuss my research on this topic in 12 different Institutions during 2020-2023. Additionally I have participated in the organization of the scientific workshop: "Self-interacting Dark Matter: Models, Simulations and Signals", at Pollica Physics Center (Italy, 15-30 June 2023).

Awards: I was awarded The John Hodgson Research grant (AU$3k, University of Melbourne) in 2015 for my novel theory of halo mass growth. In 2019 I was ranked in the top 10% of scientists in my field by the Dutch Research Council and was awarded the VENI grant (Eur$250k).

5.1.2 . The circumgalactic medium and galaxy gas accretion

The baryon cycle encompasses a series of intricate processes, such as gas accretion, star formation, chemical enrichment, and large scale outflows, all of which collectively determine the rate at which galaxies grow in mass. These processes interact across various scales: the interstellar medium (ISM), circumgalactic medium (CGM), and intergalactic medium (IGM), establishing a casual connection between them. A longstanding question revolves around understanding the cosmological inflow of gas from the IGM, through the CGM, and eventually into the ISM. In Correa et al. (2018a), I analysed this aspect and developed an analytical criterion to identify the conditions under which a corona of hot gas forms in the CGM. This criterion, applied to cosmological simulations, enabled the derivation of a dark matter halo mass threshold required for the formation of a hot halo (hot corona).

Expanding on this work, I investigated how the intricate interplay between gas cooling and heating from the IGM, and through the CGM, drives the total gas accretion rate onto the ISM (Correa et al. 2018b). This research was expanded to include an analysis of the environmental factors influencing galaxy gas accretion (van de Voort et al. 2017). Additionally, a thorough analysis was conducted on the physical properties of gas accretion, including spatial characteristics, density, temperature, and metallicity (Wright et al. 2021). Furthermore, my work inspired investigations into the impact of the gas accretion rate on the abundance of metals within galaxies (Collacchioni et al. 2020, 2021).

Conferences/Seminars: I was an invited speaker in a Circumgalactic meeting in Berlin, Germany, in September 2019 to talk about "Low-metallicity regions as indicators of recent gas inflow". I have also contributed to 5 international conferences during 2016 - 2019 and presented this research.

5.1.3 . Galaxy morphology

Another important scientific contribution is related to my studies of galaxy morphology. Through a series of publications (Correa et al. 2017; Trayford et al. 2019; Correa et al. 2019), I showed that the correlation between galaxy mass, intrinsic color, and morphology arises from galaxy-formation models that successfully reproduce the observed galaxy mass function and sizes. Interestingly, galaxies do not change their intrinsic colour simultaneously with changes in morphology (Correa et al. 2019).

Moreover, in Correa & Schaye (2020), I provided predictions indicating that at fixed halo mass, galaxies exhibiting a disc morphology tend to be more massive than spheroidal galaxies. This trend arises from their earlier formation and the hosting of less massive central black holes, which are not able to eject energy in

the form of jets, preventing surrounding gas to cool and form stars. These findings contribute valuable insights into the complex interplay among galaxy morphology, galaxy mass, and the influence of central black holes on shaping galaxy properties.

Conferences/Seminars: I was invited as a review speaker at the EAS annual meeting, symposium 'Crossing the characteristic mass scales in galaxy evolution', in Leiden, The Netherlands (2020), to discuss about my research on galaxy morphology. I participated in 3 international meetings & conferences on this topic and given talks during 2017-2020. I also organised the Stellar & Gas Kinematics in Galaxies Symposium at EAS and acted as chair of the meeting (Leiden 2020).

5.1.4 . Cosmological simulations of galaxy formation

Understanding how galaxies form and evolve over cosmic time stands as a fundamental question in modern astrophysics. However, cosmological time- and length-scales are so large that the evolution of individual galaxies cannot be directly observed. To study galaxy evolution, we need to model it. Yet, the key physical forces shaping galaxies —gravity, hydrodynamics, star formation, supernovae, and black holes—are highly nonlinear, posing challenges for semi-analytic models. Consequently, hydrodynamical cosmological simulations have emerged as the preferred tool for conducting controlled experiments on galaxy formation and evolution while accurately reproducing the large-scale structures of the visible universe.

As a postdoctoral researcher at Leiden University, I gained expertise in the analysis and development of the EAGLE cosmological simulation series (Schaye et al. 2015). Upon joining the University of Amsterdam as an NWO-VENI fellow, I took the initiative to lead a simulations project, TangoSIDM, aiming to unravel the self-interacting nature of dark matter (SIDM). This led to an important scientific contribution: the development of a novel implementation of SIDM (Correa et al. 2022) in the new open-source, fast and accurate hydrodynamics solver SWIFT (Schaller et al. (2023)).

The TangoSIDM simulations include the updated galaxy formation model from the EAGLE simulation series (Chapter 4). The simulations have shown that SIDM decreases the number of low-mass satellite galaxies around the Milky Way, it changes the shape of dark matter haloes, and it produces a diversity in the dark matter distribution within dwarf galaxies (Correa et al. 2022).

Awards: From my expertise on cosmological simulations, I have become a known figure within Europe's computational astrophysics groups. I have been awarded 5 million CPU hours by the PRACE (HPC European Network) and 1.5 million by the Surfara Network (Dutch National HPC). I have also been awarded the HPC-Europa3 Individual Research grant (120 thousand in core-CPU hours and €3k).

Conferences/Seminars: I participated in the organization of the workshop: "Towards unified sub-grid prescriptions for galaxy modelling", at Lorenz Center (Leiden, The Netherlands) during September 2023. Additionally, I contributed in the organization of the conference "Building Galaxies from Scratch: Advances and Challenges in Simulating Galaxy Evolution", during 19-23 February 2024 in Vienna.

5.2 . Student supervision experience

I have had the privilege over the last few years to serve as an advisor, mentor and co-supervisor to 11 students from diverse backgrounds. I list below the projects of the students, including supervision period, faculty co-supervisors and links to thesis and/or published articles as supporting evidence.

- 03/2021 - Present. Noemi Anau Montel. PhD Student, University of Amsterdam. Supervisor of her project, Signatures of self-interacting dark matter in local dwarf galaxies. Faculty co-supervisor: A/Prof. Christoph Weniger. I have been Noemi's daily supervisor for the TangoSIDM project. Noemi has contributed to the project (link to publication) and her leading author paper is currently in preparation. I have also guided Noemi in a parallel project of strong lensing (link to publication). Noemi's expected PhD graduation date: September 2024. I have guided Noemi throughout multiple applications for postdoctoral positions. Noemi will start as a MPA fellow at the Max Planck Institute for Astrophysics in Munich, in October.

- 09/2021 - 09/2023. Fabian Zimmer. PhD Student, University of Amsterdam. I co-supervised his project, Local Neutrino Clustering, with faculty supervisor, A/Prof. Shinichiro Ando. I have been Fabian's daily supervisor during the project which culminated in a publication [link]. Fabian's expected PhD graduation date: July 2025.

- 09/2022 - 03/2024. Leon Kamermans. Master Student, University of Amsterdam. I co-supervised Leon's project, Signatures of self-interacting dark matter in black hole binaries, with faculty supervisor, Prof. Gianfranco Bertone. Supporting evidence: link to master thesis. I have served as Leon's daily supervisor, including my transition period while moving institutions from the University of Amsterdam to CEA Paris-Saclay.

- 09/2021 - 09/2022. Athithya Aravinthan. Master Student, University of Amsterdam. I was the main supervisor of Athithya's master project. Thesis: Evolution of satellite galaxies under gravothermal core-collapse. Co-supervisor: A/Prof. Shinichiro Ando. Supporting evidence: link to master

thesis. Athithya is currently a PhD student in the Physics and Astronomy track at Ruhr-Universität Bochum, Germany.

- 09/2020 - 09/2021. Androniki Dimitriou. Master student, University of Amsterdam. Thesis: Reconstructing the halo spatial distribution and halo mass function using Neural Networks. Co-supervisor: A/Prof. Christoph Weniger. Supporting evidence: link to master thesis and link to publication. Androniki is a PhD student at the Instituto de Fisica Corpuscular, University of Valencia, Spain.

- 02/2019 - 06/2019. Florencia Collacchioni. PhD student from La Plata National University, Argentina. In 2019 I applied for funding to the LACEGAL network in order to invite Florencia for a three months internship at Leiden University in 2019. I supervised Florencia's project: Metallicity gradient as tracer of recent gas accretion, during this time.

- 09/2018 - 09/2019. Eva van Weenen. Master student, Leiden University in the joint program Astronomy-Data Science. Thesis: Machine learning with the EAGLE simulation. Co-supervisor: Prof. Joop Schaye. Supporting evidence: link to master thesis. After Leiden, Eva pursued a PhD degree at ETH Zurich. She is currently an AI Research Engineer at the Bosch Center for AI, Germany.

- 02/2019 - 09/2019. Julius Hendrix and Willem Kroese. Bachelor students, Leiden University. Joint-bachelor Thesis: Red sequence to Blue cloud galaxies in EAGLE. Co-supervisor: Prof. Joop Schaye. Supporting evidence: link to bachelor thesis. I had the opportunity to mentor Julius and Willem for their bachelor research project.

- 09/2017 - 09/2018. Malavika Vasist. Master student, Leiden University. Thesis: The impact of mergers on galaxy properties in the EAGLE simulations. Co-supervisor: Prof. Joop Schaye. Supporting evidence: link to master thesis. I have guided Malavika during her applications for PhD positions. Malavika is currently a PhD student at the University of Liege, Belgium.

- 09/2016 - 09/2017. Aswin Vijayan. Master student, Leiden University. Thesis: Analysing the impact of environment on the concentration of dark matter halos. Co-supervisor: Prof. Joop Schaye. Supporting evidence: link to master thesis. Aswin was my first student, and I have maintained contact with him as I supported him through his applications for PhD and subsequent postdoctoral positions. Aswin successfully obtained his PhD

from the University of Sussex, UK, and he is currently a Dawn Fellow at the Cosmic Dawn Center at DTU, Denmark.

In addition, I have participated in the Examination board of two PhD degrees:

- University of La Laguna (Spain). Member of the Doctoral committee to evaluate the PhD Thesis of Daniel Walo Martín in December 2022. Supporting evidence: link to Walo Martín PhD thesis, link to my examination report.

- Leiden University (The Netherlands). Member of the Doctoral committee to evaluate the PhD Thesis of Bart Clauwens in December 2017. Supporting evidence: link to Bart Clauwens PhD thesis, where in page 3 I am listed as "promotiecommissie" (examination board).

6 - Conclusions

This chapter summarizes the main findings presented in this thesis and discusses ideas for future work.

6.1 . Summary of the key findings and contributions presented in this thesis

When we investigate the nature of dark matter, we can start with basic questions. If dark matter is made of particles, do those particles have mass? Do they experience forces? SIDM tries to answer these questions.

At the time of writing there is evidence that motivates to look for SIDM in the realm of small-scales. Figure 6.1 illustrates three examples where recent astronomical observations disagree with the latest theoretical predictions that assume ΛCDM and include the impact of baryonic physics. On one side, there seems to be an excess of galaxy-galaxy gravitational lensing probability measured in the CLASH "gold" sample (top-left panel). The study of Meneghetti et al. (2022) computed strong lenses produced by dark matter substructures from galaxy clusters, and reported that the lensing probability exceeds by one order of magnitude current theoretical predictions. This finding was further supported by Ragagnin et al. (2022), who concluded that regardless of the adopted numerical resolution and feedback model, numerical simulations are unable to simultaneously reproduce the observed stellar masses and compactness (or high dark matter central densities) of galaxy clusters substructures able to produce such observed high strong lensing effect. The ability of dark matter to produce strong lensing depends primarily on its compactness and high densities, a feature that is unique to core collapse evolution. However, it's important to point out that there is still skepticism around the findings of Meneghetti et al. (2022) due to the fact that no other study has reproduced their results.

Other examples in Figure 6.1 include the low dark matter content in the central regions of ultra-diffuse dwarf galaxies (Mancera Piña et al. 2022; Kong et al. 2022),

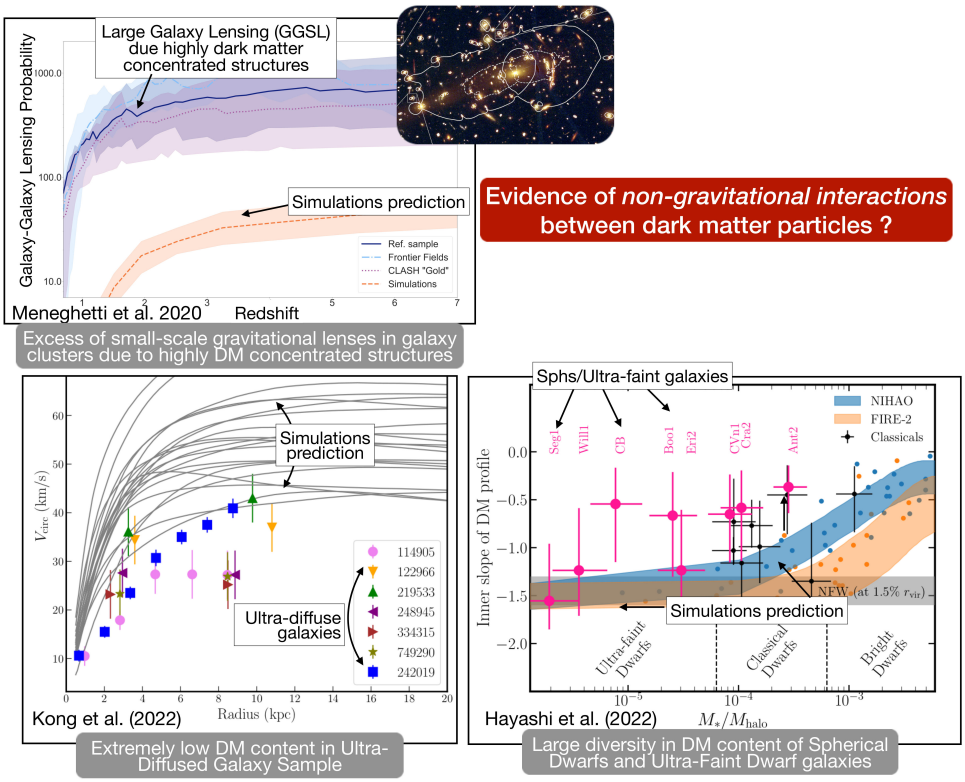

Figure 6.1: Examples where observations disagree with the latest theoretical predictions that assume the cold and collisionless dark matter paradigm and include the impact of baryonic physics. Top-left panel: the gravitational lensing measured in galaxy clusters is larger than expected, indicating that the dark matter distribution is much more concentrated in these clusters. Bottom-left panel: the rotational curves of ultra-diffuse dwarf galaxies are much lower than expected, suggesting that these galaxies contain less dark matter in their central regions. Bottom-right panel: not all the dark matter in the spheroidal and ultra-faint dwarf galaxies follows the steep density profile predicted by simulations, instead dark matter shows a diverse distribution.

as evidenced by their rotational curves (bottom-left panel). The formation of ultra-diffuse galaxies is still under debate, while SIDM could account for the low central dark matter content, other mechanisms, such as supernova explosions or environmental effects, also pose a viable explanation.

Finally, the bottom-right panel in Figure 6.1 shows that not all the dark matter in the spheroidal and ultra-faint dwarf galaxies follows the steep density profile predicted by simulations, instead dark matter shows a diverse distribution (Hayashi et al. 2022). This is one of the most challenging observations to-date that lack a convincing explanation within the CDM framework (Sales et al. 2022). Baryons are not expected to play a role in these systems, due to the fact that the spheroidal and ultra-faint satellite dwarf galaxies are mostly gas-poor.

Can SIDM explain these observations? If that's the case, how has it been proposed to explain them? Chapter 2 demonstrates that the satellite dwarf galaxies of the Milky Way can have very high or low central dark matter densities because of SIDM. The interactions among dark matter particles expel particles to further out orbits, over time dark matter expands and its density decreases. This can also explain the low dark matter content observed in ultra-diffuse dwarf galaxies. However, when dark matter particle interactions are extremely frequent (in the regime of $\sigma/m_\chi > 10$ cm^{2}g^{-1}), the interactions heat the central dark matter core, causing it to rapidly contract and rise in density as it enters in gravothermal core collapse (e.g. Balberg et al. 2002; Nishikawa et al. 2020). This could also account for the observed excess of gravitational lensing. Overly concentrated dark matter haloes undergoing core collapse might produce this excess lensing effect. Additionally, it could explain the variations in dark matter content among nearby dwarf galaxies. These variations arise as satellites are caught in haloes experiencing either core expansion or core collapse phases.

The study presented in Chapter 2 explored a new aspect of the σ/m_χ parameter space by examining the dwarf satellite galaxies orbiting the Milky Way. It proposed that dark matter behaves almost like it's not colliding at all on the scale of galaxy clusters (where σ/m_χ is less than 1 cm^{2}g^{-1}), but it acts more like a fluid that can collide on the scale of dwarf galaxies (with σ/m_χ potentially reaching as high as 100 cm^{2}g^{-1}). This result is supported by particle physics models of dark matter (e.g. Arkani-Hamed et al. 2009; Buckley & Fox 2010; Boddy et al. 2014b; Tulin & Yu 2018). According to these models, if dark matter particles (χ) interact, their interactions would be mediated by a lighter particle (ϕ). This setup naturally leads to cross sections that depend on the relative velocity of the dark matter particles. With the presence of this lighter particle, a new channel for dark matter annihilation opens up, allowing thermal freeze-out to occur through the process $\chi\chi \to \phi\phi$. This mechanism could explain the observed abundance of dark matter today, even with very small couplings between the mediator and Standard Model

particles. Furthermore, the results from Chapter 2 have been confirmed through numerical simulations (Correa et al. 2022; Yang et al. 2023).

Chapter 3 utilizes the TangoSIDM suite of cosmological simulations to investigate how constant and velocity-dependent self-interactions among dark matter particles affect the evolution and internal properties of satellite haloes around Milky Way-type hosts. Similar to Chapter 2, which was inspired by the observed relationship between central density and pericenter distance in classical dwarf spheroidal galaxies of the Milky Way, as measured by Gaia, this chapter examines inner densities, maximum dark matter halo masses, orbital pericenter distances, and correlations among these variables in simulated satellite haloes under different dark matter models. The study finds that while dark matter particle interactions minimally affect the orbital dynamics of satellites, the relation between orbital pericenter, inner density, and peak mass (or velocity) could serve as valuable probes for imposing rigorous observational constraints on CDM and SIDM models. Noemi Anau Montel focuses on comparing the CDM model and the velocity-dependent SIDM model, SigmaVel100, which reaches a momentum transfer cross-section of $100\ \mathrm{cm}^2/\mathrm{g}$ at $10\ \mathrm{km\,s}^{-1}$. She shows that to some extent, the observations favor the CDM model.

If we consider the pericenter distances measured by Battaglia et al. (2022), who accounted for the perturbation of the Milky Way potential by the Large Magellanic Cloud, the classical dwarfs do not show a correlation in the density-pericenter plane. Additionally, in the density-peak halo mass plane, classical dwarfs (excluding Fornax) do indicate a correlation: satellites with higher central densities were in higher mass haloes. Both of these results align with the predictions of the CDM model. However, the SigmaVel100 model suggests that in 30% of Milky Way-type systems, there is a strong anti-correlation in the density-pericenter plane, but no correlation in the density-peak halo mass plane. This scenario matches observations only if we consider pericenter distances calculated based on an isolated Milky Way potential and include Fornax in the analysis of the density-halo mass plane.

Nevertheless, there are reasons to consider the impact of the Large Magellanic Cloud on the Milky Way potential and to exclude Fornax from the analysis. Obsevations, such as the rotational velocity of the Large Magellanic Cloud (van der Marel & Kallivayalil 2014), perturbations of the Milky Way's disk (Laporte et al. 2018), and the dynamics of the ATLAS, Tucana III, Orphan and Sagittarius streams (Erkal et al. 2018, 2019; Vasiliev et al. 2021) indicate the Large Magellanic Cloud is massive, with a mass of $(1{-}2.5) \times 10^{11}\mathrm{M}_\odot$, and that it significantly perturbs the Milky Way's gravitational potential. Fornax has a stellar-to-total mass ratio of 2×10^{-3}, suggesting that the dark matter in its central regions has been likely dynamically heated by stellar feedback (Read et al. 2019).

The conclusions drawn in Chapter 3 have significant implications. They challenge the conclusions of the SIDM cross sections derived in Chapter 2 for the

classical dwarf galaxies. This challenge arises because the analysis heavily depends on how the orbits of these satellites are modeled. This shows the need for more research into the role of SIDM and how it interacts with the effects of baryons in dwarf galaxies. This will be further discussed in Section 6.2.

The exploration of the SIDM parameter space has made a lot of progress in the last few years. Until recently, SIDM was not considered a viable model that could explain the diversity of dark matter within dwarf galaxies, nor the gravitational lensing excess of galaxy clusters, which are shown in Fig. 6.1. This skepticism stemmed from a lack of astrophysical evidence supporting frequent interactions among dark matter (with $\sigma/m_\chi > 10$ cm^{2}g^{-1}) on the scales of dwarf galaxies. Recent studies (e.g., references 2 in Fig. 6.2) concluded that the high central dark matter densities observed in some dwarfs (e.g., Draco I) suggest that dark matter is weakly self-interacting (with $\sigma/m_\chi < 0.57$ cm^{2}g^{-1}). Yet, these findings couldn't account for the existence of dwarf galaxies with low dark matter densities. This changed after the findings of Chapter 2, where the concept of core expansion (seen in high central densities) and core collapse (seen in low central densities) was proposed as evolutionary stages of galaxies. These findings led to new constraints on σ/m_χ, as shown by the blue symbols in Fig. 6.2.

Fig. 6.2 presents a summary of the latest exploration of the SIDM parameter space. It shows the SIDM cross section as a function of dark matter velocity. Dark matter particles with velocities >1000 km/s reside in cluster-size galaxies (as it has been indicated in the top x-axis), whereas dark matter particles with low-velocities, <100 km/s, are in dwarf galaxies. The figure illustrates limits on the $\sigma/m_\chi < 1$ cm^{2}g^{-1} parameter region (orange arrow), that include the upper limits from galaxy clusters studies (references 4), and the constraints on the high central dark matter densities from dwarf galaxies (references 2). Notably, in the region corresponding to dwarf galaxies, there is a lower limit of $\sigma/m_\chi \geq 1$ cm^{2}g^{-1} (references 1), indicating the minimum cross section required for dwarf galaxies to have low central densities. Additionally, the figure highlights an upper limit on Milky Way mass-scales of $\sigma/m_\chi \leq 10$ cm^{2}g^{-1} (references 3), driven by the effects of excessive dark matter particle interactions on satellite galaxies.

Chapter 4 analyses the impact of baryonic physics in SIDM predictions, and paints a very different picture that drastically changes the SIDM parameter space. I show in this chapter that large σ/m_χ at the scale of Milky Way-mass galaxies lead to SIDM thermalization, causing dark matter to accumulate in the central regions. This accumulation results in density profiles steeper than those produced by CDM from adiabatic contraction. The enhanced dark matter density in the central regions of galaxies causes a significant deviation from observational data at the 95% significance level, prompting it to rule out some velocity-dependent SIDM models. This new exclusion zone proposed by Chapter 4 is shown in the purple

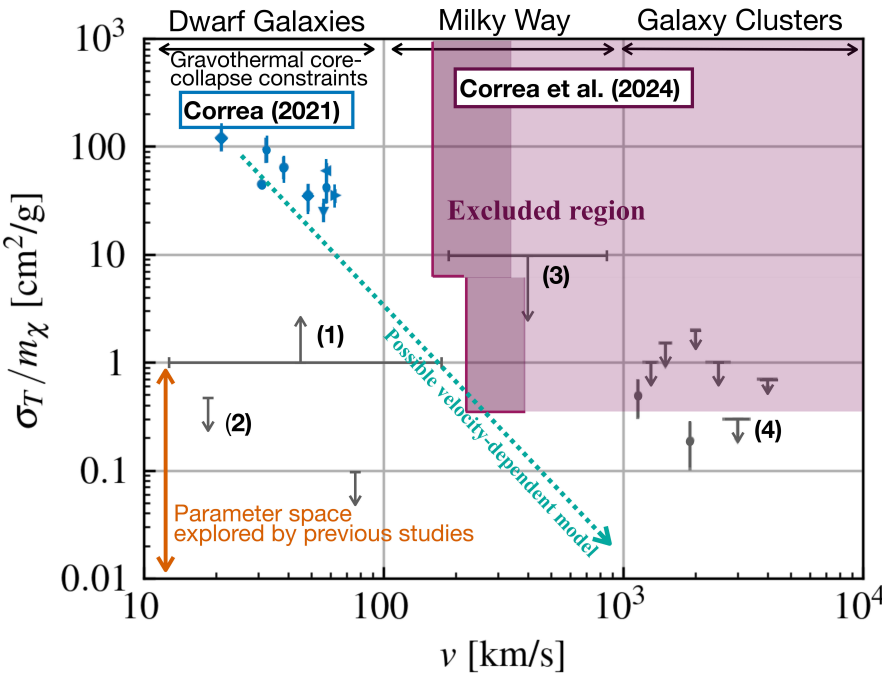

References:

(1): Constraints on DM cores measured in dwarf galaxies: Colin et al. (2002); Rocha et al. (2013); Zavala et al. (2013); Vogelsberger et al. (2019); Robles et al. (2019)

(2): Constraints on steep DM density profiles measured in dwarf galaxies: Kaplinghat et al. (2016); Read et al. (2018); Vally & Yu (2018); Hayashi et al. (2021); Ebisu et al. (2022)

(3): Constraints on number of satellites around the Milky Way: Vogelsberger et al. (2016); Nadler et al. (2019); **Correa (2023)**

(4): Galaxy clusters constraints: Randal et al. (2008); Peter et al. (2008); Dawson et al. (2013); Jee et al. (2014); Massey et al. (2015); Harvey et al. (2015); Wittmann et al. (2018); Sanguski et al. (2021); Andrade et al. (2022)

Figure 6.2: SIDM cross section as a function of dark matter velocity. High-velocity dark matter particles reside in cluster-size galaxies, whereas low-velocity particles are in dwarf galaxies. The figure highlights the most recent constraints on the SIDM parameter space, where measurements of the cross section for the dwarf classical satellites are highlighted (blue symbols, Chapter 2), along with the recent constrains from Milky Way-size galaxies (purple regions, Chapter 4). Additional constraints are shown in (1-4) with the respective references shown below the figure.

region in Fig. 6.2.

While the findings of Chapter 4 impose strong constraints on velocity-dependent models, it does not entirely rule them out. We could argue that SIDM models derived in Chapter 2, with a cross section reaching 100 cm^2g^{-1} at 10 km s^{-1}, and decreasing to less than 1 cm^2g^{-1} at 150 km s^{-1}, are still allowed and motivated by observations of dwarf galaxies and dark haloes (Fig. 6.1). However, Chapter 3 challenges the derivations of Chapter 2.

Throughout my investigation into SIDM, I've maintained an open-minded approach, striving to comprehend every aspect of both observational and simulated data. As such, I believe that analyzing the SIDM parameter space within dwarf galaxies will be crucial for advancing our understanding of the self-interacting nature of dark matter in the years ahead.

"Believe in the primacy of doubt, not as a blemish upon our ability to know but as the essence of knowing. The alternative to uncertainty is authority, against which science has fought for centuries." —Richard Feynman.

6.2 . Future prospects and directions for further research

We are entering a new era of "Cosmic Vision". In the coming years, the Rubin Observatory, Euclid, the Roman Telescope, and ARRAKIHS, will provide us with images and spectra for millions of galaxies at intermediate and low redshifts. This data will be crucial for answering one of the most pressing questions of our time: *what is the nature of Dark Matter?* However, to advance in this field, there is an urgent necessity for state-of-the-art theoretical models to complement and interpret the coming observational data. For this reason, I plan to launch an interdisciplinary scientific program over the next few years, bringing together computer science, astrophysics, and particle physics. I'll focus on three main areas: (1) developing advanced theoretical models, (2) applying inference techniques from simulated data to real observations, and (3) making predictions for upcoming surveys.

In the following subsections I provide more details on my future directions.

6.2.1 . Simulations program

I plan to produce a new series of high-resolution hydrodynamic simulations of galaxies, covering various ranges of dark matter parameter space and sub-grid model parameters. To achieve this, I'll develop a new series of zoom-in simulations, integrating the latest improvements in the galaxy formation model from the EAGLE simulation series (Correa & Schaye 2020; Schaye et al. 2015), and the SIDM physics model of the TangoSIDM simulations (Correa et al. 2022, 2024). This step will be

	Dwarf galaxies	Milky Way-mass galaxies
	20-30 galaxies	1-3 galaxies
Stellar masses:	$10^6 - 10^9 M_\odot$	$10^{10} M_\odot$
Particle mass resolution:	1000 $M_\odot$	7000 $M_\odot$
Gravitational softening:	100 pc	400 pc
Lagrangian volume:	5 R_{vir}	5 R_{vir}
Expected CPU time:	10,000 hours/galaxy	1 million hours/galaxy

Table 6.1: Planned simulation set.

key to exploring the interplay between dark matter physics and baryonic physics, facilitating the interpretation, prediction, and identification of SIDM features in observational data.

This project will necessitate the completion of the following tasks:

Model calibration. This task involves generating zoom-in simulations with enhanced resolution of specific regions around galaxies of interest from the parent cosmological boxes from Correa et al. (2024). Given that the efficacy of subgrid model parameters governing supernovae and active galactic nucleus (AGN) feedback is resolution dependent, our initial focus is on determining optimal models' parameters for baryonic physics. These parameters should result in galaxies with comparable masses and sizes to those modelled in the parent cosmological simulation. Additionally, efforts will be directed towards delineating subgrid parameter ranges that lead to galaxies with bursty/smooth star formation and/or weak/strong stellar feedback.

Initial conditions. The current TangoSIDM cosmological boxes were produced from initial conditions that do not include a cut-off in the power spectrum. This work will expand upon my previous efforts by producing WDM and SIDM initial conditions. I plan to use the monofonIC code (Hahn et al. 2020) to generate a cut-off in the primordial power spectrum as a function of warm dark matter mass. I will also update monofonIC by incorporating dark acoustic oscillations in the power spectrum (e.g. Cyr-Racine et al. 2016).

Production of zoom-in boxes. Using the zoom-in technique in the SWIFT code (Schaller et al. 2023), a sample of dwarf galaxies will be resimulated with high resolution (see Table 6.1 for details).

Innovative aspects

Code development. I currently lead the TangoSIDM simulation team. We have developed a novel implementation of SIDM (Correa et al. 2022) in the new code SWIFT (Schaller et al. 2023). SWIFT is an open-source, fast and accurate hydrodynamics solver that was specifically designed to be efficient on many

core systems with several levels of parallelisation including vectorisation. It uses state-of-the-art algorithms to solve the equations of hydrodynamics and a more accurate gravity solver. SWIFT has proven to be an order of magnitude faster than the code Gadget used for the EAGLE simulations (Schaller et al. 2018). The galaxy modelling from the EAGLE simulation project (Schaye et al. 2015) has been successfully implemented in SWIFT.

New dark matter physics modules. The TangoSIDM simulations stand out in the field because of the novel implementation of interactions between dark matter particles, that have been modelled as elastic and anisotropic collisions following a new stochastic, SPH-inspired approach (see Correa et al. 2022). Different from previous studies (e.g. Robertson et al. 2019), the search radius, which encloses a region where a dark matter particle has the probability of interacting with its neighbours, is not constant, instead it is adjusted according to the local density, allowing to better track the centre of objects.

For the non-gravitational dark matter interactions, I assume that the scattering potential follows the Yukawa potential (Ibe & Yu 2010), that produces an azimuthally-symmetric differential cross section. The resulting σ/m_χ depends on the dark matter particles velocity, the dark matter particle mass, m_χ, the mediator mass, m_ϕ, of the interaction, and the coupling strength α. These parameters can be adjusted so that the rate of scattering is important in dark matter haloes of particular mass while being negligible in more massive haloes.

Updated galaxy formation module. The EAGLE galaxy formation module implemented in TangoSIDM (Correa et al. 2024) contains several updates regarding the smoothed particle hydrodynamics scheme, that deals with the gas evolution and conduction across shocks, preventing spurious radiative losses in feedback events (Borrow et al. 2022), gas cooling tables (Ploeckinger & Schaye 2020), supernovae feedback (Chaikin et al. 2022), and parameter calibration strategy (Kugel & Borrow 2022). For more details, see Chapter 4.

Expected results and impact

The new series of zoom-in simulations will provide detailed and statistical descriptions of the dark matter haloes internal structure (expansion phase and gravothermal collapse evolution), and mass distribution (impact on stellar orbits, dynamical heating, HI gas rotational maps). This unique information will allow the exploration of novel physical phenomena emerging from the stellar and gas kinematics in dwarf galaxies, and from the satellites population Milky Way-mass and cluster-size systems. The resultant data product will serve as a foundation resource for interpreting forthcoming observations from instruments such as Euclid, the Rubin Observatory, the Roman telescope, and ARRAKIHS.

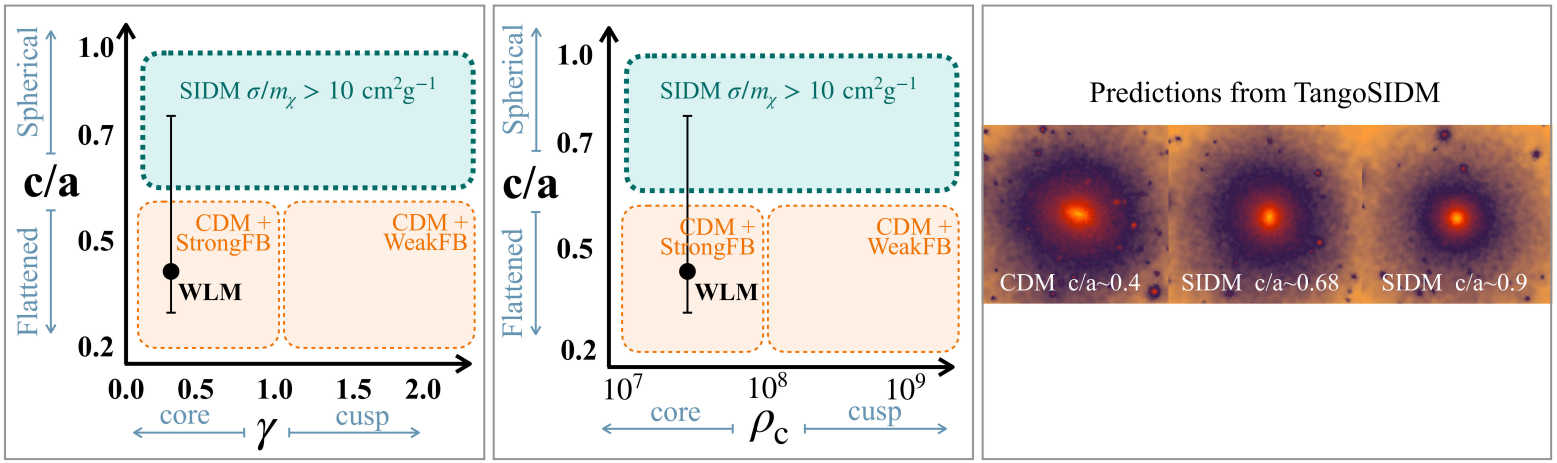

Figure 6.3: Left panel: Dark matter axis ratio, c/a, as a function of the dark matter inner density slope, γ. The shaded regions mark the predictions for the SIDM paradigm (green area) and CDM + weak/strong stellar feedback (orange regions). The black symbol corresponds to the determination from Leung et al. (2021). Middle panel: same as left panel but showing the dark matter axis ratio, c/a, as a function of the dark matter central density, ρ_c. Right panel: Projected dark matter density from a central halo. The images correspond to the same halo under CDM (left), SIDM velocity-dependent (middle) and SIDM constant (right).

6.2.2 . Gas & stellar kinematics in dwarf galaxies

The determination of the dark matter distribution within low-mass dwarf galaxies poses a significant challenge. Observations in this domain reveal diverse dark matter distributions (Oman et al. 2015), ranging from gas-rich dwarf galaxies exhibiting steeply rising rotational curves (indicative of being dark matter-dominated in their central regions), to dwarf galaxies having slowly rising rotational curves (suggesting a deficit in the amount of mass in their inner regions). Over the past decade, this diversity has been attributed to baryonic processes, wherein fluctuations in the gravitational potential driven by gas dynamics (e.g. inflows/outflows due to cooling, stellar winds and supernovae) influence the central dark matter densities (e.g. Pontzen & Governato 2012; Teyssier et al. 2013; Oñorbe et al. 2015; Dutton et al. 2016). Specifically, under CDM, galaxies with strong stellar feedback exhibit "cored" dark matter density profiles, meaning a low dark matter central density, ρ_c, and a nearly zero inner dark matter density slope, $\gamma \rightarrow 0$. On the other hand, galaxies with weak stellar feedback display "cuspy" dark matter profiles, characterized by large ρ_c, and $\gamma \rightarrow 1$. Under SIDM, the diversity in the dark matter distribution within dwarfs can be explained without invoking baryonic physics (the diversity corresponds to stages of expansion or collapse of dark matter).

The fact that the diversity in dark matter central densities also extends to gas-poor satellite dwarf galaxies (e.g. Read et al. 2019; Charles et al. 2022; Borukhovetskaya et al. 2022; Hayashi et al. 2022), where observations reveal both low central densities (such as in Fornax, Andromeda XXV, Eridanus II, Crater II, Antlia II, among other dwarf galaxies) and high-densities cases (such as in Draco, Wilman I, among several ultra-faint and classical spheroidal galaxies), challenges the explanatory power of the CDM + baryons model, thus motivating the consideration of the SIDM hypothesis. However, alternative explanations, including inaccuracies in distance and inclination measurements (e.g. Oman et al. 2015; Read et al. 2016), observational errors in kinematic data (Roper et al. 2023), or tidal interactions removing dark matter from central regions (e.g. Genina et al. 2022), support the CDM scenario. Therefore, the crucial question arises: *how can we break the degeneracy of CDM + baryons vs. SIDM, and differentiate between both scenarios?*

Proposal

This project proposes a solution based on a recent study by Leung et al. (2021), where the authors analysed the isolated dwarf galaxy WLM and demonstrated that by combining measurements from the HI gas rotation curve with solutions from the Jeans' equations based on the stellar kinematic, they could simultaneously

determine key parameters of the 3-D dark matter distribution, including the inner density slope (γ), the axis ratio (c/a), and the stellar orbital anisotropy. My preliminary analysis indicates that these parameters, along with the dark matter central density (ρ_c), can break the degeneracy between CDM + baryons and SIDM, and prove, or ultimately rule out, SIDM at the small scales.

The main objective is: to analyse the gas and stellar kinematics of a sample of gas-rich dwarf galaxies, determine their ρ_c, γ, and c/a, and utilize this parameter distribution to constrain SIDM. A key deliverable of this project will be the derivation of robust constraints of SIDM, while accounting for both baryonic physics and SIDM velocity-dependent model parameters.

Description

The left and middle panels of Fig. 6.3 show c/a as a function of γ, and ρ_c, respectively. In these panels, regions with $c/a < 0.6$ (representing elliptical haloes) and large ρ_c with $\gamma \to 1$ (indicating cuspy profiles) correspond to the scenario of CDM + weak stellar feedback. Similarly, regions with $c/a < 0.6$ and low ρ_c with $\gamma \to 0$ (representing cored profiles) correspond to the scenario of CDM + strong stellar feedback. The determination of ρ_c, γ, and c/a for WLM is indicated by the black symbol (Leung et al. 2021; Read et al. 2019). Although the study of Leung et al. (2021) suggests that WLM challenges SIDM, various aspects need to be revisited. My preliminary analysis indicates that if $\sigma/m_\chi > 10$ cm^{2}g^{-1} for dwarf galaxies, then $c/a > 0.7$ (representing spherical haloes), and ρ_c and γ will exhibit significant scatter, regardless of stellar feedback strength. To further illustrate this point, the right panel of Fig. 6.3 shows a qualitative description of the same halo's shape under CDM, and two SIDM models. I find that while a SIDM model with a constant cross section yields the same axis ratio regardless of radius, velocity-dependent SIDM models show that the axis ratio varies with radial distance. Haloes at low radii tend to have spherical shape ($c/a > 0.7$), transitioning to an ellipsoidal shape ($c/a < 0.5$) at large radii due to infrequent particles interactions in low-density regions. The plan for this project is to include additional data points in the left and middle panels of Fig. 6.3. I also intend to account for baryonic physics and SIDM velocity-dependent model parameters for each individual galaxies, and ultimately present a robust derivation from the entire sample.

Expected results and impact

The data point for WLM in Fig. 6.3 indicates that the most probably explanation for the 3-D dark matter distribution in this dwarf is CDM + Strong feedback. For this project I anticipate confirming this result. Firstly, the recent work of McQuinn et al. (2024), shows that 50% of WM's stellar mass was formed during the last 5 Gyrs, thus prompting for a large number of supernovae explosions. Secondly,

the axial ratio determination from Leung et al. (2021) is derived from the central regions of the halo, where any presence of SIDM should have led to isotropization of the halo. This strongly suggests the exclusion of SIDM at small scales, which combined with the recent constrains presented in Chapter 4 (Fig. 6.2), it would imply that dark matter is not self-interacting. However, it's important to note that ruling out an entire paradigm based on a single galaxy is premature. A robust sample and extensive theoretical study are required to definitively ascertain the validity of SIDM. Such a finding would carry significant implications across various fields, from theoretical astrophysics to particle physics.

6.2.3 . Satellite luminosity function

Motivation

If dark matter is warm and/or self-interacting, it could greatly suppress the number of faint low-mass galaxies and delay structure formation. Consequently, the clustering of galaxies over cosmic time, as well as the galaxies' properties, will change relative to CDM predictions. With forthcoming observations from missions like Euclid, alongside future instruments such as the Rubin Observatory, the Roman telescope, and the ARRAKIHS satellite, the main goal of this project is to develop robust predictions that would lead to stringent constraints on the nature of dark matter.

Of particular interest to this project are low-mass, faint satellite dwarf galaxies. In previous studies (Dekker et al. 2022; Anau Montel et al. 2023), with students from the University of Amsterdan, we have demonstrated that the number of low-mass satellites around the Milky Way is suppressed if the dark matter particle has a mass lower than 3 keV (see Fig. 6.4, left panel). Should Euclid fail to observe very ultra-faint dwarf galaxies, despite them being within the range of detectability, it would imply the presence of a physical mechanism inhibiting their formation. One explanation is that warm and/or self-interacting dark matter prevented the formation of the dark matter haloes needed to host these galaxies. Another possibility, studied extensively in recent years, is the influence of baryonic physics. Processes like reionization, stellar feedback, and the warm intergalactic medium, can heat the cold star forming gas, thereby preventing the formation of these very low-mass galaxies. The question is then, *how can we differentiate between these two scenarios?*

Proposal

A recent study (Nadler et al. 2024) has shown that even if we were able to observe the complete satellite population of several Milky Way-mass systems, it would not be possible to distinguish the effects of dark matter physics and baryonic

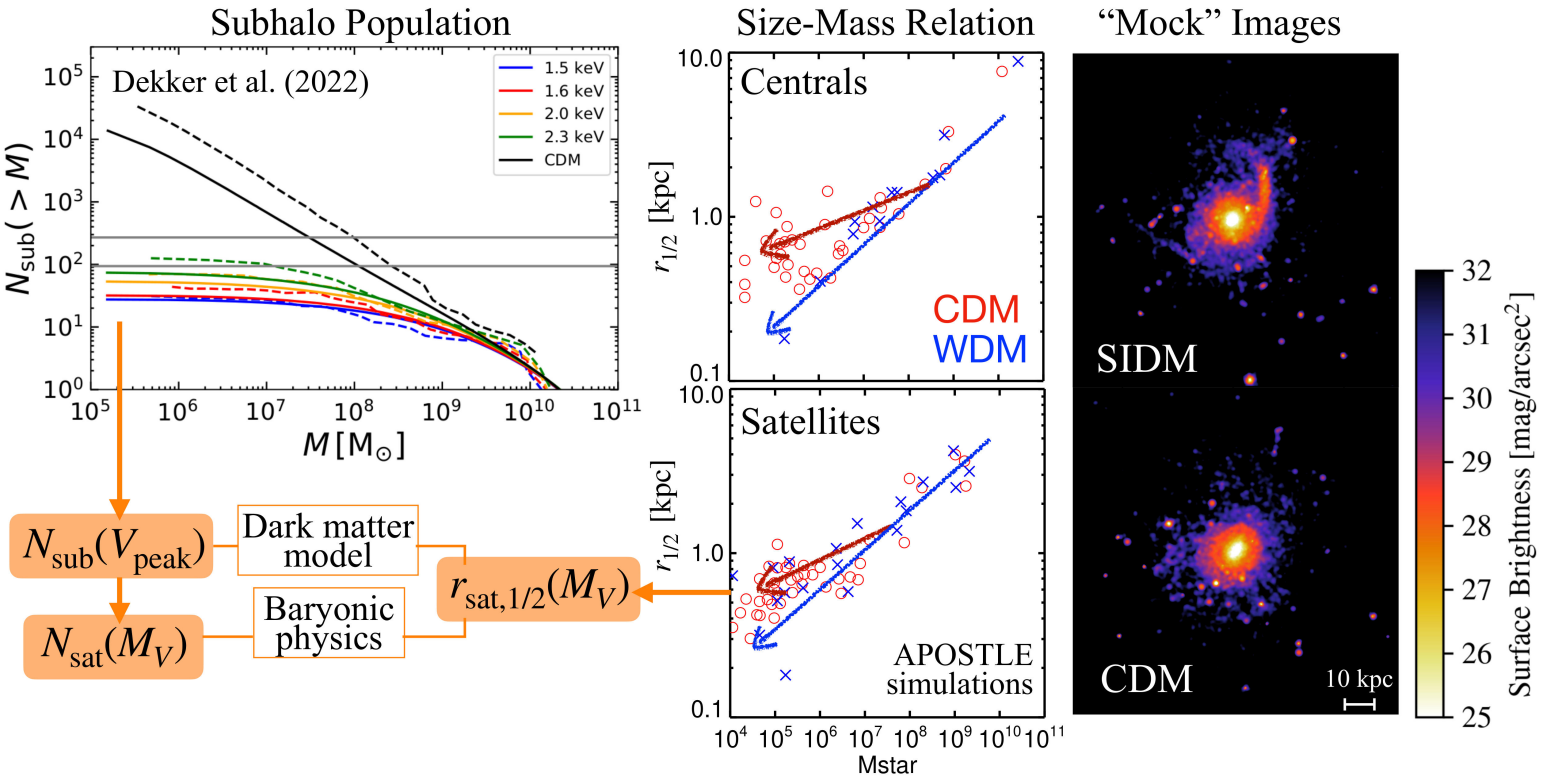

Figure 6.4: Left panel, example of a subhalo population distribution around a Milky Way-mass galaxy. This distribution was produced analytically from the Press-Schechter formalism (see Dekker et al. 2022). Middle panel: Stellar mass-size relation taken from the Apostle simulations (Sawala et al. 2016, courtesy Dr. Fattahi). The figure shows that while galaxies lower than 10^7 $M_\odot$ prefer sizes of the order of 700 pc, this is not the case of galaxies under WDM that tend to have smaller sizes. Right panel: Mock observations of the same Milky Way-mass galaxy taken from the TangoSIDM cosmological boxes.

physics on the satellites number counts. This demonstrates the necessity for further investigation to disentangle the influence of baryons versus dark matter. In this context, this project proposes that examining the luminosity-size relation of satellite galaxies holds the key to break this degeneracy.

As of now, only one simulation has successfully replicated the luminosity-size relation of the ultra-faint dwarf satellites galaxies of the Milky Way and the Large Magellanic Cloud, as recently highlighted by Richstein et al. (2024) and Revaz (2023). Other simulations, despite possessing competitive numerical resolution, have simulated ultra-faint analogs that are 2-3 times larger in size. This disparity could be due to a number of reasons: potential overestimation of stellar feedback hindering early and compact formation of these systems, or numerical effects such as spurious heating from modelling of dark matter and stars as collisionless particles, resulting in more extended galaxies (Ludlow et al. 2023). Another avenue explored in this project pertains to the nature of dark matter.

The work of Revaz (2023) recently showed that only ultra-faint dwarfs experiencing minimal perturbations from other satellites or dark matter substructures managed to maintain their compact sizes of 30 pc. Conversely, those subjected to significant dynamical interactions have exhibited growth in size. This suggests that if dark matter is warm, a reduced number of low-mass satellite galaxies and the absence of dark substructures could enable the persistence of compact sizes for ultra-faint dwarfs (middle panel Fig. 6.4). On other hand, if dark matter is self-interacting, ultra-faint dwarfs would form more extended than in CDM, due to dynamical heating from interactions between dark matter particles (4). Galaxy sizes, therefore, pose as a powerful constraint for the nature of dark matter.

The objective of this project is then to do a combined analysis of the luminosity function and luminosity-size relation of Milky Way satellite galaxies, with the goal of demonstrating that leveraging both of these observables can break the baryons/dark matter degeneracy.

I will develop a model for the population of satellite galaxies. I will begin by generating a population of dark matter subhaloes around a Milly Way-mass galaxy (e.g. left panel Fig. 6.4), based on the dark matter mass (M_{WDM}). I will associate satellite galaxies to the subhaloes using an extrapolated abundance matching relation (e.g. Loveday et al. 2015). Subsequently, from each subhalo's peak maximum circular velocity, I will predict the satellite's absolute V-band magnitude, M_V, while incorporating a certain degree of scatter in the derivation of the absolute magnitude. To determine the satellites' surface brightness, I will model their projected half-light radii, $r_{1/2}$, by assuming a luminosity-size relation, $r_{1/2} = AM_V^n$, wherein the parameters A and n will be functions of the dark matter model and feedback strength. Lastly, I will model the fraction, $f_{\rm gal}$, of subhaloes that host satellite galaxies as a function of the peak subhalo mass by following

Nadler et al. (2024),

$$f_{\rm gal}(M_{\rm peak}) = \frac{1}{2}\left[1 + {\rm erf}\left(\frac{\log_{10}(M_{\rm peak}/M_{50})}{\sqrt{2}S_{\rm gal}}\right)\right],$$

where M_{50} and $S_{\rm gal}$ are parameters that depend on feedback strength.

To calibrate the model parameters $\theta = (A, n, M_{50}, S_{\rm gal}, M_{WDM})$, I will use the zoom-in simulations of Milky Way-mass galaxies (Table 6.1), generated under CDM, WDM and SIDM, as well as variations in sub-grid feedback prescriptions. The goal is to establish informed priors for each scenario (dark matter vs baryonic physics), draw from their respective distributions, and generate numerous realizations of the satellite luminosity function and luminosity-size relation. I will create "mock" observational data from the simulations (see right panel Fig. 6.4), representing satellite luminosity functions and luminosity-size relations akin to real observations. Subsequently, I will conduct a validation analysis by determining the most likely model realization for each scenario (CDM, WDM and SIDM) based on the mock simulated data.

As a final step, I will apply the model to real observational data: the Milky Way satellite population as detected by the Dark Energy Survey (Abbott et al. 2018) and Pan-STARRS1 (Chambers et al. 2016), along with the luminosity-size relation recently compiled in Richstein et al. (2024).

The goal of this project is to develop a robust methodology that will facilitate the exploitation of the next-generation of surveys targeting faint satellite galaxies, enabling to constrain the parameter space governing galaxy formation and dark matter physics.

6.2.4 . Stellar streams

Another avenue of exploration in this working package involves the observation of stellar streams. These streams are formed through the tidal disruption of stellar clusters or dwarf galaxies by the gravitational potential of the Milky Way, exhibiting a relatively uniform stellar density along their length. However, gravitational perturbations caused by the passing of dark matter substructures can disrupt the stream, creating regions of low stellar density or gaps, whose size increases with time. A key prediction of CDM is that a large number of dark matter substructures should exist in Milky Way-like galaxies, thus resulting in observable perturbations and gaps in the density distribution of observed stellar streams (Banik et al. 2018). If dark matter is warm, the prevalence of dark substructures would be diminished, reducing the presence of perturbations in nearby stellar streams. Conversely, if dark matter is self-interacting, my preliminary analysis suggests that the frequent number of collisions between the dark matter particles would further perturb the

streams, making them quite extended (see e.g. right panel in Fig. 6.4).

6.3 . Reflection on the author's academic journey

I was born in Concepción del Uruguay, a city on the border of Argentina and Uruguay, to a 23 year old girl who was studying to become a school teacher. Despite humble beginnings, I was fortunate. Thanks to my mother's encouragement, I played lots of sports, I studied mathematics, English, even chess, read a lot of books, and watched Carl Sagan's Cosmos series a thousand times. Eventually, I chose astrophysics as my career path. During my time at university, I thrived. It deepened my passion for the subject, and I formed strong friendships that supported me throughout my studies. As a PhD student, my supervisor's relaxed approach allowed me to choose research projects I was passionate about, and he always encouraged me to explore my own ideas further.

The years between 2016 and 2019 were pivotal in my academic journey as I did my first postdoctoral position at Leiden University. I joined a diverse group of 58 postdocs from around the globe, all with the shared goal of pursuing careers in academia. During this time, I gained a deep understanding of the competitive nature of the field, and I received extensive training. I participated in workshops on grant proposal writing. I dedicated time each week to thoroughly studying two papers and presenting them during journal clubs, which sharpened my critical thinking and debating skills. In Leiden, I also acquired valuable expertise in designing research projects, setting clear goals, and maintaining a focused direction in my research endeavors.

At Leiden, I had the opportunity to supervise master's students, guiding them through projects of my own design. This experience was crucial for my growth as a researcher, teaching me project management and how to provide effective guidance in research and academia.

A significant milestone in my career was receiving the VENI grant, I was chosen from 1400 applicants. This grant gave me scientific independence and allowed me to test my ability to conduct a research project fueled by my own design, curiosity, and determination. This thesis serves as evidence of my success.

While my research interests have broadened over time, they have remained focused on dark matter haloes, galaxy formation, and cosmology since my PhD. At Leiden, I gained expertise in numerical simulations. As a VENI fellow in Amsterdam, I integrated these areas into the TangoSIDM project, connecting dark matter, galaxy formation, and cosmological simulations.

I believe the future in research is interdisciplinary and global. My career goals revolve around becoming an internationally recognized expert in a new field that merges astrophysics, particle physics, and computer science. Ultimately, I aspire to

lead advancements in dark matter detection through cross-disciplinary approaches.

Achieving a deeper understanding of dark matter in the next decade will require overcoming various challenges beyond traditional astrophysics studies. This includes delving into particle theories and experiments, as well as mastering evolving techniques such as numerical simulations of galaxy formation and artificial intelligence-based statistical inference.

Rather than solely relying on particle detection programs to unravel the mysteries of dark matter, I advocate for synergy among scientific fields. By fostering collaboration across disciplines, we can accelerate the progress and unlock new insights into the nature of dark matter.

In closing, I want to acknowledge that I've been fortunate not to encounter significant challenges in my academic journey. I owe much of this to the unwavering support of my mentors, specially to my postdoctoral advisor at Leiden, who went above and beyond to provide the feedback I needed. Also thanks to the support of my husband, whom I met in 2016 and to whom this thesis is dedicated.

Additionally, I want to remark that maintaining a healthy work-life balance has been key. Beyond my academic pursuits, I have personal goals, such as gaining the necessary experience as skipper of a sailing vessel to obtain a coastal skipper license and sail from Amsterdam to Buenos Aires![1] I also aspire to complete a 24-hour running race, among other ultrarunning endurance challenges[2].

As I embark on the next chapter of my life, I carry with me the lessons, friendships, and cherished memories from my time as a postdoctoral researcher. As I write these lines I feel a deep sense of growth and gratitude for the transformative journey I've experienced.

[1] I currently hold the day skipper license, and roughly 7 years of sailing experience.

[2] My current best performance is the completion of a 100 km race, finished in third place!, in Belgium in 2022.

A - Appendix: Chapter 2

A.1 . Gravothermal collapse model: Further details

In this Appendix we provide additional details on the numerical implementation for solving the gravothermal collapse model introduced in Section 2.2.1.

We begin by defining a new set of dimensionless variables based on the mass and length scales, $M_0 = 4\pi r_s^3 \rho_s$ and $R_0 = r_s$, where ρ_s and r_s are the scale density and radius, respectively, of the initial NFW profile. These quantities lead to consistent normalization scales for the other variables: $\rho_0 = \rho s$, $v_0^2 = GM_0/R_0$ (with G gravitational constant), $\sigma_0 = 4\pi R_0^2 M_0^{-1}$, $L_0 = GM_0^2/(t_0 R_0)$ and $t_0^{-1} = a\sigma_m v_0 \rho_0$.

Nondimensionless variables result $\tilde{r} = r/R_0$, $\tilde{m} = m/M_0$, $\tilde{v} = v/v_0$, $\tilde{L} = L/L_0$, $\tilde{\sigma}_m = \sigma_m/\sigma_0$ and $\tilde{t} = t/t_0$, which are then used to rewrite eqs. (2.1-2.5) in a dimensionless form

$$\frac{\partial \tilde{m}}{\partial \tilde{r}} = \tilde{r}^2 \tilde{\rho}, \tag{A.1}$$

$$\frac{\partial(\tilde{\rho}\tilde{v}^2)}{\partial \tilde{r}} = -\frac{\tilde{m}\tilde{\rho}}{\tilde{r}}, \tag{A.2}$$

$$\tilde{L} = -\frac{3}{2}\tilde{r}^2 \tilde{v} \left(\frac{a}{b}\tilde{\sigma}_m^2 + \frac{1}{C\tilde{\rho}\tilde{v}^2} \right)^{-1} \frac{\partial \tilde{v}^2}{\partial \tilde{r}}, \tag{A.3}$$

$$\frac{\partial \tilde{L}}{\partial \tilde{r}} = -\tilde{r}^2 \tilde{\rho}\tilde{v}^2 \left(\frac{\partial}{\partial \tilde{t}} \right)_m \log\left(\frac{\tilde{v}^3}{\tilde{\rho}} \right). \tag{A.4}$$

The initial density profile is used to calculate $\tilde{m}$ and $\tilde{v}$ through eqs. (A.1-A.2). Those, along with the cross section, are used to calculate $\tilde{L}$ from eq. (A.3). We allow a small passage of time $\Delta\tilde{t}$ (given by eq. 2.11) and compute the new density $\tilde{\rho}$ that solves eq. (A.4). After this we go back to solving eqs (A.1-A.3).

A.2 . Gravitational tidal stripping model: Model validation

Section 2.2.3 introduces the gravitational tidal stripping modeling applied in this work. An important aspect of the model is the application of the transfer function $H(r, t, f_b, c_{200}) = \rho(r)/\rho(r, t = 0)$ derived by Green & van den Bosch (2019) to non-NFW like haloes. In this Appendix we show that applying the transfer function to cored-shape density profiles is a good approximation by comparing the evolution of the profile with that predicted by the tidal heating model.

Tidal heating refers to adiabatic heating produced from rapid gravitational encounters between the satellite and the parent halo that can change the density

profile of the satellite. We follow the formalism of the energy rate deposited by a gravitational encounter of Pullen et al. (2014), Taylor & Babul (2001) and Gnedin et al. (1999), which states that the energy transfered to the subhalo though tidal heating is

$$\Delta E(r) = \frac{1}{2}\left[\int_0^t \bar{F}_{\rm tid}\mathrm{d}t\right]^2, \tag{A.5}$$

$$= \frac{1}{2}\left[\int_0^t \frac{GM_0}{R^3}[(3\mu-\hat{u})(\bar{n}\cdot\bar{r})\bar{n}-\mu\bar{r}]\mathrm{d}t\right]^2, \tag{A.6}$$

where $\bar{F}_{\rm tid}$ is the tidal force per unit mass, M_0 is the MW mass, R the distance to the MW center, $\mu(R) = M(<R)/M_0$ the normalized profile, $\hat{u} = \mathrm{d}\mu(R)/\mathrm{d}\ln R$, $\bar{n} = \bar{R}/R$ the direction to the center of the satellite and $\bar{r}$ the radius-vector in the subhalo.

Assuming mass conservation and no shell crossings allows to track the expansion of a subhalo mass element with heating as follows

$$\frac{1}{r_f} = \frac{1}{r_i} - \frac{2\Delta E(r_i)}{Gm(<r_i)}, \tag{A.7}$$

$$\rho(r_f,t_n) = \left[1-\frac{2r_i\Delta E(r_i)}{Gm(<r_i)}\right]^4\left[1+\frac{4r_i\Delta E(r_i)}{Gm(<r_i)} - \frac{8\pi r_i^4\Delta E(r_i)}{Gm(<r_i)^2}\rho(r_i,t_{n-1})\right]^{-1}\rho(r_i,t_{n-1}), \tag{A.8}$$

where r_f is the radius of the shell at time step t_n, r_i is the radius of the shell at the previous time step t_{n-1}, $m(<r_i)$ is the subhalo's mass enclosed within r_i. See Pullen et al. (2014) for further details.

Fig. A.1 compares the evolution of a subhalo with an initial cored profile following the Green & van den Bosch (2019) transfer function (see Section 2.3 for more details) and the tidal heating model (eqs. A.7-A.8). The figure shows that the transfer function (applied to a cored profile, green line) is in good agreement with the tidal heating model (dashed red line), and both density profiles are mostly altered in the outer regions.

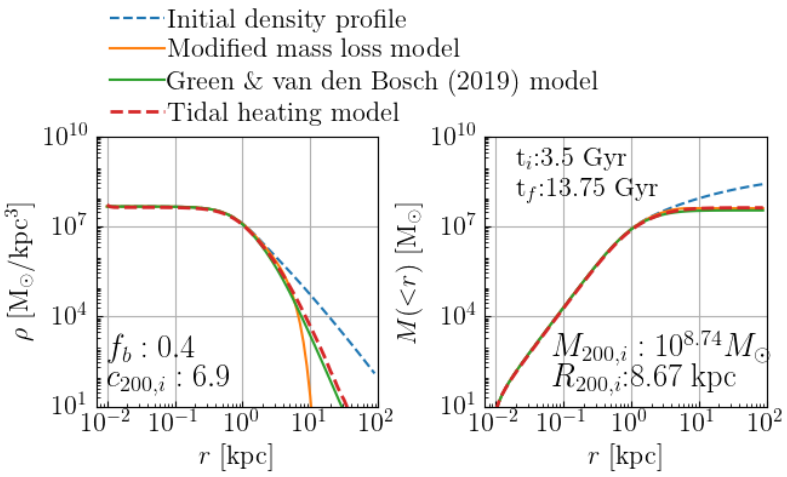

Figure A.1: Density (left) and enclosed mass (right) as a function of radius for a subhalo that has an initial virial mass of $10^{8.74}\,\mathrm{M}_\odot$, an initial cored profile, it follows the orbit of UM over 10 Gyr as it loses 60% of its initial mass ($f_b = 0.4$). The blue dashed line corresponds to the initial density and mass profile, whereas the orange/green solid and red dashed lines correspond to the final profiles after 10 Gyr. Orange and green solid lines correspond to the profile evolved using Green & van den Bosch (2019) transfer function (see Section 2.3 for more details), the red dashed line shows the evolution of the density profile after applying eqs. (A.7-A.8). The figure shows that the transfer function (applied to a cored profile, green line) is in good agreement with the tidal heating model (dashed red line), and both density profiles are mostly altered in the outer regions.

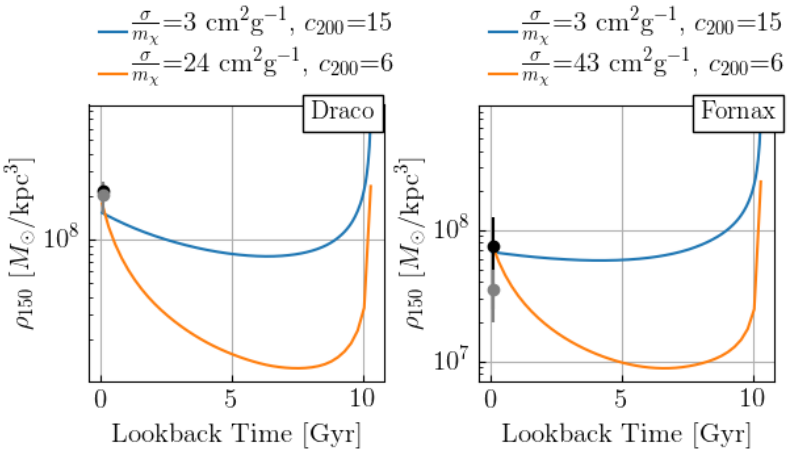

Figure A.2: Draco's (left) and Fornax's (right) DM density at 150 pc, ρ_{150}, as a function of lookback time. In the left panel the coloured lines correspond to the subhalo model initialised with a cross section of $\sigma/m_\chi = 3$ cm^{2}g^{-1} and concentration parameter of $c_{200,\rm init} = 15$ (blue line) and $\sigma/m_\chi = 24$ cm^{2}g^{-1} and $c_{200,\rm init} = 6.3$ (orange line). Similarly, in the right panel the model was initialised with a cross section of $\sigma/m_\chi = 3$ cm^{2}g^{-1} and concentration parameter of $c_{200,\rm init} = 15$ (blue line) and $\sigma/m_\chi = 43$ cm^{2}g^{-1} and $c_{200,\rm init} = 6.3$ (orange line). The figure shows the large impact of the concentration parameter that initializes the NFW profile. If higher values of c_{200} were assumed as starting point, lower values of σ/m_χ would be needed to reproduce ρ_{150} (shown in symbols), as reported by Kaplinghat et al. (2019), who assumed an isothermal cored profile (grey symbol) as well as NFW (black symbol).

A.3 . Impact of initial conditions: changing c_{200}

The core collapse time-scale is shorter for low-concentration systems. In Section 2.4.4 we discussed how changing the initial concentration parameters in our model impacts our results. Here we show an specific example. We compare the evolution of the central DM density, ρ_{150}, from Draco and Fornax, models that were run with different initial concentrations and cross sections.

Fig. A.2 shows ρ_{150} as a function of lookback time for Draco (left panel) and Fornax (right panel). The lines in the panels correspond to the models initialised with a cross section of $\sigma/m_\chi = 3$ cm^{2}g^{-1} and concentration parameter of $c_{200,\rm init} = 15$ (blue lines), and $\sigma/m_\chi = 24$ cm^{2}g^{-1} (43 cm^{2}g^{-1} for Fornax) and $c_{200,\rm init} = 6.3$ (orange lines). It can be seen that the concentration parameter largely impacts the evolution of ρ_{150}. We conclude that if higher values of $c_{200,\rm init}$ were assumed as a starting point, lower values of σ/m_χ would be needed

to reproduce ρ_{150} (shown in symbols taken from Kaplinghat et al. 2019).

A.4 . Impact of initial conditions: changing $M_{\rm init}$

Section 2.3.2 concludes that all MW dSphs need to be in gravothermal core collapse in order to explain the observational data. We commented that this result, however, strongly depends on the initial virial mass of the systems, $M_{200,\rm init}$, which is not chosen at random, it is tuned so that the systems, in their final state, have a virial mass that reproduces the observational estimations.

In this section we show that changing the initial virial masses of systems such as LeoII, Draco and Carina in 20%, changes the final central DM densities of these subhaloes in up to 50%. Fig. A.3 shows the DM density at 150 pc, ρ_{150}, as a function of lookback time for the models of LeoII (top-left panel), Draco (top-right panel) and Carina (bottom-left panel). The coloured lines correspond to the subhaloes initialised with the same cross section ($\sigma/m_\chi = 120$ cm^{2}g^{-1} for LeoII, 24 cm^{2}g^{-1} for Draco and 40 cm^{2}g^{-1} for Carina), but different initial virial masses.

The top panels show that the models of LeoII and Draco lower their final DM densities from $3\times10^8\,\mathrm{M}_\odot$ kpc^{-3} to $1.5\times10^8\,\mathrm{M}_\odot$ kpc^{-3}, and from $4\times10^8\,\mathrm{M}_\odot$ kpc^{-3} to $2\times10^8\,\mathrm{M}_\odot$ kpc^{-3}, respectively. The bottom panels shows that for Carina, an initial virial mass of $10^{9.3}\,\mathrm{M}_\odot$ leads to a final DM density of $2\times10^8\,\mathrm{M}_\odot$ kpc^{-3}, lowering the initial mass by 20% results in a DM density of $9\times10^7\,\mathrm{M}_\odot$ kpc^{-3}, and further lowering the initial mass by 50% results in a DM density of $4\times10^7\,\mathrm{M}_\odot$ kpc^{-3}.

A.5 . Impact of Milky Way mass

The mass of the Milky Way (MW) can impact the results presented in Section 2.3 by altering the orbital evolution of the dwarfs (shown in Fig. 2.1), as well as the rate of mass loss by increasing/decreasing the tidal radius above which mass is tidally stripped. In this Section we investigate how changing the MW mass from $10^{12}\,\mathrm{M}_\odot$ (default value adopted throughout the work) to $0.8\times10^{12}\,\mathrm{M}_\odot$ or $1.6\times10^{12}\,\mathrm{M}_\odot$, changes the final estimates of the DM density of dwarf subhaloes undergoing gravothermal collapse.

Fig. A.4 shows Carina's DM density at 150 pc, ρ_{150}, as a function of lookback time. The various subhalo models shown in the figure were all initialised with a cross section of $\sigma/m_\chi = 34$ cm^{2}g^{-1} and a MW mass of: $0.8\times10^{12}\,\mathrm{M}_\odot$ (shown in blue solid line), $10^{12}\,\mathrm{M}_\odot$ (red dashed line) and $1.6\times10^{12}\,\mathrm{M}_\odot$ (yellow solid line). The figure shows that a high MW mass, induces a higher rate of mass loss from gravitational tidal stripping, and therefore further accelerates the subhaloes' gravothermal collapse, resulting in subhaloes with higher central DM densities.

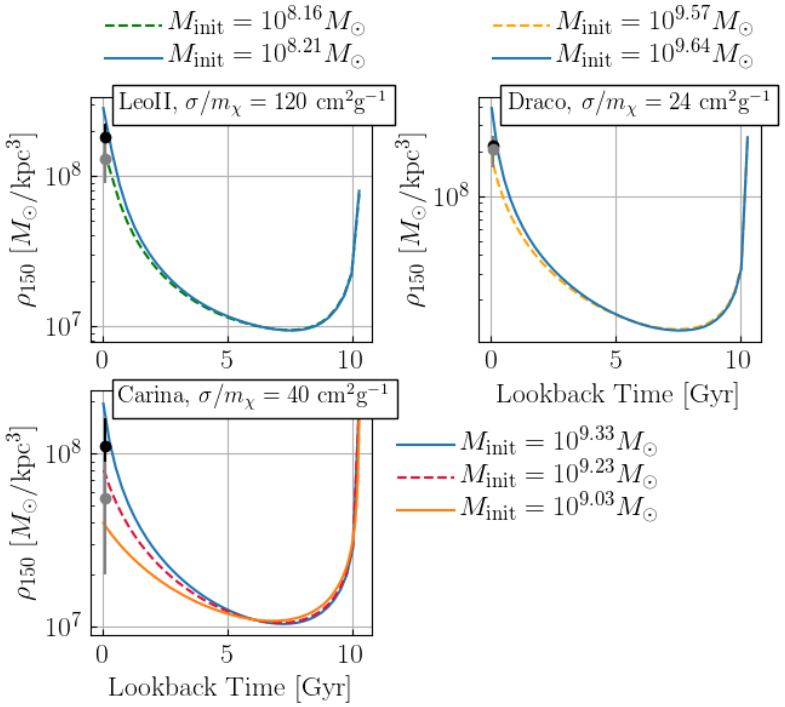

Figure A.3: DM density at 150 pc, ρ_{150}, as a function of lookback time for the models of LeoII (top-left panel), Draco (top-right panel) and Carina (bottom-left panel). The coloured lines correspond to the subhaloes initialised with the same cross section ($\sigma/m_\chi = 120$ cm^{2}g^{-1} for LeoII, 24 cm^{2}g^{-1} for Draco and 40 cm^{2}g^{-1} for Carina), but different initial virial masses. The symbols show the values of ρ_{150} (and M_{200}) taken from Kaplinghat et al. (2019), who assumed an isothermal cored profile (grey symbol) as well as NFW (black symbol). The figure shows how the initial mass of the models impact on the final DM density profile.

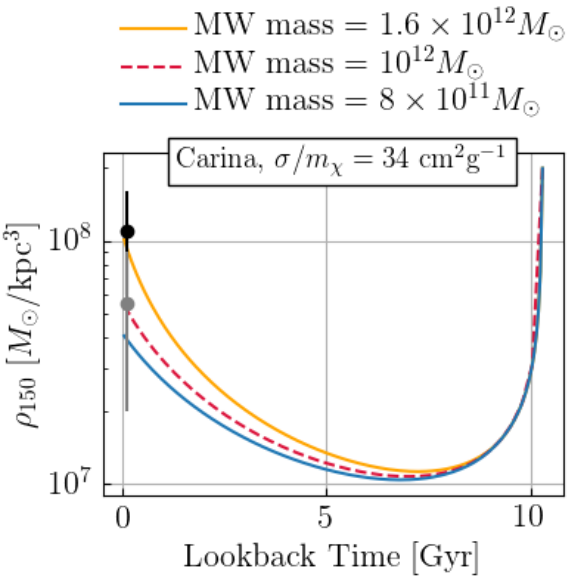

Figure A.4: Carina's DM density at 150 pc, ρ_{150}, as a function of lookback time. The coloured lines correspond to the subhalo model initialised with a cross section of $\sigma/m_\chi = 34$ cm^{2}g^{-1}, but different values for MW mass. The symbols show the values of ρ_{150} (and M_{200}) taken from Kaplinghat et al. (2019), who assumed an isothermal cored profile (grey symbol) as well as NFW (black symbol). The figure shows that assuming a MW mass of $1.6 \times 10^{12}\,\mathrm{M}_\odot$ ($0.8 \times 10^{12}\,\mathrm{M}_\odot$) requires a factor of ≈ 1.2 lower (higher) σ/m_χ to reproduce the observed central DM densities.

On the contrary, a lower MW mass produces subhaloes with lower central DM densities.

For Carina, but this also applies to the other dwarf models, increasing (decreasing) the MW mass in a factor of 1.6 (1.2), increases (decreases) the central DM density in a factor of 2 (1.2). This implies that assuming a MW mass of $1.6 \times 10^{12}\,\mathrm{M}_\odot$, requires a factor of up to ≈ 1.2 lower cross sections to reproduce the observed central DM densities, or alternatively assuming a MW mass of $0.8 \times 10^{12}\,\mathrm{M}_\odot$, requires a factor of ≈ 1.2 larger cross sections.

A.6 . Impact of Truncation time

The truncation time, $t_{\rm trunc}$, is a free parameter that regulates the frequency over which the subhaloes' density profile is truncated. In Section 2.2.3 we showed that the largest changes of the density profile occurs in the outskirt of the subhalo, beyond the virial radius, such change in the profile is, nevertheless, important because it lowers the pressure of the extended subhalo, it gets therefore colder as it readjusts to hydrostatic equilibrium. Section 2.3.2 shows that this favours the conditions for gravothermal core collapse.

In this section we investigate how changing $t_{\rm trunc}$ from 250 Myr (default value) to 350 or 150 Myr, alters the final central DM density of subhaloes. Fig. A.5 shows the Carina model initialised with a cross section of $\sigma/m_\chi = 34$ cm^{2}g^{-1}. The top panel shows the DM density at 150 pc, ρ_{150}, as a function of lookback time, whereas the bottom panel shows the evolution of the virial mass, M_{200}. The coloured lines correspond to the subhalo model initialised with the same cross section and initial mass, but different values for the truncation time as indicated in the legends. It can be seen from the figure that a more frequent truncation accelerates gravothermal core collapse and subhaloes reach higher ρ_{150} at present time. Conversely, a less frequent truncation of the density profile, decelerates gravothermal core collapse and subhaloes reach lower ρ_{150}.

For the specific cross section of $\sigma/m_\chi = 34$ cm^{2}g^{-1}, the models with different $t_{\rm trunc}$ reach ρ_{150} and M_{200} at present time in agreement with the observational estimations (within the uncertainties). Lowering $t_{\rm trunc}$ to 150 Myr, yields 50% higher central DM densities, while increasing $t_{\rm trunc}$ to 350 Myr, yields 30% lower central DM densities. This implies that changing $t_{\rm trunc}$ from 250 to 150 Myr (or 350 Myr), increases (decreases) the cross sections range that reproduces the observed central DM densities in up to a factor of 1.12 (1.13). Therefore the main effect of $t_{\rm trunc}$ in our results is to increase or decrease the normalization of the cross section-velocity relation, but it does not alters the shape of the relation.

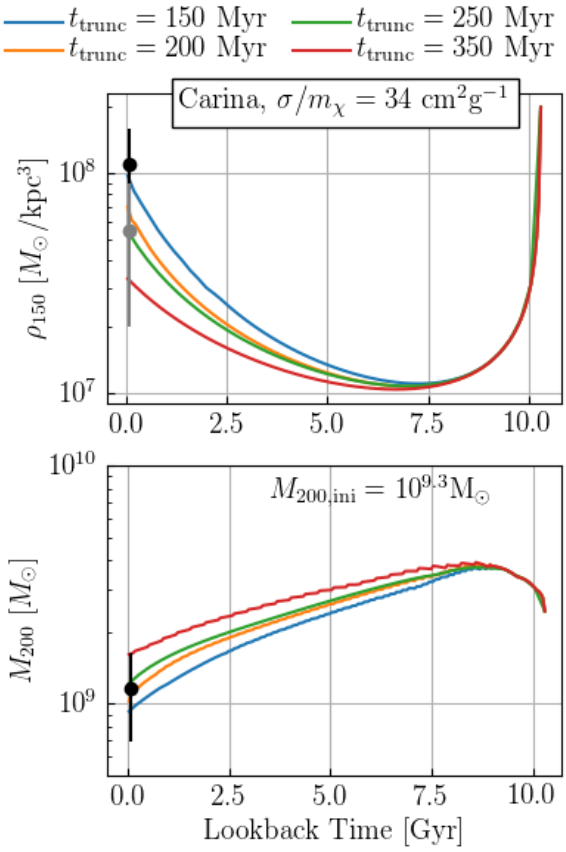

Figure A.5: Carina's DM density at 150 pc, ρ_{150} (top panel), and virial mass, M_{200} (bottom panel), as a function of lookback time. The coloured lines correspond to the subhalo model initialised with the same cross section (of $\sigma/m_\chi = 34$ cm^{2}g^{-1}) and initial mass, but different values for the truncation time, $t_{\rm trunc}$, that determines the frequency over which subhaloes' density profile is truncated due to mass loss. The symbols show the values of ρ_{150} (and M_{200}) taken from Kaplinghat et al. (2019), who assumed an isothermal cored profile (grey symbol) as well as NFW (black symbol). The figure shows that a more frequent truncation, accelerates gravothermal core collapse and subhaloes reach higher ρ_{150} at present time. Conversely, a less frequent truncation of the density profile, decelerates gravothermal core collapse and subhaloes reach lower ρ_{150}.

B - Appendix: Chapter 3

B.1 . Simulated data selection

In this section, we describe our selected host haloes and their satellites from the six boxes described in Section 3.2. In Tab. B.1, we show how many Milky Way sized host haloes, with virial masses ranging between 6×10^{11} $\mathrm{M}_{\odot}$ and 2×10^{12} $\mathrm{M}_{\odot}$ at $z = 0$, we have analyzed in our simulations. Moreover, we show how many satellites of the selected hosts with bound masses above 10^{9} $\mathrm{M}_{\odot}$ we considered in our analysis for each simulation.

In Fig. B.1 we show the distribution in bound mass at redshift $z = 0$ for the selected satellite sample. Typical bound masses at $z = 0$ are of $10^{9.4}$ $\mathrm{M}_{\odot}$ across all simulations. In Fig. B.2 we show the distribution in peak mass for the selected satellite sample. Typical peak masses at $z = 0$ are of $10^{9.5}$ $\mathrm{M}_{\odot}$ across all simulations, with minimum peak masses reaching 10^{8} $\mathrm{M}_{\odot}$.

B.2 . Central density fit

In this section, we discuss the fitting to the central density profiles of simulated haloes to estimate $\rho(150\ \mathrm{pc})$.

B.2.1 . Density profile models

The NFW profile (Navarro et al., 1997) can be characterized by the scale radius r_s and the scale density ρ_s, taking the following functional form

$$\rho_{\mathrm{NFW}}(r) = \frac{\rho_s}{(r/r_s)(1 + r/r_s)^2}. \tag{B.1}$$

Robertson et al. (2021) showed how the isothermal Jeans model (Kaplinghat et al., 2016) can be used to generate a density profile that accounts for the effects of

Simulation name	Milky Way sized host haloes	Selected satellites
`CDM`	34	430
`SigmaConst01`	33	414
`SigmaConst10`	31	329
`SigmaVel20`	33	401
`SigmaVel60`	33	403
`SigmaVel100`	33	397

Table B.1: In this table we show how many Milky Way sized host haloes and their satellites we considered in our analysis for each simulation.

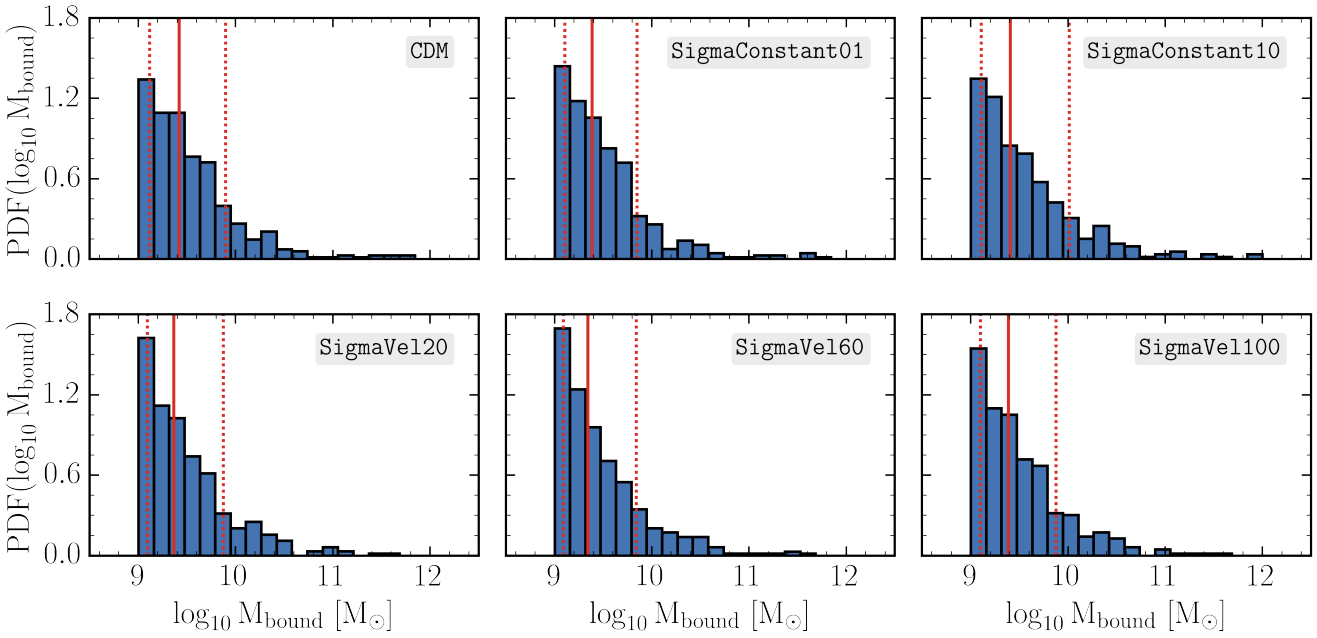

Figure B.1: We show the distribution of the bounded mass at redshift $z = 0$ of our satellite sample for the `CDM` (top-left), `SigmaConstant1` (top-middle), `SigmaConstant10` (top-right), `SigmaVel20` (bottom-left), `SigmaVel60` (bottom-middle) and `SigmaVel100` (bottom-right) models. We show in solid red line the median and in dashed red lines the 16-84th percentiles.

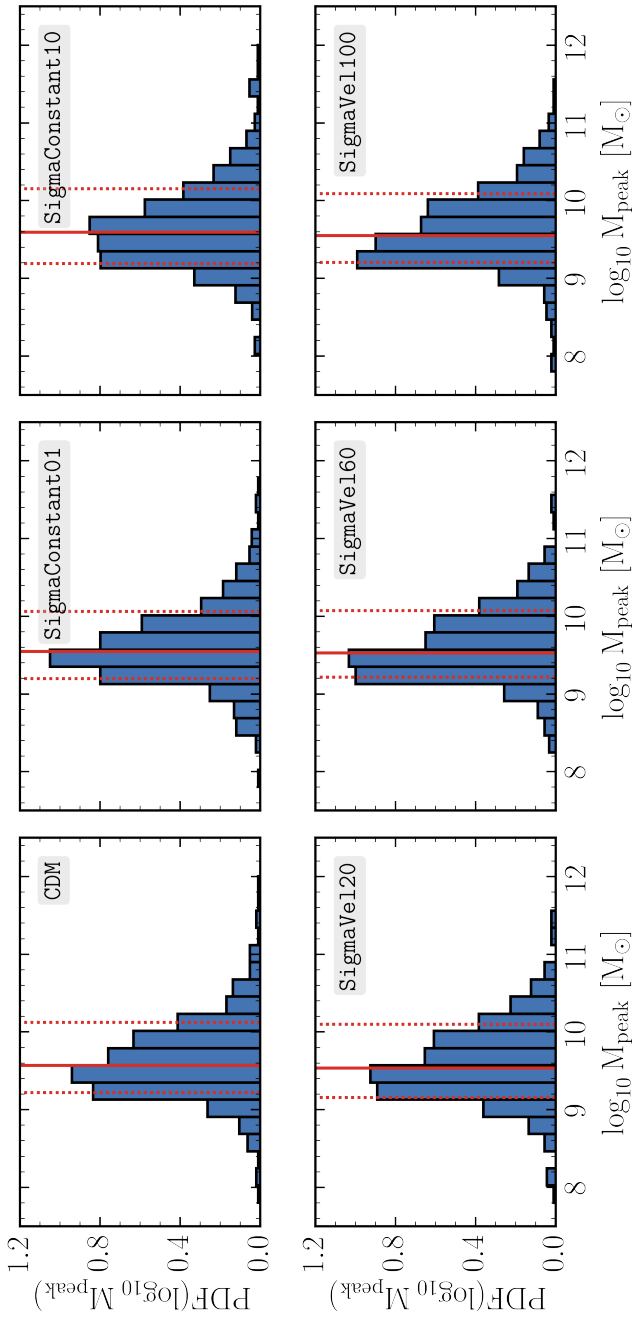

Figure B.2: Same as Fig. B.1, but for the distribution of the peak mass of our satellite sample.

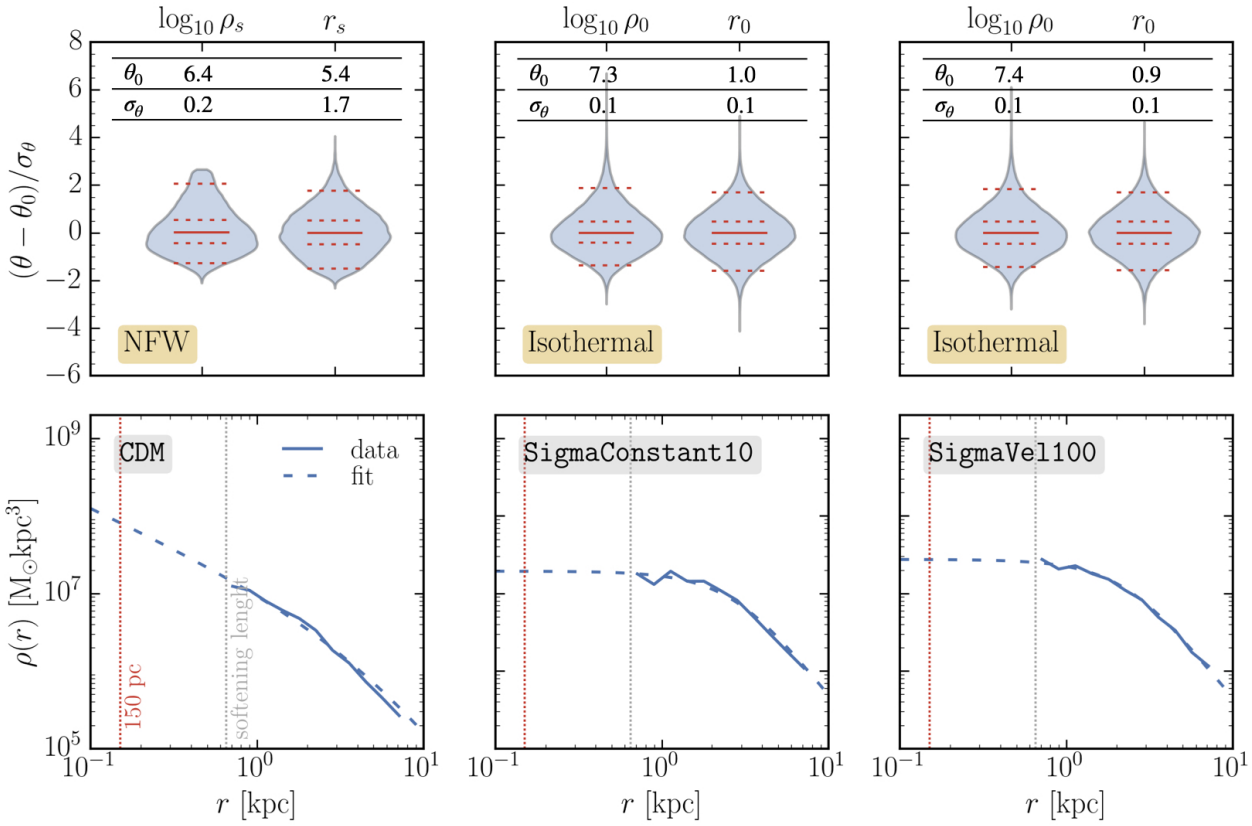

Figure B.3: Example of a fit for a satellite halo matched between three different boxes (`CDM`, `SigmaConstant10`, and `SigmaVel160`). In the CDM case, we use a NFW profile, whereas for the SIDM cases we use an isothermal profile. *Top:* The top panels show the results of the MCMC fit through 'violin plots', that depict 1D marginal posterior distributions of the parameters obtained from the MCMC fit. To aid comparison across parameters and facilitate a more concise depiction of the results, all 1D posterior samples are scaled by the median value, θ_0, and normalized by the standard deviations of the posterior, σ_θ. We show in dashed red lines the 5-95th and the 32-68th percentiles. *Bottom:* The bottom panels show the simulated density profile with a solid lines, with the best-fitting profile shown by the dashed line. The grey dotted lines indicate the softening scale (see text for definition).

dark matter self-interactions, starting from an NFW profile and a SIDM cross-section. Assuming that SIDM is in hydrostatic equilibrium and considering the DM-only case, they demonstrated that the isothermal profile can be defined by two free parameters, a scale radius r_0 and a scale density ρ_0, taking the following functional form

$$\rho_{\rm iso}(r) = \rho_0 f(r/r_0), \tag{B.2}$$

where $f(x) = \exp(y)$ can be found numerically integrating

$$\frac{\mathrm{d}^2 y}{\mathrm{d}x^2} + \frac{2}{x}\frac{\mathrm{d}y}{\mathrm{d}x} + \exp(y) = 0, \tag{B.3}$$

and imposing the boundary conditions $y(0) = 0$ and $\mathrm{d}y/\mathrm{d}x|_{x=0} = 0$, given that simulated SIDM haloes have constant central density cores. For a complete derivation we invite the reader to see Robertson et al. (2021, Section 2.2).

Note to the reader: This section is currently in preparation.

B.2.2 . Density profile MCMC fit

Robertson et al. (2021) fitted simulated SIDM haloes density profiles by matching an isothermal profile for the inner part of the density profile with a NFW profile for the external part, in order to constrain their mass, concentration, and cross-section. In this work, we follow their fitting procedure but do not perform the matching. Instead, since our goal is to have an estimate of $\rho(150\ \mathrm{pc})$, we focus on fitting only the inner part of the density profiles with a NFW profile (Eq. B.1) for CDM haloes, and with an isothermal profile (Eq. B.2) for SIDM haloes.

In order to find the best fit (maximum likelihood) parameter values for our density profile, we perform an MCMC scan of the parameter space. We first sample the input parameters (scale radius and density) from their priors. We then generate the (NFW or isothermal) model density profile at each point in the parameter space. We finally compute a likelihood by comparing the model density profile with the measured density profile from the simulations. For both NFW and isothermal profiles, we assume uniform priors over the scale radius, $\mathcal{U}(0.001, 10)$, and the $\log_{10}$ scale density, $\mathcal{U}(3, 10)$. We define the log-likelihood as

$$\log L = -\frac{1}{2}\sum_{i=1}^{N_{\rm bins}} \left(\frac{\log_{10}\rho_{\rm sim}(r_i) - \log_{10}\rho_{\rm model}(r_i)}{\delta \log_{10}\rho} \right)^2, \tag{B.4}$$

and assume an uncorrelated error of $\delta \log_{10}\rho = 0.1$. The bins r_i are taken at the same logarithmically-spaced radii at which the density profiles are computed from the simulations. We only fit the inner part of the density profiles, ranging between $0.712\ \mathrm{kpc}$ and $7.12\ \mathrm{kpc}$.

In Fig. B.3 we show an example of fit for a satellite halo matched between three different models (`CDM`, `SigmaConstant10`, and `SigmaVel100`). In the CDM case, we show a fit for a NFW profile, whereas for the SIDM cases we use an isothermal profile. The bottom panels show the simulated density profile as a solid lines, with the best-fitting profile shown with a dashed line. In the top panels we show the results of the MCMC fit through 'violin plots'.

Note to the reader: This section is currently in preparation.

B.2.3 . Central density and maximum circular velocity

Figure B.4 shows the relation between the estimated inner density at $150\ \mathrm{pc}$, $\rho(150\ \mathrm{pc})$, the maximum circular velocity at $z = 0$, $\mathrm{V}_{\mathrm{max}}(z = 0)$, and the maximum circular velocity prior to infall, $\mathrm{V}_{\mathrm{peak}}$. It can be seen from the figure that higher $\mathrm{V}_{\mathrm{max}}(z = 0)$ corresponds to higher central density. In addition, the scatter of the relation increases in the SIDM models relative to CDM, due to the effect of the dark matter particles' interactions in diversifying the satellites' densities.

Note to the reader: This section is currently in preparation.

B.3 . Pericenter distribution

In Fig. B.5 we show the pericenter distribution of the selected satellites for our simulations. We notice a slightly larger scatter in the satellites orbits in the `SigmaConstant10` model with a larger median for the pericenter distance. This is expected due to the larger interactions between dark matter particles in the `SigmaConstant10` model.

B.4 . Correlation coefficients

In order to assess the correlation between inner structural properties and pericenter distances of our satellite sample we compute the Pearson and Spearman correlation coefficients for datasets of interest. The results can be found in Table B.2. Specifically, with the Pearson correlation coefficient we measure the linear correlation between the two quantities of interests, whereas with the Spearman correlation coefficient we asses how well the relationship between the two variables of interest can be described using a monotonic function.

Note to the reader: This section is currently in preparation.

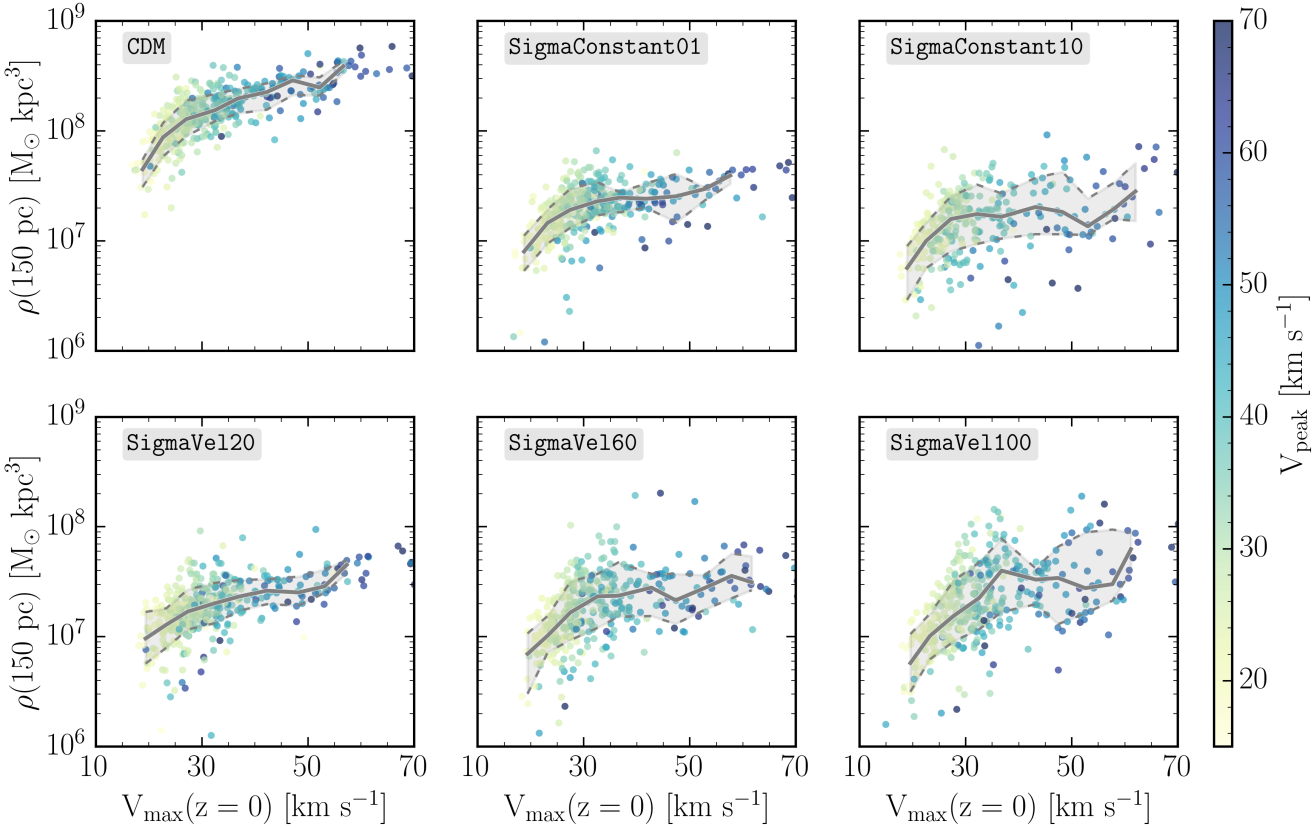

Figure B.4: Satellites inner density at 150 kpc, $\rho(150\ \mathrm{kpc})$ versus their maximum velocity at redshift $z = 0$, $\mathrm{V}_{\mathrm{max}}$, highlighted by their maximum circular velocity prior to infall, $\mathrm{V}_{\mathrm{peak}}$. The solid lines represent the median trends and the dashed lines represent the 16-84th percentiles for the `CDM` (top-left), `SigmaConstant1` (top-middle), `SigmaConstant10` (top-right), `SigmaVel20` (bottom-left), `SigmaVel60` (bottom-middle) and `SigmaVel100` (bottom-right) models.

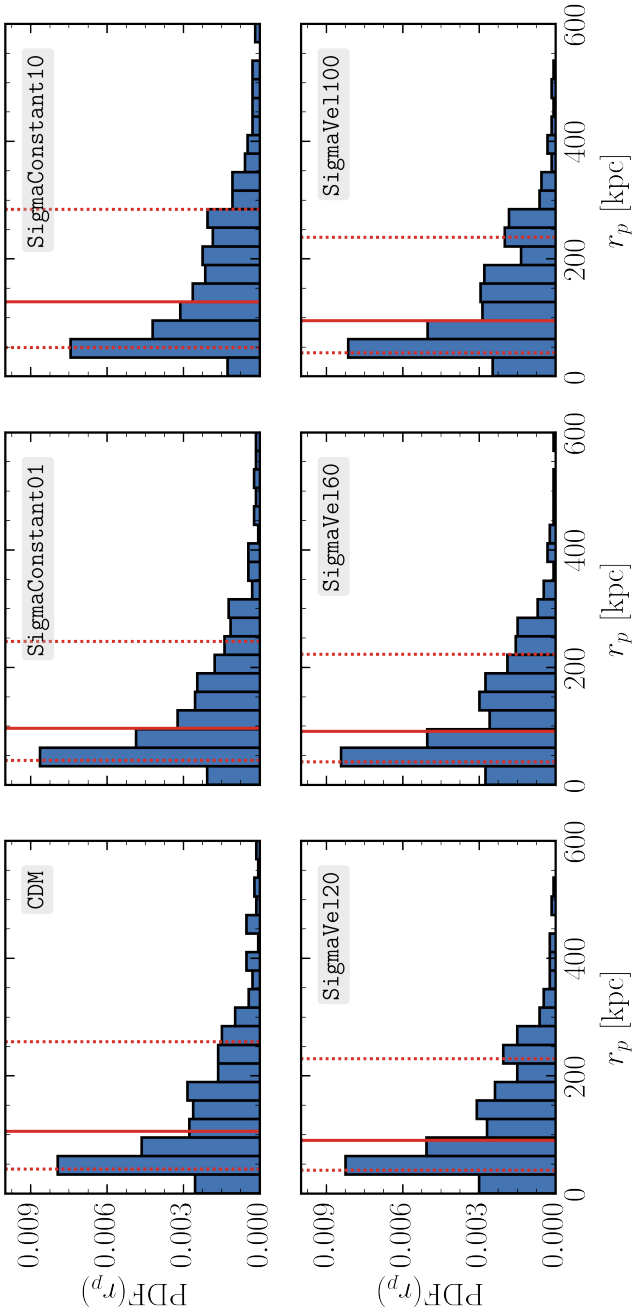

Figure B.5: Same as Fig. B.1, but for the distribution of the pericenter of our satellite sample.

Simulation name	$\rho(150\text{ pc}) - r_p$		$V_{max}(z=0) - r_p$		$V_{peak} - r_p$	
	Pearson	Spearman	Pearson	Spearman	Pearson	Spearman
CDM	0.04	-0.17	0.16	-0.04	0.09	-0.17
SigmaConst01	-0.07	-0.13	0.10	-0.11	0.02	-0.22
SigmaConst10	-0.06	0.05	0.31	0.10	0.19	-0.13
SigmaVel20	-0.05	-0.07	0.14	0.03	-0.03	-0.20
SigmaVel60	-0.12	-0.18	0.17	-0.05	0.02	-0.22
SigmaVel100	-0.24	-0.26	0.11	-0.09	-0.05	-0.23

Table B.2: Pearson and Spearman correlation coefficients for datasets of interest as described in each column title.

Simulation name	$V_{max}(z=0)/V_{peak} - r_p$	
	Pearson	Spearman
CDM	0.10	0.39
SigmaConst01	0.08	0.41
SigmaConst10	0.17	0.50
SigmaVel20	0.13	0.47
SigmaVel60	0.09	0.47
SigmaVel100	0.06	0.43

Table B.3: Pearson and Spearman correlation coefficients for datasets of interest as described in each column title.

B.5 . Maximum circular velocity prior to infall

We include Figure B.6 to aid comparison with Hayashi et al. (2020, Fig. 8), Ebisu et al. (2022, Fig. 1), and Yang et al. (2023, Fig. 11). Figure B.6 is similar to Figure 3.2, but the satellites are now color coded by their maximum circular velocity prior to infall, V_{peak}. Interestingly, we notice how V_{peak} correlates with the inner density for the CDM model, with satellites with larger inner densities having larger V_{peak}. This is not the case for the SIDM models, where satellites with large inner densities can also have lower V_{peak} values, and vice-versa. As suggested by Yang et al. (2023), these correlated predictions suggest that a joint fit to these observables would provide a stringent test of SIDM physics.

Note to the reader: This section is currently in preparation.

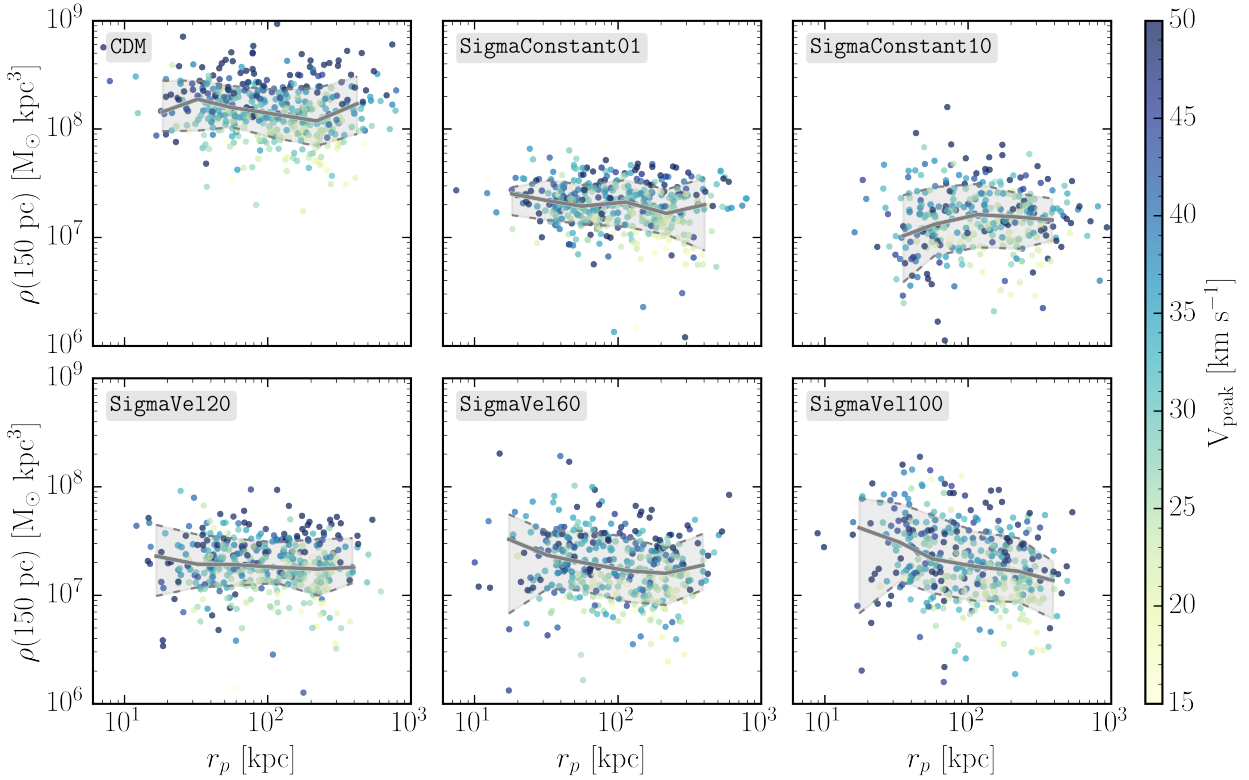

Figure B.6: Same as Figure 3.2, but with the maximum circular velocity prior to infall $\mathrm{V}_{\mathrm{peak}}$ of the satellite haloes highlighted by the colour bar. The solid lines represent the median trends and the dashed lines containing the shaded region represent the 16-84th percentiles for the `CDM` (top-left), `SigmaConstant1` (top-middle), `SigmaConstant10` (top-right), `SigmaVel20` (bottom-left), `SigmaVel60` (bottom-middle) and `SigmaVel100` (bottom-right) models.

C - Appendix: Chapter 4

C.1 . Galaxy Stellar Mass Function

Fig. C.1 shows the $z = 0$ galaxy stellar mass function for the WeakStellarFB (left panel) and Reference (right panel) galaxy formation models under the CDM (blue lines), SigmaVel60 (purple line), SigmaVel30 (red line) and SigmaConstant10 (orange line) schemes. The simulation results are compared to the original EAGLE REF model (Schaye et al. 2015), and to the DR4 Galaxy And Mass Assembly (GAMA) survey (Driver et al. 2022). The EAGLE data shown throughout this section is taken from the EAGLE reference model run in a (25 Mpc)^3 box with the same resolution as the TangoSIDM simulations, which were also run in a (25 Mpc)^3 volume.

Both Reference and WeakStellarFB produce a galaxy number density in the stellar mass range $10^8 - 10^{11}$ $\mathrm{M}_\odot$ that is in close agreement with EAGLE and within 0.2 dex of the observational data. While Fig. C.1 seems to indicate that SIDM does not strongly affect the galaxy stellar mass function, it does decrease the number of satellites (as shown in Vogelsberger et al. 2012; Nadler et al. 2020; Correa et al. 2022). SIDM interactions enhance the disruption of subhaloes by tidal stripping from the host. We find that from the 685 satellite galaxies in the stellar mass range $10^{7-10}\mathrm{M}_\odot$ from the Reference/CDM model, 639 (93%) survive in the Reference/SigmaVel60 model and 544 (79%) survive in the Reference/SigmaConstant10 model.

C.2 . Density evolution

This appendix expands the discussion presented in Section 4.3, where we showed that under SIDM halo dark matter density profiles evolve differently than under CDM (Fig. 4.4). We have found that as galaxies within SIDM haloes grow in mass, baryons assume a dominant role in the galaxies' central gravitational potential. Consequently, dark matter particles thermalise through frequent interactions, accumulating in the center of the baryon-dominated potential. Fig. C.2 shows the density evolution of the 32 most massive haloes from the WeakStellarFB model under CDM (left panel) and SigmaVel60 (middle panel), and from the Reference model under SigmaVel60 (right panel). The coloured lines represent the median density evolution between redshifts 0 and 2. In the WeakStellarFB models, the early dominance of baryons in the central potential results in the rapid formation highly cuspy density profiles, which for SIDM remains with minimal evolution in the redshift range zero to two. In contrast, under CDM haloes there is a slight

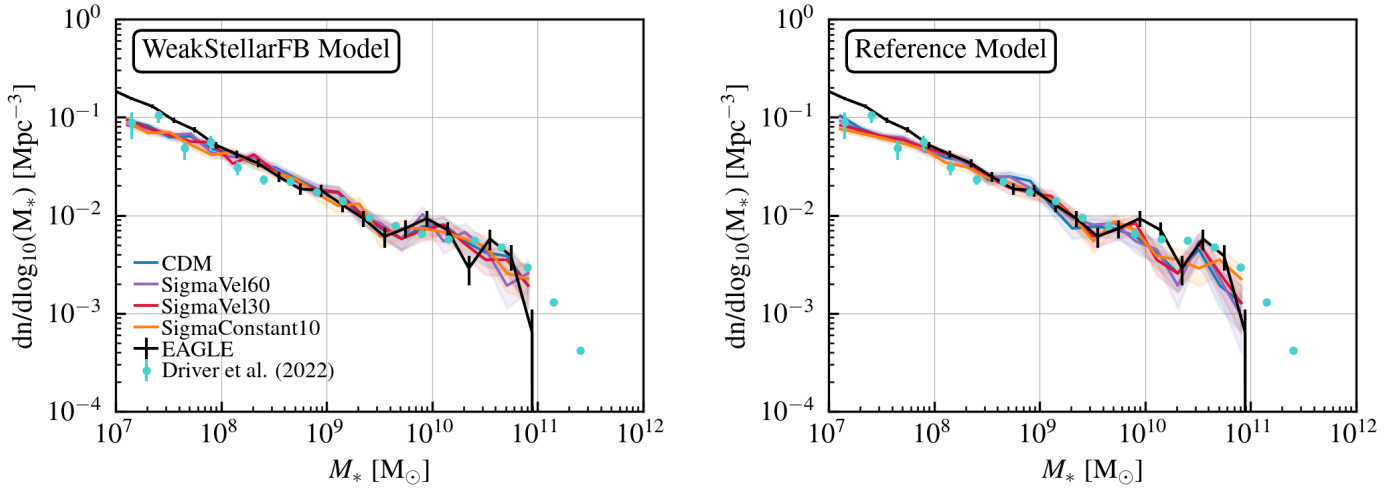

Figure C.1: The galaxy stellar mass function at $z = 0$ for the 'WeakStellarFB' (left panel) and 'Reference' (right panel) galaxy formation models under the CDM (blue lines), SigmaVel60 (purple line), SigmaVel30 (red line) and SigmaConstant10 (orange line) schemes. The black line corresponds to the galaxy stellar mass function of the original EAGLE 25 REF model and the green line corresponds the measurements from the DR4 GAMA survey at $z < 0.1$ (Driver et al. 2022). Both models, Reference and WeakStellarFB, produce a galaxy number density in the stellar mass range $10^8 - 10^{11}$ $\mathrm{M}_\odot$ that is in agreement with EAGLE and the observational data within 0.2 dex. Note that the models considered here were calibrated to reproduce the $z = 0$ galaxy stellar mass function.

decrease in cuspiness by redshift zero. The right panel of Fig. C.2 demonstrates that, in the SigmaVel60/Reference model, the median central density of haloes slightly increases over time, as was the case for the SigmaVel30/Reference model.

C.3 . Assembly history

Section 4.6.1 reported an important discrepancy found in massive disc galaxies within the SIDM framework when compared to observations in the Tully-Fisher plane. This discrepancy was translated into an exclusion zone within the SIDM parameter space. Our approach involved identifying velocity-cross section pairs that lead to the formation of galaxies with exceedingly large $V_{\rm circ}(R_{\rm eff})$. In this section, we provide further details on the methodology employed to determine the lower limits for velocity and cross section, above which the SigmaVel30 and SigmaVel60 models are ruled out.

To identify these velocity-cross section pairs, we select all disc galaxies from the Reference + SigmaVel30 and Reference + SigmaVel60 models with stellar masses larger than 10^{10} $\rm M_{\odot}$ and $1.3{\times}10^{10}$ $\rm M_{\odot}$, respectively. We follow the assembly histories of the haloes hosting these galaxies across the simulation snapshots until redshift 2 (the redshift below which the haloes' density profiles are well resolved and commence substantial evolution). The left panel of Fig. C.3 shows the mass accretion history $M_{200}(z)$, of the haloes from the SigmaVel30 (dark blue lines) and SigmaVel60 (light blue lines) models under the Reference galaxy model. Converting $M_{200}(z)$ into circular velocity, $V_{\rm circ}(z)$, we show these values in the second form the left panel of Fig. C.3.

We assume that $V_{\rm circ}(z)$ corresponds to the average velocity of the dark matter particles within these haloes. Therefore, to estimate the corresponding average dark matter particle cross sections of these haloes, we use eq. (4.1), assume $v = V_{\rm circ}(z)$ and integrate over the scattering angle (as done in eq. 4.2). The evolution of the dark matter haloes' average cross sections, σ_T/m_χ, as a function of redshift is shown in the second panel from the right. The right most panel displays the cross section as a function of the haloes circular velocities for the SigmaVel30 and SigmaVel60 models (grey lines). As expected, all the velocity-cross section pairs that were obtained from the haloes' evolution align with the velocity-σ_T/m_χ relation from the models (eq. 4.2).

In the last step, at each redshift we determine the 16-84th percentiles in the distribution of the haloes circular velocities. We highlight these percentage ranges in red in the right panel and mark them as the limits above which the SigmaVel30 and SigmaVel60 models produce overly enhanced central dark matter densities in massive disc galaxies. Therefore, these limits represent the lower bounds above which the SigmaVel30 and SigmaVel60 models are ruled out with 98% and 95%

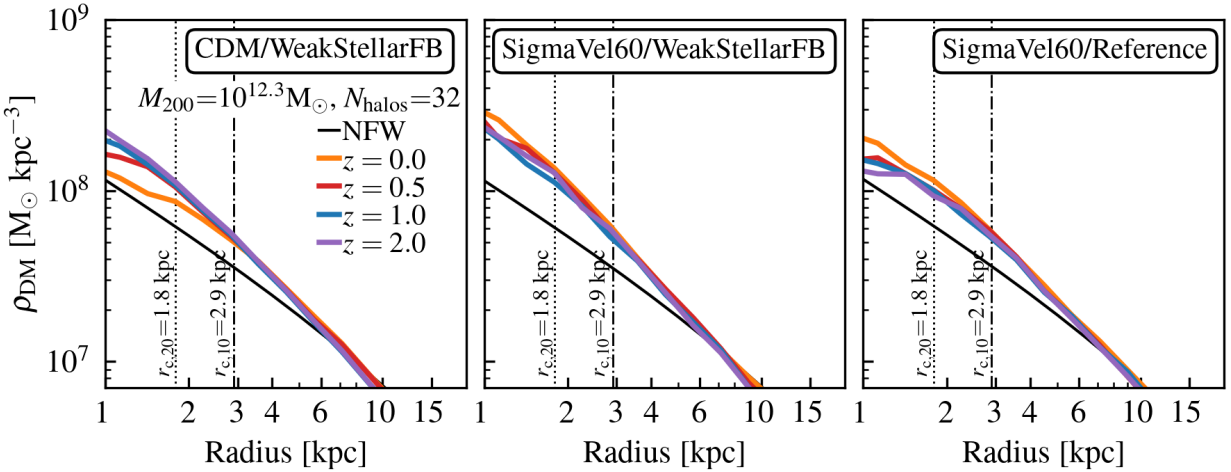

Figure C.2: Stacked median dark matter density profile, $\rho_{\rm DM}$, for the 32 most massive haloes from the WeakStellarFB model under CDM (left panel) and SigmaVel60 (middle panel), and from the Reference model under SigmaVel60 (right panel). The coloured lines show the median values at different redshifts, and the black solid line shows the NFW profile of the haloes at redshift zero. The black dashed-dotted lines indicate the convergence radius (see Section 4.4 for the definition). The median density profiles of haloes over time in WeakStellarFB/CDM are cuspy by redshift 2 and slightly decrease by redshift zero. For the WeakStellarFB/SigmaVel60 model, the median density profiles of the haloes is cuspier by redshift 2, and they do not largely evolve towards redshift zero.

Table C.1: Observational data used in this work. Column 2 provides the sample the galaxy belongs to: 'S' (SPARC, Lelli et al. 2016), 'R' (Reyes et al. 2011), 'P' (Pizagno et al. 2007). Note that for the Reyes et al. and Pizagno et al. datasets, the galaxy names correspond to their SDSS names. The complete table can be found online in http://www.tangosidm.com.

Name	Sample	M_* [$M_\odot$]	$R_{\rm eff}$ [kpc]	$V_{\rm circ}(R_{\rm eff})$ [km s^{-1}]
ESO079-G014	S	2.59e+10	7.23	140.99
ESO116-G012	S	2.15e+09	2.75	80.63
ESO563-G021	S	1.56e+11	10.59	294.74
F568-3	S	4.17e+09	7.47	91.87
F568-V1	S	1.91e+09	4.40	101.01
J001006.61-002609.7	R	9.64e+09	2.42	94.86
J001708.75-005728.9	R	4.57e+09	3.13	107.83
J002844.82+160058.8	R	2.91e+10	6.08	106.65
J003112.09-002426.4	R	1.53e+10	2.00	138.94
J004916.23+154821.0	R	7.49e+09	5.65	107.57
J004935.71+010655.2	R	3.72e+10	5.40	117.47
J011750.26+133026.3	R	3.80e+09	3.83	65.96
J012317.00-005421.6	R	1.71e+10	2.33	137.88
J012340.12+004056.4	R	2.14e+10	3.01	156.31
J012438.08-000346.4	P	2.07e+10	6.69	161.71
J013142.14-005559.9	P	6.72e+10	13.90	225.19
J013600.15+003948.6	P	3.10e+10	6.15	179.73
J013752.69+010234.8	P	5.29e+10	8.18	277.10
J014121.94+002215.7	P	1.88e+10	3.27	195.82
J015746.24-011229.9	P	8.53e+10	7.19	310.80
J015840.93+003145.2	P	4.78e+10	9.46	189.52
...	.	...	...	...

confidence, respectively.

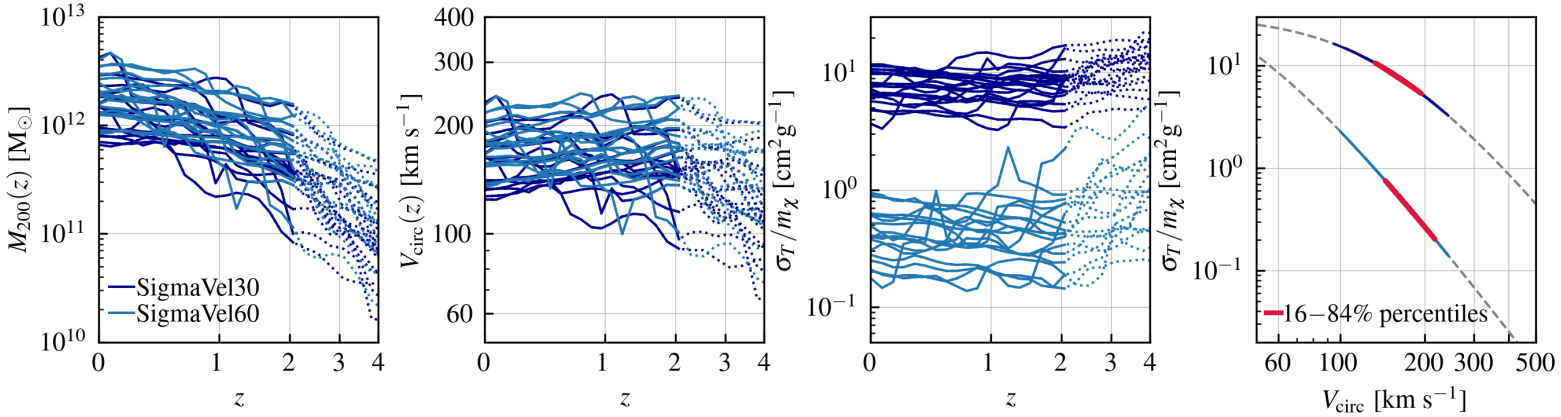

Figure C.3: *Left panel*: Mass assembly, $M_{200}(z)$, illustrating the evolution of haloes hosting galaxies that exhibit significant deviations from observations in the $z = 0$ Tully-Fisher plane. Dark blue lines represent the mass evolution of individual haloes from the SigmaVel30 model, while light blue lines correspond to the SigmaVel60 model. *Second panel from the left*: Circular velocity, $V_{\rm circ}(z)$, as a function of redshift for the same haloes as in the left panel. *Second panel from the right*: Cross section, computed from the circular velocity, as a function of redshift. *Right panel*: Velocity-cross section plane. The grey dashed lines mark the cross section dependence for the SigmaVel30 and SigmaVel60 models. The red limits mark the 16th-84th percentiles of the haloes' evolution in the cross section-velocity plane.

Bibliography

Abbott T. M. C., et al., 2018, MNRAS, 480, 3879

Abbott T. M. C., et al., 2022, Phys. Rev. D, 105, 023520

Adhikari S., et al., 2022, arXiv e-prints, p. arXiv:2207.10638

Adhikari G., et al., 2023, Scientific Reports, 13, 4676

Agrawal P., Cyr-Racine F.-Y., Pinner D., Randall L., 2023, Physics of the Dark Universe, 42, 101347

Aihara H., et al., 2018, PASJ, 70, S8

Alam S., et al., 2021, Phys. Rev. D, 103, 083533

Alestas G., Kazantzidis L., Perivolaropoulos L., 2020, Phys. Rev. D, 101, 123516

Alvarez G., Yu H.-B., 2020, Phys. Rev. D, 101, 043002

Amendola L., Tocchini-Valentini D., 2002, Physical Review D, 66

Amon A., et al., 2023, MNRAS, 518, 477

An R., Feng C., Wang B., 2018, J. Cosmology Astropart. Phys., 2018, 038

Anau Montel N., Coogan A., Correa C., Karchev K., Weniger C., 2023, MNRAS, 518, 2746

Andrade K. E., Fuson J., Gad-Nasr S., Kong D., Minor Q., Roberts M. G., Kaplinghat M., 2022, MNRAS, 510, 54

Andrade K. E., Kaplinghat M., Valli M., 2023, Halo Densities and Pericenter Distances of the Bright Milky Way Satellites as a Test of Dark Matter Physics (`arXiv:2311.01528`)

Aprile E., et al., 2023, Phys. Rev. Lett., 131, 041003

Arkani-Hamed N., Finkbeiner D. P., Slatyer T. R., Weiner N., 2009, Phys. Rev. D, 79, 015014

Asencio E., Banik I., Kroupa P., 2021, MNRAS, 500, 5249

Avila-Reese V., Zavala J., Firmani C., Hernández-Toledo H. M., 2008, AJ, 136, 1340

Bahé Y. M., et al., 2022, MNRAS, 516, 167

Balberg S., Shapiro S. L., Inagaki S., 2002, ApJ, 568, 475

Banerjee A., Adhikari S., Dalal N., More S., Kravtsov A., 2020, J. Cosmology Astropart. Phys., 2020, 024

Banik I., Zhao H., 2022, Symmetry, 14, 1331

Banik N., Bertone G., Bovy J., Bozorgnia N., 2018, J. Cosmology Astropart. Phys., 2018, 061

Banik N., Bovy J., Bertone G., Erkal D., de Boer T. J. L., 2021, J. Cosmology Astropart. Phys., 2021, 043

Barman R. K., Bélanger G., Bhattacherjee B., Godbole R., Sengupta D., Tata X., 2021, Phys. Rev. D, 103, 015029

Battaglia G., Taibi S., Thomas G. F., Fritz T. K., 2022, Astronomy & Astrophysics, 657, A54

Bauer A. E., et al., 2013, MNRAS, 434, 209

Behroozi P., Wechsler R. H., Hearin A. P., Conroy C., 2019, MNRAS, 488, 3143

Bell E. F., de Jong R. S., 2001, ApJ, 550, 212

Bell E. F., McIntosh D. H., Katz N., Weinberg M. D., 2003, ApJS, 149, 289

Beltrán Jiménez J., Bettoni D., Figueruelo D., Teppa Pannia F. A., Tsujikawa S., 2021, Phys. Rev. D, 104, 103503

Bennett C. L., et al., 2011, ApJS, 192, 17

Bernabei R., et al., 2021, Nuclear Physics and Atomic Energy, 22, 329

Bhattacharya A., Esmaili A., Palomares-Ruiz S., Sarcevic I., 2019, J. Cosmology Astropart. Phys., 2019, 051

Boddy K. K., Feng J. L., Kaplinghat M., Tait T. M. P., 2014a, Phys. Rev. D, 89, 115017

Boddy K. K., Feng J. L., Kaplinghat M., Shadmi Y., Tait T. M. P., 2014b, Phys. Rev. D, 90, 095016

Boddy K. K., Kaplinghat M., Kwa A., Peter A. H. G., 2016, Phys. Rev. D, 94, 123017

Boddy K. K., et al., 2022, Journal of High Energy Astrophysics, 35, 112

Booth C. M., Schaye J., 2009, MNRAS, 398, 53

Borrow J., Schaller M., Bower R. G., Schaye J., 2022, MNRAS, 511, 2367

Borrow J., Schaller M., Bahé Y. M., Schaye J., Ludlow A. D., Ploeckinger S., Nobels F. S. J., Altamura E., 2023, MNRAS, 526, 2441

Borukhovetskaya A., Navarro J. F., Errani R., Fattahi A., 2022, MNRAS, 512, 5247

Boveia A., Doglioni C., 2018, Annual Review of Nuclear and Particle Science, 68, 429

Bovy J., 2015, ApJS, 216, 29

Boyarsky A., Drewes M., Lasserre T., Mertens S., Ruchayskiy O., 2019, Progress in Particle and Nuclear Physics, 104, 1

Boylan-Kolchin M., Bullock J. S., Kaplinghat M., 2011, MNRAS, 415, L40

Boylan-Kolchin M., Bullock J. S., Kaplinghat M., 2012, MNRAS, 422, 1203

Brook C. B., Stinson G., Gibson B. K., Roškar R., Wadsley J., Quinn T., 2012, MNRAS, 419, 771

Brooks A. M., Zolotov A., 2014, ApJ, 786, 87

Brooks A. M., Papastergis E., Christensen C. R., Governato F., Stilp A., Quinn T. R., Wadsley J., 2017, ApJ, 850, 97

Brouwer M. M., et al., 2021, A&A, 650, A113

Brown A. G. A., et al., 2018, A&A, 616, A1

Buckley M. R., Fox P. J., 2010, Phys. Rev. D, 81, 083522

Buckley M. R., Zavala J., Cyr-Racine F.-Y., Sigurdson K., Vogelsberger M., 2014, Phys. Rev. D, 90, 043524

Burger J. D., Zavala J., Sales L. V., Vogelsberger M., Marinacci F., Torrey P., 2022, MNRAS, 513, 3458

Cañas R., Elahi P. J., Welker C., del P Lagos C., Power C., Dubois Y., Pichon C., 2019, MNRAS, 482, 2039

Cardona-Barrero S., Battaglia G., Nipoti C., DiCintio A., 2023, Monthly Notices of the Royal Astronomical Society, 522, 3058–3066

Catinella B., et al., 2023, MNRAS, 519, 1098

Cattaneo A., Salucci P., Papastergis E., 2014, ApJ, 783, 66

Chabrier G., 2003, PASP, 115, 763

Chaikin E., Schaye J., Schaller M., Bahé Y. M., Nobels F. S. J., Ploeckinger S., 2022, MNRAS, 514, 249

Chambers K. C., et al., 2016, arXiv e-prints, p. arXiv:1612.05560

Chang Y.-Y., van der Wel A., da Cunha E., Rix H.-W., 2015, ApJS, 219, 8

Chapman S., Cowling T., Burnett D., Cercignani C., 1990, The Mathematical Theory of Non-uniform Gases: An Account of the Kinetic Theory of Viscosity, Thermal Conduction and Diffusion in Gases. Cambridge Mathematical Library, Cambridge University Press, https://books.google.nl/books?id=Cbp5JP2OTrwC

Charles E. J. E., et al., 2022, arXiv e-prints, p. arXiv:2209.15022

Cline J. M., 2021, arXiv e-prints, p. arXiv:2108.10314

Clowe D., Bradač M., Gonzalez A. H., Markevitch M., Randall S. W., Jones C., Zaritsky D., 2006, ApJ, 648, L109

Cole S., et al., 2005, MNRAS, 362, 505

Colín P., Avila-Reese V., Valenzuela O., Firmani C., 2002, ApJ, 581, 777

Collacchioni F., Lagos C. D. P., Mitchell P. D., Schaye J., Wisnioski E., Cora S. A., Correa C. A., 2020, MNRAS, 495, 2827

Collacchioni F., Correa C. A., Lagos C. D. P., Cora S. A., 2021, Boletin de la Asociacion Argentina de Astronomia La Plata Argentina, 62, 165

Correa C. A., 2021, MNRAS, 503, 920

Correa C. A., 2023, SciPost Phys. Proc., p. 059

Correa C. A., Schaye J., 2020, MNRAS, 499, 3578

Correa C. A., Wyithe J. S. B., Schaye J., Duffy A. R., 2015a, MNRAS, 450, 1514

Correa C. A., Wyithe J. S. B., Schaye J., Duffy A. R., 2015b, MNRAS, 450, 1521

Correa C. A., Wyithe J. S. B., Schaye J., Duffy A. R., 2015c, MNRAS, 452, 1217

Correa C. A., Schaye J., Clauwens B., Bower R. G., Crain R. A., Schaller M., Theuns T., Thob A. C. R., 2017, MNRAS, 472, L45

Correa C. A., Schaye J., Wyithe J. S. B., Duffy A. R., Theuns T., Crain R. A., Bower R. G., 2018a, MNRAS, 473, 538

Correa C. A., Schaye J., van de Voort F., Duffy A. R., Wyithe J. S. B., 2018b, MNRAS, 478, 255

Correa C. A., Schaye J., Trayford J. W., 2019, MNRAS, 484, 4401

Correa C. A., Schaller M., Ploeckinger S., Anau Montel N., Weniger C., Ando S., 2022, MNRAS, 517, 3045

Correa C., Schaller M., Schaye J., Ploeckinger S., Borrow J., Bahe Y., 2024, arXiv e-prints, p. arXiv:2403.09186

Crain R. A., et al., 2015, MNRAS, 450, 1937

Cyr-Racine F.-Y., Sigurdson K., Zavala J., Bringmann T., Vogelsberger M., Pfrommer C., 2016, Phys. Rev. D, 93, 123527

D'Onghia E., Springel V., Hernquist L., Keres D., 2010, ApJ, 709, 1138

Dalal N., Kravtsov A., 2022, arXiv e-prints, p. arXiv:2203.05750

Dalla Vecchia C., Schaye J., 2012, MNRAS, 426, 140

Das S., Maharana A., Poulin V., Sharma R. K., 2022, Phys. Rev. D, 105, 103503

Davé R., Spergel D. N., Steinhardt P. J., Wandelt B. D., 2001, ApJ, 547, 574

Dawson W., et al., 2013, in American Astronomical Society Meeting Abstracts #221. p. 125.04

Dekker A., Ando S., Correa C. A., Ng K. C. Y., 2022, Phys. Rev. D, 106, 123026

Desmond H., Wechsler R. H., 2015, MNRAS, 454, 322

Despali G., Sparre M., Vegetti S., Vogelsberger M., Zavala J., Marinacci F., 2019, MNRAS, 484, 4563

Dessert C., Rodd N. L., Safdi B. R., 2020, Science, 367, 1465

Dhal S., Singh S., Konar K., Paul R. K., 2023, Experimental Astronomy, 56, 715

Di Cintio A., Brook C. B., Dutton A. A., Macciò A. V., Stinson G. S., Knebe A., 2014, MNRAS, 441, 2986

Diaz Rivero A., Miranda V., Dvorkin C., 2019, Phys. Rev. D, 100, 063504

Dickinson C., et al., 2004, MNRAS, 353, 732

Dooley G. A., Peter A. H. G., Vogelsberger M., Zavala J., Frebel A., 2016, MNRAS, 461, 710

Driver S. P., et al., 2022, MNRAS, 513, 439

Dutton A. A., van den Bosch F. C., 2012, MNRAS, 421, 608

Dutton A. A., Macciò A. V., Frings J., Wang L., Stinson G. S., Penzo C., Kang X., 2016, MNRAS, 457, L74

Ebisu T., Ishiyama T., Hayashi K., 2022, Phys. Rev. D, 105, 023016

Einasto J., Kaasik A., Saar E., 1974, Nature, 250, 309

Eisenstein D. J., et al., 2005, ApJ, 633, 560

Elahi P. J., Thacker R. J., Widrow L. M., 2011, MNRAS, 418, 320

Elahi P. J., Cañas R., Poulton R. J. J., Tobar R. J., Willis J. S., Lagos C. d. P., Power C., Robotham A. S. G., 2019a, Publ. Astron. Soc. Australia, 36, e021

Elahi P. J., Poulton R. J. J., Tobar R. J., Cañas R., Lagos C. d. P., Power C., Robotham A. S. G., 2019b, Publ. Astron. Soc. Australia, 36, e028

Elbert O. D., Bullock J. S., Garrison-Kimmel S., Rocha M., Oñorbe J., Peter A. H. G., 2015, MNRAS, 453, 29

Elbert O. D., Bullock J. S., Kaplinghat M., Garrison-Kimmel S., Graus A. S., Rocha M., 2018, ApJ, 853, 109

Engler C., et al., 2021, MNRAS, 507, 4211

Erkal D., et al., 2018, MNRAS, 481, 3148

Erkal D., et al., 2019, MNRAS, 487, 2685

Essig R., McDermott S. D., Yu H.-B., Zhong Y.-M., 2019, Phys. Rev. Lett., 123, 121102

Farrar G. R., Peebles P. J. E., 2004, The Astrophysical Journal, 604, 1–11

Fattahi A., et al., 2016, MNRAS, 457, 844

Faucher-Giguère C.-A., 2020, MNRAS, 493, 1614

Feng J. L., Kaplinghat M., Yu H.-B., 2010, Phys. Rev. D, 82, 083525

Ferrero I., et al., 2017, MNRAS, 464, 4736

Flores R. A., Primack J. R., 1994, ApJ, 427, L1

Folsom D., Slone O., Lisanti M., Jiang F., Kaplinghat M., 2023, Probabilistic Inference of the Structure and Orbit of Milky Way Satellites with Semi-Analytic Modeling (arXiv:2311.05676)

Font A. S., McCarthy I. G., Belokurov V., 2021, MNRAS, 505, 783

Fritz T. K., Battaglia G., Pawlowski M. S., Kallivayalil N., van der Marel R., Sohn S. T., Brook C., Besla G., 2018, A&A, 619, A103

Gaia Collaboration et al., 2021, A&A, 649, A1

Gallazzi A., Brinchmann J., Charlot S., White S. D. M., 2008, MNRAS, 383, 1439

Garrison-Kimmel S., Boylan-Kolchin M., Bullock J. S., Kirby E. N., 2014, MNRAS, 444, 222

Gelmini G., Gondolo P., 2006, Phys. Rev. D, 74, 023510

Genina A., Read J. I., Fattahi A., Frenk C. S., 2022, MNRAS, 510, 2186

Gilman D., Bovy J., Treu T., Nierenberg A., Birrer S., Benson A., Sameie O., 2021, MNRAS, 507, 2432

Gilman D., Zhong Y.-M., Bovy J., 2023, Phys. Rev. D, 107, 103008

Gnedin O. Y., 2006, in Mamon G. A., Combes F., Deffayet C., Fort B., eds, EAS Publications Series Vol. 20, EAS Publications Series. pp 59–64 (arXiv:astro-ph/0510539), doi:10.1051/eas:2006048

Gnedin O. Y., Hernquist L., Ostriker J. P., 1999, ApJ, 514, 109

Gonzalez A. H., Sivanandam S., Zabludoff A. I., Zaritsky D., 2013, ApJ, 778, 14

Governato F., et al., 2010, Nature, 463, 203

Governato F., et al., 2012, MNRAS, 422, 1231

Green S. B., van den Bosch F. C., 2019, MNRAS, 490, 2091

Greengard L., Rokhlin V., 1987, Journal of Computational Physics, 73, 325

Hahn O., Michaux M., Rampf C., Uhlemann C., Angulo R. E., 2020, MUSIC2-monofonIC: 3LPT initial condition generator, Astrophysics Source Code Library, record ascl:2008.024

Han J., Cole S., Frenk C. S., Jing Y., 2016, MNRAS, 457, 1208

Hanany S., et al., 2000, ApJ, 545, L5

Harvey D., Massey R., Kitching T., Taylor A., Tittley E., 2015, Science, 347, 1462

Harvey D., Revaz Y., Robertson A., Hausammann L., 2018, MNRAS, 481, L89

Harvey D., Robertson A., Massey R., McCarthy I. G., 2019, MNRAS, 488, 1572

Hayashi K., Chiba M., Ishiyama T., 2020, ApJ, 904, 45

Hayashi K., Ibe M., Kobayashi S., Nakayama Y., Shirai S., 2021, Phys. Rev. D, 103, 023017

Hayashi K., Hirai Y., Chiba M., Ishiyama T., 2022, arXiv e-prints, p. arXiv:2206.02821

Helmi A., et al., 2018, A&A, 616, A12

Hildebrandt H., et al., 2017, MNRAS, 465, 1454

Hooper D., 2022, arXiv e-prints, p. arXiv:2209.14370

Hopkins P. F., et al., 2018, MNRAS, 480, 800

Ibe M., Yu H.-B., 2010, Physics Letters B, 692, 70

Iršič V., Viel M., Haehnelt M. G., Bolton J. S., Becker G. D., 2017, Phys. Rev. Lett., 119, 031302

Ishiyama T., et al., 2021, Monthly Notices of the Royal Astronomical Society, 506, 4210

Jardel J. R., Gebhardt K., 2012, ApJ, 746, 89

Jenkins A., 2010, MNRAS, 403, 1859

Jenkins A., 2013, MNRAS, 434, 2094

Jiang F., van den Bosch F. C., 2017, MNRAS, 472, 657

Jiang F., et al., 2023, MNRAS, 521, 4630

Kahlhoefer F., Schmidt-Hoberg K., Frandsen M. T., Sarkar S., 2013, Monthly Notices of the Royal Astronomical Society, 437, 2865–2881

Kahlhoefer F., Schmidt-Hoberg K., Kummer J., Sarkar S., 2015, MNRAS, 452, L54

Kahlhoefer F., Kaplinghat M., Slatyer T. R., Wu C.-L., 2019, J. Cosmology Astropart. Phys., 2019, 010

Kamada A., Kaplinghat M., Pace A. B., Yu H.-B., 2017, Phys. Rev. Lett., 119, 111102

Kaplan D. E., Krnjaic G. Z., Rehermann K. R., Wells C. M., 2010, J. Cosmology Astropart. Phys., 2010, 021

Kaplinghat M., Tulin S., Yu H.-B., 2016, Phys. Rev. Lett., 116, 041302

Kaplinghat M., Valli M., Yu H.-B., 2019, MNRAS, 490, 231

Kelley T., Bullock J. S., Garrison-Kimmel S., Boylan-Kolchin M., Pawlowski M. S., Graus A. S., 2019, MNRAS, 487, 4409

Kennicutt Robert C. J., 1998, ApJ, 498, 541

Kim S. Y., Peter A. H. G., Wittman D., 2017, MNRAS, 469, 1414

King I., 1962, AJ, 67, 471

Klypin A., Kravtsov A. V., Valenzuela O., Prada F., 1999, ApJ, 522, 82

Koda J., Shapiro P. R., 2011, MNRAS, 415, 1125

Komatsu E., et al., 2011, ApJS, 192, 18

Kong D., Kaplinghat M., Yu H.-B., Fraternali F., Mancera Piña P. E., 2022, ApJ, 936, 166

Kugel R., Borrow J., 2022, The Journal of Open Source Software, 7, 4240

Kuijken K., et al., 2019, A&A, 625, A2

Kummer J., Brüggen M., Dolag K., Kahlhoefer F., Schmidt-Hoberg K., 2019, MNRAS, 487, 354

Lange R., et al., 2015, MNRAS, 447, 2603

Laporte C. F. P., Gómez F. A., Besla G., Johnston K. V., Garavito-Camargo N., 2018, MNRAS, 473, 1218

Lelli F., McGaugh S. S., Schombert J. M., 2016, AJ, 152, 157

Lelli F., McGaugh S. S., Schombert J. M., Pawlowski M. S., 2017, ApJ, 836, 152

Leung G. Y. C., Leaman R., Battaglia G., van de Ven G., Brooks A. M., Peñarrubia J., Venn K. A., 2021, MNRAS, 500, 410

Li P., Lelli F., McGaugh S., Schombert J., 2018, A&A, 615, A3

Loeb A., Weiner N., 2011, Physical Review Letters, 106

Loveday J., et al., 2015, MNRAS, 451, 1540

Ludlow A. D., Schaye J., Schaller M., Richings J., 2019a, MNRAS, 488, L123

Ludlow A. D., Schaye J., Bower R., 2019b, MNRAS, 488, 3663

Ludlow A. D., Fall S. M., Wilkinson M. J., Schaye J., Obreschkow D., 2023, MNRAS, 525, 5614

Lynden-Bell D., Eggleton P. P., 1980, MNRAS, 191, 483

Lynden-Bell D., Wood R., 1968, Monthly Notices of the Royal Astronomical Society, 138, 495

Macciò A. V., Udrescu S. M., Dutton A. A., Obreja A., Wang L., Stinson G. R., Kang X., 2016, arXiv e-prints, p. arXiv:1607.01028

Mace C., Zeng Z. C., Peter A. H. G., Du X., Yang S., Benson A., Vogelsberger M., 2024, Convergence Tests of Self-Interacting Dark Matter Simulations (arXiv:2402.01604)

Macias O., van Leijen H., Song D., Ando S., Horiuchi S., Crocker R. M., 2021, MNRAS, 506, 1741

Mancera Piña P. E., Fraternali F., Oosterloo T., Adams E. A. K., Oman K. A., Leisman L., 2022, MNRAS, 512, 3230

Marra V., Perivolaropoulos L., 2021, Phys. Rev. D, 104, L021303

Massey R., et al., 2015, MNRAS, 449, 3393

McAlpine S., et al., 2016, Astronomy and Computing, 15, 72

McAlpine S., et al., 2022, MNRAS, 512, 5823

McGaugh S. S., 2012, AJ, 143, 40

McGaugh S. S., Li P., Lelli F., Schombert J. M., 2018, Nature Astronomy, 2, 924

McQuinn K. B. W., et al., 2024, ApJ, 961, 16

Meneghetti M., et al., 2022, A&A, 668, A188

Milgrom M., 1983, ApJ, 270, 365

Miller A. L., Zhao Y., 2023, Phys. Rev. Lett., 131, 081401

Miralda-Escudé J., 2002, ApJ, 564, 60

Moore B., 1994, Nature, 370, 629

Moore B., Quinn T., Governato F., Stadel J., Lake G., 1999, MNRAS, 310, 1147

Nadler E. O., Banerjee A., Adhikari S., Mao Y.-Y., Wechsler R. H., 2020, arXiv e-prints, p. arXiv:2001.08754

Nadler E. O., et al., 2021, Phys. Rev. Lett., 126, 091101

Nadler E. O., Yang D., Yu H.-B., 2023, ApJ, 958, L39

Nadler E. O., Gluscevic V., Driskell T., Wechsler R. H., Moustakas L. A., Benson A., Mao Y.-Y., 2024, arXiv e-prints, p. arXiv:2401.10318

Navarro J. F., Eke V. R., Frenk C. S., 1996, MNRAS, 283, L72

Navarro J. F., Frenk C. S., White S. D. M., 1997, ApJ, 490, 493

Newman A. B., Ellis R. S., Treu T., 2015, ApJ, 814, 26

Nishikawa H., Boddy K. K., Kaplinghat M., 2020, Phys. Rev. D, 101, 063009

Oñorbe J., Boylan-Kolchin M., Bullock J. S., Hopkins P. F., Kereš D., Faucher-Giguère C.-A., Quataert E., Murray N., 2015, MNRAS, 454, 2092

Ogiya G., van den Bosch F. C., Hahn O., Green S. B., Miller T. B., Burkert A., 2019, MNRAS, 485, 189

Oh S.-H., Brook C., Governato F., Brinks E., Mayer L., de Blok W. J. G., Brooks A., Walter F., 2011, AJ, 142, 24

Oman K. A., et al., 2015, MNRAS, 452, 3650

Orkney M. D. A., et al., 2022, MNRAS, 515, 185

Ostriker J. P., Peebles P. J. E., Yahil A., 1974, ApJ, 193, L1

Papastergis E., Giovanelli R., Haynes M. P., Shankar F., 2015, A&A, 574, A113

Pascale R., Posti L., Nipoti C., Binney J., 2018, MNRAS, 480, 927

Peebles P. J. E., 1982, ApJ, 263, L1

Perivolaropoulos L., Skara F., 2022, New Astron. Rev., 95, 101659

Perlmutter S., et al., 1999, ApJ, 517, 565

Peter A. H. G., Rocha M., Bullock J. S., Kaplinghat M., 2013, MNRAS, 430, 105

Pillepich A., et al., 2018, MNRAS, 473, 4077

Pizagno J., et al., 2007, AJ, 134, 945

Planck Collaboration et al., 2014a, A&A, 571, A16

Planck Collaboration et al., 2014b, A&A, 571, A20

Planck Collaboration et al., 2020, A&A, 641, A6

Ploeckinger S., Schaye J., 2020, MNRAS, 497, 4857

Pontzen A., Governato F., 2012, MNRAS, 421, 3464

Portinari L., Sommer-Larsen J., Tantalo R., 2004, MNRAS, 347, 691

Pospelov M., Ritz A., Voloshin M., 2008, Phys. Rev. D, 78, 115012

Poulin V., Smith T. L., Karwal T., Kamionkowski M., 2019, Phys. Rev. Lett., 122, 221301

Powell D. M., Vegetti S., McKean J. P., White S. D. M., Ferreira E. G. M., May S., Spingola C., 2023, MNRAS, 524, L84

Press W. H., Schechter P., 1974, ApJ, 187, 425

Pullen A. R., Benson A. J., Moustakas L. A., 2014, ApJ, 792, 24

Ragagnin A., et al., 2022, A&A, 665, A16

Randall S. W., Markevitch M., Clowe D., Gonzalez A. H., Bradač M., 2008, ApJ, 679, 1173

Read J. I., Gilmore G., 2005, MNRAS, 356, 107

Read J. I., Iorio G., Agertz O., Fraternali F., 2016, MNRAS, 462, 3628

Read J. I., Walker M. G., Steger P., 2018, MNRAS, 481, 860

Read J. I., Walker M. G., Steger P., 2019, MNRAS, 484, 1401

Reichardt C. L., et al., 2009, ApJ, 694, 1200

Ren T., Kwa A., Kaplinghat M., Yu H.-B., 2019, Physical Review X, 9, 031020

Revaz Y., 2023, A&A, 679, A2

Reyes R., Mandelbaum R., Gunn J. E., Pizagno J., Lackner C. N., 2011, MNRAS, 417, 2347

Richstein H., et al., 2024, arXiv e-prints, p. arXiv:2402.08731

Riess A. G., et al., 1998, AJ, 116, 1009

Riess A. G., Casertano S., Yuan W., Bowers J. B., Macri L., Zinn J. C., Scolnic D., 2021, ApJ, 908, L6

Riess A. G., et al., 2022, ApJ, 934, L7

Ristea A., Cortese L., Fraser-McKelvie A., Catinella B., van de Sande J., Croom S. M., Swinbank A. M., 2024, MNRAS, 527, 7438

Robertson A., Massey R., Eke V., 2017, MNRAS, 467, 4719

Robertson A., Harvey D., Massey R., Eke V., McCarthy I. G., Jauzac M., Li B., Schaye J., 2019, MNRAS, 488, 3646

Robertson A., Massey R., Eke V., Schaye J., Theuns T., 2021, MNRAS, 501, 4610

Robles V. H., Bullock J. S., 2021, Monthly Notices of the Royal Astronomical Society, 503, 5232

Robles V. H., et al., 2017, MNRAS, 472, 2945

Robles V. H., Kelley T., Bullock J. S., Kaplinghat M., 2019, MNRAS, 490, 2117

Rocha M., Peter A. H. G., Bullock J. S., Kaplinghat M., Garrison-Kimmel S., Oñorbe J., Moustakas L. A., 2013, MNRAS, 430, 81

Rogers K. K., Peiris H. V., 2021, Phys. Rev. Lett., 126, 071302

Roper F. A., Oman K. A., Frenk C. S., Benítez-Llambay A., Navarro J. F., Santos-Santos I. M. E., 2023, MNRAS, 521, 1316

Rose J. C., Torrey P., Vogelsberger M., O'Neil S., 2022, MNRAS,

Rubin V. C., Ford W. K. J., Thonnard N., 1978, ApJ, 225, L107

Rubin V. C., Ford W. K. J., Roberts M. S., 1979, ApJ, 230, 35

Sagunski L., Gad-Nasr S., Colquhoun B., Robertson A., Tulin S., 2021, J. Cosmology Astropart. Phys., 2021, 024

Sales L. V., Navarro J. F., Schaye J., Dalla Vecchia C., Springel V., Booth C. M., 2010, MNRAS, 409, 1541

Sales L. V., Wetzel A., Fattahi A., 2022, Nature Astronomy, 6, 897

Sameie O., Yu H.-B., Sales L. V., Vogelsberger M., Zavala J., 2020, Phys. Rev. Lett., 124, 141102

Sameie O., et al., 2021, MNRAS, 507, 720

Santos-Santos I. M. E., et al., 2020, MNRAS, 495, 58

Sawala T., et al., 2016, MNRAS, 457, 1931

Schaller M., et al., 2015, MNRAS, 451, 1247

Schaller M., Gonnet P., Draper P. W., Chalk A. B. G., Bower R. G., Willis J., Hausammann L., 2018, SWIFT: SPH With Inter-dependent Fine-grained Tasking, Astrophysics Source Code Library, record ascl:1805.020 (ascl:1805.020)

Schaller M., et al., 2023, arXiv e-prints, p. arXiv:2305.13380

Schaye J., Dalla Vecchia C., 2008, MNRAS, 383, 1210

Schaye J., et al., 2015, MNRAS, 446, 521

Scheck D., Sanders J. S., Biffi V., Dolag K., Bulbul E., Liu A., 2023, A&A, 670, A33

Schombert J., McGaugh S., 2014, Publ. Astron. Soc. Australia, 31, e036

Schumann M., 2019, Journal of Physics G Nuclear Physics, 46, 103003

Shah N., Adhikari S., 2023, arXiv e-prints, p. arXiv:2308.16342

Shapiro S. L., 2018, Phys. Rev. D, 98, 023021

Shen X., Hopkins P. F., Necib L., Jiang F., Boylan-Kolchin M., Wetzel A., 2021, MNRAS, 506, 4421

Silverman M., Bullock J. S., Kaplinghat M., Robles V. H., Valli M., 2023, MNRAS, 518, 2418

Simon J. D., 2019, ARA&A, 57, 375

Sipp M., LaChance P., Croft R., Ni Y., Di Matteo T., 2023, MNRAS, 525, 1807

Slone O., Jiang F., Lisanti M., Kaplinghat M., 2023, Phys. Rev. D, 107, 043014

Smoot G. F., et al., 1992, ApJ, 396, L1

Spergel D. N., Steinhardt P. J., 2000, Phys. Rev. Lett., 84, 3760

Springel V., Frenk C. S., White S. D. M., 2006, Nature, 440, 1137

Steinmetz M., Navarro J. F., 1999, ApJ, 513, 555

Taylor J. E., Babul A., 2001, ApJ, 559, 716

Teyssier R., Pontzen A., Dubois Y., Read J. I., 2013, MNRAS, 429, 3068

Tollerud E. J., Boylan-Kolchin M., Bullock J. S., 2014, MNRAS, 440, 3511

Tollet E., Cattaneo A., Mamon G. A., Moutard T., van den Bosch F. C., 2017, MNRAS, 471, 4170

Trayford J. W., et al., 2015, MNRAS, 452, 2879

Trayford J. W., Frenk C. S., Theuns T., Schaye J., Correa C., 2019, MNRAS, 483, 744

Tsai Y.-D., McGehee R., Murayama H., 2020, arXiv e-prints, p. arXiv:2008.08608

Tulin S., Yu H.-B., 2018, Phys. Rep., 730, 1

Tulin S., Yu H.-B., Zurek K. M., 2013, Phys. Rev. D, 87, 115007

Tully R. B., Fisher J. R., 1977, A&A, 54, 661

Turner H. C., Lovell M. R., Zavala J., Vogelsberger M., 2021, MNRAS, 505, 5327

Valli M., Yu H.-B., 2018, Nature Astronomy, 2, 907

Vasiliev E., Belokurov V., Erkal D., 2021, MNRAS, 501, 2279

Vogelsberger M., Sijacki D., Kereš D., Springel V., Hernquist L., 2012, MNRAS, 425, 3024

Vogelsberger M., Zavala J., Simpson C., Jenkins A., 2014, MNRAS, 444, 3684

Vogelsberger M., Zavala J., Cyr-Racine F.-Y., Pfrommer C., Bringmann T., Sigurdson K., 2016, MNRAS, 460, 1399

Vogelsberger M., Zavala J., Schutz K., Slatyer T. R., 2019, MNRAS, 484, 5437

Wang J., Frenk C. S., Navarro J. F., Gao L., Sawala T., 2012, MNRAS, 424, 2715

Wang J., Bose S., Frenk C. S., Gao L., Jenkins A., Springel V., White S. D. M., 2020, Nature, 585, 39

Wetzel A. R., Hopkins P. F., Kim J.-h., Faucher-Giguère C.-A., Kereš D., Quataert E., 2016, ApJ, 827, L23

Wiersma R. P. C., Schaye J., Theuns T., Dalla Vecchia C., Tornatore L., 2009, MNRAS, 399, 574

Wittenburg N., Kroupa P., Banik I., Candlish G., Samaras N., 2023, MNRAS, 523, 453

Wittman D., Golovich N., Dawson W. A., 2018, ApJ, 869, 104

Wright R. J., Lagos C. d. P., Power C., Correa C. A., 2021, MNRAS, 504, 5702

Yang D., Nadler E. O., Yu H.-B., 2023, ApJ, 949, 67

Yoshida N., Springel V., White S. D. M., Tormen G., 2000, ApJ, 544, L87

Zavala J., Vogelsberger M., Walker M. G., 2013, MNRAS, 431, L20

Zeng Z. C., Peter A. H. G., Du X., Benson A., Kim S., Jiang F., Cyr-Racine F.-Y., Vogelsberger M., 2022, Monthly Notices of the Royal Astronomical Society, 513, 4845

Ziegler B. L., et al., 2002, ApJ, 564, L69

de Bernardis P., et al., 2000, Nature, 404, 955

de Blok W. J. G., Walter F., Brinks E., Trachternach C., Oh S. H., Kennicutt R. C. J., 2008, AJ, 136, 2648

van de Voort F., Bahé Y. M., Bower R. G., Correa C. A., Crain R. A., Schaye J., Theuns T., 2017, MNRAS, 466, 3460

van den Bosch F. C., 2017, MNRAS, 468, 885

van den Bosch F. C., Ogiya G., Hahn O., Burkert A., 2018, MNRAS, 474, 3043

van der Marel R. P., Kallivayalil N., 2014, ApJ, 781, 121